2018

Investigation of the use of novel ceramic oxide nanoparticles to improve the clinical outcome of radiation therapies

Sally R. McKinnon
University of Wollongong

INVESTIGATION OF THE USE OF NOVEL CERAMIC OXIDE NANOPARTICLES TO IMPROVE THE CLINICAL OUTCOME OF RADIATION THERAPIES

A Dissertation Submitted in Fulfilment of
the Requirements for the Award of the Degree of

Doctor of Philosophy

from

UNIVERSITY OF WOLLONGONG

by

Sally R. McKinnon

B. Med. Rad. Physics (Advanced)

School of Physics
Faculty of Engineering and Information Sciences

CERTIFICATION

I, Sally R. McKinnon, declare that this thesis, submitted in fulfilment of the requirements for the award of Doctor of Philosophy, in the School of Physics, Faculty of Engineering and Information Sciences, University of Wollongong, is wholly my own work unless otherwise referenced or acknowledged. The document has not been submitted for qualifications at any other academic institution.

Sally R. McKinnon
August 2018

Table of Contents

List of Tables

List of Figures

Investigation of the use of novel ceramic oxide nanoparticles to improve the clinical outcome of radiation therapies

Sally R. McKinnon

A Thesis for

School of Physics
University of Wollongong

ABSTRACT

The use of nanoparticles (NPs) to enhance the efficacy of different radiotherapy techniques is investigated by means of Monte Carlo simulation in this PhD project. The dose enhancement of radiation therapy in order to increase the ratio of tumour cell killing to normal tissue damage is an area of much interest in the medical physics research community. With increasing spatial and energy modulation of radiotherapy beams, the dose to tumour tissue can be intensified whilst sparing neighbouring healthy tissue. The advancement in capabilities of beam modulation does however have limitations and this is why methods of dose escalation preferential to cancerous tumour cells are an interesting area of current research.

Nanoparticle dose enhancement shows great potential for the optimisation of radiation therapy modalities which is demonstrated in simulations and by experimental evidence. In order for NP dose enhancement to be applied in a clinical radiotherapy setting, a thorough fundamental study of the mechanism of dose enhancement is required. The mechanism of physical dose enhancement of radiation therapy modalities, including conventional X-ray and proton therapy, is studied by means of Geant4 Monte Carlo simulations presented in this thesis.

This PhD thesis presents simulation studies on both micro- and nano-scales calculating dose enhancement from novel ceramic oxide NPs, compared to widely studied, dose enhancing gold NPs. Customised Geant4 simulations have been developed in this project to model dose enhancement in water volumes in proximity to various NPs, approximating the conditions of radiation dose enhancement in cells or tissue. The effect of size, shape, concentration and distribution of the NPs within a cell volume is investigated by means of Geant4 simulations.

A Geant4 Monte Carlo simulation has been developed to model the dose distribution and secondary electron production enhancement in a cell population due to ceramic oxide NPs. The effect of various NP and simulation parameters including NP type, size, distribution and photon field energy have been investigated and are presented in this thesis. Results have shown potential dose enhancement from ceramic oxide NPs and also support and explain

the experimental results obtained by collaborating biological researchers.

The track structure simulation approach is used to calculate radial dose distributions around various NPs in proton therapy. This is an topic of recent interest to research, potentially combining the dosimetric benefits of proton therapy with the dose enhancing and radiation sensitizing capabilities of high-Z nanoparticles, including ceramic oxide NPs which are the focus of this PhD project. The dose enhancement effect with respect to proton energy, NP material, geometry and other simulation factors are presented as well as the simulation of the secondary electron yield from a C_{60} NP, compared to the analytical calculation of low energy electron emission from decay of collective plasmon excitation. The influence and effect of fundamental physics parameters on simulation results is presented including the effect of atomic deexcitation and improved interaction cross-sections lowering the energy range of simulations with more up to date Geant4 versions.

KEYWORDS: External Beam Radiation Therapy, Proton Therapy, Nanoparticles, Monte Carlo Simulation, Geant4, Dose Enhancement

Acknowledgements

I would like to thank my supervisors and the staff of the Centre for Medical Radiation Physics (CMRP) for their support and guidance over the duration of my PhD candidature. I especially acknowledge the major role in the completion of this project of my principle supervisor, Dr Susanna Guatelli. Susanna has been a constant source of positive encouragement, inspiration and academic support throughout my postgraduate research project and I would like to thank her for the tireless work she does on behalf of and as a dedicated advocate for her students. The guidance and support of Distinguished Professor Anatoly Rosenfeld has also been very much appreciated over the years that I have been a part of the CMRP.

My fellow postgraduate students in the CMRP and the School of Physics at the University of Wollongong deserve special mention and my thanks. The constantly encouraging and positive attitudes of my colleagues has been an invaluable source of inspiration to me over the past few years and I greatly appreciate the friendships formed with this group of wonderful people. In particular I would like to acknowledge Lachlan Chartier, for his assistance with the use of the computer cluster, as well as Elette Engels for her collaborative work in her undergraduate research and honours year project.

I would like to thank the University of Wollongong Information Technology Services (ITS) for computing time on the UOW High Performance Computing Cluster. The technical support of Dr Dean Cutajar to utilise the CMRP computer cluster has also been extremely helpful. I would like to acknowledge the Targeted Nano-Therapies (TNT) group at the University of Wollongong, in particular the group leaders Dr Moeava Tehei and Associate Professor Michael Lerch for their commitment to collaborative research and the invaluable discussions and insight provided on this project.

Lastly, I would like to acknowledge the continuous, unflagging and ongoing support of my friends (most especially, my housemates past and present), my sisters and my parents who have all supported me with patience and kindness, no matter how stressed and unsociable I have been, I know it can't have been easy for you at times, so thank you for sticking by me.

This research has been conducted with the support of the Australian Government Research Training Program Scholarship.

List of Publications

Alexey Verkhovtsev, **Sally McKinnon**, Pablo de Vera, Eugene Surdutovich, Susanna Guatelli, Andrei V. Korol, Anatoly Rosenfeld, Andrey V. Solov'yov (2015) "Comparative analysis of the secondary electron yield from carbon nanoparticles and pure water medium." *The European Physical Journal D* 69(4): 1-9.

H.N. Tran, M. Karamitros, V.N. Ivanchenko, S. Guatelli, **S. McKinnon**, K. Murakami, T. Sasaki, S. Okada, M.C. Bordage, Z. Francis, Z. El Bitar, M.A. Bernal, J.I. Shin, S.B. Lee, Ph. Barberet, T.T. Tran, J.M.C. Brown, T.V. Nhan Hao, S. Incerti (2016) "Geant4 Monte Carlo simulation of absorbed dose and radiolysis yields enhancement from a gold nanoparticle under MeV proton irradiation" *Nuclear Instruments and Methods in Physics Research B* 373: 126-139.

Sally McKinnon, Elette Engels, Moeava Tehei, Konstantin Konstantinov, Stéphanie Corde, Sianne Oktaria, Sebastien Incerti, Michael Lerch, Anatoly Rosenfeld, Susanna Guatelli (2016) "Study of the effect of ceramic Ta_2O_5 nanoparticle distribution on cellular dose enhancement in a kilovoltage photon field" *Physica Medica* 32(10): 1216-24.

Callum Stewart, Konstantin Konstantinov, **Sally McKinnon**, Susanna Guatelli, Michael Lerch, Anatoly Rosenfeld, Moeava Tehei, and Stéphanie Corde (2016) "First proof of bismuth oxide nanoparticles as efficient radiosensitisers on highly radioresistant cancer cells" *Physica Medica* 32(11): 1444-52.

Elette Engels, Stéphanie Corde, **Sally McKinnon**, Moeava Tehei, Konstantin Konstantinov, Sebastien Incerti, Anatoly Rosenfeld, Michael Lerch, and Susanna Guatelli (2016) "Optimizing dose enhancement with ta nanoparticles for synchrotron microbeam activated

radiation therapy." *Physica Medica* 32(12): 1852-61.

Sally McKinnon, Susanna Guatelli, Sebastien Incerti, Vladimir Ivanchenko, Moeava Tehei, Michael Lerch, Stéphanie Corde, Konstantin Konstantinov, Anatoly Rosenfeld (2016) "Local dose enhancement of proton therapy by ceramic oxide nanoparticles investigated with Geant4 simulations" *Physica Medica* 32(12): 1584-93.

List of Conference Presentations

Sally McKinnon, Susanna Guatelli, Peter Lazarakis, George Takacs, Michael Lerch, Sebastien Incerti, and Anatoly Rosenfeld "Enhancement of proton therapy by means of High-Z nanoparticles: a Monte Carlo simulation study" Oral Presentation, 4th Modelling of Tumours (MOT) Meeting, Adelaide, 2012

Sally McKinnon, Susanna Guatelli, Peter Lazarakis, George Takacs, Michael Lerch, Sebastien Incerti, and Anatoly Rosenfeld "Enhancement of proton therapy with gold nanoparticles: a Monte Carlo simulation study" Oral Presentation, EPSM, Gold Coast, 2012

Sally McKinnon, Susanna Guatelli, Peter Lazarakis, George Takacs, Michael Lerch, Sebastien Incerti, and Anatoly Rosenfeld "Enhancement of proton therapy with gold nanoparticles: a Monte Carlo simulation study" Oral Presentation, Nano-IBCT Workshop Madrid, Spain, 2012

Sally McKinnon, Susanna Guatelli, George Takacs, Michael Lerch, Peter Lazarakis, Sebastien Incerti, and Anatoly Rosenfeld "Enhancement of Proton Therapy with High-Z Nanoparticles: a Monte Carlo Simulation Study" Oral Presentation, 2nd Geant4 Australian School and Monte Carlo Workshop, Wollongong, 2013

Sally McKinnon, Susanna Guatelli, George Takacs, Michael Lerch, Peter Lazarakis, Sebastien Incerti, and Anatoly Rosenfeld "Enhancement of Proton Therapy by High-Z Nanoparticles: Geant4 Monte Carlo simulation study" Poster Presentation, 2nd Nano-IBCT Conference Sopot, Poland, 2013 [1]

Sally McKinnon, Susanna Guatelli, Michael Lerch, Sebastien Incerti, and Anatoly Rosenfeld "Nanoscale Enhancement of Proton Therapy by High-Z Nanoparticles Investigated with Monte Carlo Simulation" Oral Presentation, CSM Melbourne, 2014

Sally McKinnon, Susanna Guatelli, Sebastien Incerti, Stephanie Corde, Konstantin Konstantinov, Moeava Tehei, Michael Lerch, and Anatoly Rosenfeld "Geant4 Simulation of Dose Enhancement of a Proton Beam by Nanoparticles" Oral Presentation, MMND-IPCT Port Douglas, 2014

Sally McKinnon, Susanna Guatelli, Sebastien Incerti, Stephanie Corde, Konstantin Konstantinov, Moeava Tehei, Michael Lerch, and Anatoly Rosenfeld "Dose Enhancement of a Proton Beam by Nanoparticles investigated by Geant4 Simulation" Oral Presentation, IEEE NSS-MIC Seattle, USA, 2014

Sally McKinnon, Elette Engels, Moeava Tehei, Konstantin Konstantinov, Stéphanie Corde, Sianne Oktaria, Sebastien Incerti, Michael Lerch, Anatoly Rosenfeld, Susanna Guatelli "Study of the effect of ceramic Ta_2O_5 nanoparticle distribution on cellular dose enhancement in a kilovoltage photon field" Poster Presentation, 14th International Workshop on Radiation Damage to DNA, Melbourne, 2016

List of Abbreviations

CNS	central nervous system
DEF	dose enhancement factor
DER	dose enhancement ratio
DSB	Double Strand Break
EBRT	External Beam Radiation Therapy
EF	enhancement factor
IMRT	Intensity Modulated Radiotherapy
LEM	Local Effect Model
LET	linear energy transfer
linac	linear accelerator
MLC	multi-leaf collimator
MRT	Microbeam Radiation Therapy
NP	Nanoparticle
PER	protection enhancement ratio
PIXE	Particle Induced X-Ray Emission
RBE	relative biological effectiveness
REF	radiosensitization enhancement factor
ROS	Reactive Oxygen Species

SER	sensitisation enhancement ratio
SOBP	Spread Out Bragg Peak
SSB	Single Strand Break

Chapter 1

Introduction

1.1 Introduction

Cancer is one of the leading causes of death in the world today [2]. As stated by the World Health Organisation, in 2012 there were 14 million new cancer cases, and 8 million deaths related to cancer [2]. This is an issue globally both socially and economically, with cancer being a leading cause of death across all continents. Cancer occurs when there is uncontrolled proliferation of cells within the body.

Approximately 50% of cancer patients are prescribed radiation therapy (also called radiotherapy) as part of their treatment [3]. Radiotherapy aims to irreparably damage the tumour cells including cellular DNA or other cell structures [4] which results in cell death (by several possible mechanisms) and prevention of cell proliferation by inhibiting the ability of cells to replicate [4]. The continuous refinement of radiotherapy techniques is an important area of research in order to increase the survival of patients and at the same time to lower the chance of negative side effects from radiotherapy treatment. A major issue for consideration in the development of radiation therapy treatments is, therefore, the minimisation of unwanted damaging radiation dose delivered to normal, healthy tissue in the process of

delivering a dose sufficient to achieve the goal of tumour control. Damage to normal tissue can result in collateral effects such as early side-effects which give patients a reduced quality of life, as well as an increased risk of secondary cancer induction some time after treatment.

The application of nanoparticles (NPs) within a target tumour is a novel proposed method to enhance the clinical outcomes of radiation therapy by increasing the effectiveness of dose delivered to the tumour and reducing the probability of normal tissue complications. High atomic number (high-Z) NPs are currently investigated as possible solutions to improve the clinical outcome of radiotherapy whilst at the same time reducing the negative side effects of radiation damage to healthy tissue. This technology consists of embedding NPs in the tumour, often by means of chemical agents, followed by irradiation. Because of their high atomic number, the presence of NPs increases the dose delivered to target tumours, with the possibility of optimising the treatment delivery, eventually reducing the collateral effects. Therefore, NP enhanced radiation therapy is a current and promising area of research targeting the improvement of cancer treatment.

This research project is dedicated to the investigation of the dose enhancement produced by novel ceramic oxides in conventional X-ray radiotherapy and proton therapy. This project was conducted in collaboration with the University of Wollongong's Institute for Superconducting and Electronic Materials (ISEM) and the Illawarra Health and Medical Research Institute (IHMRI) to evaluate novel ceramic materials developed at ISEM for radio-enhancement. Novel ceramic oxide nanomaterials have different characteristics from the widely studied gold NPs, both in terms of their chemical and biological behaviour in cells and the physical interaction of radiation with them. It is therefore important to carefully study such proposed ceramic NPs ceramic oxide nanoparticles to understand the basis of their dose enhancement of radiation therapy.

This project investigates the role of Ta_2O_5, Bi_2O_3 and CeO_2 NPs to enhance the effectiveness of kV and MV photon, and proton radiation therapy. This study has been performed by means of Monte Carlo simulations.

1.1.1 Radiobiology of Cancer Therapy

The aim of radiotherapy is to cause damage to tumour cells, including cellular DNA, so that the tumour cells die and do not divide and spread. The mechanism causing tumour cell death in radiation therapy is a combination of physical, chemical, and biological processes including direct ionization and energy deposition (direct damage), increased water radiolysis and free radical actions (indirect damage). Direct damage occurs when either primary or secondary radiation directly breaks the DNA double helix structure whereas indirect damage occurs when reactive oxygen species (ROS) are created in the vicinity of cell nucleus, and cause damage to the DNA structure by physical-chemical and chemical reactions [7]. ROS are species of reactive oxygen with a free electron in the outer electron shell which allows the molecule, or radical, to readily react with other molecules [6].

DNA damage can occur by several mechanisms, including single strand breaks (SSB) and double strand breaks (DSB). SSBs result when damage occurs to a single strand of the DNA double helix. Likewise, DSBs result when both strands of the DNA double helix structure are damaged within a few base pairs of each break [8]. Figure 1.1 shows the difference between a SSB and a DSB. Two SSBs can be considered a DSB when located within less than 10 base pairs, as determined by the ability of these to be detected as DSBs by electrophoresis [9].

SSBs are simple to repair but DSBs are much more complicated and are more likely to result in biological effects such as cell death or mutation. Correct repair of DSB is important in

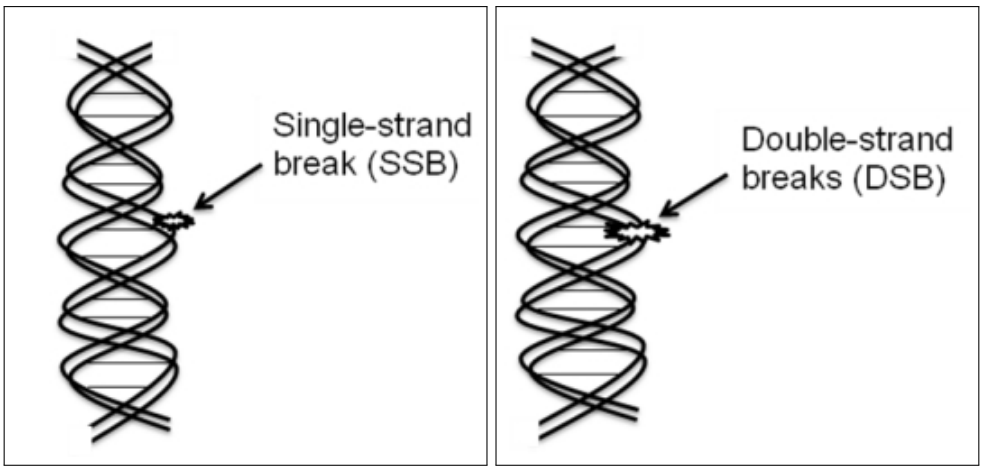

Figure 1.1: Graphical representation of a single-strand break of a DNA double helix (left) compared to a double-strand break (right). Figure reproduced from Baskar et al. (2012).

order to avoid mutation in the DNA which may lead to carcinogenesis [10]. There are multiple pathways to the repair of DSBs including homologous recombination and DNA end-joining [10]. If DSBs are repaired by homologous repair, there is a possibility of errors in the DNA being introduced.

Reactive species are found in elevated levels in cancer tissue, which contributes to enhanced, out of control cell proliferation typically seen in tumour growth. A major part of the effectiveness of radiotherapy is thought to be due to the action of free radical species above normal elevated levels in cancer cells [5], resulting in indirect damage to cells and DNA. There remains a balance in cancer cells between ROS and antioxidant actions which can be exploited in order to promote cell killing of cancerous cells.

The increased action of free radicals in tumours as a consequence of therapeutic irradiation, results in the increased killing of the tumour cells. This is why the action of free radicals is an important factor when studying the enhancement mechanisms applicable in radiotherapy. If the production of free radicals can be enhanced within a tumour during radiation therapy treatment, it is possible that this will result in an improved outcome for cancer patients.

The resistance of some cancer cells, for example glioblastoma cells, to the damage of ionizing radiation (radioresistance) poses problems for the treatment of these types of tumours with radiotherapy [11]. Glioblastoma is a highly radioresistant form of cancer in the brain [12]. Treatment of glioblastoma with chemotherapy is challenging due to the difficulty of delivering the drugs to the tumour across the blood-brain barrier. When the effectiveness of radiotherapy is reduced, and surgery is limited by the location of a tumour (for example in sensitive areas of the brain) it would be desirable to increase the sensitivity of tumour cells to radiation. Nanoparticles have been shown to have the potential to achieve this goal [11].

1.1.2 Radiation Therapy Techniques

This project investigates the effect of NPs in conventional (low and high energy X-ray) radiotherapy and proton therapy. X-ray and electron radiotherapy are the only EBRT modalities available clinically at this time in Australia, while proton and heavy-ion therapy are envisioned for the future. In the next few years proton therapy will become available at the Royal Adelaide Hospital in South Australia [13, 14].

EBRT is most commonly delivered by a high-energy photon beam from a megavoltage linear accelerator (linac) but may also be delivered by kilovoltage X-ray sources for the treatment of more superficial lesions. Linear accelerator technology has developed since the middle of the 20th century to achieve the current technology used in cancer therapy today. A megavoltage photon beam is produced by an electron beam originating from an electron gun, accelerated along a waveguide and then directed by bending magnets to hit a target, producing X-rays by bremsstrahlung interactions [15, ch. 1]. The photon beam is then shaped and modulated depending on the treatment requirements and prescription, as well as the machine's capabilities and limitations.

EBRT commonly consists of fractionated (multiple treatments delivered over several days or weeks) delivery of therapeutic doses of radiation. Fractionation allows a higher total dose to be delivered to tumour tissue while normal tissue is better able to recover from collateral damage. The fractionation and dose prescription are tumour-site dependent as well as depending on the treatment intent (i.e. palliative or curative intent). The conformation of treatment beams to target shape is achieved in modern radiotherapy centres by a technology known as Intensity-Modulated Radiotherapy (IMRT). IMRT allows the shape of the incident beam to be modulated during treatment by means of a multi-leaf collimator (MLC). The MLC allows for dose to be delivered with a greater conformity to tumour volume, while sparing nearby sensitive organs.

X-ray and γ-ray radiotherapy are characterised by high entrance dose and also significant exit dose. Proton therapy, in contrast to X-ray or γ-ray radiotherapy, uses a beam of heavy charged particles to deliver therapeutic dose to tumour tissue [16]. The main advantages of proton therapy over photon radiotherapy modalities is the ability to get strong conformity of dose deposition to the target tumour volume to enable better sparing of healthy tissue and the elimination of exit dose to patients' normal tissue. Proton therapy is suited to radioresistant, deep-seated tumours, and tumours located in close proximity to sensitive organs or tissue.

The range of monoenergetic protons is well-defined as the depth dose distribution exhibits the characteristic Bragg peak shown in Figure 1.2. In order to deliver dose to a volume greater than the narrow part of tumour tissue at the end of the Bragg peak, several proton beams of different energies are combined so that the Bragg peak is able to be essentially "spread out" over the tumour volume - in a Spread-Out Bragg Peak (SOBP).

Studies have been performed to assess the efficacy of proton therapy for the treatment of tumours at various sites in the body, with mixed results. A review of the advantages of

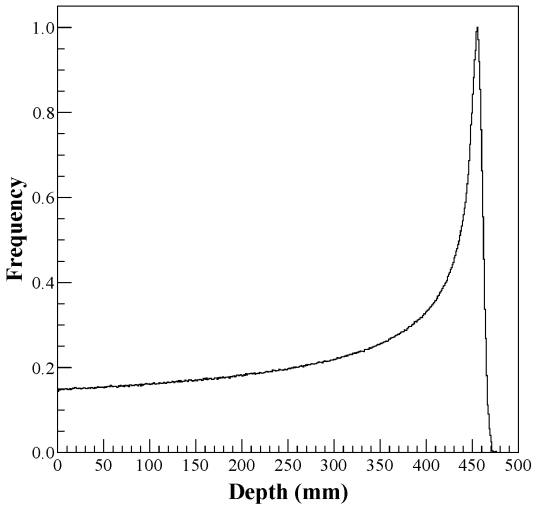

Figure 1.2: Simulated depth dose curve showing the Bragg Peak from 280 MeV proton beam incident on water phantom.

proton therapy for the treatment of tumours of the central nervous system (CNS) is presented by Gridley et al. (2010). These researchers reviewed data from proton therapy studies, including comparisons with photon radiotherapy techniques, and found that in the case of tumours of the CNS proton therapy has the potential to treat the tumour volume with lower toxicity to normal tissue and greater clinical outcomes.

The advantages of proton therapy over conventional therapy also include increased relative biological effectiveness (RBE) in the Bragg peak, or SOBP region. Nikjoo et al. (1999) showed computationally the factors which contribute to the biological effectiveness of electrons, protons and alpha particles. This study shows that for a 4 MeV proton beam 61% of DSBs are caused by direct damage while 39% are due to indirect damage deriving from free radicals.

Protons can interact by means of electronic or nuclear interactions [18]. A nuclear interaction may occur when a heavy charged particle of sufficient energy impacts the nucleus of a target atom [19, p. 164]. This type of interaction has a low probability in the therapeutic proton energy range, however is still significant as it will result in secondary neutrons

which can deposit dose outside the target volume [18]. Paganetti (2002) showed through Monte Carlo simulation that in a representative clinical proton therapy beam (160 MeV primary protons) about 20% of primary protons underwent nuclear interactions in the water medium. Secondary neutrons were then able to react and produced secondary protons, resulting in a dose distribution beyond the Bragg peak, and outside the target tumour volume. Paganetti (2002) reported that the contribution of neutron dose at a point 2 cm distal and lateral to the target volume was less than 0.02% of the SOBP dose with 160 MeV primary protons. Figure 1.3 reproduces the depth-dose profiles due to primary or secondary particles from Paganetti (2002). The biological effect of this dose, in terms of secondary cancer risk, is negligible [18].

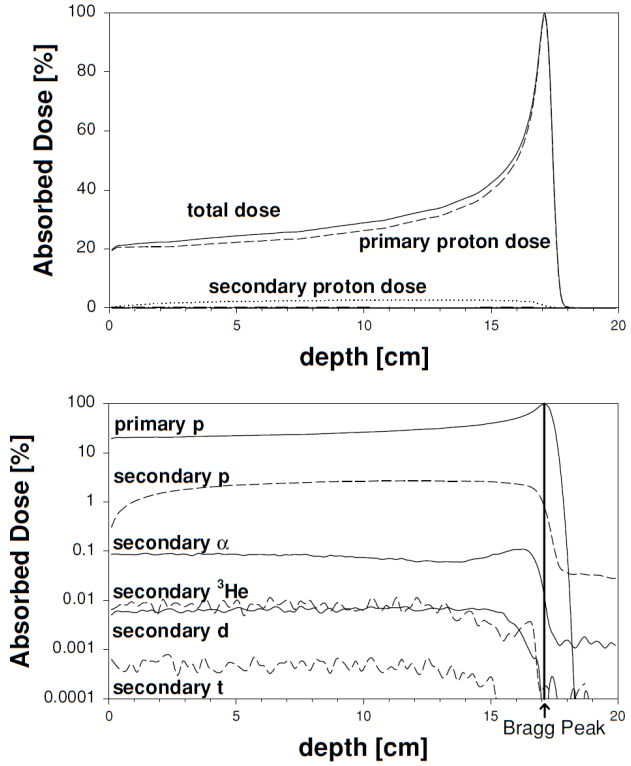

Figure 1.3: The upper figure shows the total dose and the dose due to primary and secondary protons. The lower figure compares, on a logarithmic scale, the doses due to different types of particles (solid lines: primary protons (p), secondary α and deuterons (d); dashed lines: secondary p, ^{3}He, tritons (t)). A vertical line indicates the position of the maximum of the Bragg peak. Figure reproduced from Paganetti (2002).

1.1.3 Nanoparticle Dose Enhancement of Radiation Therapy

1.1.3.1 X-ray Radiotherapy

The concept behind NP radio-enhancement utilizes the ability of high-Z materials, such as increasing the number of photoelectric interactions, to produce a higher number of low energy electrons resulting in an enhanced dose at the interface between the NP and the surrounding tumour. The increased electron density and photon attenuation coefficients with increasing Z, in the case of kilovoltage photons, explains the fundamental mechanism or the origin of radio-enhancement, however in the megavoltage photon range, energy absorption is much lower.

Terminology and calculated or measured factors used to describe radiation dose enhancement (radio-enhancement) caused by NPs varies between authors and research groups. Some terms commonly used to measure radio-enhancement are dose enhancement ratio (DER), sensitiser or sensitisation enhancement ratio (SER), radiosensitization enhancement factor (REF) and dose enhancement factor (DEF) or enhancement factor (EF). Alternatively, radio-protective NP behaviour may be described using a factor such as a protection enhancement ratio (PER) [20]. $PER_{SF=10\%}$ is defined in Briggs et al. (2013) as the ratio of doses in the presence of NP to the control, at 10% cell survival. SER is defined by Jain et al. (2011) as the ratio of areas under the surviving fraction curves of untreated cells compared to cells treated with a nanoparticle-sensitiser. Brown et al. (2013) describe a sensitisation enhancement ratio (SER) calculated as the ratio of doses required with and without NP giving 10% surviving fraction on a cell survival curve. DEF is defined by Alqathami et al. (2013) in their paper on a 3D radiochromic dosimeter as the ratio between the slopes of dose vs. change in optical density plots of a dosimeter doped with NPs and of a control. DER is frequently used in Monte Carlo studies and is generalised as the ratio of dose deposited with nanoparticle

material to that without NP material [24, 25]. As the most widely accepted term for description of Monte Carlo simulation study, DER will be used in the majority of the discussion in this thesis.

The dose enhancement in kilovoltage or megavoltage irradiation is the result of different physical effects, due to the difference in absorption of photons between these energies. In the case of gold, at photon energies below around 500 keV, the photoelectric effect cross-section dominates the total attenuation cross-section, while at higher energies Compton scattering becomes more significant as well as pair production above the 1.022 MeV threshold, as shown in Figure 1.4a. The photoelectric mass attenuation coefficient at low energy is related to the photon energy and material atomic number (Z), as shown in Equation 1.1 obtained from Attix [2004, p. 140].

$$\frac{\mu_{photoelectric}}{\rho} \propto \left(\frac{Z}{E}\right)^{n} \qquad (\mathrm{cm}^2/\mathrm{g}) \qquad \text{where } n = 3\text{-}4 \tag{1.1}$$

Pair production occurs above the threshold of 1.022 MeV and results in the absorption of the incident photon with energy transferred to an electron-positron pair. The mass attenuation coefficient of pair production is directly proportional to the atomic number of the medium, as shown in Equation 1.2 obtained from Attix [2004, p. 150].

$$\frac{\mu_{pairproduction}}{\rho} \propto Z \qquad (\mathrm{cm}^2/\mathrm{g}) \tag{1.2}$$

The mass attenuation coefficient associated with Compton scattering is not dependent on the atomic number of the medium. Each interaction type contributes to the total attenuation as

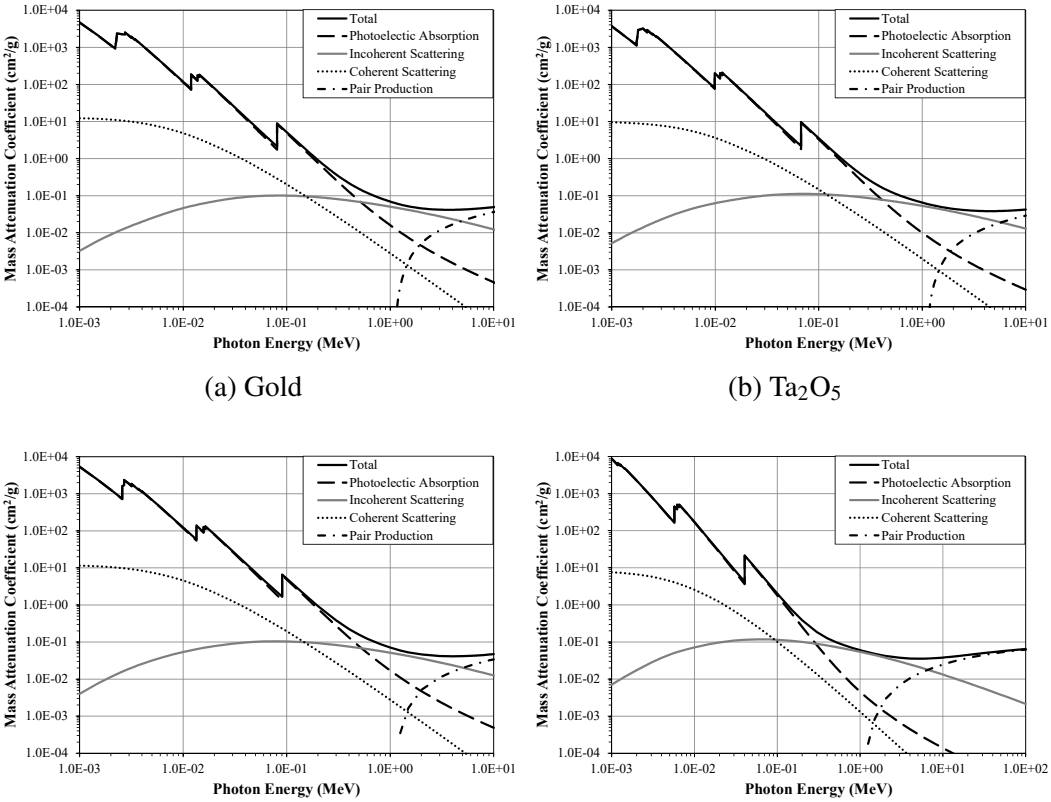

(a) Gold (b) Ta_2O_5

(c) Bi_2O_3 (d) CeO_2

Figure 1.4: Mass attenuation coefficients in Au, Ta_2O_5, Bi_2O_3, and CeO_2. Total mass attenuation coefficient (solid black line) comprises photoelectric absorption (dashed line), Compton scattering (grey line), coherent (Rayleigh) scattering (dotted line) and pair production (dot and dash line) [26].

shown in Equation 1.3

$$\frac{\mu_{total}}{\rho} = \frac{\mu_{photoelectric}}{\rho} + \frac{\mu_{compton}}{\rho} + \frac{\mu_{pairproduction}}{\rho} + \frac{\mu_{rayleigh}}{\rho} \qquad (\mathrm{cm}^2/\mathrm{g}) \qquad (1.3)$$

Figure 1.4 shows the total mass attenuation coefficients and the contribution from each type of photon interaction in gold (Au), Ta_2O_5, CeO_2 and Bi_2O_3 with data obtained from Berger et al. (2010).

Table 1.1: Atomic number, K-, L-, an M-edge energy of the high-Z atoms in the NPs under study [26, 27].

		Au	Bi	Ta	Ce
	Atomic number (Z)	79	83	73	58
	K-edge (keV)	80.7	90.5	67.4	40.4
L-series	L_I-edge (keV)	14.3	16.4	11.7	6.5
	L_{II}-edge (keV)	13.7	15.7	11.1	6.1
	L_{III}-edge (keV)	11.9	13.4	9.9	5.7
M-series	M_I-edge (keV)	3.4	4.0	2.7	1.4
	M_{II}-edge (keV)	3.1	3.7	2.5	1.3
	M_{III}-edge (keV)	2.7	3.2	2.2	1.2
	M_{IV}-edge (keV)	2.3	2.7	1.8	0.9
	M_V-edge (keV)	2.2	2.6	1.7	0.8

The atomic number, and K-, L- and M-edges for each high-Z element studied in this PhD project are shown in Table 1.1. The K-edge of the mass attenuation coefficient of a medium, with respect to photon energy, occurs at the binding energy of the K-shell electrons in the atom. The L- and M-edges each correspond to binding energy of electrons from these shells respectively. There is a peak observed and then a sharp drop-off at this K-edge and at the lower energy L- and M- series of binding energies. This is important in high-Z NP dose enhancement as it is desirable for the interaction probability to be highest, and so it can be important to select incident photon energies with respect to targeting the K-edge of the NP material, in order to maximise the dose enhancement with respect to water.

Figure 1.5 shows the ratio (converted to percentage difference) of total mass absorption coefficients in gold to water, for photons with energy from 1 keV to 100 MeV [26]. Figure 1.5a shows the comparison between elemental gold and water. Figure 1.5b shows the ratio in the case of a 1% solution of gold in water, calculated by scaling the total mass absorption coefficients for water and gold combined in such a solution. A concentration of this mag-

nitude is a reasonable example case, according to the literature [21]. The contrast of these two figures shows that the effect of gold NPs in terms of dose enhancement is more complex than an exclusively macroscopic dose enhancement effect, which can only account for a small increase in photon absorption. This is why investigations on the micro- and nanoscale are essential to understand the fundamental mechanism of radiosensitisation observed in *in vitro* experiments.

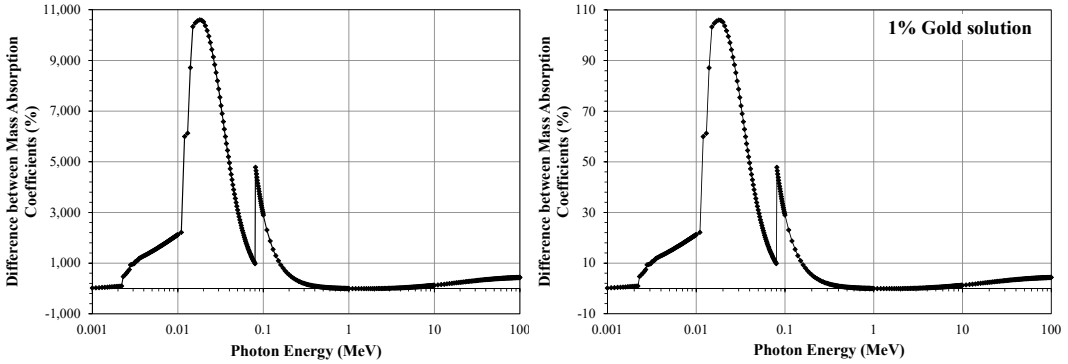

(a) Au / H_2O (b) 1% Au / H_2O

Figure 1.5: Departure of the ratio of mass absorption coefficient in gold to water from unity (given as a percentage) [26]. Pure gold (a) and a 1% solution of gold in water (b) are shown in each panel respectively.

1.1.3.2 Proton therapy

The interaction of charged particles with matter consists of Coulombic interaction resulting in ionised or excited atoms, or nuclear interaction [19, ch. 8]. These interactions result in a continuous slowing down of a particle travelling though matter which results in the sharp drop-off in the depth-dose profile, know as the Bragg peak. The cross-section of production of secondary electrons is dependent on the density of the medium, and inversely dependent on the square of the velocity of the incident particle [28].

The Bethe-Bloch stopping power equation describing the energy loss of charged particles in

a medium is shown in Equation 1.4 [29, p. 252].

$$S_{col} = -\frac{1}{\rho}\frac{dE}{dx} = 4\pi \frac{N_A}{A}\left(\frac{e^2}{4\pi\epsilon_0}\right)^2 \frac{z^2}{m_e c^2 \beta^2} Z\left[ln\,\frac{2m_e c^2}{I} + ln\,\frac{\beta^2}{1-\beta^2} - \beta^2 - \frac{C}{Z} - \delta\right] \quad (\mathrm{MeV.cm^2/g}) \tag{1.4}$$

where the parameters are defined as follows:

β	$= \frac{v}{c}$
v	velocity of the incident particle
c	speed of light
m_e	electron mass at rest
e	charge of the electron
N_A	Avogadro constant
z	atomic number of the incident particle
Z	atomic number of the medium
A	atomic mass number of the medium
I	mean ionisation/excitation potential of the medium
$\frac{C}{Z}$	shell correction
δ	density correction

For low kinetic energies the stopping power curve increases to a peak in the case of incident protons [29]. In the kinetic energy range relevant to proton therapy the stopping power increases then decreases with increasing kinetic energy. Lower energy primary particles produce a higher number of δ-electrons. As there is only a small variation in the Z/A term of the equation between most elements this term causes the stopping power to vary only slightly between materials. Therefore the energy loss of a particular particle through equivalent thickness (g/cm^2) absorber will be approximately the same for materials of different atomic

number [29].

The dose enhancement in proton therapy by means of NPs is a relatively new area of research [30, 31]. The nature of proton energy deposition in dense tracks of ionised secondary electrons means the dose enhancement mechanism and outcomes differ from NP enhanced X-ray radiotherapy. An increase in low energy electron production is unlikely to be the result of physical proton interaction with a high-Z NP, but rather the interaction of secondary electrons in the NP and these electrons will induce further direct and indirect damage to cells. Dose enhancement of already high-LET incident particles in the SOBP region should improve the tumour control outcomes in proton therapy.

1.2 Motivation

1.2.1 Proposed Ceramic Nanoparticles

At the ISEM novel NP materials are synthesised, developed and studied. The Targeted Nano-Therapies (TNT) Group at the University of Wollongong studies the possible application of such novel compounds to enhance radiotherapy [107, 108]. Novel materials studied in this PhD project include tantalum pentoxide (Ta_2O_5), bismuth oxide (Bi_2O_3), and cerium oxide (CeO_2). Ta_2O_5 and Bi_2O_3 are studied by the TNT Group as radio-enhancers, while CeO_2 as a radio-protector [20, 22, 32–35].

Tantalum pentoxide (Ta_2O_5) is a ceramic compound which, when engineered as a nanostructured particle, has been shown to be an effective radiosensitizer for radiation resistant rat brain 9L cancer cells exposed to 10 MV photon irradiation [22]. The high-Z of tantalum ($Z_{Ta} = 73$) causes Ta_2O_5 to behave as a high-Z NP whilst it is also biocompatible [32]. Figure 1.6 shows a transmission electron microscopy image of nanoscale Ta_2O_5 NPs.

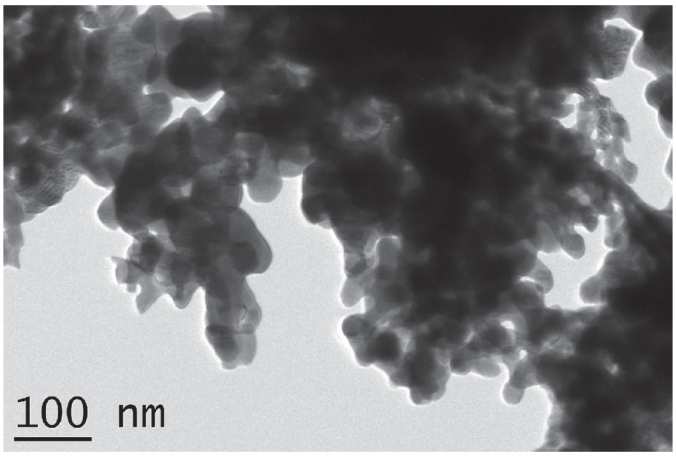

Figure 1.6: High-resolution transmission electron microscopy image of Ta_2O_5 NPs. Figure reproduced from Brown et al. (2013).

The sensitising effect on 9L rat brain gliosarcoma (brain tumour) cells of Ta_2O_5 NPs combined with 10 MV photon irradiation has been demonstrated [22, 32]. Brown et al. (2013) found an SER of 1.33 with 50 - 70 nm diameter Ta_2O_5 NPs. The researchers exposed the tumour cells to NPs of increasing concentration from 50 to 500 µg/mL and showed enhanced radiosensitivity of the cells with increasing concentration of NP.

Brown et al. (2017) have since reported the effect on these radioresistant 9L tumour cell killing of Ta_2O_5 NP preparation technique and X-ray beam energy [32]. The paper presents results of Ta_2O_5 NPs in concentrations of 50 and 500 µg/mL combined with 150 kVp or 10 MV photon irradiation showing most dose enhancement under 10 MV irradiation with Ta_2O_5 NPs fabricated using a precipitation technique. The increased radio-enhancement at the higher photon beam energy can be explained by the tendency of these types of NPs to collect in aggregates of several hundred microns diameter. This aggregation limits the effectiveness of the lower energy dose enhancement due to self-absorption within the NP material.

Bismuth oxide (Bi_2O_3) nanomaterials have been shown to enhance the effects of kilovolt-

age radiotherapy irradiation of a 3D radiochromic dosimeter [23]. The high-Z of bismuth ($Z_{Bi} = 83$), higher even than gold, contributes to Bi_2O_3 being an effective radio-enhancer. Alqathami et al. (2013) examined the dose distribution enhancement with the application of 50 mM of 50 nm Bi_2O_3 NPs in a multi-compartment 3D radiochromic dosimeter and presented dose enhancement factors (DEF), defined as the ratio of the response of the dosimeter with NP and without NP doping. The study found DEF of 1.90 with Bi_2O_3 NP doping of the dosimeter irradiated to 10 Gy under a 100 kV X-ray beam. Although this study does not take into account biological or chemical effects which may occur in cells, it does demonstrate physical dose enhancement in the presence of Bi_2O_3 NPs.

Bi_2O_3 NPs have been fabricated and optimised at the ISEM with the final goal of applying them as a radio-enhancer in radiotherapy [33]. Bi_2O_3 NPs are under study for their potential combination with drug coatings in order to develop a theranostic system [35].

Figure 1.7 shows the platelet morphology of Bi_2O_3 NPs fabricated at the ISEM [34]. This study examined the effect of a Bi_2O_3 NP in a concentration of 50 µg/mL on 9L gliosarcoma cell line under 125 kVp and 10 MV photon irradiation. The influence of the shape of the nanoceramic materials produced at the ISEM is addressed in the paper by means of Monte Carlo simulation study developed during this PhD project. Comparison of various material geometries in terms of dose distribution enhancement will be described in this thesis and was motivated by the observed morphology of these Bi_2O_3 NPs.

The application of NPs in radiotherapy as a radio-protector reducing normal tissue damage in proximity to tumour target tissue is another area of research interest [36–38]. Cerium oxide (CeO_2) NPs have been investigated for use as a radio-protector in cells under X-ray or gamma irradiation [36, 37]. This material has the property of free-radical scavenging which provides protection against damage of this mechanism from radiation. The application of

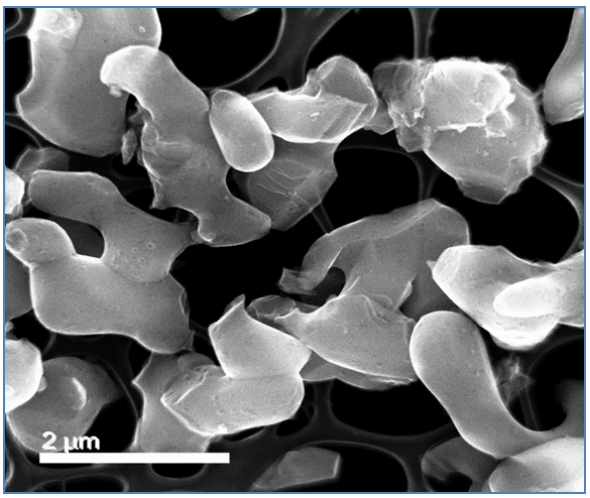

Figure 1.7: Transmission electron microscopy (TEM) image of Bi_2O_3 nanoceramic platelets. Figure reproduced from article - Stewart et al. (2016).

a radio-protector allows for sufficient damage to tumour cells to be achieved while normal cells are less susceptible to the damage due to protective NPs working to the advantage of normal cells. At the same time CeO_2 NPs are effectively high-Z NPs ($Z_{Ce} = 58$) and therefore will enhance secondary electron production in proportion to increasing Z [20]. The protective nature of these particles is deduced from their applicability as antioxidants, which outweighs the negative effect of increased production of secondary electrons due to their high Z [20].

Figure 1.8 shows cell survival curves comparing the survival of radioresistant 9L gliosarcomas under megavoltage or kilovoltage photon irradiation with the application of CeO_2 NPs. This figure demonstrates the difference in response with the application of 50 µg/mL concentration of CeO_2 NPs on cells to 10 MV and 150 kVp X-ray beams. The protective properties of CeO_2 NPs are shown to be more effective under the megavoltage irradiation and this is due to the lower proportion of photoelectric interactions expected to occur under 10 MV photon irradiation (where Compton scattering is dominant), compared to in the 150 kVp field (where the photoelectric effect is dominant). This means that the enhancement of the production photoelectrons and subsequent dose deposition is balance by the free

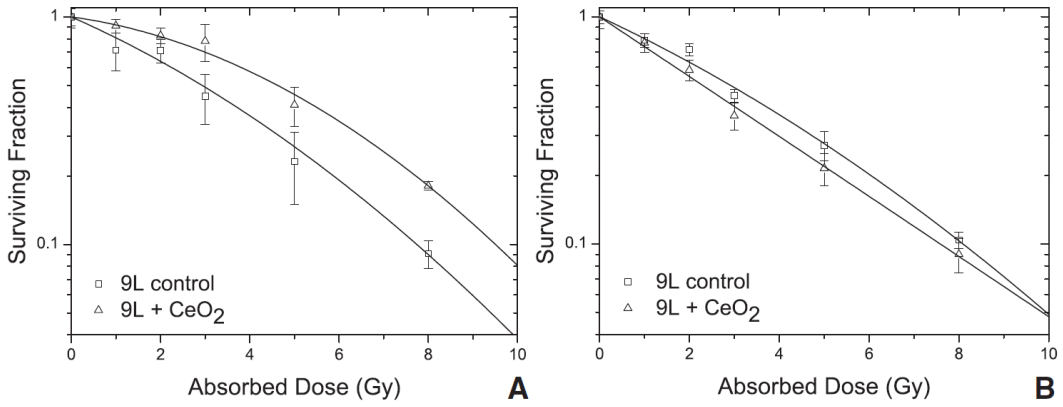

Figure 1.8: Cell survival curves after irradiation with 10 MV (A) or 150 kVp (B) X-ray beams in the presence (triangle) and absence (square) of 50 µg/mL of CeO_2 NPs. Figure reproduced from Briggs et al. (2013).

radical scavenging properties and this balance is closer to equality in the kilovoltage case and the protective properties are dominant in the megavoltage.

1.3 Literature Review

1.3.1 Nanoparticle Dose Enhancement of Radiotherapy

Jain et al. (2011) and Chithrani et al. (2010) have shown dose enhancement in megavoltage photon radiotherapy treatment by gold NPs. Jain et al. (2011) demonstrated radiosensitization of MDA-MB-231 breast cancer cells by gold nanoparticles in megavoltage radiotherapy. The authors used a gold nanoparticle concentration of 12 μM. The study reported sensitizer enhancement ratios (SERs) of 1.41, 1.29 and 1.16 for breast cancer cells under 160 kVp, 6 MV and 15 MV photon irradiation respectively. The authors suggest a possible biological mechanism of radio-enhancement, for example causing increased ROS production and hypoxia, could account for the radio-enhancement reported in the MV field. Chithrani et al. (2010) used a much lower gold nanoparticle concentration of 1×10^{-3}% in their studies of dose enhancement by nanoparticles.

McMahon et al. (2011) showed, by means of Monte Carlo simulation, that the mechanism of dose enhancement in kilovoltage radiotherapy by gold NPs must take into account nanoscale effects. The enhancement of the dose within a few hundred nanometres of the NP surface is primarily due to Auger electrons generated after 40 keV photon interaction in the NP depositing energy in the surrounding water. The dose enhancement was shown in this study to fall off rapidly beyond the range of the low energy, Auger electrons [40].

McMahon et al. (2011b) reported Monte Carlo simulation results of dose enhancement by gold NPs irradiated in megavoltage photon fields. The authors modelled the effect of the dose enhancement due to a 0.05% by mass concentration of NPs on MDA-MB-231 cells and compared the results to previously published clonogenic survival results [21]. These researchers were able to demonstrate dose enhancement in the MV photon field, at a depth

of 5 cm in water. Although Compton scattering dominates at higher photon energies, interactions in the NP at the depth of interest are dominated by electron impact and photoelectric interactions due to scattered photons and secondary electron in the water phantom [41].

The change in the dose enhancement effect of high-Z NPs with respect to x-ray beam spectra is an important aspect of NP dose enhancement study. Studies have demonstrated dose enhancement in both kilovoltage and megavoltage radiotherapy beams [22, 32, 39, 41].

In the case of a kilovoltage beam it is possible theoretically to select beam energy in order to optimise dose enhancement depending on NP material to select the optimum energy for photoelectric interactions [42]. This is because enhancement of tumour cell killing with the application of nanoparticles is thought to be due in part to an increase in the production of secondary electrons local to the NP. This also results in an increase in low energy Auger electron production and cascades which can be connected to complex damage to DNA if the source is close to the nucleus in the cell target. For example, gold is expected to be most effective for kV beams with mean beam energy of around 100 keV, or just above the K-edge of gold. This optimisation could potentially be adopted in microbeam radiation therapy as well [42].

Experimental results have shown radio-enhancement from NPs in both kilovoltage and megavoltage photon radiation therapy. Chithrani et al. (2010) compared dose enhancement due to 50 nm gold NPs (with a concentration of 1×10^{-3}%) in cells irradiated by photon beams from 105 kVp up to 6 MV. This study found (at a level of 10% on the cell survival curve) a maximum radiosensitization enhancement factor (REF) of (1.66 ± 0.05) for the 105 kVp photon irradiation (compared to 220 kVp and 6 MV photon irradiations). The REF was calculated as the ratio of dose required with and without the application of NPs to achieve 10% survival in HeLa cells. The study reported a REF of (1.17 ± 0.02) for the

6 MV irradiation.

McMahon et al. (2011b) showed by a Monte Carlo simulation study a potential reason for dose enhancement in MV photon field is due to the presence of lower energy photons at depth in a phantom due to scattering of the primary photons. They also showed the effect of secondary electron ionisations within a NP is important in MV photon fields [41].

1.3.2 Nanoparticles for Radio-enhancement

Nanoparticles are usually less than 100 nm in size and are fabricated with desirable properties such as bio-compatibility, preferential uptake by cells, targeting to tumour cells, as contrast in imaging, and as drug carriers [43].

Hainfeld et al. (2004) showed for the first time *in vivo* evidence in mice with subcutaneous mammary carcinomas of the dose enhancement in radiotherapy by means of NPs. This study reported an increase in the one-year survival from 20% to 86% in mice receiving intravenous injection of 1.9 nm gold NPs combined with 250 kVp X-ray therapy, compared to mice receiving the radiotherapy alone [44]. The NP concentrations delivered were 1.35 and 2.70 g Au/kg in 0.01 ml per g mouse weight. Zheng and Sanche (2009) showed the enhancement of damage to DNA irradiated with 60 keV electrons with the application of fabricated (5 ± 2) nm diameter gold NPs with a concentration of (0.5 ± 0.2) μM.

Since then, gold NPs have been shown to enhance the effects of ionising radiation by many studies on cell and animal models and also by simulation studies. Gold is relatively inert and biocompatible material which are desirable characteristics for dose enhancement in a biological setting. Several studies have investigated the dose enhancement from 1.9 nm gold NPs fabricated by Nanoprobes, Inc. (Yaphank, New York) [44, 46, 47]. Larger gold

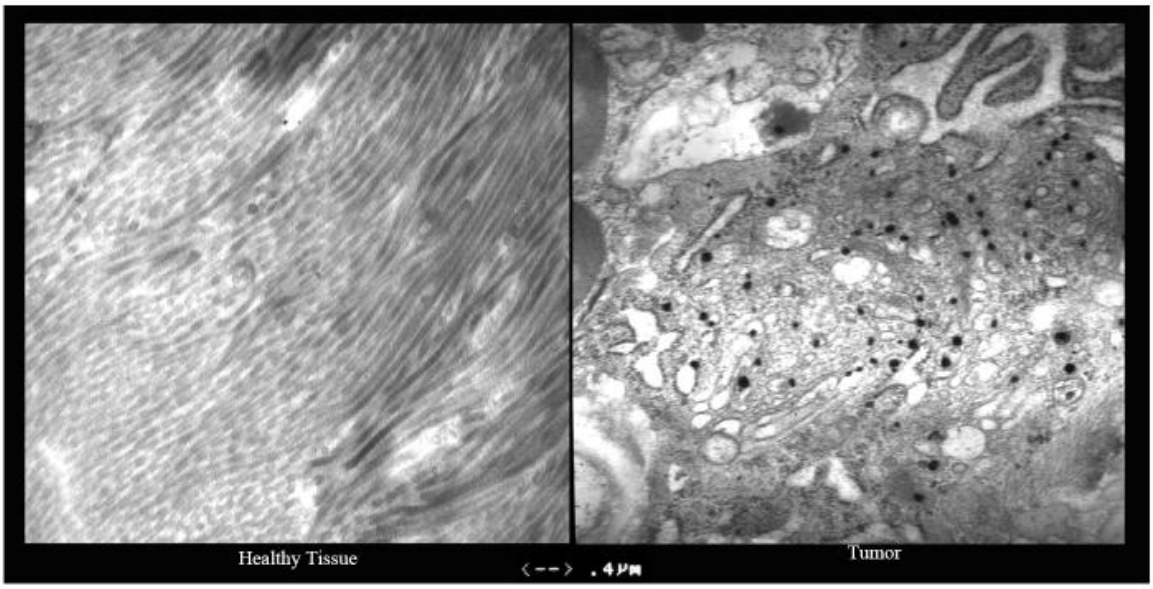

Figure 1.9: Electron micrographs from a patient with inoperable ductal carcinoma of the breast. Magnification is 20,000 X, and the line at the bottom is 0.4 μm. Black dots in the tumour micrograph are gold NPs. Figure reproduced from Libutti et al. (2010).

NPs have also been fabricated and studied for their effectiveness as dose enhancers, based on a fabrication method developed by Turkevich et al. (1951) [49].

Libutti et al. (2010) have since reported results of a phase I dose escalation trial testing the toxicity in humans of a nanomedicine, CYT-6091, consisting of recombinant human tumour necrosis factor alpha (rhTNF) and thiolyated polyethylene glycol bonded to 27 nm gold NPs. The study showed that a higher dose of the rhTNF was able to be delivered when bound to PEGylated gold NPs than in previous studies of the drug alone as well as preferential uptake by tumour tissue, compared to healthy tissue (shown in Figure 1.9). Although this trial was aimed to study the dose and targeted delivery of the rhTNF, it shows *in vivo* evidence of the application of gold NPs in a human trial.

Iron oxide and platinum materials are under investigation as potential radio-enhancers [51, 52]. Novel NP materials under study also include ceramic oxides. These compounds have high-Z properties and are also developed to be relatively biocompatible, possibly due to the

oxide bonding [32].

Theranostic systems are designed to combine diagnostic and therapeutic capabilities of NPs. Gadolinium-based nanomaterials have been investigated because of their dual functionality, acting as a radiation enhancer of traditional X-ray or γ-ray radiotherapy, heavy-ion or proton therapy as well as acting as an MRI contrast agent (theranostics) [53–56]. By combining chemotherapeutic or tumour-targeting drugs with CT or MRI contrast-enhancing nanomaterials, it is suggested that an advantageous combination of effects can be achieved [35].

Carbon nanomaterials have been studied to investigate how to improve the outcome of patients undergoing breast cancer surgery as well as improving radiotherapy outcomes [57, 58]. Monte Carlo simulation has also shown the advantage of increased concentration of carbon in cells to enhance particle therapy due to the stopping power advantage of carbon [59]. This is an area of ongoing development and research interest.

1.3.2.1 Effect of NP Size

Gold NPs of varying sizes have been used in previous studies of dose enhancement in X-ray irradiation of DNA, cells and in animal studies. Gold NPs with a diameter of 1.9 nm have been widely studied [44, 47] and also larger diameters, up to 92 nm [49]. The change in effectiveness with increasing NP diameter is due to a combination of effects including toxicity, uptake by cells or tumour vasculature and physical interaction with treatment beam.

Experiments using plasmid-DNA to measure dose enhancement in kilovoltage (10 keV - 80 keV) photon irradiation from gold NPs have examined the effect of NP concentration, and NP size on the increase of damage to DNA [49]. Brun et al. (2009) found the greatest dose enhancement at high NP concentration, relative to the concentration of DNA. The NP concentration was kept constant (5 nM) in order to compare the dose enhancement factor

with respect to NP diameter. The researchers showed an increased dose enhancement factor for larger diameter NP (up to 92 nm diameter) with 49 keV effective X-rays on plasmid DNA.

Jiang et al. (2008) investigated the size-dependence of cell uptake of gold NPs with surfaces modified with Herceptin molecules. The dependence of NP uptake by human breast cancer SK-BR-3 cells of gold NPs with Herceptin surface coating on the NP diameter (2-100 nm) was reported in this study. The researchers found that the gold NPs with diameter of 40-50 nm was optimal for Herceptin binding and subsequent cellular uptake.

Chithrani et al. (2010) compared cellular uptake of three NP sizes (14, 50 and 74 nm) and found the 50 nm particles exhibited the highest level of cellular uptake in a HeLa cell culture. A 1 nM concentration of gold nanoparticle solution was used. This concurs with the previous result of Jiang et al. (2008) who found optimum uptake by NPs in the 40-50 nm diameter range on a breast cancer cell line.

The cellular uptake of NPs by cells depends on several processes, including the size of pores in tumour vasculature, and interactions of NP and any surface modification with cellular membranes, influencing mechanisms of internalisation.

1.3.3 Dose Enhancement of Proton Therapy

Studies have shown the potential dose enhancement in proton and heavy-ion therapy by high-Z NPs by *in vitro* [30, 31] and *in vivo* experiments [61].

Proton therapy has been shown to have increased killing capabilities of malignant cell lines with the application of pegylated gold NPs. Pegylated NPs have their surface modified with polyethylene glycol (PEG) which leads to an increased uptake and concentration of NPs

within a tumour and reduced concentration in healthy tissue [30]. The PEG coating also works to counteract the immune response which, in the absence of surface modification, leads to the excretion of a large proportion of intravenously injected Au NPs [30]. Liu et al. (2010) studied the nanoparticle-induced dose enhancement of the irradiation of two cancer cell lines. The study used mouse breast cancer cells and colorectal adenocarcinoma cells treated with pegylated gold NPs in concentrations of 400, 500 or 1000 μM. An enhancement in cell killing of 2 - 11.9% under 3 MeV proton irradiation is reported in this study [30].

Gold NPs have been shown to enhance the radiobiological efficiency of proton therapy killing prostate cancer cells [31]. Polf et al. (2011) reported an increased RBE of approximately 15 - 20% in the effectiveness of proton radiation therapy killing prostate tumour cells. They applied gold NPs with diameter = (44 ± 8) nm to DU145 human prostate carcinoma cells under three experimental conditions. The first was cell treated with an internalising bacteriophage ("phage") combined with gold NPs [62], described as Au-treated cells. The researchers compared the cells' response with two control situations - the first with the internalising phage only (to examine any sensitising effect of this component) and the second with neither phage nor gold NPs. After application of the NP material and incubation, the researchers found NP uptake of approximately 1 ng/cell. Treatment with a clinical ^{60}Co photon source was used as a comparison for the purpose of calculating the RBE. Two different measures of RBE were used - 10% cell survival fraction and 50% survival, or RBE_{10} and RBE_{50} respectively. The study reported a 20% increase in RBE_{10}, from 1.6 to 1.9 when cells were treated with the gold NP and a 15% increase in RBE_{50} from 1.3 to 1.5. The survival curves are shown in Figure 1.10.

Nanoparticle enhanced proton therapy has been shown to be effective compared to non-enhanced proton therapy in an *in vivo* animal study [63]. Kim et al. (2010) showed an increase effectiveness using *in vivo* mouse models and *in vitro* CT26 tumours studies with

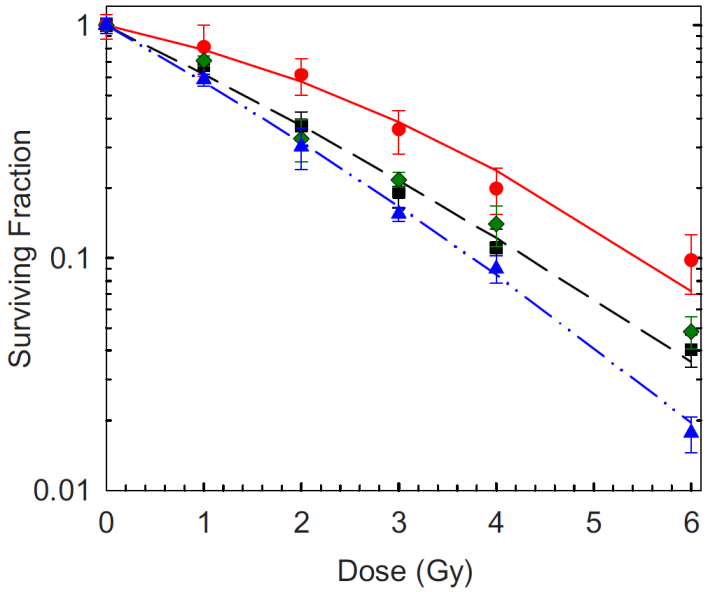

Figure 1.10: Cell survival as a function of dose for untreated cells irradiated with ^{60}Co (red circles) and proton (black squares) beams, as well as for phage-only (green diamonds) and Au-treated (blue triangles) cells irradiated with protons. Figure reproduced from Polf et al. (2011).

45 MeV proton irradiation. Gold or iron NPs with concentrations of 0.1 - 2 mg/ml were introduced to the cells before irradiation. The cell study showed increased dose enhancement in proton therapy with increasing gold and iron NP concentration. They attributed this result to particle induce X-ray emission (PIXE) from the NPs. They found that with injection of NP in concentration 300 mg/kg body weight there was increased tumour regression of 33 - 65% compared to 25% on the control.

In a comment on this research Dollinger (2011) pointed out that the statistical proportions of energy being transferred to a NP from incident protons is extremely low and any resultant energy deposition from PIXE, or other energy transfer modes such as increased electron emission, will be statistically insignificant in the overall scenario. In a subsequent comment on this research Le Sech et al. (2012) agreed with Dollinger's critic of the work and presented an alternative interpretation of the results, suggesting that the increase in tumour cell death should be attributed to increased free radical activity, namely water radiolysis, rather

than PIXE as described by Kim et al. (2010).

Kim et al. (2012) have since published further research into proton therapy enhanced with NPs. This paper again showed the dose enhancement in proton therapy with 100 - 300 mg/kg body weight with increasing radiation dose to tumour in mice.

The effect of free radical production enhancement has been further examined in the context of high-Z NP enhanced, high-LET radiation [66]. Porcel et al. (2012) compared the damage to DNA induced by different LET incident radiation in the presence of molecular platinum (Pt) or Pt NPs (Z_{Pt} = 78). The researchers compared gamma rays, fast helium particles and fast carbon ions. A particularly interesting finding of the study was that the 90% of the increased DNA damage induced by the presence of Pt could be attributed to the activity of free radicals, in particular water radicals. The researchers state that the effect of the presence of the NPs is to create an initial increase in secondary electrons which then induce the production of free radicals which have the most impact on DNA damage.

These studies show that radio-enhancement by NPs in proton therapy is a complex system involving direct and indirect effects, the complete mechanisms of which we are yet to fully understand.

1.4 Methods

1.4.1 Study of Nanoparticle Dose Enhancement

Monte Carlo simulations are a useful tool to investigate the physics foundation of the mechanism of dose enhancement produced by NPs in radiation therapy and to characterise important associated physics quantities such as the energy deposition and the energy spectra

of the electrons emitted by the NP, to provide an insight into both the direct and indirect damage of radiation.

Geant4 [67–69] and other Monte Carlo simulation codes model particle interactions either in event-by-event tracking or condensed history approximations [70]. A condensed history approximation [71] of particle interaction can be implemented, where appropriate, in order to minimise execution time requirement of simulations. In large geometries particle interactions are modelled with enough accuracy by approximating many interactions in a particle track as a single "condensed" step undertaken by the particle. This approach is valid when tracking particle interactions where energy loss is greater than about 1 keV, determined by the binding energy of electrons in the medium, [72, 73] however, for lower energy (shorter range) particle interactions, more accurate models are required. To model particle tracks below this general limit of 1 keV (or in some cases 100 - 250 eV), at small particle ranges of micro- and nanometres, event-by-event transport codes allowing modelling of energy loss down to very low energies become necessary [73].

1.4.2 Track structure Monte Carlo codes

When investigating dose enhancement due to NPs it is advantageous to use techniques that model dose deposition on the nanoscale in order to accurately assess damage to DNA. Photon dose deposition can be approximated as a uniform dose spread, on the scale of the cellular environment. The dose response of tissue (represented by survival curves) can therefore be related to absolute absorbed dose in the tissue.

In the case of traditional radiation therapy this macroscopic approach is sufficient to predict the biological response of tissue to photon radiation dose however with the recent development of proton and heavy-ion therapy this way of understanding cell response to damage

is insufficient. Ions deposit dose in non-uniform, dense ionisation tracks and so the dose distribution is not uniform across a small volume such as the cell. This means that the total absorbed dose is not necessarily the best quantity to relate to biological effect in this case. A more complex understanding of the track-structure is important to be able to predict dose-response curves [74, 75].

Radial dose distribution around ion tracks are used to assess the dose-response in tissue of proton or heavy-ion irradiation [76]. Cucinotta et al. (1999) describe methods to model biological damage from radiation by modelling radial dose or ionisation distributions, and ionisation clustering.

Micro- and nano- scale simulations of event-by-event track structure of secondary electron tracks becomes a useful tool when assessing the local clustering of ionisations within a cell. This allows the known photon dose and corresponding cell response to be related to radial dose quantities in ion beam radiation therapy.

Previous studies have investigated secondary electron yield and dose enhancement in the presence of different NPs [24, 25, 40, 77–85]. Gold NPs have been studied extensively due to their wide use in early biological studies of dose enhancement [77, 80, 83]. Other NP materials studied include a variety of metallic NPs [82].

Earlier simulation studies of dose enhancement from nanoparticles model a uniform distribution of calculated concentration of NP within a tumour volume irradiated by various photon sources [77]. Jones et al. (2010) used the Monte Carlo code EGSnrc to simulate the secondary electron spectra within a tumour with an approximated concentration of embedded gold NPs under ^{125}I, ^{103}Pd, ^{169}Yb, ^{192}Ir, 50 kVp and 6 MV X-ray irradiation. This study showed an increased number of secondary electrons in the tumour when NPs are placed

in tumour loaded with an equivalent to 7 mg Au/g of tumour. The microscopic dose distribution around a gold NP was subsequently simulated using another code, NOREC [86]. NOREC is a Monte Carlo code applicable to tracking electrons down to low energy in liquid water, tracking secondary electron down to 7.4 eV in water. This study is limited in that it does not take into account the NP geometry or nano- or microscale effects on DNA damage but only takes into account the difference of the electron yield within the tumour with and without the gold NPs. The microscopic distribution of NPs within cells is an important factor when considering the magnitude of dose enhancement, as will be investigated in this PhD thesis.

Nanoparticles have been shown in previous simulation studies to be dose enhancing in brachytherapy, kilovoltage, and megavoltage radiation fields [78]. Lechtman et al. (2011) investigated, by means of a combination of the Monte Carlo codes, MCNP-5 and PENELOPE 2008.1, the enhancement of photoelectric interactions within gold NPs and dose enhancement surrounding gold NPs with respect to NP diameter and photon energy. Enhancement was calculated in terms of the increase in photoelectric absorption cross-section in a 1 mm thick region, the spectra from which was used as a primary source for a subsequent nanoscale simulation. The study reported increased dose enhancement efficiency in terms of gold NP mass concentration for smaller diameter NPs, in lower energy fields. This is due to the increased likelihood of low energy Auger electrons escaping smaller NPs.

With the advancement of the available physics models, subsequent research has modelled NPs dose enhancement in photon fields on the nanoscale [40]. McMahon et al. (2011) used Geant4 to model secondary electron production from and dose enhancement around a single gold NP with an incident photon beam. This study then used the local effect model (LEM) [87] to compare simulation results to cell survival data [40]. The basic premise of the LEM as described in Scholz and Elsässer (2007) is "...that the local biological effect,

i.e. the biological damage in a small subvolume of the cell nucleus is solely determined by the expectation value of the energy deposition in that subvolume and is independent of the particular radiation type leading to that energy deposition". This model examines the track structure of energy deposition on a nanoscale and relates this to photon dose response, depending on cell or tissue type.

The effect of the incident photon energy has been studied by means of nanoscale Monte Carlo simulation [80]. Chow et al. (2012) used Geant4 to simulate the secondary electron spectra from a 100 nm diameter gold NP irradiated by kilovoltage photon beams. The dose distribution around the NP was simulated with the Monte Carlo code, NOREC. Geant4 with Penelope models was used to create electrons down to 250 eV. The study did not find a significant difference between the low energy part of the secondary electron spectra from the three photon beams studied - 35, 73.3 and 660 keV. The higher energy photons showed wider spread of energy deposition [80]. This occurs because of the different photon interaction processes which become more dominant at higher photon energies, resulting in a more divergent beam, and higher energy secondaries which will travel further in a medium, depositing energy at a greater distance from their origin.

Clinically realistic phantom configurations have been developed in Geant4 and the dose enhancement effect of gold NPs calculated in this context [24]. Douglass et al. (2013) reported a Monte Carlo study of the dose enhancement effect of gold NPs in a randomised cell model, irradiated by kilovoltage and megavoltage photon fields. The researchers reported dose enhancement ratios (DERs) in a model of cells (with randomised diameter between 9 and 15 μm) due to 80 kVp and 6 MV photon fields. They showed greater dose enhancement in the kilovoltage field, and a dose enhancement dependent on the geometrical configuration of the gold NP, either in a 400 nm diameter aggregate, cluster, or in a 300 nm layer around the nucleus. On the scale of the cell these simulations revealed Auger electrons had

an insignificant effect on dose enhancement [24].

The importance of the selection of the geometry of a Monte Carlo simulation has be reported only recently [85]. Zygmanski et al. (2013) examined the effect of simulation geometry when assessing the dose enhancement properties in the case of gold NPs. This study reports the effect on DER of small generated source sizes and with reducing source to NP distance. Zygmanski et al. (2013) also showed by means of their Monte Carlo simulations that increasing gold NP clustering in X-ray radiotherapy translates to a nonlinear dose enhancement. The work presented in this thesis differentiates from ref [85] in the type of nanoparticle aggregate considered and in the shape of the aggregate, dictated by our experimental observations described in Chapter 3. Results in Chapter 3 show a saturation effect with increasing ceramic NP concentration in a cell population which is in agreement with a similar trend described in ref [85], although this is for the case of clustered gold NPs in solution.

The simulation study presented in this thesis (Chapter 3) further examines and compares the effect of a completely homogeneous distribution of NP materials as well as the magnitude of the effect of atomic de-excitation on the DER. The simulation study reported in ref [85] was performed in two stages utilising a phase space file technique for storing results of the first stage to then use as input to a more refined second stage. The effect of the secondary source size and distance to target is examined by Zygmanski et al. (2013). These considerations are not directly applicable in the case of simulations presented in this thesis as the present work was performed as a single simulation step, including realistic depth in phantom to correspond to experimental measurements.

Zygmanski et al. (2013) presented a method to relate simulated dose enhancement in the form of a calculated DER to biological quantities such as RBE and linear quadratic model

parameters, α and β by utilising a local effect model framework [87].

Wälzlein et al. (2014) used the Monte Carlo code TRAX (developed at GSI, Darmstadt, Germany) to model secondary electron production from five types of metallic NPs (Fe, Ag, Gd, Pt and Au). They investigated the electron production and subsequent dose enhancement by these NPs with 2 and 22 nm radius with directly incident 2, 80 or 300 MeV monoenergetic protons. Their study modelled ionisation, excitation and elastic scattering interactions in each NP material and water as well as production of Auger electrons and plasmon excitation in the NPs. This study reported dose enhancement of up to a factor of 2. The researchers showed that Auger electrons are produced with low energy and contribute to dose enhancement close to the NP surface.

Lin et al. (2014) compared the dose enhancement from monoenergetic protons, a clinical proton spectrum, monoenergetic kilovoltage photon sources and a clinical 150 kVp and a 6 MV photon spectra. Lin et al. used the Monte Carlo package, TOPAS, which is a user-interface of Geant4 (based on program version 9.6p02, in this case) to model 50 nm diameter gold NPs. The researchers used Penelope physics models in the gold NP with a cut-off of 250 eV. The dose enhancement factor (DEF) was defined in this study as the ratio of dose in water with a GNP to a sphere of water up to 10 μm distant from the GNP surface. This study reported a DEF in the proton beam of a factor up to 14 (independent of proton energy). The dose enhancement reported in the photon fields varied with photon energy and had a much larger effect at a larger distance from the NP compared to proton dose enhancement. This study was not able to track secondary Auger electrons below 250 eV which would have an effect on the dose enhancement in the nanometre region close to the NP surface.

1.4.3 Geant4

Geant4 is a simulation toolkit for the simulation of the production and transport of radiation in matter [67–69]. Geant4 is maintained by an international collaboration who continue to develop the code to improve the accuracy of the physics models and expand the functionality of the software. Geant4 is based on Object-Oriented technology and is written in the C++ programming language. Geant4 can be used for nano- and micro-dosimetric applications as it is possible to model the transport of particles from within nanoscale objects, such as the DNA-helix, up to human phantoms and detectors [88, 89]. Physics models in Geant4 cover interactions from very low energy (tracking down to nanoscale range), up to high energy physics.

Particle transport in Geant4 is limited by range cuts or energy thresholds. Range cuts are converted to material-specific energy thresholds at the point of initialisation. By the implementation of production cuts, particles with a range lower than a set threshold will not be created in the simulation. Particles that are produced above this threshold are then tracked to zero range, unless special user defined cuts are invoked for a particular volume.

In most experimental situations relevant to medical physics, accuracy to a micron-scale is sufficient for good agreement with verified experimental results. However, in the field of nanomedicine, the tracking of particles on the nanoscale (down to the eV level) becomes increasingly important.

Currently, low energy models in most solid state materials in Geant4 are limited to production and transport of secondary electrons above a 100 eV threshold cut when using Penelope models [90]. Penelope models are inherited from the PENELOPE (PENetration an Energy LOss of Positrons and Electrons) code which simulates the transport of electrons

and positrons in a medium by combined simulation technique of event-by-event and multiple scattering calculations [90, 91]. Geant4-DNA allows for transportation of electrons event-by-event down to 0 eV.

Geant4-DNA is an extension to Geant4 which allows the event-by-event tracking of particles in liquid water down to the nanometre scale [92, 93]. At present, cross-sections are only implemented in Geant4-DNA for liquid water. However, development of a wider range of models is ongoing within the Geant4-DNA project [94]. Models in Geant4-DNA allow the event-by-event tracking of a variety of particles including electrons, protons, hydrogen atoms, helium ions and an increasing number of heavy-ions. The particle interactions and relevant models implemented in Geant4-DNA are shown in Table 1.2. Gamma photon interactions are modelled using Geant4 Livermore cross-sections by default.

Table 1.2: Physical interactions modelled with Geant4-DNA (table adapted from `geant4-dna.org` [94]). Models applied in Geant4 v.10

	Interaction	Process Class	Model Class	Min. Energy	Max. Energy	Kill
Electron	elastic scattering	G4DNAElastic	G4DNAChampionElasticModel	0 eV	1 MeV	7.4 eV
	electronic excitation	G4DNAExcitation	G4DNABornExcitationModel	9 eV	1 MeV	-
	ionisation	G4DNAIonisation	G4DNABornIonisationModel	11 eV	1 MeV	-
	vibrational excitation	G4DNAVibExcitation	G4DNASancheExcitationModel	2 eV	100 eV	-
	attachment	G4DNAAttachment	G4DNAMeltonAttachmentModel	4 eV	13 eV	-
Proton	electronic excitation	G4DNAExcitation	G4DNAMillerGreenExcitationModel	10 eV	500 keV	-
			G4DNABornExcitationModel	500 keV	100 MeV	-
	ionisation	G4DNAIonisation	G4DNARuddIonisationModel	0 eV	500 keV	100 eV
			G4DNABornIonisationModel	500 keV	100 MeV	-
	electron capture	G4DNAChargeDecrease	G4DNADingfelderChargeDecreaseModel	100 eV	100 MeV	-
H	electronic excitation	G4DNAExcitation	G4DNAMillerGreenExcitationModel	10 eV	500 keV	-
	ionisation	G4DNAIonisation	G4DNARuddIonisationModel	0 keV	100 MeV	100 eV
	charge increase	G4DNAChargeIncrease	G4DNADingfelderChargeIncreaseModel	100 eV	100 MeV	-
Li, Be, B, C, N, O, Si, Fe	ionisation	G4DNAIonisation	G4DNARuddIonisationExtendedModel	0.5 MeV/u	$1x10^6$ MeV/u	-

The Physics Reference Manual [70] also describes how Geant4 handles atomic relaxation including fluorescence, Auger electron production and Particle Induced X-ray Emission (PIXE). These processes describe X-rays and electrons emitted as an atom relaxes back to neutrality after some process causing atomic excitation. The Auger process is important in the simulation of NP induced dose enhancement of radiation therapy and is implemented in Geant4 for $5 < Z < 100$ elements. Geant4 generates two random shell numbers - the first for selecting the electron that will fill the vacancy from the previous interaction, and the second to determine from which shell the Auger electron is emitted.

Recent advances included in the evolving physics models of Geant4 allow for the simulation of complete Auger cascades in version 10.2Beta, on top of the Auger electron emissions included in the Geant4 version used for the simulations presented in this thesis [95]. Incerti et al. (2016) shows emission from nano-sized Au volumes of Auger electron cascades. Figure 1.11 shows the way in which Auger electron emission is modelled in Geant4 up to version 10.1 and visually shows the part of the process omitted before the more recent Geant4 release.

Figure 1.11 represents a Auger electron emission after an electron is ejected after ionisation induced by an incident particle (blue sphere). The figure represents a KL_3M_1 Auger transition. The vacancy ("V1") left by the electron (green sphere) filling the vacancy ("V0") on the K-shell after ionization of an electron (red sphere) is taken into account by Geant4. However, the "V2" vacancy left by the emitted Auger electron (purple sphere) is neglected in Geant4 version 10.1 and earlier releases.

Examples of use of Geant4 and Geant4-DNA very low energy extension in nanodosimetry include studies of the interaction of particles with DNA dinucleosome previously described [88], as well as the study of the track structure in water of proton or electron tracks [96–101].

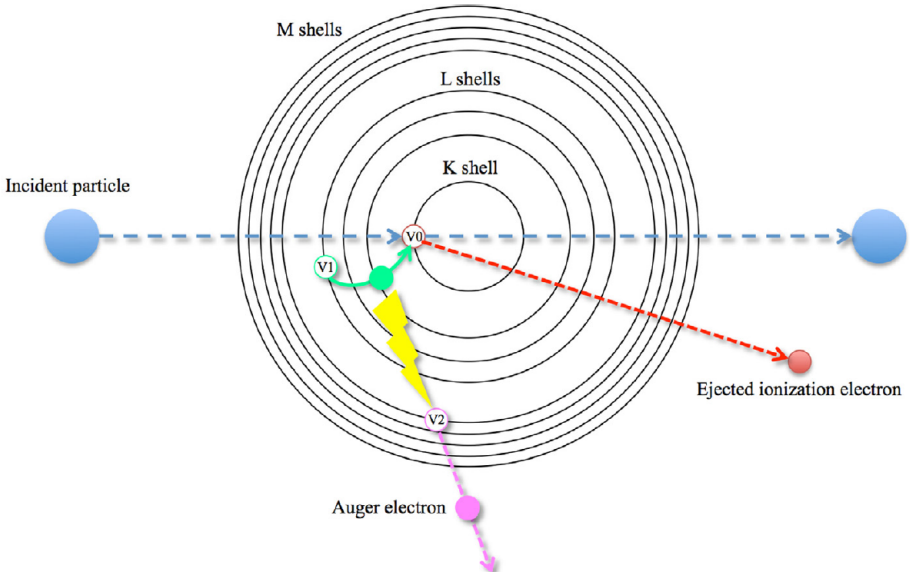

Figure 1.11: Illustration of the limitation of Geant4 for the tracking of Auger electron vacancies up to Geant4 release 10.1 (December 2014) (adapted from https://www.ikp.unikoeln.de/research/pixe/). Figure reproduced from Incerti et al. (2016) [95]. Further described in text.

The application of Geant4-DNA for nanodosimetric modelling of radial dependence of energy deposition has been studied in the case of liquid water [96]. Incerti et al. (2014) studied with Geant4-DNA the radial energy deposition from ion tracks in liquid water on a nanoscale, important for the calculation of radiobiological quantities. The researchers reported a comparison of Geant4-DNA calculated radial energy deposition with reference data and found good agreement.

The dose in microscopic volumes has also be calculated with Geant4-DNA models [97]. Byrne et al. (2013) examined the dose due to low energy electrons and photons on a microscopic cell. The number of ionisations and energy deposited in a modelled cell cytoplasm and nucleus was calculated for the photon and electron energies studied, relevant to out-of-field radiation in photon radiotherapy. The cell model consisted of a 5 μm radius spherical cell containing a 2 μm radius spherical nucleus with the approximated chemical composition of each. Geometry of this scale allowed for the application of low energy physics models,

rather than event-by-event tracking such as Geant-DNA (which is only applicable in liquid water at present). The study showed there are proportionally more ionisations occurring in the cytoplasm, compared to the cell nucleus and that the composition and size of cellular structures is important when considering out of field dose in photon radiotherapy.

Nanoscale Geant4-DNA simulations calculate the dose effects as well as ionisation clustering from particle tracks [99, 100]. Lazarakis et al. (2012) examined the nanoscale dose effects and track structure due to particle interactions in nanosized volumes [99, 100]. This research used Geant4-DNA to calculate the effect of magnetic field on the track structure of protons, electrons and alpha particles [99]. The Geant4-DNA code was compared with the PTB MC track structure code PTra, finding most difference in the simulation of electrons below 300 eV [100].

Lazarakis et al. (2018) recently investigated the energy deposition by electrons in liquid water with various physics models and parameters selected in Geant4. Liquid water spheres of increasing diameter (from 1 nm to 1 m) were modelled with electron beams of energies from 50 eV to 10 keV. This study reported the agreement between condensed history and track structure models available in Geant4. The best agreement between the condensed history and Geant4-DNA models was reported to be for Livermore with a low (10 eV) cut, compared to Penelope and higher production cuts.

1.5 Summary

Nanoparticles show a great potential for enhancement of radiation therapy including photon radiotherapy and proton therapy. The enhancement of the dose delivery to a tumour volume may allow for the reduction in the overall dose delivered to normal tissue, reducing the likelihood of adverse effects to the patient such as secondary cancer induction. Studies in the field of NP dose enhancement of radiation therapy have demonstrated the dose enhancement in simulation, cell, and small animal studies, as described in the literature review.

The body of research in this field aims to ultimately incorporate NP-induced enhancement into radiation therapy treatments in order to improve outcomes for patients. Preliminary clinical trial studies of the safety of nanoparticles for use in humans have shown promising results as to their safety for use in a clinical setting [50]. The effect on cells and tissues of NP combined with radiation is a combination of biological, chemical and physical interactions. For the ultimate goal of clinical implementation of NP enhanced radiation therapy to be realised, a detailed understanding of the physical mechanism of dose enhancement is required. The further elaboration of the fundamental physical interactions within a NP and in surrounding medium is an important area of study in this field.

The fundamental cause of potential physical dose enhancement in different radiation therapy modalities including conventional megavoltage and kilovoltage X-ray as well as proton therapy is an important aspect to study as different effects will come into play for varying photon energy, and particle types. Monte Carlo simulations provide a useful tool to investigate NP induced dose enhancement in radiation therapy. The effect of the size, shape, concentration and distribution of NPs within a cell volume is important when studying the dose enhancement deriving from NPs in radiotherapy.

This thesis will describe several Geant4 Monte Carlo simulations designed to investigate multiple aspects of NP-induced enhancement of radiation dose in clinical radiation therapy fields. Enhancement of dose in cells due to novel ceramic oxide NPs as well as the nanoscale dose distribution around a single nanosphere of variable material are investigated by means of customised Monte Carlo simulations. The limitations of the Monte Carlo models used are investigated and discussed in the context of nanoscale simulations. Ultimately, this thesis aims to present various techniques used and results of studies of several factors influencing the enhancement of radiation dose due to NPs.

Chapter 2 describes the results of the Monte Carlo simulation study of dose enhancement from novel ceramic oxide NPs irradiated with realistic kilovoltage and megavoltage photon radiotherapy treatment beams. Chapter 3 describes the extension of the application described in Chapter 2 to the investigation of dose enhancement in realistic cell geometry, examining the effect of NP aggregation and morphology.

Chapter 4 examines the nanoscale radial dose distribution around high-Z NPs in proton therapy. A customised Geant4 Monte Carlo code has been developed to allow the modelling of proton interactions in a nano-sized volume of ceramic oxide material and to track secondary particles to the level of the DNA, in water. A study was performed to evaluate the effect of plasmon excitations on the secondary electron yield originating from a carbon NP, due to an incident proton beam typical of the Bragg peak position in proton therapy. This work was performed in collaboration the MBN Research Center in Frankfurt, Germany and the Monte Carlo simulation aspect of this study was developed as part of this PhD project. Results of this study have been published in Verkhovtsev et al. (2015b) and are included in Chapter 4.

This work is an important contribution to the body of research into NP enhanced radiation therapy as the fundamental physical dose enhancement must be understood in combination

with biological and experimental results. Chapter 5 summarises the outcomes of this project and outlines directions for the future development of this work.

Chapter 2

Dose Enhancement by Nanoparticles in Conventional X-Ray Radiotherapy

The enhancement of photon radiotherapy by gold and ceramic oxide NPs has been demonstrated in experimental studies described in Chapter 1. This chapter now presents the first Monte Carlo simulation study of the dose enhancement in conventional X-ray radiotherapy by novel ceramic oxide NPs. This is the first study aimed to calculate and quantify the dose enhancement, secondary electron spectrum and LET of secondary electrons produced within novel ceramic oxide NPs with respect to gold NPs in kilovoltage or megavoltage photon fields. Of the ceramic oxide NP materials studied Ta_2O_5 and Bi_2O_3 are investigated as potential radio-enhancers whilst CeO_2 is known as a radio-protector (see Chapter 1). Gold was selected for comparison as it is a well known and widely studied radio-enhancer (see Chapter 1).

2.1 Methods: the Geant4 simulation application

Monte Carlo simulations were performed using Geant4 version 9.6 patch 2 and version 10.1 to verify the consistency of the results between the two versions of the Geant4 toolkit [67, 68]. The simulation set-up consisted of an array of spherical water volumes with 10 μm diameter, modelling cells. The array of cells is shown in Figure 2.1 placed in a water phantom at a depth of 6 mm or 25 mm corresponding approximately to the depth of maximum energy deposition in the case of a kilovoltage and megavoltage beam, respectively. The location of the cells is also dictated by the necessary experimental conditions, as described in refs [22, 32].

A 10 μm diameter spherical NP is located in the centre of the cell array, as shown in Figure 2.1b, modelling an aggregate of NPs. The material of this NP aggregate sphere is defined as Au, CeO_2, Ta_2O_5, Bi_2O_3, or water in the case of no NP. Modelling of cells and the NP aggregate as simple spherical volumes is an approximation which does not take into account the real morphology of NP aggregate or cells however this approach is adequate to compare the different NPs in terms of energy deposition and secondary electron spectra.

The Low Energy Electromagnetic Physics package [103] with Penelope physics models was selected to describe particle interactions. This choice was dictated by the capability of the Penelope model to track secondary electrons down to 100 eV (limit recommended in ref [91]), coupled with shorter simulation execution times compared to Geant4-DNA very low energy extensions. Although event-by-event Monte Carlo codes are the state of the art to study the effect of radiation at cellular and subcellular level, Stewart et al. (2002) showed that Penelope physics models can be used to estimate physical quantities of interest at cellular level with an agreement between 1% and 25% with event-by-event Monte Carlo codes when calculating the mean specific energy. Lazarakis et al. (2018) reported the difference between

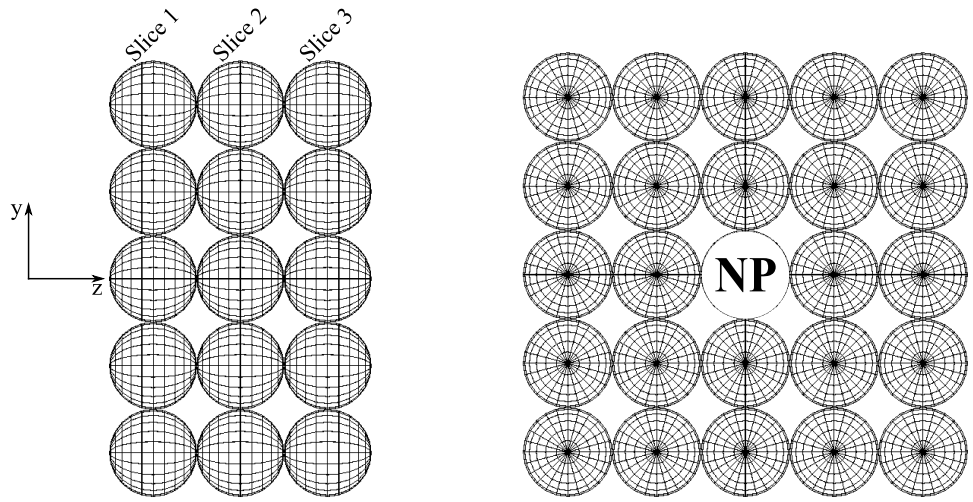

(a) Y-Z plane (b) X-Y plane

Figure 2.1: Geometry of cell array with solid NP sphere.

types of physics models in Geant4 and showed that for a target diameter applicable in this project (10 μm) results from condensed history models correlate well with track structure models such as Geant4-DNA. Atomic deexcitation, including Auger electron emission and fluorescence, were modelled in the simulation.

A 100 μm × 100 μm square photon source was incident normally on the edge of the phantom. Figure 2.2 shows the incident photon spectra. The kilovoltage photon source spectra used were provided by Prince of Wales Hospital, Randwick and were modelled using the SpekCalc software [105]. The 150 kVp spectrum (Figure 2.2b) was simulated using SpekCalc v1.1 and corresponds to the beam generated by a Nucletron Oldelft Therapax DXT 300 Series 3 Orthovoltage unit (Nucletron B.V., Veenendaal, The Netherlands) peak accelerating potential of 150 kV, Tungsten anode, inherent filtration of 3 mm Beryllium, additional filtration of 1.5 mm Aluminium and 0.35 mm Copper; first half value layer (HVL) of 0.67 mm Cu [105]. The 125 kVp spectrum was also obtained using the SpekCalc software and corresponds to the beam generated with peak voltage of 125 kV, Tungsten anode, inherent filtration of 3 mm Beryllium, additional filtration of 2.5 mm Aluminium and 0.1 mm

Copper; first HVL of 0.285 mm Cu. The 10 MV spectrum was obtained from ARPANSA [104].

The dose enhancement from each NP material in the kV and MV photon radiation fields compared to dose in the water phantom, without NPs, are studied. The total dose delivered to each of the cells was calculated as well as the secondary electron spectrum and the resulting LET of electrons entering cells. The spectrum of the secondary electrons originating from each type of photon interaction modelled (photoelectric, Compton scattering, pair production) was examined for each NP material. The proportion of these secondary electrons escaping each NP volume was also scored. The resulting LET of secondary electrons was determined using the secondary electrons' kinetic energy, and electron stopping power data from ref [106].

The dose enhancement due to the presence of a high-Z NP sphere was calculated as a ratio of the dose in the presence of the NP sphere to the dose with water in the NP sphere and expressed as a dose enhancement ratio (DER) shown in Equation 2.1.

$$DER = \frac{D_{\mathrm{NP}}}{D_{\mathrm{C}}^{*}} \tag{2.1}$$

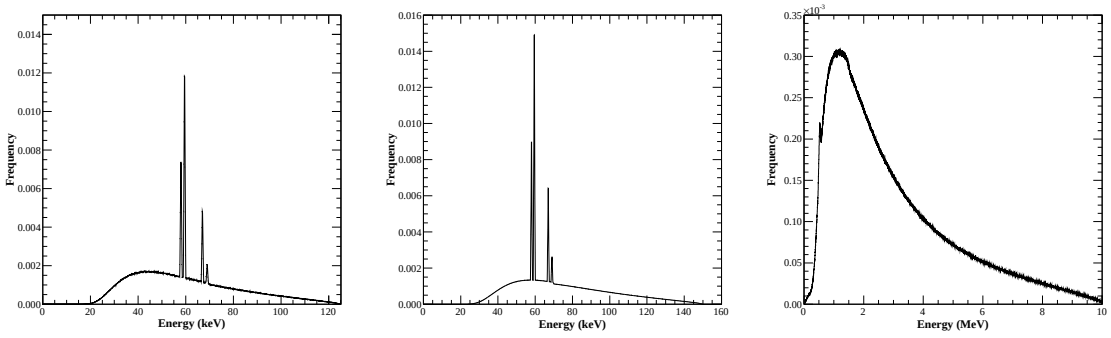

(a) 125 kVp (b) 150 kVp (c) 10MV

Figure 2.2: Incident photon energy spectra modelled in the simulation study, in terms of frequency per primary photon [104, 105]

where D_{NP} = dose in the cells with a NP sphere, and
D_C^* = dose in the cells with a water sphere

The secondary electrons produced within the NP material, and entering cells in the array were also analysed in terms of kinetic energy and LET. A comparison of electrons entering cells in close proximity to the NP aggregate and cells further away allows an understanding of the range of the physical dose enhancement effect. The mean energy of secondary electrons emitted from the NP is compared to that of electrons from a water sphere and the range of the secondary electrons is analysed.

2.2 Results

2.2.1 Dose enhancement produced by different NP types

The DER calculated (using Equation 2.1) for each NP material under study was mapped onto 2D maps. Dose enhancement maps are represented with square bins, although it should be noted that in the simulation set-up the dose was in reality calculated in spherical volumes of 10 μm diameter. The DER is determined by increased production of secondary electrons, however, with higher density and Z, such electrons also tend to be absorbed more easily by the NP itself.

Figure 2.3 shows the DER 2D maps obtained in the case of each photon spectrum under study incident on a Au NP. The DER is maximum in the cell downstream of the high-Z sphere and is also high in the cells adjacent to the sphere. It is important to note than the scale on the 2D DER maps from the megavoltage incident beam simulation is five times smaller than the scale applied to the kilovoltage due to the much lower DERs observed in this case and this applies also to Figures 2.4, 2.5 and 2.6. A DER of (7.5 ± 0.15) is observed

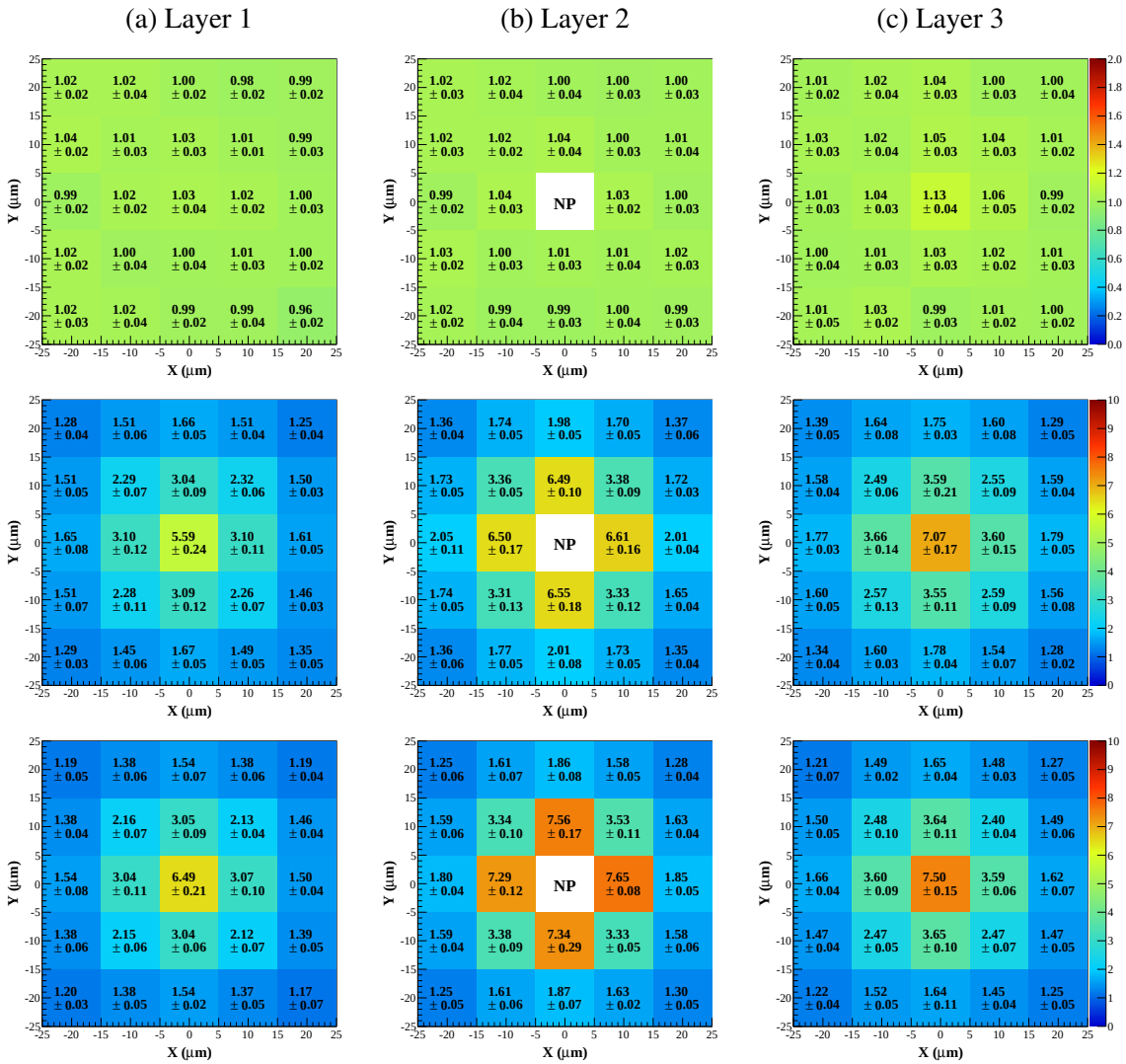

Figure 2.3: DER distribution due to Au NP in a 10 MV (top row), 150 kVp (middle row), and 125 kVp (bottom row) photon radiation field. Layers 1-3 are defined in Figure 2.1a.

in the cell immediately downstream of the high-Z gold sphere with a 125 kVp incident photon radiation field. This compared to a maximum DER in the same cells of (7.07 ± 0.17) in the 150 kVp and (1.13 ± 0.04) in the 10 MV photon radiation fields. The dose enhancement observed in the 10 MV photon radiation field is more subtle than the lower energy photon fields. The dose enhancement in the kilovoltage photon radiation field is due primarily to an increase in photoelectric interactions, however in the 10 MV photon field Compton scattering is the more dominant process (see Figure 1.4a) and the enhancement of

photoelectric interactions is lower.

Figure 2.4 shows the DER maps due to a 10 μm sphere of Bi_2O_3 in the cell array with each of the three photon radiation fields under study. A maximum DER of (7.20 ± 0.16) was found for the case of the Bi_2O_3 NP with a 125 kVp incident photon radiation field. This is a significant enhancement in the cell immediately behind the NP sphere, compared to that seen in the presence of the Au NP sphere of (7.50 ± 0.15). Similar to the Au NP case, the DERs due to the Bi_2O_3NP in the 10 MV photon radiation field are much less significant than those calculated in the kV photon fields.

Figures 2.5 and 2.6 show the DER maps due to Ta_2O_5 and CeO_2 NPs, respectively for each incident photon radiation field. A maximum DER of (5.80 ± 0.08) is observed in the cell immediately downstream of the high-Z Ta_2O_5 sphere with a 125 kVp incident photon radiation field. This compared to a maximum DER of (5.29 ± 0.12) in the 150 kVp photon beam and (1.03 ± 0.03), or a negligibly small enhancement, in the 10 MV case. A maximum DER of (5.38 ± 0.11) is observed in the cell immediately downstream of the CeO_2 sphere with a 125 kVp incident beam. This compared to a maximum DER of (5.27 ± 0.11) in the 150 kVp beam and (1.05 ± 0.02) in the 10 MV case.

The DER calculated for the cell immediately behind each NP type and energy studied is shown in Table 2.1. This is also the maximum DER of all cells (DER_{max}) in all NP cases and occurs due to forward ejected electrons being in close proximity to this cell. The mean total DER over all the cells and the DER with depth of slice, or layer (shown in Figure 2.1a) were calculated in order to analyse the difference in enhancement depending on location of the NP sphere with respect to the cells. The total DER calculated across the array and for each layer are also shown in Table 2.1.

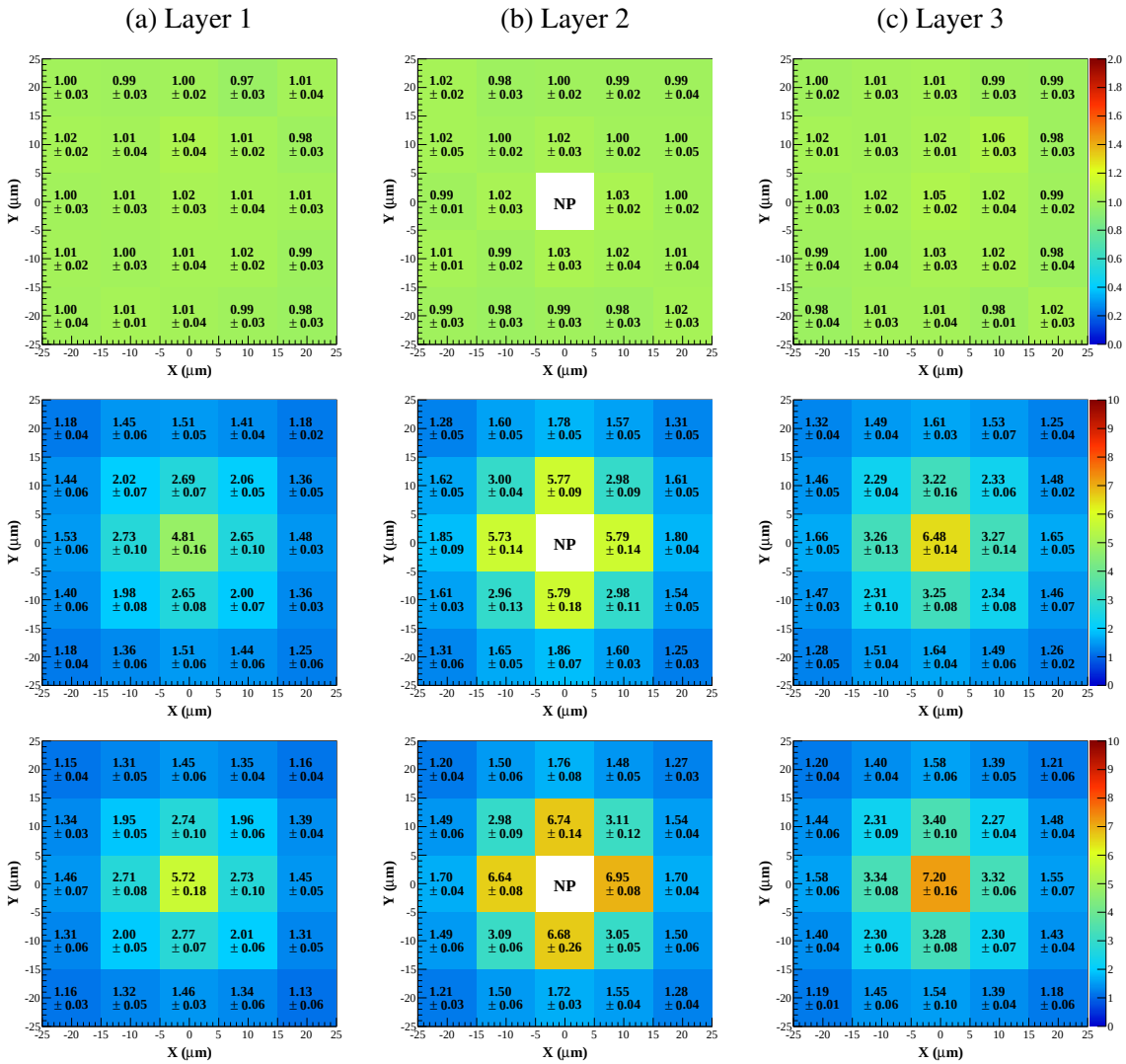

Figure 2.4: DER distribution due to Bi_2O_3 NP in a 10 MV (top row), 150 kVp (middle row), and 125 kVp (bottom row) photon radiation field. Layers 1-3 are defined in Figure 2.1a.

It is observed that Au is the most enhancing NP material across the photon energies studied, followed by Bi_2O_3. The radiosensitising Ta_2O_5 shows significant enhancement while the radio-protector CeO_2 shows the lowest radiation enhancement capability.

The 125 kVp spectrum simulations show more dose enhancement compared to the higher energy, 150 kVp incident photons. This is due to the differences in the interaction cross-sections corresponding to the photon energies in each spectrum, described in Chapter 1.

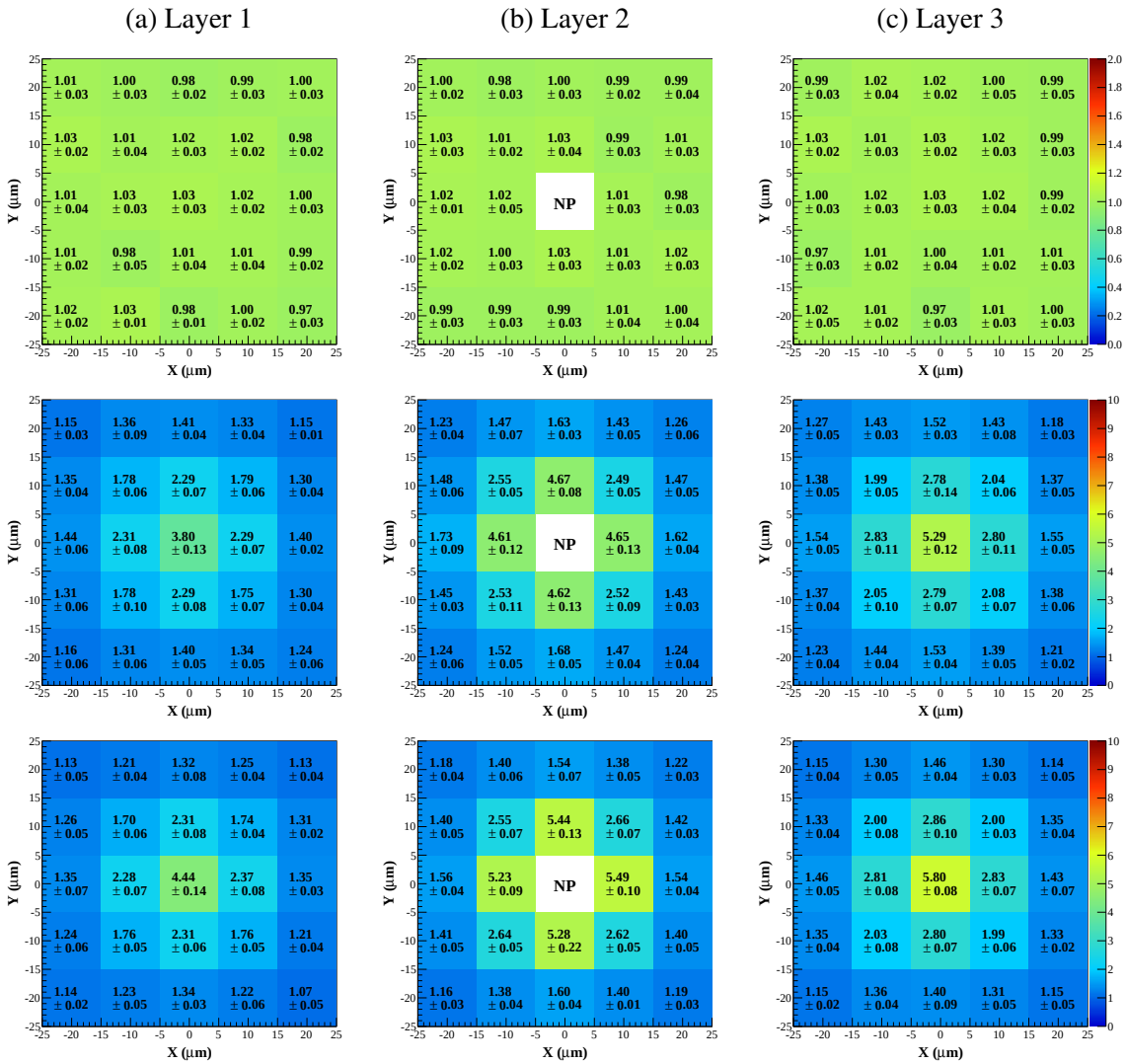

Figure 2.5: DER distribution due to Ta_2O_5 NP in a 10 MV (top row), 150 kVp (middle row), and 125 kVp (bottom row) photon radiation field. Layers 1-3 are defined in Figure 2.1a.

The mean energy of the 125 kVp and 150 kVp incident photon fields are 60 keV and 73 keV respectively. The K-edge for gold occurs at around 80 keV. The K-edge for other NP materials are shown in Table 1.1.

The DER is much more strongly observed in both of the kilovoltage beams, compared to the 10 MV photon radiation field. However, experimental measurements with MV photon fields show an increase in biological efficacy that would correspond to a larger dose enhancement

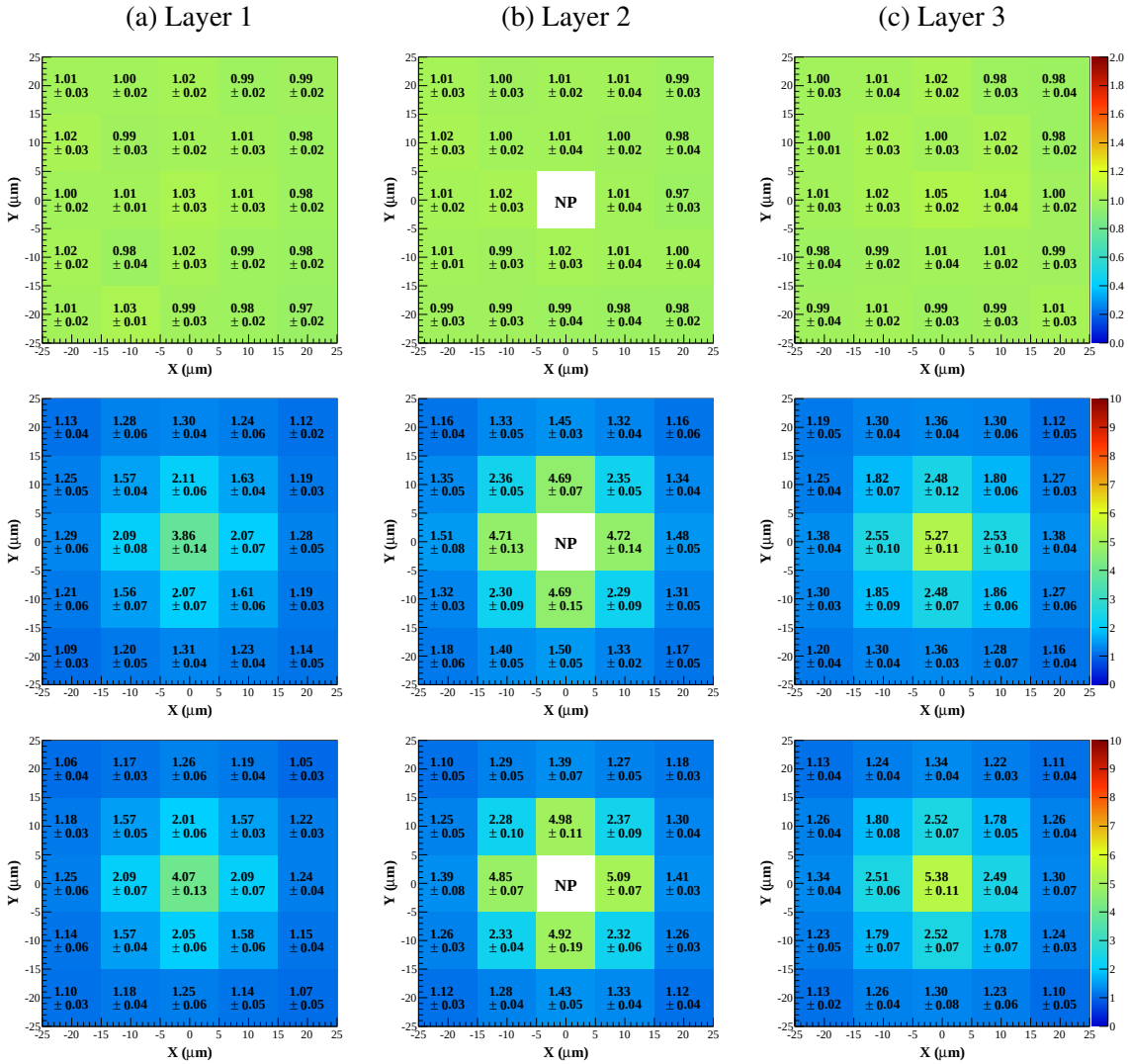

Figure 2.6: DER distribution due to CeO_2 NP in a 10 MV (top row), 150 kVp (middle row), and 125 kVp (bottom row) photon radiation field. Layers 1-3 are defined in Figure 2.1a.

than what is predicted by simulation [39, 41, 81]. This may be due to the biological and chemical mechanisms not accounted for in the physical dose enhancement simulation.

The simulations show there is potentially an ability to select optimised beam energy to obtain the maximum DER. Through the use of simulated results, beam energy could be selected to target the maximum of the interaction cross-section of a NP material placed within a tumour, whilst normal tissue damage is by comparison lower.

Table 2.1: Total DER in all cells, in each cell layer, and in the cell immediately downstream of the NP aggregate.

		Au	Ta_2O_5	CeO_2	Bi_2O_3
Total DER	125 kVp	2.34 ± 0.01	1.90 ± 0.01	1.74 ± 0.01	2.18 ± 0.01
	150 kVp	2.37 ± 0.01	1.90 ± 0.01	1.77 ± 0.01	2.15 ± 0.01
	10 MV	1.013 ± 0.004	1.006 ± 0.004	1.002 ± 0.006	1.005 ± 0.004
Layer 1 DER	125 kVp	1.97 ± 0.02	1.62 ± 0.01	1.49 ± 0.01	1.83 ± 0.01
	150 kVp	2.04 ± 0.02	1.64 ± 0.01	1.52 ± 0.01	1.83 ± 0.01
	10 MV	1.007 ± 0.007	1.005 ± 0.005	1.000 ± 0.004	1.004 ± 0.006
Layer 2 DER	125 kVp	2.87 ± 0.03	2.26 ± 0.02	2.07 ± 0.02	2.63 ± 0.02
	150 kVp	2.80 ± 0.02	2.18 ± 0.01	2.07 ± 0.01	2.52 ± 0.02
	10 MV	1.010 ± 0.005	1.005 ± 0.006	1.00 ± 0.01	1.004 ± 0.007
Layer 3 DER	125 kVp	2.21 ± 0.02	1.85 ± 0.02	1.69 ± 0.01	2.09 ± 0.02
	150 kVp	2.27 ± 0.02	1.88 ± 0.01	1.72 ± 0.02	2.10 ± 0.02
	10 MV	1.023 ± 0.004	1.007 ± 0.005	1.005 ± 0.005	1.007 ± 0.004
$Cell_{max}$ DER	125 kVp	7.50 ± 0.15	5.80 ± 0.08	5.38 ± 0.11	7.20 ± 0.16
	150 kVp	7.07 ± 0.17	5.29 ± 0.12	5.27 ± 0.11	6.48 ± 0.14
	10 MV	1.13 ± 0.04	1.03 ± 0.03	1.05 ± 0.02	1.05 ± 0.02

2.2.2 Secondary Electron Spectra and LET

The high DER observed in the cells around the high-Z NP spheres is due to electrons knocked out from the high-Z NP materials. The kinetic energy and resulting LET of secondary electrons entering all cells in the array were analysed with and without the NP included and with respect to different NP materials. Figure 2.7 shows the LET of secondary electrons created within the NP region, with respect to the type of NP and Figure 2.8 shows the LET of those electrons which then escape the NP volume. There is a significant increase in high-LET secondary electron production observed in both the 125 kVp and 150 kVp simulations in the NPs compared to water. The increased production of secondary electrons is less significant in the 10 MV simulation.

The LET of emitted electrons in Figure 2.8 effectively show the characteristics of the secondary electrons created within the NP which are not self-absorbed by the NP before escaping the volume. The number of escaping electrons is clearly much smaller (relative to the case of a water sphere) in the 10 MV compared to both of the kilovoltage simulations.

Figure 2.9 shows the kinetic energy spectra of electrons entering all of the cells for each photon radiation field under study whilst Figure 2.10 shows the resulting LET of these elec-

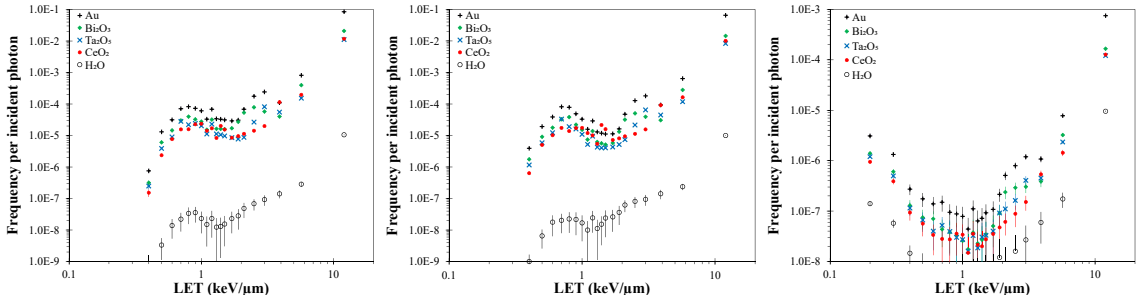

(a) 125 kVp (b) 150 kVp (c) 10 MV

Figure 2.7: LET of secondary electrons created within the NP with each incident photon beam.

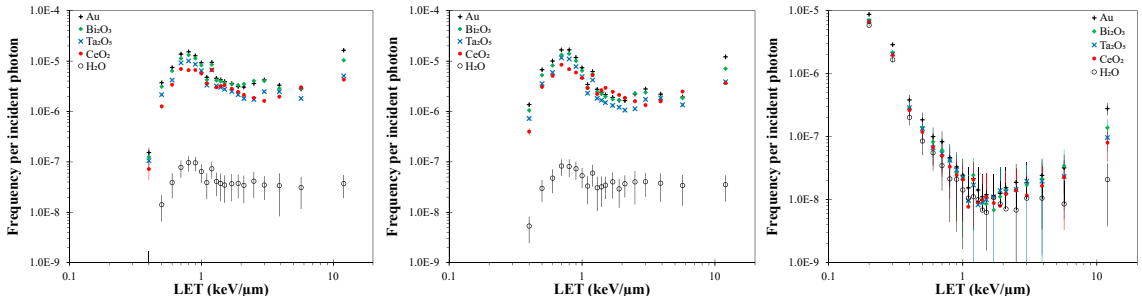

(a) 125 kVp (b) 150 kVp (c) 10 MV

Figure 2.8: LET of secondary electrons created within the NP and escaping the NP with each incident photon beam.

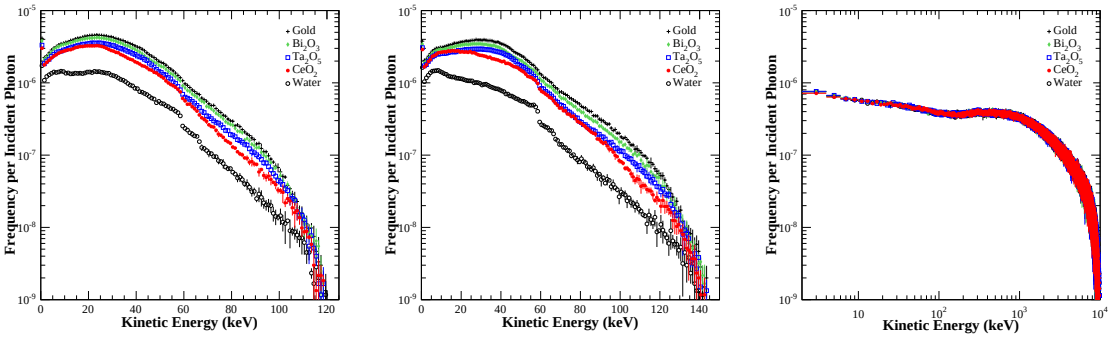

(a) 125 kVp (b) 150 kVp (c) 10 MV

Figure 2.9: Kinetic energy spectra of secondary electrons entering all cells in the array with each incident photon radiation field.

trons. These figures show the enhanced number of secondary electrons, compared to water. Electrons counted in this situation include those created within the NP volume as well as secondary electrons from the surrounding water phantom and neighbouring cells.

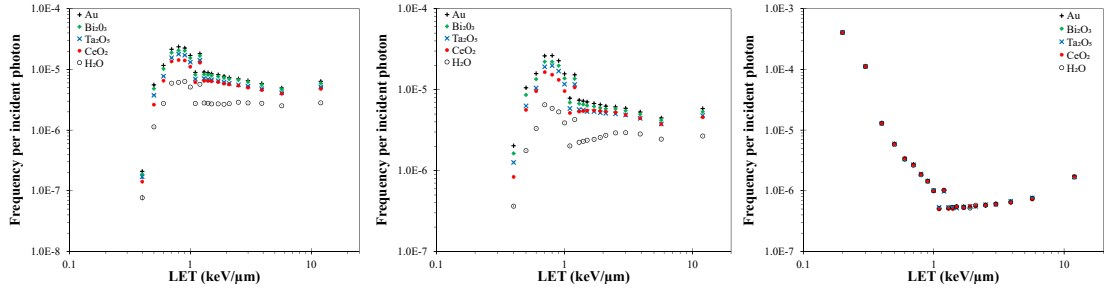

(a) 125 kVp (b) 150 kVp (c) 10 MV

Figure 2.10: LET of secondary electrons entering all cells in the array with respect to NP type.

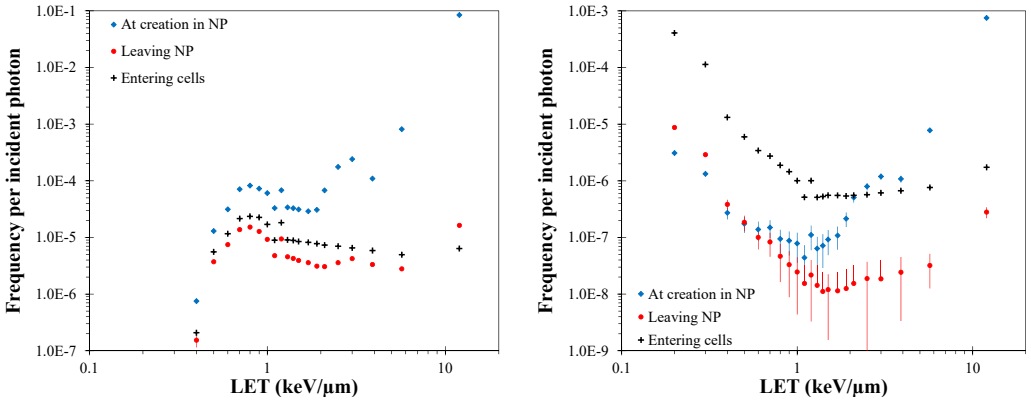

(a) 125 kVp radiation field (b) 10 MV radiation field

Figure 2.11: LET of secondary electrons originating within the Au NP, escaping the Au NP, and entering all cells in the array in each radiation field. Points without minimum error bars have errors which go below zero.

Figures 2.9 and 2.10 show, in the kinetic energy and resulting LET respectively, clear enhancement of electrons entering into the cells of the population due to different NP materials in the two kilovoltage beams. It can be observed that in the case of the megavoltage photon field there is no significant enhancement. This happens because at MeV energies Compton scattering dominates and the cross-section is independent from the atomic number and so the LET does not change. The photon interaction cross-sections are shown in Figure 1.4.

Figure 2.11 shows for the case of the Au NP a direct comparison of the secondary electron spectra created within the NP, leaving the NP and the total spectra entering all cells, per incident photon.

In both the 125 kVp and 10 MV photon field examples, the high-LET secondary electrons produced in the NP (blue curves) are, to a large degree, absorbed within the NP. This can be seen in the lower number of secondary electrons leaving the NP (red curves). The total spectrum of secondary electrons entering cells includes all sources, including those scattered in from surrounding water medium. In the case of the 10 MV photon radiation field, there is a lower proportion of secondary electrons produced due to interaction with the NP material

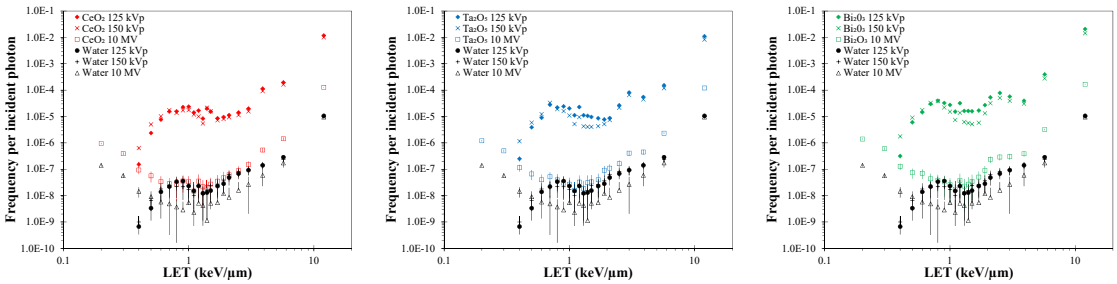

(a) CeO_2 (b) Ta_2O_5 (c) Bi_2O_3

Figure 2.12: LET of secondary electrons created inside the NP with three incident photon radiation fields incident on NPs or water.

with a higher proportion of electron entering cells due to interactions of the higher energy photons in the medium. This indicates that in general secondary electrons in the megavoltage photon radiation field will act over a larger range compared to those in the kilovoltage case. Figure 2.11b shows on the same plot the secondary electron spectra created in and escaping the NP and the increased lower-LET electrons entering cells. This shows that the higher-LET secondary electrons produced in the NP are likely to be absorbed that there is a greater number of lower-LET (high kinetic energy) secondary electrons entering the cell population as a whole.

Figure 2.12 shows that the number of higher LET electrons produced in the NP is increased for all materials studied with the lower energy photons in the 125 kVp and 150 kVp spectra compared to 10 MV incident photon spectrum. A comparison of the LET of electrons entering cells with 125 kVp, 150 kVp, or 10 MV incident beam shows the effect of the beam energy on selectivity of enhancement from NPs in the kilovoltage photon irradiation. It can be observed that in the kV beams the additional electrons have higher LET for all the NP materials under study. In the 10 MV photon field the lower LET (higher kinetic energy) electrons are more prominent than the high-LET, low range electrons and there is minimal enhancement observed comparing the electron spectra with and without NPs.

Figures 2.11 and 2.12 show LET of secondary electrons at various points in the simulation geometry. These figures demonstrate the mechanism of dose enhancement in the cells. Not all secondary electrons produced in and emitted from the NP materials will reach the surrounding cells. The higher LET, low kinetic energy secondary electrons will have a lower range, a lower probability to escape the NP, and a lower probability to reach the surrounding cells compared to higher energy electrons. The range of secondary electrons depends on their kinetic energy and on the material through which they are transported. The range of low energy electrons in different materials is shown in Table 2.2 and Figure 2.13 with data obtained from Berger et al. (2005).

Table 2.2 and Figure 2.13 demonstrate that the low energy part of the spectrum will have a lower probability to escape the high-Z NPs if they are created at a distance greater than 1 µm from the surface. These low energy electrons will also travel less than 10 µm in the water medium before they are absorbed meaning the effect of these electrons will remain localised to the NP material for the most part.

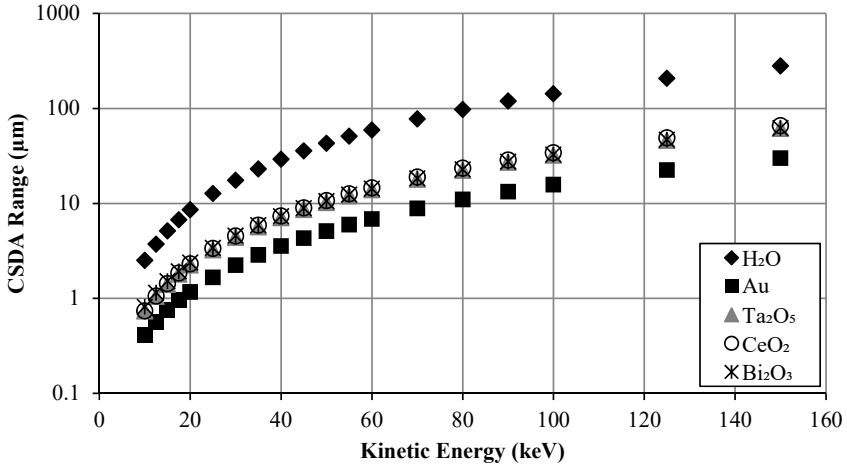

Figure 2.13: Continuous-slowing-down approximation (CSDA) range of low energy secondary electrons in NP materials, and water, with respect to electron kinetic energy. Data obtained from Berger et al. (2005)

Table 2.2: Range of low energy secondary electrons in NP materials, and water, with respect to the electron kinetic energy. Data obtained from Berger et al. (2005)

Kinetic Energy (keV)	H_2O (μm)	Au (μm)	Ta_2O_5 (μm)	CeO_2 (μm)	Bi_2O_3 (μm)
10	2.52	0.41	0.74	0.74	0.82
20	8.57	1.17	2.25	2.31	2.39
30	17.6	2.24	4.40	4.56	4.59
50	43.2	5.13	10.3	10.8	10.6
100	143.1	15.8	32.3	34.2	32.8

2.2.3 Effect of Atomic Deexcitation

Atomic deexcitation (AD) processes (Auger electron emission and fluorescence) are activated in the simulations. The effect of the secondary electrons produced from AD processes was quantified by running paired simulations with and without the AD processes. The resulting secondary electron spectra were then analysed and subtracted from one another in order to extract the component of the spectra attributable to AD processes. Counts falling within error of zero, or within error of the original spectra are disregarded. Similarly, the effect on the DER was calculated. Figure 2.14 shows the spectra of secondary electrons that originated from AD processes.

Atomic deexcitation electrons have low kinetic energy and therefore interact and deposit dose close to the point of creation. This means that on the micron-scale of the cell array simulated in this study the effect of AD electrons is effectively swamped by higher energy secondary electrons. The effect of Auger electrons has been observed on the nanoscale [40]; however, this is not quantified in the present study due to the micron-size of the cell volumes defined in the simulation set up.

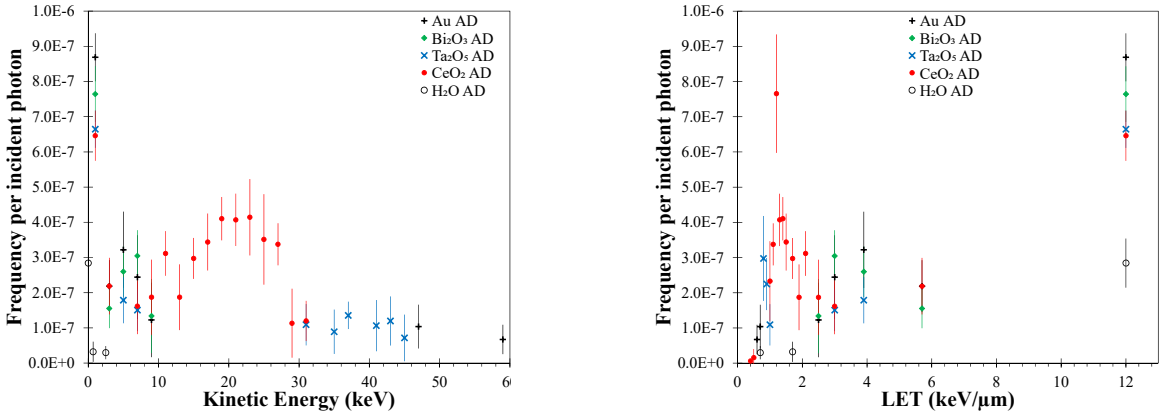

Figure 2.14: Kinetic energy and LET of secondary electrons originating from AD.

2.3 Discussion

These simulations demonstrate the effect of incident photon beam spectra on the dose enhancement capabilities caused by the difference in interaction cross-sections between high and low energy photons, as described in detail in Chapter 1. Lower energy photons, as found predominantly in the 125 kVp and 150 kVp X-ray spectra, are more likely to interact by means of the photoelectric effect (shown in Figure 1.4). At higher photon energies (up to 10 MeV in the spectrum studied in this project) Compton scattering becomes the dominant type of interaction. Therapeutic photon spectra (including the one referred to in this simulation) are not monoenergetic, and the mean energy of photons is lower (around 2 MeV for the 10 MeV case) and therefore photoelectric interactions are not an insignificant component of the photon interactions in the NP material.

Figure 1.5 shows the increased mass absorption coefficients of photons in gold compared to water for the cases of pure gold, and a 1% solution of gold in water. Using the mass absorption coefficient ratios an estimate can be made of the increased photon absorption expected in a solution containing gold. An increase in the mass absorption coefficient in a 1% gold solution is estimated from this data to be 33%, 26% and 0.2% for the 125 kVp, 150 kVp,

and 10 MV fields, respectively. This demonstrates the theoretical advantage of high-Z NP induced enhancement of photon interactions being most prevalent for lower energy photons (less than a few hundred keV). The contrast in the order of magnitude of the observed dose enhancement in the cell simulation in the kilovoltage and megavoltage photon beams (from Table 2.1, it is about 130% compared to 1%, respectively) is in agreement with this estimate from the mass absorption coefficient ratio.

The simulation results in this chapter demonstrate a higher overall dose enhancement compared to the theoretical estimate of increased photon absorption. This is due to the larger mass of gold modelled as a spherical NP in the simulation rather than a homogeneous 1% gold solution in water. The average effect of the increased probability of photon absorption is not the quantity calculated in this simulation as the aim was to examine the effect of NP material in close proximity to modelled cells and the micron-scale effects rather than the effect of a homogeneous solution of NP in water. The difference in dose enhancement observed also promotes the importance of the study of realistic NP geometries and NP internalisation into cells or coating of cells (rather than homogeneous solution approximations) when measuring and calculating dose enhancement in this type of situation, on the scale of the cell.

Both the estimate based on the increase in the absorption of photons and the simulation study presented in this chapter predominantly account for the effect of primary photons interacting in the region of interest. The simulation does not take into account the total effect of all electrons (e.g. Compton scattered) which are scattered into the region of interest, which may form a significant portion of the dose deposited in the region close to the NP. The fact that radiosensitisation of cells is observed under higher energy irradiation in experimental studies [21, 32] indicates that there is an increase in the number of damaging particles reaching cells which is not accounted for by the modelling of the photon and secondary electron

interactions in this study.

In the case of the kilovoltage photons the increase in photoelectrons is a dominant factor. However, the simulations show that local dose enhancement from increased secondary electrons produced in the NP is a less significant component in the megavoltage photon field. The simulations have shown a significant increase in secondary electrons with relatively high-LET entering cells in the population in the case of the kilovoltage photon radiation fields however there was no significant increase observed in the megavoltage photon radiation field. The small increase in secondary electrons produced within the high-Z NPs in the 10 MV field is not translated into an increase in secondary electrons entering cells in the array due to the majority of created electrons being reabsorbed within the NP itself (as demonstrated in Figure 2.8c). The effect on DER of the distance from the high-Z material is further examined and discussed in Chapter 3.

2.4 Conclusion

The study of dose enhancement by ceramic nanoparticles in kilovoltage and megavoltage photon radiotherapy beams incident on a modelled cell population has been investigated by means of Geant4 simulations with results being presented in this chapter. The micron-scale simulations presented in this chapter show that ceramic oxide NPs enhance the secondary electron production and dose deposition in cells.

The fundamental physical interaction of incident photon radiation within high-Z NPs is increased compared to water, with the highest increase observed in the kilovoltage primary photon field, compared to the megavoltage field. This outcome is to be expected when the photon interaction cross-sections for each photon energy range are compared. The prefer-

ential dose enhancement in the kilovoltage photon fields is due to the strong dependence of the photoelectric effect interaction cross-section with increasing atomic number of the NP material where photoelectric interactions dominate at photon energies below about 100 keV (see Figures 1.4 and 1.5 in Chapter 1). In the simulation study presented in this chapter, the physical dose enhancement is observed to be in agreement with these theoretical interaction probabilities.

All ceramic oxides studied (Bi_2O_3, Ta_2O_5 and CeO_2) showed dose enhancement in comparison to water, and were most effective in the kilovoltage photon field. This is in agreement with cell studies described in the Chapter 1 literature review. In the case of CeO_2, the literature describes a radio-protecting free radical scavenger with dose-enhancing high-Z properties which act in a contradictory manner. The Geant4 simulations in this chapter have shown that dose deposition is enhanced in the presence of CeO_2 and this demonstrates the need, when using this material as a radio-protector, to take into account the high-Z enhancement capabilities of this NP material, especially in the kilovoltage energy range where photoelectric interactions are most important.

Briggs et al. (2013) reported a decrease in the radio-protection effect of CeO_2 NPs in cells with both 10 MV and 150 kVp photon irradiations. This cell survival study on the radioresistant 9L rat brain gliosarcoma cells reported an increase in the cell killing effect of the radiation in the kilovoltage X-ray field. This observed effect is postulated to be attributable to a change in the enhanced secondary electron production at this energy in particular, due to the relatively high-Z of CeO_2 (Z_{eff} = 54). The Geant4 simulations presented in this chapter support this suggestion, as they have shown the dose enhancement effect of CeO_2 NPs to be significant, compared to other known radiation enhancing NPs such as gold and Ta_2O_5. The effect is especially prominent in the kilovoltage photon fields, which corresponds to the experimental results previously reported by Briggs et al. (2013).

The role of the shape and distribution of NPs on calculated dose enhancement within a simulation is further investigated in Chapter 3.

Chapter 3

Characteristics of Ceramic Oxide Nanoparticles

This chapter will describe studies of particular types of ceramic oxide nanoparticles and their distribution amongst cells. The dose enhancement effect of Ta_2O_5 and Bi_2O_3 NP materials is studied in detail in terms of the concentration and distribution of NPs. The effect of the NP distribution and shape is investigated by means of a modification of the simulation formalism explained in Chapter 2.

3.1 Enhancement by Bi_2O_3: Dependence on NP Shape

Unlike gold NPs, which are predominantly spherical in shape [39], Bi_2O_3 NPs tend to exhibit a flatter morphology [33], and can be described more precisely as NP "plates" or as having a platelet morphology. Figure 1.7 in Chapter 1 shows the platelet morphology of Bi_2O_3 NPs fabricated in the study published in the journal article Stewart et al. (2016) (see Appendix A). The Bi_2O_3 NP plates tend to lie flat on top of cells in the experimental cell culture.

This Monte Carlo simulation study was aimed to investigate the physical mechanisms behind the results of the cell experiments conducted at IHMRI at the University of Wollongong, with respect to the shape of the NP aggregate in the cell culture.

3.1.1 Methods: the Geant4 simulation application

The same simulation application described in Section 2.1 was used with only the NP shape changed. Several different geometries were selected for this study - a sphere (analagous to Au NP), a plate (for Bi_2O_3 NP) of increasing thickness, and a cube to model the effect of a bulk of NP. The dimensions of the shapes under study are: a sphere with 10 μm diameter, a 10 μm × 10 μm × 10 μm cube, a 10 μm × 10 μm × 1 μm plate, and a 10 μm × 10 μm × 5 μm plate. Figure 3.1 shows the different geometries and NP aggregate positioning in the cell array with the photon radiation field incident from the left.

The simulated 125 kVp and 10 MV radiation fields and the physics component are the same as in the previously described simulation application, in Section 2.1. A total of 6×10^6 and 3.5×10^6 primary photons were incident on the phantom in order to achieve sufficient statistical results in the kV and MV beam simulations, respectively.

The DER was calculated as per Equation 2.1. A weighted dose enhancement ratio (DER_w) was also used to evaluate the effect of NP shape with respect to the total mass of NP placed in the geometry. Equation 3.1 shows how DER_w is calculated from the DER.

$$DER_w = \frac{(DER - 1)}{m_{NP}} \tag{3.1}$$

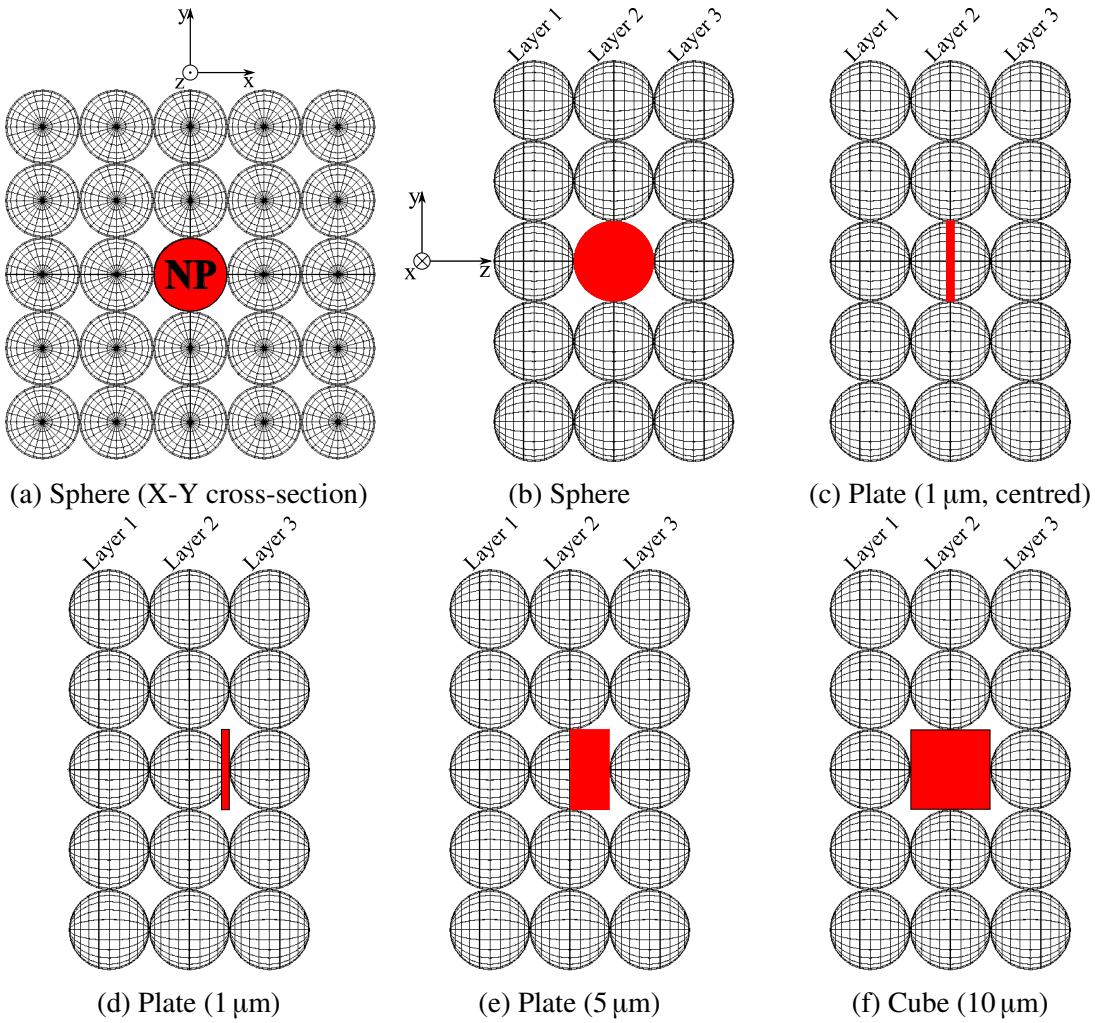

(a) Sphere (X-Y cross-section) (b) Sphere (c) Plate (1 µm, centred)

(d) Plate (1 µm) (e) Plate (5 µm) (f) Cube (10 µm)

Figure 3.1: Shapes of Bi_2O_3 NP aggregate under study and placement within cell array. Note that the beam is incident in the positive z-direction, shown here in Fig.3.1b.

3.1.2 Results

The dose enhancement produced by the Bi_2O_3 sphere, cube, and plate placed in the cell array was calculated in terms of DER shown in Equation 2.1. The DER in each cell in cell layer 3, "downstream" of the NP, are shown in 2D maps in Figure 3.2 in the 125 kVp photon field. The top row of the 2D maps shows for each cell the calculated DER whereas the bottom row shows the DER_w, scaled to the mass of NP in the geometry according to Equation 3.1, in order to examine the dose enhancement per unit mass of NP dependence

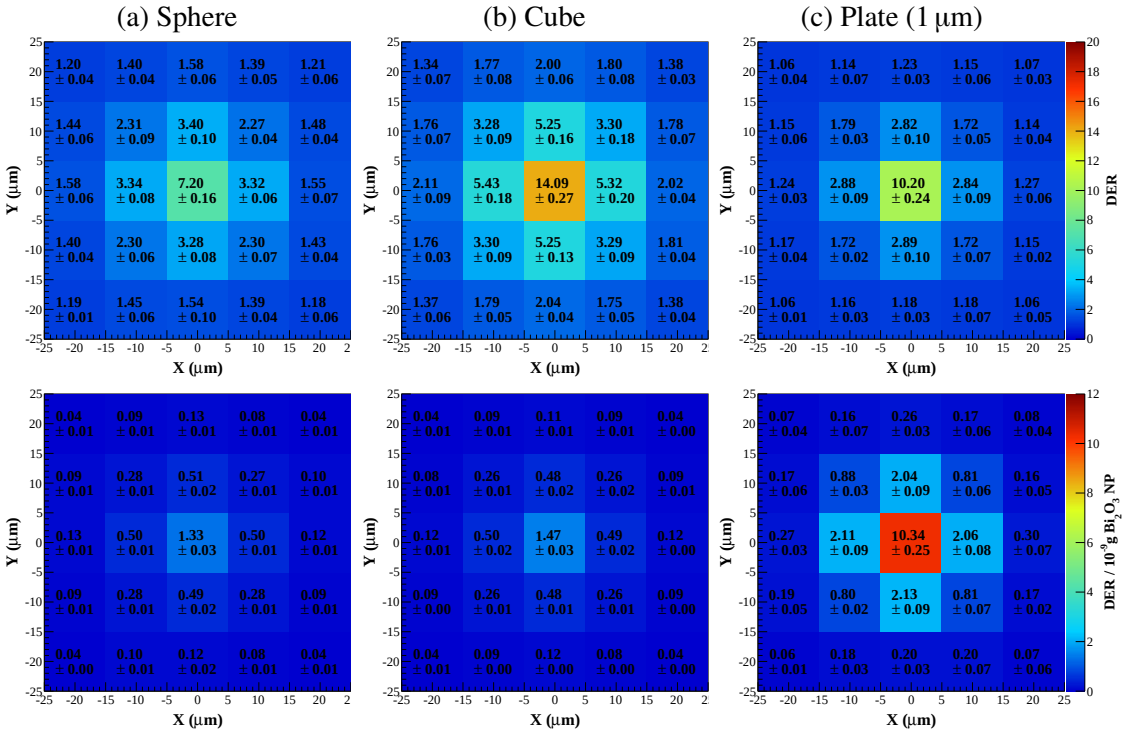

Figure 3.2: DER maps of cell layer 3 in 125 kVp radiation field with Bi_2O_3 NP material in different geometrical configurations a: Sphere, b: Cube and c: Plate (placed at the edge of cell layer 3, as shown in Figure 3.1d). Bottom row shows DER_w scaled to mass of Bi_2O_3 in the different shapes.

on the geometry.

It can be observed in the 125 kVp photon field that the DER obtained in the case of a cube is larger than that of the sphere and plate configurations, however, the DER_w scaled to the mass of NP, the plate geometry is superior in terms of dose enhancement. This is due to the higher surface area to volume (SA:V) ratio in the case of the plate ($2.4 \times 10^6\ m^{-1}$), compared to the surface area to volume ratios of the cube and sphere (both equal to $0.6 \times 10^6\ m^{-1}$). The results for the 10 MV incident beam simulation are not shown as the 2D DER maps showed no significant enhancement of the megavoltage beam.

Table 3.1 shows the DER due to each NP shape with respect to depth of cell layer and incident photon radiation beam energy. The total DER in the cell population is reported as

Table 3.1: DER with respect to NP aggregate shape in kV and MV photon radiation fields. Layer 1, 2 and 3 refer to cell layers defined in Figure 2.1a.

	125 kVp		
DER	Sphere	Cube	Plate
Layer 1	(1.83 ± 0.01)	(2.60 ± 0.02)	(1.15 ± 0.01)
Layer 2	(2.63 ± 0.02)	(4.20 ± 0.02)	(1.40 ± 0.01)
Layer 3	(2.09 ± 0.02)	(3.06 ± 0.02)	(1.87 ± 0.01)
Total	(2.18 ± 0.01)	(3.27 ± 0.02)	(1.48 ± 0.01)
	10 MV		
Layer 1	(1.004 ± 0.006)	(1.02 ± 0.01)	(1.00 ± 0.01)
Layer 2	(1.004 ± 0.007)	(1.02 ± 0.01)	(1.00 ± 0.01)
Layer 3	(1.007 ± 0.004)	(1.021 ± 0.004)	(1.00 ± 0.01)
Total	(1.005 ± 0.004)	(1.02 ± 0.01)	(1.002 ± 0.005)

well as the average DER in each cell layer, including layer 3 immediately downstream of the NP Bi_2O_3 NP aggregate. It can be observed that the DER obtained in the case of a cube is larger than that of the sphere and plate configurations. However, when the enhancement is scaled to the mass of NP the advantage of a plate geometry becomes clear. Table 3.2 shows the DER_w scaled with respect to NP mass, for three NP shapes simulated in the 125 kVp and 10 MV photon fields.

The data in Tables 3.1 and 3.2 clearly show higher DER in the kilovoltage case, compared to insignificant enhancement in the megavoltage photon field simulation. The DER is observed to be higher in the kilovoltage case, compared to the megavoltage with a total DER of (2.18 ± 0.01), (3.27 ± 0.02), and (1.48 ± 0.01) around the Bi_2O_3 sphere, cube and plate respectively in the kilovoltage beam compared to (1.005 ± 0.004), (1.02 ± 0.01), and (1.002 ± 0.005) for Bi_2O_3 sphere, cube and plate with the 10 MV beam. The increasing DER corresponds to increasing mass of Bi_2O_3 NP placed within the geometry.

When the enhancement is scaled to the mass of NP (per g NP) the weighted dose enhance-

Table 3.2: DER_w with respect to NP aggregate shape weighted to total NP mass in kV and MV photon radiation fields. Layers 1, 2 and 3 refer to cell layers defined in Figure 2.1a.

DER_w ($/g_{NP}$)	**125 kVp**		
	Sphere	Cube	Plate
Layer 1	$(1.77 \pm 0.01)\times10^8$	$(1.80 \pm 0.01)\times10^8$	$(1.64 \pm 0.01)\times10^8$
Layer 2	$(3.51 \pm 0.02)\times10^8$	$(3.59 \pm 0.02)\times10^8$	$(4.53 \pm 0.03)\times10^8$
Layer 3	$(2.34 \pm 0.02)\times10^8$	$(2.31 \pm 0.01)\times10^8$	$(9.82 \pm 0.07)\times10^8$
Total	$(2.53 \pm 0.01)\times10^8$	$(2.56 \pm 0.01)\times10^8$	$(5.34 \pm 0.02)\times10^8$
	10 MV		
Layer 1	$(0.00854 \pm 0.00005)\times10^8$	$(0.0175 \pm 0.0001)\times10^8$	$(-0.0403 \pm 0.0002)\times10^8$
Layer 2	$(0.00745 \pm 0.00004)\times10^8$	$(0.0273 \pm 0.0002)\times10^8$	$(0.0421 \pm 0.0003)\times10^8$
Layer 3	$(0.0152 \pm 0.0001)\times10^8$	$(0.0236 \pm 0.0002)\times10^8$	$(0.0578 \pm 0.0003)\times10^8$
Total	$(0.01042 \pm 0.00004)\times10^8$	$(0.0228 \pm 0.0001)\times10^8$	$(0.0195 \pm 0.0001)\times10^8$

ment ratio (DER_w) in the 125 kVp field becomes $(2.53 \pm 0.01)\times10^8 g^{-1}$, $(2.56 \pm 0.01)\times10^8 g^{-1}$, and $(5.34 \pm 0.02)\times10^8 g^{-1}$ for the sphere, cube, and plate geometries, respectively. The very low DER calculated in the 10 MV fields results in DER_w that are insignificant and orders of magnitude smaller than in the 125 kVp case shown. It is clear from the scaled DER_w shown in Table 3.2 that the plate is the most effective geometrical configuration, with respect to NP mass. This is due to the increased proportion of secondary electrons able to escape the NP, enter surrounding cells, and deposit extra dose in those cells. The plate has a SA:V ratio which is four times higher than that of the cube or the sphere. Consequently, a higher proportion of electrons (from these simulation results, approximately five times) created within the plate go on to escape the NP volume in the simulation compared to either the cube or sphere.

Figure 3.3 shows in the 125 kVp field for all geometries simulated the DER and DER_w with respect to radial distance from the centre of the NP aggregate, in layer 2 (shown in Figure 3.1). Figure 3.3a shows the DER is highest in the case of the 10 µm sided cube followed by

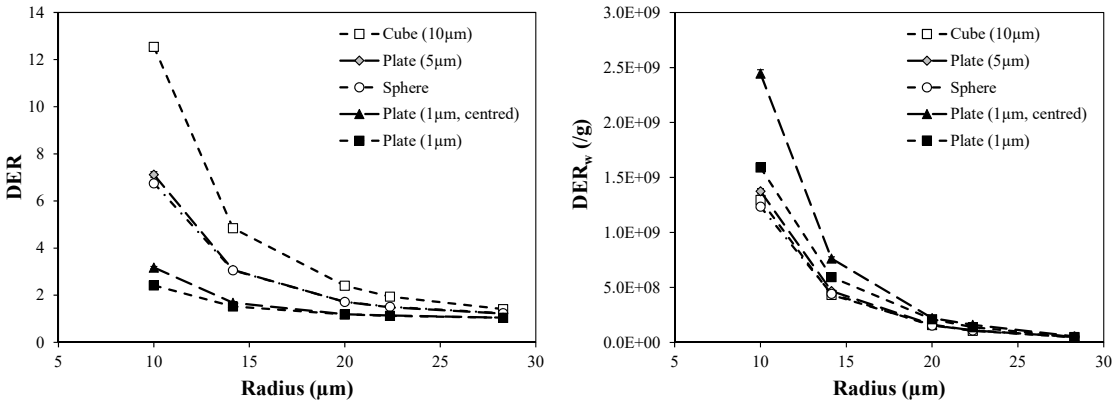

(a) DER (b) DER_w

Figure 3.3: DER and DER_w in layer 2 with respect to radial distance from the aggregate centre in 125 kVp photon radiation field with Bi_2O_3 NP material in different geometrical configurations.

the 5 µm wide plate and 5 µm radius sphere with the lower DER observed for the 1 µm wide plates placed either in the centre of the array, or against layer 3 (bottom layer) of cells. These results indicated that the DER is most effected by the total size (or mass) of NP aggregated in the centre of the cell population.

Figure 3.3b shows that when scaled with respect to NP mass in the cell array, the narrow 1 µm plate geometry is the most effective geometry per unit mass due to the high surface area to volume ratio previously described. The results show in the cell volumes close to the NP aggregate the DER_w is higher in proximity to the centred plate compared to the off-centre plate. This is due to the fact that dose is calculated only in the spherical cells in the array and so the centred plate has an advantage being in direct contact with, and centred on, neighbouring cells in layer 2.

The change in DER and DER_w with respect to radial distance from the aggregate centre in cell layer 3 (below the NP aggregate) for the 125 kVp field are shown in Figure 3.4. In a realistic cell population, the NPs tend to settle on top of a single layer of cells, as described in the literature review section. Therefore, it is valuable to also examine the DER in layer 3

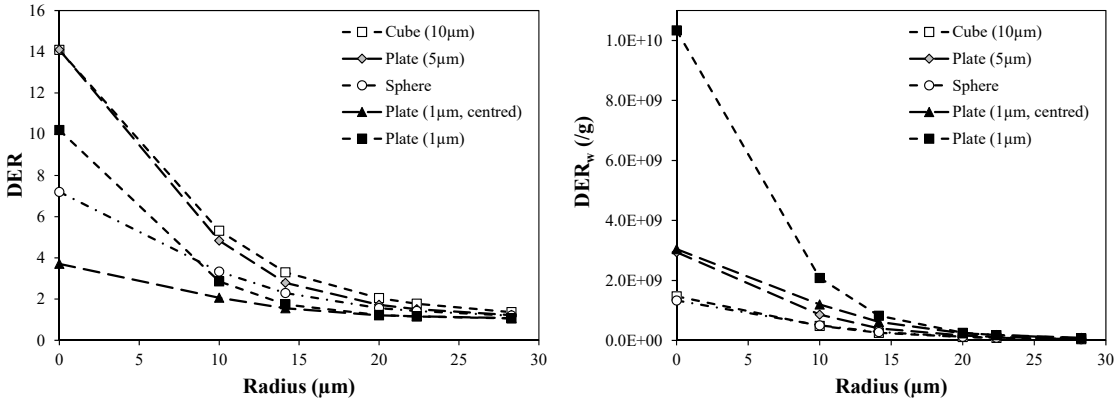

(a) DER (b) DER_w

Figure 3.4: DER and DER_w in cell layer 3 with respect to radial distance from the aggregate centre under 125 kVp photon radiation field with Bi_2O_3 NP material in different geometrical configurations.

of cells below the NP aggregate. Figure 3.4 shows the dose enhancement (DER and DER_w) in this cell layer. Again, before scaling to mass of NP, the 10 μm sided cube has the highest DER, however the 5 μm wide plate has a similarly high DER effect. The 1 μm wide plates are observed to result in a lower dose enhancement, with preferential enhancement found when the thin NP aggregate plate is in close proximity to the cell layer. When the dose enhancement is calculated with respect to NP mass in the aggregate the plate geometry is again the most efficient enhancer, in terms of DER_w.

Figure 3.3 shows the high DER in close proximity to the NP drops significantly at distances of 20 - 30 μm from the NP material, in layer 2. Figure 3.4 shows the same drop-off in layer 3, behind the NP aggregates. Comparing the radial dependence of DER observed around a 1 μm plate centred in the geometry to the identical plate placed against layer 3 demonstrates the dose enhancement effects of both plate positions are similar in cells at and beyond a radial distance of 20 μm. In the cells closest to the NP aggregate the 1 μm plate placed in closer proximity to the cells in layer 3 results in a higher DER compared to the same plate placed at the centre, 5 μm from the cell layer.

The radial dependence of the DER in the case of the 10 MV photon radiation field is shown in Figure 3.5. As indicated previously by the DER data presented in Tables 3.1 and 3.2 the DER in the megavoltage radiation field is much lower than in the kilovoltage case. This is again reflected in the plot of DER with respect to radial distance. The DER is highest in the cells closest to the NP aggregate for all geometries studied, however in contrast to the kilovoltage case, the DER increases after initially dropping off from the initial maximum. This is due to the difference in the quality of the secondary electron spectra generated from the megavoltage photon field. Figure 2.12c in the previous chapter showed the LET of secondary electrons entering all cells in the population with respect to photon radiation field spectra. In the case of megavoltage photon spectra, there are more low-LET electrons entering the cells, compared to in the kilovoltage photon radiation fields. High-LET electrons, by their very definition, are more likely to deposit their energy close to their origination point due to their lower range. Electrons with energy greater than about 50 keV can have a range which is greater than the cell at the furthest distance from the NP aggregate in the cell population (see Figure 2.13). The CSDA range of, for example, a 1 MeV electron in water is more than 4 mm. The mean kinetic energy of secondary electrons entering cells in the population within a 10 MV photon radiation field is approximately 2.2 MeV. These electrons can have a range that is greater than 10 mm and will therefore deposit much of their energy at a large distance from the point of interaction with a NP. The secondary electrons from the kilovoltage photons will, in contrast, deposit their energy more locally and so a larger dose enhancement is observed in cells close to the high-Z NP aggregates in this case.

The kinetic energy spectra as well as the linear energy transfer (LET) of secondary electrons entering the cells in the array were analysed to assess the change in the quality of the secondary electrons due to the presence of each NP aggregate geometry. Figure 3.6 shows the effect of Bi_2O_3 NP geometry on the secondary electron spectra and LET with each photon radiation field under study.

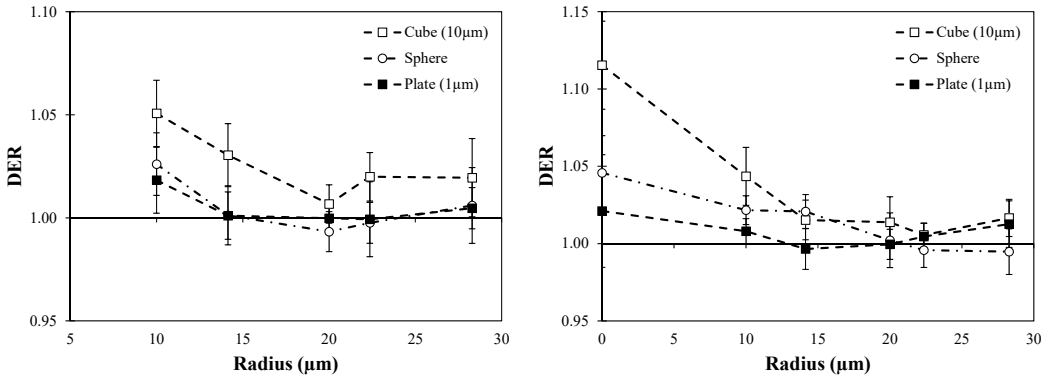

(a) Layer 2 (b) Layer 3

Figure 3.5: Radial dependence of the DER in a 10 MV photon radiation field with respect to geometrical configuration of Bi_2O_3 NP.

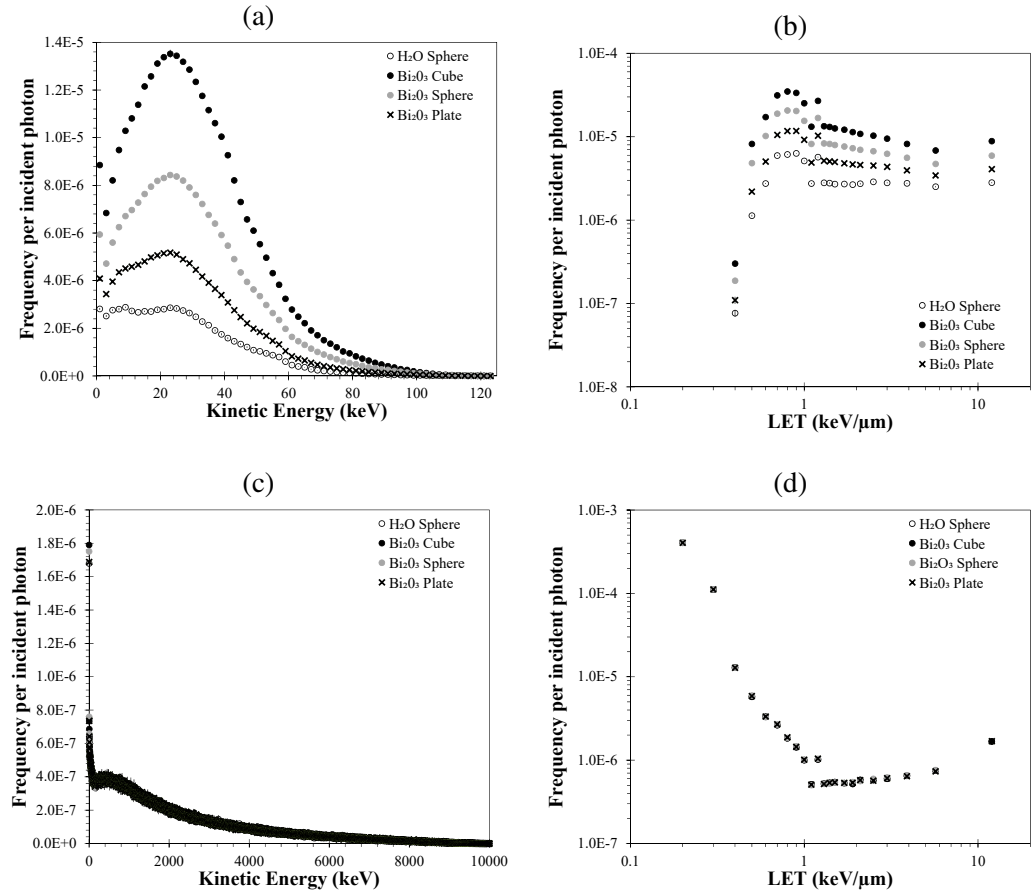

Figure 3.6: Kinetic energy and LET spectra of secondary electrons entering all cells with incident 125 kVp, (a) and (b), and a 10 MV photon radiation fields, (c) and (d). Bi_2O_3 NPs in the three geometrical configurations are compared to water (hollow circle).

Figures 3.6c and 3.6d show the secondary electron spectra and LET are not significantly enhanced by the placement of the Bi_2O_3 NP in the 10 MV photon beam. This is in contrast to the kilovoltage case (Figure 3.6a and 3.6b) where it is clear there is enhancement of the secondary electron production with the greatest increase in number of secondary electrons observed in the case of the cube geometry, followed by the sphere and plate.

These secondary electron spectra support the DER reported in Figure 3.2, and Table 3.1 for the 125 kVp and 10 MV photon fields. The enhancement of secondary electron production is dependent on the geometry, with the cubic geometry providing the highest number of secondary electrons due to the absolute increase in the mass of Bi_2O_3 NP material placed in the cell array. When the increase in DER is calculated with respect to mass of NP (DER_w), it is clear that the plate geometry is the most efficient radio-enhancer, with respect to mass of NP. This is due to the increased chance of secondary electrons to be absorbed within the NP aggregate itself with increasing geometrical size. The plate geometry allows more electrons to escape the surface as the thickness of the plate is 1 μm, which is less than the range in Bi_2O_3 of a 12 keV electron [106], meaning most of the electrons will be able to escape the NP aggregate. By contrast, the range of a 50 keV electron in Bi_2O_3 is 10.6 μm which means electrons with energy lower than this, created in the centre of the cube will have a low probability of escape.

Secondary electrons can also be analysed in terms of those entering cells either in front of or behind the NP aggregate. Essentially this is a means of identifying the effect of forward- or back-scattering of electrons in addition to the total of all scattered electrons in the phantom which then enter the cells of interest. Figure 3.7 shows the LET of secondary electrons scattered forward or back from the NP aggregate. The calculated LET show a slight preference for forward scattering of electrons in the case of sphere or cube NP aggregates. The figure shows that for the case of the Bi_2O_3 NP plate, positioned at the surface of cell layer 3 (see

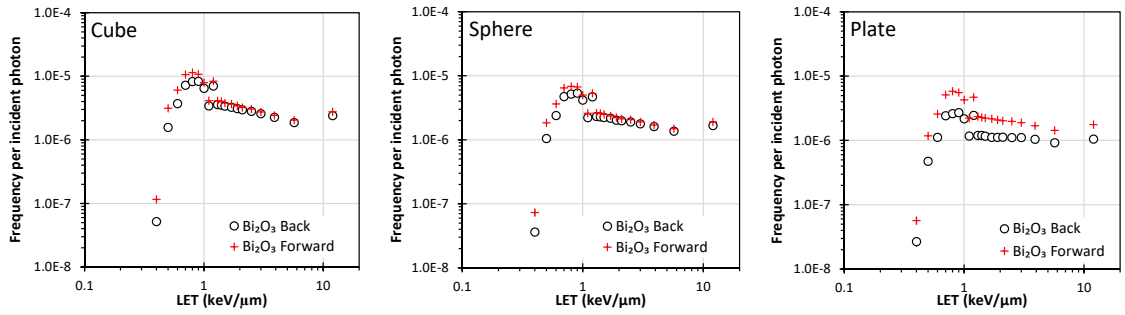

Figure 3.7: LET of secondary electrons entering cells behind (circles) and in front of (crosses) the NP aggregate.

Figure 3.1d) there is a stronger influence of electrons scattered forward than backward due predominantly to the fact that back-scattered electrons must travel through at least 9 µm of water before reaching layer 1 cells.

Atomic deexcitation simulated in this study only accounted for about 1% of the DER calculated, which is within the calculated error margins. The effect of AD processes would only be on cells local to the NP material, and predominantly on a nanoscale, due to the low energy and low range of the AD secondary electrons. The effect of AD electrons on the dose enhancement is observed to be small in this simulation due to the use of micron sized volumes to score the total dose to cells in the array. Auger electrons have a significant impact at the nanometre scale, close to the surface of the NP. However, this effect is less significant on the cellular level, as modelled in this part of the project. A simulation examining dose enhancing effects of Auger electrons and nanoscale damage to cells or DNA would require the implementation of event-by-event simulation models, such as Geant4-DNA. However in this study, only the macroscopic effect of the high-Z Bi_2O_3 NP, on the level of the cell is studied.

The next section of this chapter (Section 3.2) looks in more detail at the effect of the proximity to a sensitive volume the NP material has on dose enhancement, including, in particular, the dose enhancement attributable to atomic deexcitation electrons.

3.1.3 Summary

The Geant4 simulations demonstrated that in the kV photon field Bi_2O_3 had considerable dose enhancement properties locally with a dependence on NP geometry. The dose enhancement was shown to be significant (DER around 2-3 in the cell population, depending on geometry) in the 125 kVp photon field compared to a very small dose enhancement calculated in the 10 MV field. This is due to the strong increase in photoelectric effect cross-section (which has strong dependence on Z) in the keV photon energy range whereas Compton scattering dominates in the MeV energy range. This means that more photons are likely to interact by Compton scattering in the 10 MV photon radiation field, resulting in a difference in the secondary electron spectra, shown in Figure 3.6. In the 10 MV photon field studied there was no significant dose enhancement observed for any of the Bi_2O_3 NP morphologies. The simulation results for Bi_2O_3 under a kilovoltage beam are supported by the experimental data published by Alqathami et al (2013) reporting a dose enhancement factor of around 1.9 [23] although it is not possible to directly compare this experimental dosimetric study with the simulation conditions.

The simulation study shows that the geometry of the Bi_2O_3 aggregate affects the DER and the kinetic energy spectrum of secondary electrons. In particular the plate geometry is the most effective per unit NP mass because more electrons, originated in the plate, can reach the surrounding cells with a lower probability of being self-absorbed by the NP. This is due to the higher surface area to volume ratio, a measure of the geometrical advantage of each shape. With a higher surface area available per unit mass of NP, the likelihood of electrons escaping the bulk volume is increased.

The highest DER was observed in the cells surrounding the NP because of the low range of secondary electrons. In the 10 MV photon radiation field the radial dose distribution shows

that the dose enhancement ratio does not drop off in the same way as the kilovoltage with a slight increase in DER shown at the edge of the cell population. This is due to the difference in the secondary electron spectrum in the 10 MV photon radiation field compared to the kilovoltage photon field. The local DER observed remains very small compared to those found in the kilovoltage case.

3.2 Comparison of Ta_2O_5 NPs distributed in Shells or in Homogeneous Solution

A simulation study was performed to evaluate the effect of the geometrical distributions of Ta_2O_5 NPs in cell cultures. This study aims to investigate the physical effect of varying thickness of NP shell and geometrical distribution within a cell array on the DER and secondary electron spectra in cells. Shell thickness was shown experimentally to be related to increasing the delivered NP concentration and this behaviour is further investigated by means of Monte Carlo simulation in this project.

3.2.1 Motivation for the study

Cytotoxicity experiments conducted by researchers within the University of Wollongong's TNT research team, and published in Brown et al. (2013 and 2017) showed that exposure of the 9L cells to a higher concentration (500 µg/ml) of Ta_2O_5 NPs does not significantly increase the toxicity. In particular, photon irradiations using 150 kVp and 10 MV X-rays have shown that irradiated 9L cells, exposed to a 10-fold increase in Ta_2O_5 NP concentration, do not correspondingly indicate a significant decrease in cell survival, as may be expected [22, 32].

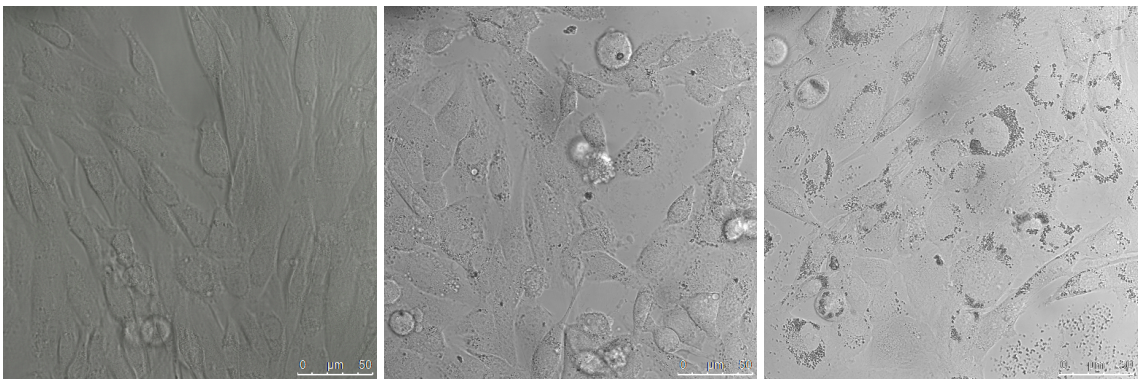

(a) control (b) 50 µg/ml (c) 500 µg/ml

Figure 3.8: Confocal microscopic image of elliptical 9L gliosarcoma cells with Ta_2O_5 NPs; control (a), after exposure of concentration 50 µg/ml (b), and 500 µg/ml (c).

Subsequent confocal microscopic images of the cell population with a Ta_2O_5 solution indicate that some NPs begin to form a "shell" around the cell nucleus. Figure 3.8 shows representative confocal microscopic images of 9L cells with Ta_2O_5 NPs. The Ta_2O_5 NPs are observed to form "shells" in the confocal image of the 500 µg/ml concentration (Figure 3.8c), compared to the 50 µg/ml concentration (Figure 3.8b). These confocal images were acquired by co-authors of a paper published and provide the motivation for the Monte Carlo simulation study [109].

Confocal images show that increasing the Ta_2O_5 concentration triggers the formation of shells of NP material around cell nuclei with an increasing shell thickness, while leaving, on average, a higher number of cells bare or with a limited number of NPs internalised. This phenomenon also translates to a lower number of cell nuclei surrounded by NP shells, separated, on average, by bigger distances. This means that some colonies of the cell population have a small concentration of NPs, whereas other colonies have several neighbouring cells with Ta_2O_5 shells, with high local concentration of NP material, as shown in Figure 3.8.

The hypothesis is that in the cell colonies characterised by high local Ta_2O_5 concentration, the NP shell contributes to physically protect the cell and/or cell nucleus from the otherwise

expected impact on cell survival, deriving from the combined NP exposure and irradiation. Increasing the thickness of the Ta_2O_5 NP shell will increase the probability of photon interaction and subsequent secondary electron production. However, an increased Ta_2O_5 shell thickness also increases the energy loss of any secondary electrons traversing the shell and possibly produces self-absorption of low energy and Auger electrons generated within the shell. This could translate to produce the saturation effect where adding more NP material does not produce higher dose enhancement.

This study investigates the physical effect on the dose enhancement of varying the NP shell thickness and distribution within a cell colony (called μ-phantom in the following sections), characterised by a high local NP concentration. The simulation model is based on the local NP distribution observed in the cell population, in the confocal images shown in Figure 3.8. The Geant4 Monte Carlo simulations provide insight into the physical mechanisms that led to the experimental cell survival curves obtained by the TNT group at the University of Wollongong.

3.2.2 Methods: the Geant4 simulation application

The simulation application is based on the same aforementioned simulation set up, as described in Section 2.1, with the dimensions and spacing of the cells being modified in this study. Figure 3.9 shows that the diameter of each cell was reduced to 8 μm in order to approximate a cell nucleus, and the cell spacing was increased to 14 μm to allow for surrounding the cells with up to 3 μm thick NP shells without causing geometry overlaps. The 8 μm diameter water spheres in this case are effectively modelling the cell nuclei of the 9L gliosarcoma cells studied experimentally. The cell nuclei and shell spacing has been set arbitrarily as currently the average distance between shells is not quantified experimentally. The simulation set up resembled the configuration of clonogenic assay experiments carried

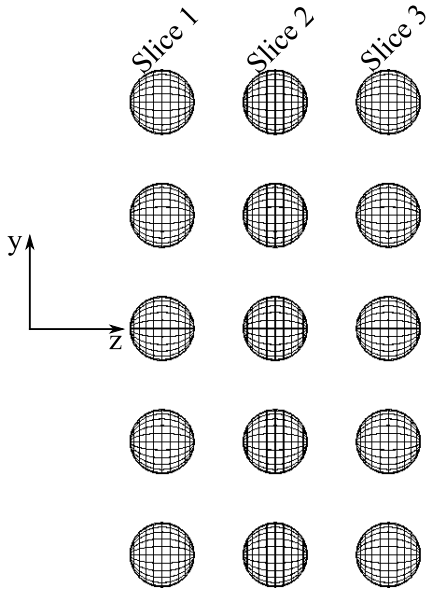

Figure 3.9: Geometry of the modified cell array, Y-Z plane.

out to determine the cell survival curves. A $70 \times 70 \times 70$ μm^3 array of cells (called here cell nuclei in a μ-phantom) was modelled, corresponding to experimental observations of different NP shell distributions in cellular colonies (see Figure 3.8), which are limited portions of the entire irradiated cellular population. The cell nuclei were placed within the water phantom as previously described in Section 2.1.

The 150 kVp photon radiation field was incident with the same dimensions as described previously and with the energy shown in Figure 2.2b. The physics interaction models selected remain the same as in the simulation application described previously, in Section 2.1.

The dose was calculated in the cell nuclei of the μ-phantom, in different NP shell configurations. The kinetic energy spectra and LET of the secondary electrons, produced by the kVp beam in the μ-phantom and in the NP shells, entering the cell nuclei have been calculated to evaluate the change in radiation quality responsible for the cell damage. The LET was calculated on the basis of the electron energy, using data from Berger *et al* (2005). The effect of AD processes was examined as well.

The dose enhancement ratio (DER) was evaluated as described in Equation 2.1, with and without Ta_2O_5 NPs distributed in the μ-phantom. The dose enhancement was examined with respect to increasing the NP concentration in the μ-phantom, compared to the dose without the NP present.

This study allowed the comparison of different concentrations of NPs and varying distributions within a cell population, in terms of energy deposition and kinetic energy (and LET) of secondary electrons. Two different types of NP distribution geometry were modelled:

1. shells of NP material placed around cells (*shell distribution*) and
2. a homogeneous distribution (*homogeneous distribution*) of NP material in water around the cells

Configuration 1) and 2) have the same total concentration of NP material.

The cell array geometry with the Ta_2O_5 NPs distributed in shells about the cell nuclei is shown in Figure 3.10 from a beams-eye-view of the μ-phantom. Several configurations of shells were investigated in this study, from a maximum of 9 shells placed around the 9 central cell nuclei of layer 2, shown in red in Figure 3.10a and then 8, 4 and a single shell (Figures 3.10b, 3.10c, and 3.10d, respectively). In Figure 3.10 shells have a thickness of from 1 μm to 3 μm as labelled. These shell distributions were selected to model the behaviour observed in clonogenic assay experiments, where some cells were observed to have no NP uptake, some sections had only a few isolated cell nuclei with shells, whereas other sections had many cells with shells close together in the colony. The DER in the central cell nucleus of layer 2 and in the total cell nuclei array in the μ-phantom was investigated for different shell distribution in order to study the effect of a NP shell touching the cell nucleus, the effect of nearby shells and the combination of these effects.

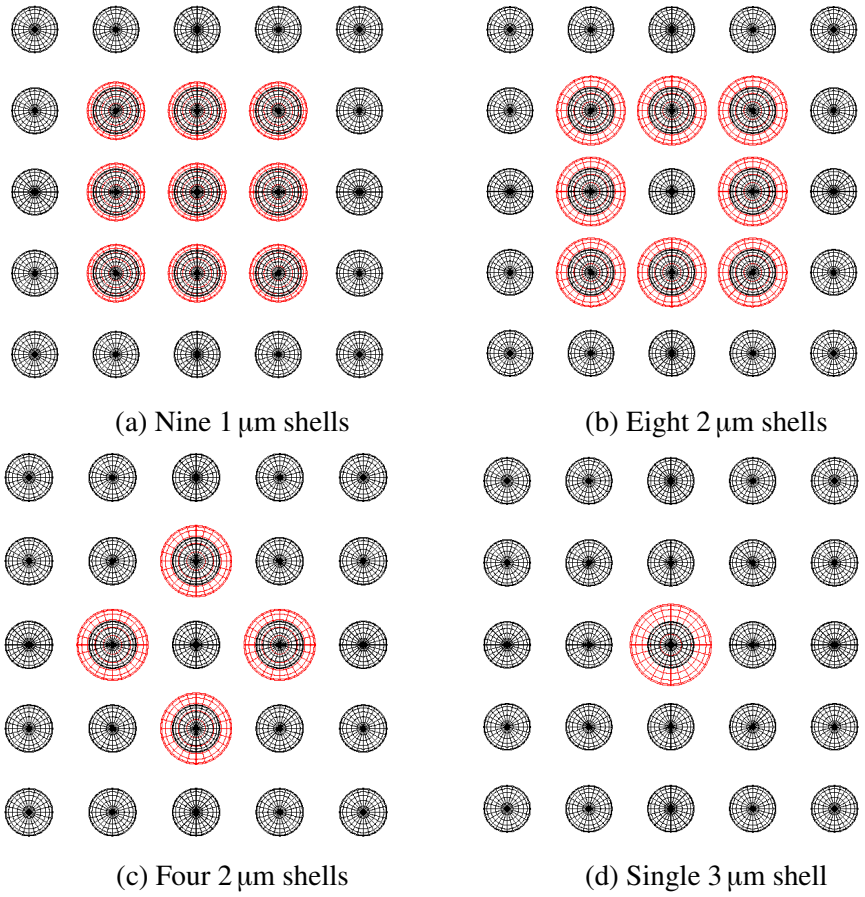

(a) Nine 1 µm shells

(b) Eight 2 µm shells

(c) Four 2 µm shells

(d) Single 3 µm shell

Figure 3.10: Configurations of geometry of cell array with Ta_2O_5 NP shells on cell nuclei in layer 2 (Fig. 3.9) from a beams-eye-view of the X-Y plane

A first study was conducted to investigate the influence of the NP shell thickness on the dose enhancement. The simulation configuration depicted in Figure 3.10d was adopted. The NP shell around the cell nucleus was increased between 1 and 7 µm. The DER was calculated in the central cell nucleus and compared for increasing shell thickness. This study was performed to determine the thickness of the NP shell where a "saturation effect" can start to be observed. The average range of secondary electrons originated by a 150 kVp beam in Ta_2O_5 is less than 5 µm, therefore electrons which deposit energy in the cell nucleus are those produced in a spherical layer of the NP with thickness equal to or less than their range in Ta_2O_5. This means that the dose enhancement capability of thicker NP shells is impeded by internal absorption of electrons, which translated in a saturation effect of the DER when

Table 3.3: Concentrations of NP in water with respect to shell thickness and configuration.

Shell Distribution	1 μm thick (*mg/ml*)	2 μm thick (*mg/ml*)	3 μm thick (*mg/ml*)
1	6.5	16.2	29.7
4	26.0	64.7	118.7
8	51.9	129.4	237.4
9	58.4	145.5	267.1

increasing the NP shell thickness.

A second study was performed to compare the DER calculated with a distribution of NP shells in the μ-phantom (presented in Figure 3.10), as observed experimentally (shown in Figure 3.8), and, alternatively, with a homogeneous distribution of NP material in water, with the same simulated concentration. This study allows the comparison of the DER due to NP distribution on the micron scale and the tendency of the NPs in the cell culture to congregate in shells around the cell nuclei, compared to being uniformly distributed among cells. Liquid water was used to model the interior of each cell volume in all simulations. The shell thickness was set equal to 1 μm, 2 μm or 3 μm in each configuration investigated, to obtain higher concentrations of NPs in the cell population. Such shell thicknesses were selected on the basis of the microscope observations such as the one depicted in Figure 3.8.

Table 3.3 reports the calculated equivalent local concentration of Ta_2O_5 in water for each simulated number of shells and shell thicknesses. The local NP concentrations calculated within the μ-phantom are high due to the localisation of material in a small volume of water.

3.2.3 Results

3.2.3.1 DER in Single Cell Nucleus with Shell

Dose enhancement due to a Ta_2O_5 NP shell placed on the central cell nucleus in the μ-phantom as shown in Figure 3.10d is represented against the NP shell thickness in Figure 3.11.

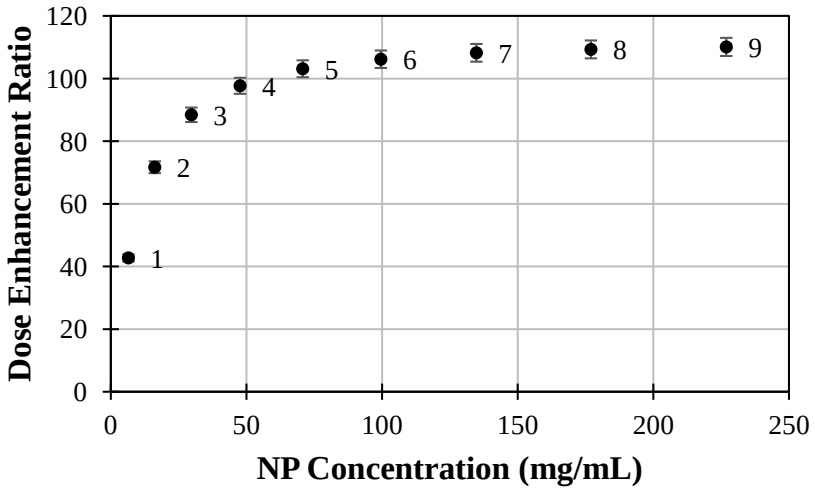

Figure 3.11: DER in central cell nucleus of the μ-phantom with increasing shell thickness of 1 to 9 μm (expressed as local NP concentration) of Ta_2O_5 NP shell around the central cell nucleus, and equal numbers of incident photons. Data points are labelled with the shell thickness (in μm).

The results of the simulation show the calculated DER increases quickly and then the increase slows down for larger shell thickness. The initial increase in the DER is due to the increasing quantity of high-Z Ta_2O_5 NP material in close proximity to the cell nucleus, however, the rate of increase of DER is reducing with thicker NP shells because of self-absorption of secondary electrons originated in the NP ceramic at a distance from the surface larger than their range.

At the same time the thickness of the NP shell does not affect the global photon fluence reaching the "active shell" close to the cells, from which the originated electrons will reach

the cell nucleus. Further increasing the shell thickness will eventually lead to decreasing DER due to photon attenuation as well.

The DER increases by 3 for each unit mg/ml increase in NP concentration, when varying the NP shell thickness from 1 μm to 2 μm. This increase is only 0.1 per mg/ml NP concentration when the NP shell thickness varies from 5 μm to 6 μm, which is an insignificant enhancement when the error margins are taken into account. This means that the effectiveness of the NP to enhance dose in the cell nucleus is reduced with increasing concentration of NP, eventually resulting in no further enhancement at all and finally decreasing DER.

The effect on the DER in cell nuclei without a shell, but in close proximity to a cell nucleus with a NP shell is revealed by examination of the DER with respect to distance from the centre of the μ-phantom, with increasing shell thickness on the central cell nucleus. Figure 3.12 shows the radial dependence of dose enhancement ratio for increasing shell thickness on the central cell nucleus. The radial distances shown in this and the next figures are dictated by the placement of the cell nuclei in the μ-phantom at distances of 14 μm from centre to centre. The figure shows a sharp drop in dose enhancement in the cell nuclei located around the shell (distance from centre $\geq$ 14 μm) compared to the DER in the central cell nuclei (distance from centre = 0 μm).

Due to increased absorption of secondary electrons produced within greater thickness of NP material the increased DER observed in the cell nuclei with the thickest layers begins to plateau. This means for example that a larger increase in DER is observed when the shell thickness is increased from 1 μm to 2 μm compared to 5 μm to 6 μm. This effect is quantified by calculating the percentage increase in DER with respect to distance of cell nucleus/nuclei from the centre of the μ-phantom. Figure 3.13 shows this behaviour of the DER with respect to changing shell thickness. The figure shows the increase in the DER (as a %) at each radial

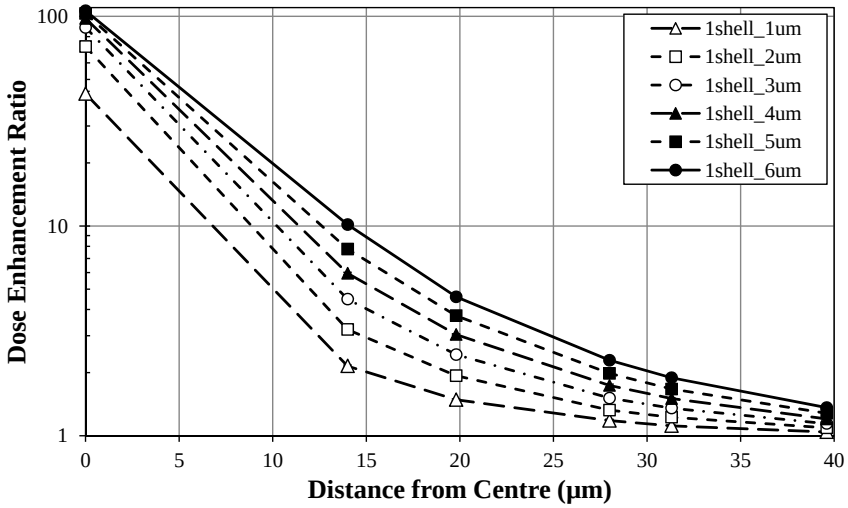

Figure 3.12: DER due to a single, central Ta_2O_5 NP shell with respect to distance from the centre of the μ-phantom. Note the radial distances are dictated by the cell positions and the Y-axis is on a logarithmic scale.

distance from the central cell nucleus compared for increasing shell thickness.

Figure 3.13a shows the average effect of increasing the shell thickness by 1 μm increments (e.g. from 1 μm to 2 μm, compared to 2 μm to 3 μm and so on). Higher energy electrons are more likely to escape the Ta_2O_5 shell and also to reach the furthest cell nuclei without being absorbed by the water medium which means the relative effect of increasing the shell thickness by 1 μm is of a similar magnitude at greater distances from the central cell nucleus about which the NP shell is placed. A large difference is seen at 0 μm (i.e. within the central cell nucleus) due to the close proximity of the Ta_2O_5 NP material to the volume in which the DER is calculated.

Figure 3.13b then compares the average effect of increasing the shell thickness by 1 μm up to 5 μm increments averaged over all shell thickness increases studied. This figure shows the effect of increasing shell thickness is observed to be large in the closest neighbouring cell nuclei as well as the central cell around which the shell is placed. The effect at a distance of 14 μm (i.e. in the closest neighbouring cell nuclei) of increasing the shell thickness from

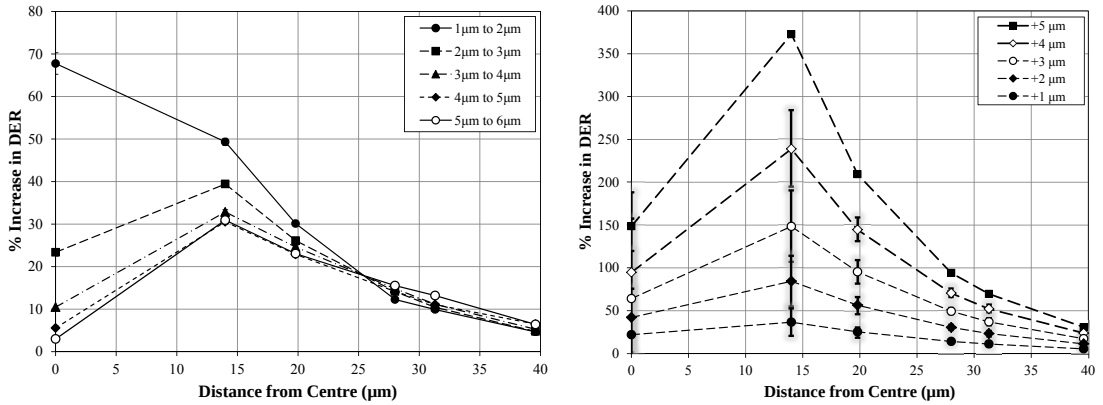

(a) Increasing shell thickness by 1 μm increments.

(b) Average effect of increasing shell thickness in +1 μm up to +5 μm increments.

Figure 3.13: Relative increase in DER due to increased thickness of a single, central Ta_2O_5 NP shell, with respect to radial distance from the centre of the μ-phantom.

1 μm to 6 μm (i.e. +5 μm), is an increase in the DER of 373%, compared to a 149% increase in the central cell nucleus. This increase in the DER with increasing shell thickness is less pronounced at greater radial distances from the central cell nucleus, dropping from 209% at around 20 μm to 94% at 28 μm, as shown in Figure 3.13b. The behaviour observed can be attributed to the combined effect of increased secondary electron production balanced against increased absorption of secondary electrons within NP shells of increasing thickness.

The kinetic energy spectra and corresponding LET of electrons entering the central cell nucleus are shown in Figure 3.14. The figure shows results for Ta_2O_5 shell thickness varying between 1 μm and 7 μm. The number of secondary electrons per incident photon increases with the shell thickness up to approximately 5 μm. For shell thickness greater than 5 μm (corresponding to the average range of secondary electrons) the number of secondary electrons does not increase significantly.

The mean kinetic energy of the secondary electrons is (31 ± 1) keV. These electrons would have a range of about 18.7 μm in water and 4.5 μm in Ta_2O_5. This means that for shell thickness greater than this range in Ta_2O_5 the enhancement is expected to be reduced due

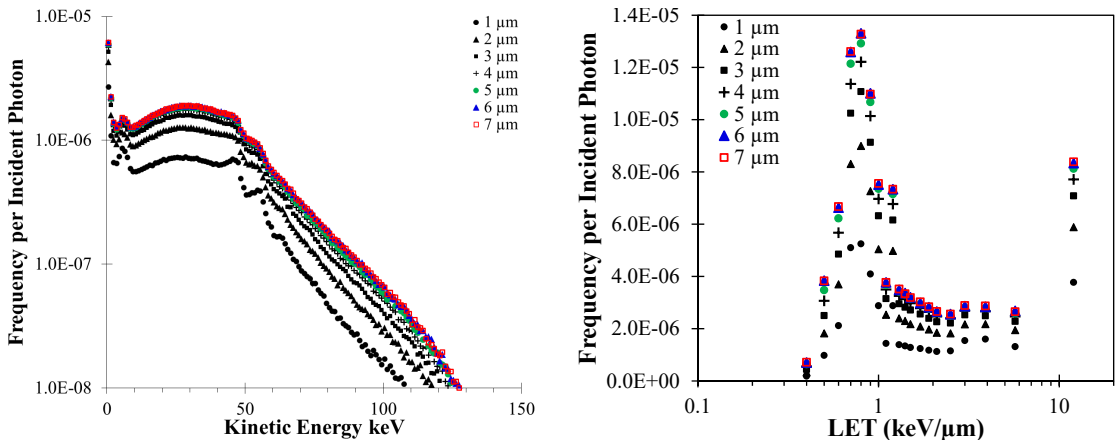

Figure 3.14: Secondary electron kinetic energy spectra (a) and LET (b) entering central cell nucleus with increasing shell thickness of Ta_2O_5 NP shell around central cell nuclei per incident photon.

to electron absorption by the NP shell. It is important to note that these spectra are from electrons entering only the central cell nucleus about which the NP shell is placed.

3.2.3.2 Effect of Spatial Distribution of Shells

Figure 3.15 shows the DER in a 150 kVp photon radiation field, in the four alternative spatial distributions of NP shells represented in Figure 3.10. It can be observed that - for the NP shell thicknesses under study - the DER increases with increasing thickness of Ta_2O_5 NPs and with the number of shells. Most dose enhancement occurs within the cell nuclei about which shells are placed, significant enhancement is still seen in neighbouring cell nuclei, with biggest dose effect in those closest to the NP shells. This means that NP shells have a dose enhancement effect over a short range (the average range of secondary electron is less than 20 µm in water) however there are longer range effects resulting in a dose enhancement ratio above 1 at larger distances from the NP shells. For example, in the case of the NP shell surrounding the central cell nucleus only, the average DER in the furthest cell nuclei is (1.34 ± 0.01) for 3 µm shell thickness. This compares to an average DER of (3.47 ± 0.02) in the

eight cell nuclei surrounding the central cell nucleus.

(a) 1 µm (b) 2 µm (c) 3 µm

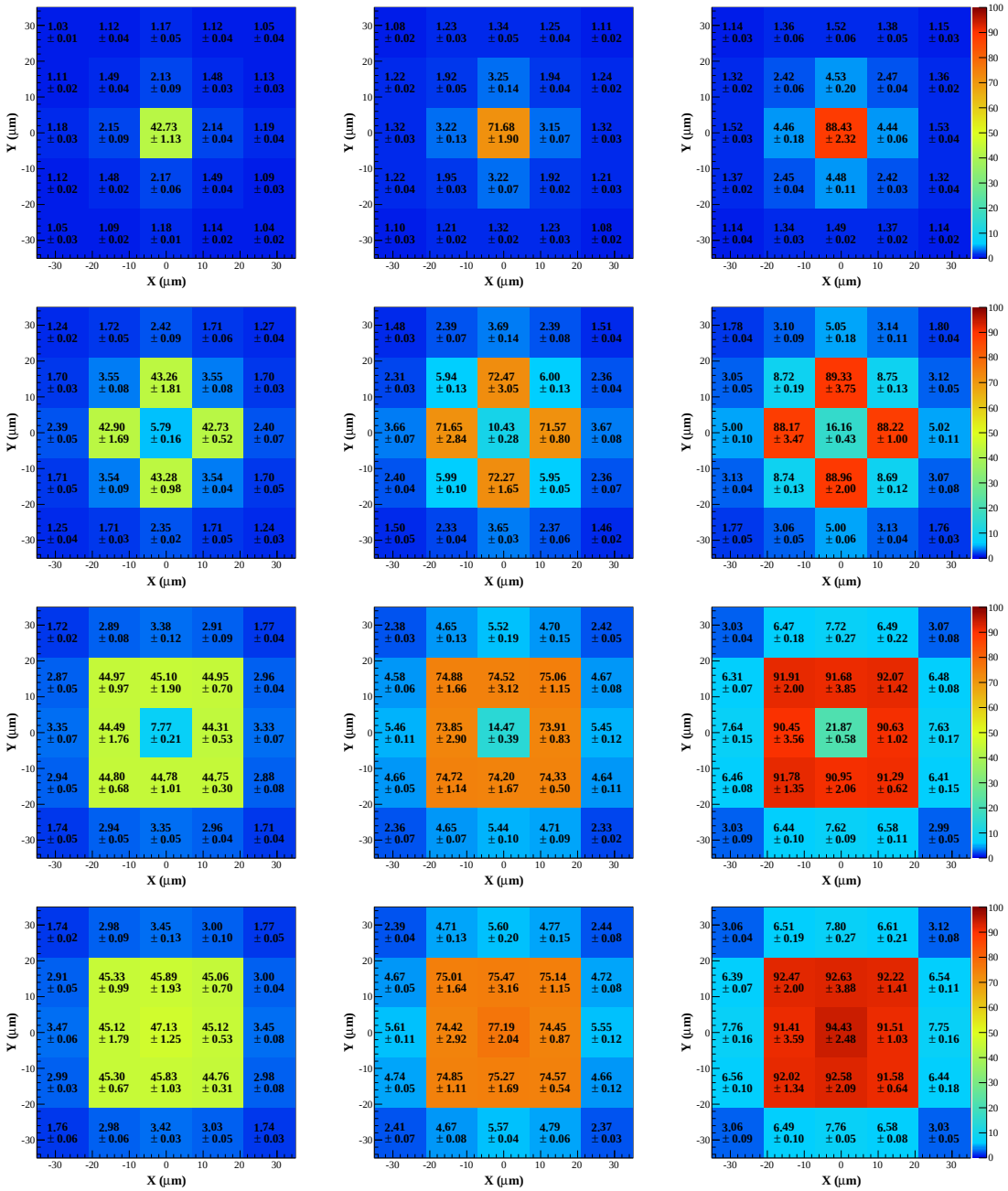

Figure 3.15: DER 2D distribution in layer 2, with a single shell (top row), 4 shells (second row), 8 shells (third) or 9 shells (bottom)

Figure 3.16 reports the DER calculated in the different NP shell configurations under study, for different local concentrations (corresponding to different NP shell thicknesses), integrated over the cell nuclei in the entire μ-phantom. The non-linear trend observed in Figure 3.16 is similar to that shown in Figure 3.11 and indicates that even though the high-Z Ta_2O_5 NP material creates an increased number of secondary electrons entering the cell nuclei, the number of secondary electrons with sufficient energy to escape the NP is reduced with an increasing thickness of the NP shell, thus reducing the rate at which the overall DER increases with NP concentration.

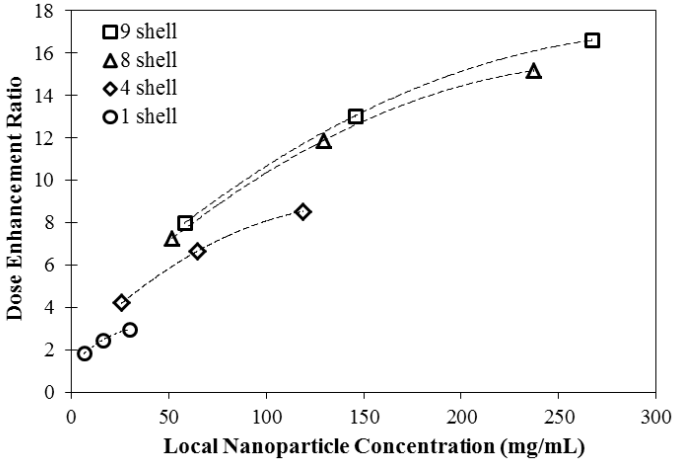

Figure 3.16: Total DER in cell array per incident photon due to NPs distributed in shells of various shell thickness (concentration) and distribution. The three points corresponding to increasing local NP concentration for each shell distribution correspond to increasing shell thicknesses of 1, 2 or 3 μm.

3.2.3.3 Secondary electron kinetic energy spectra and LET

Figure 3.17 shows the kinetic energy spectra and LET of secondary electrons entering into the central cell nucleus of layer 2 in the μ-phantom, varying the Ta_2O_5 NP shell thickness in the cases of NP shell distributions under study (Figure 3.10), with reference to the case of no NP material in the μ-phantom. The 9, 8 and 1 shell distributions are compared in Figure 3.17 in order to see the effect of a local shell, the effect of nearby shells and the combination of these.

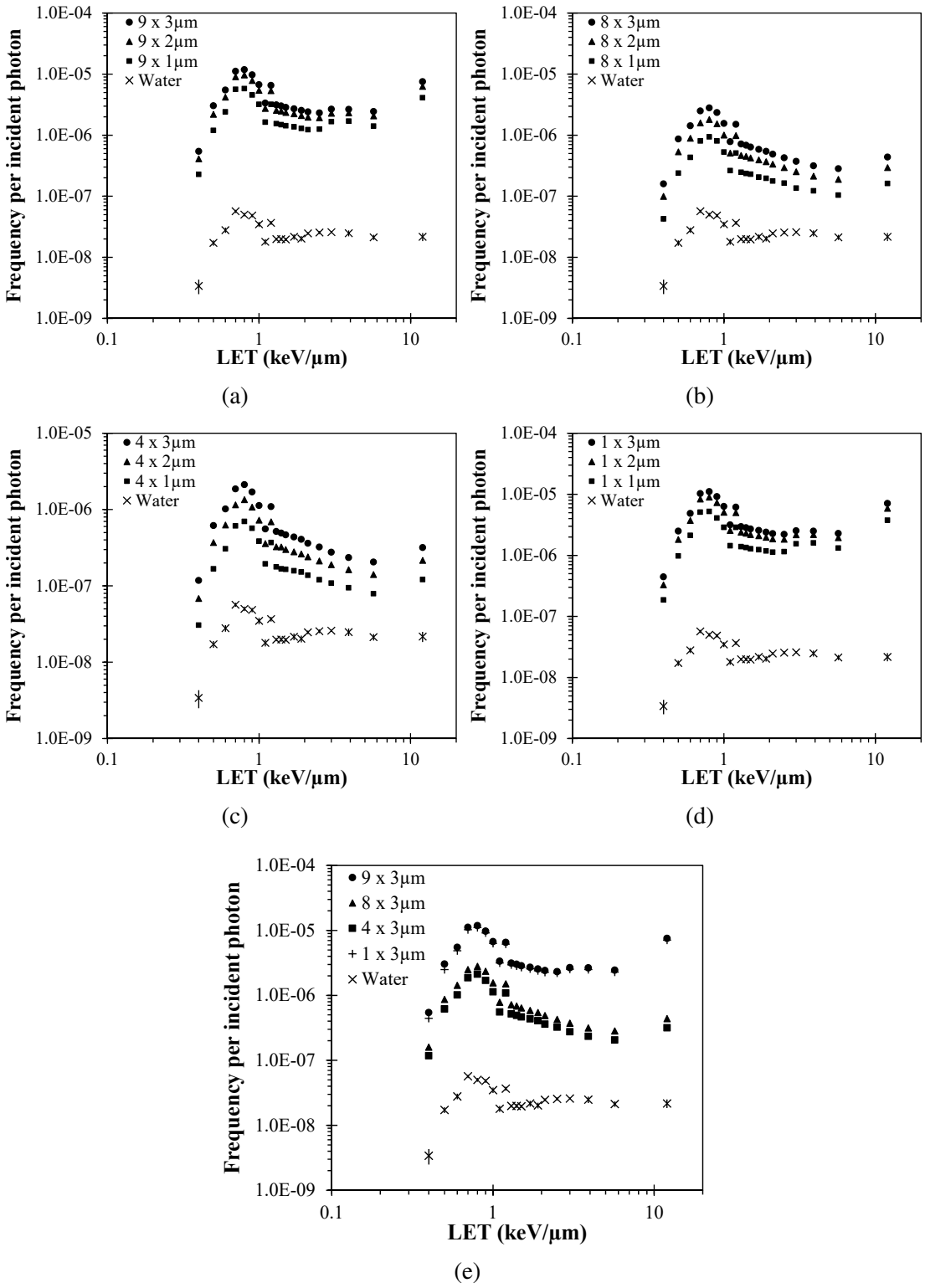

Figure 3.17: LET of electrons entering the central cell nucleus in the array with Ta_2O_5 NPs distributed in shells around 9 (a), 8 (b), 4 (c) or a single cell nucleus (d) in the array, compared to configuration without NPs (Water). The different NP shell configurations are also directly compared for the 3 µm thick shell case (e).

Table 3.4: Range of electrons in water, Ta_2O_5, and a solution of Ta_2O_5 in water.

Energy (keV)	Range in Water (μm)	Range in Ta_2O_5 (μm)	Range in 267.1 mg/ml Ta_2O_5 Solution (μm)
10	2.51	0.74	2.33
20	8.57	2.25	7.84
30	17.56	4.40	16.0
40	29.19	7.09	26.5
50	43.20	10.29	39.1
150	281.7	62.0	252.6

The mean kinetic energy of secondary electrons created within the Ta_2O_5 NP shells is around 1.5 keV. Electrons with kinetic energy less than 10 keV have a range of less than 1 μm in Ta_2O_5 as shown in Table 2.2 and Figure 2.13, reporting the range of electrons with varying kinetic energy in water, solid Ta_2O_5 NP and homogeneous Ta_2O_5 solution [106]. This results in a large proportion of the low energy electron spectra being absorbed by the Ta_2O_5 shell and not contributing to the DER in the nearby cell nuclei. The mean kinetic energy of secondary electrons escaping the NP shell was found to be around 33 keV, increasing slightly with larger shell thickness. This happens because higher energy electrons can escape the NP shell with increasing shell thickness. Low energy electrons produced in the region close to the inner surface of the shell will enter the cell nucleus, or be absorbed by the shell.

The increased frequency of high-LET electrons observed in the presence of Ta_2O_5 compared to water produces a dose enhancement within close proximity of such high-Z NPs. This effect is observed when comparing the LET spectra in the central cell nucleus without a Ta_2O_5 NP shell in close proximity (8 shell case) and with a NP shell directly on the central cell (9, or 1 shell cases) in Figure 3.17e. Secondary electrons entering cell nuclei are increased in number with increasing thickness of Ta_2O_5 shells for the kilovoltage spectrum under study.

Table 3.5: Number of secondary electrons entering cell nuclei in the array with increasing Ta_2O_5 shell thickness, expressed as a ratio with respect to water.

Number of Shells	Shell Thickness	Ratio
1	1 μm	2.48 ± 0.01
	2 μm	3.61 ± 0.02
	3 μm	4.50 ± 0.02
8	1 μm	12.38 ± 0.05
	2 μm	20.6 ± 0.1
	3 μm	26.6 ± 0.1
9	1 μm	13.75 ± 0.05
	2 μm	22.8 ± 0.1
	3 μm	29.2 ± 0.1

Table 3.5 shows the increase in the number of electrons traversing cell nuclei in proximity to increasing thickness and varying distributions of NP shells, compared to water. It is clear from these ratios that the number of electrons entering the cell nuclei in the array is increased with increasing mass of Ta_2O_5 in shells within the array.

3.2.3.4 Effect of NP Distributed in Shells or Homogeneous Solution

Figure 3.18 shows the DERs obtained with the NP shell configurations depicted in Figure 3.10 and with a homogeneous distribution of NP material in water. The NP shell configuration and the homogeneous solution have the same total concentration of NP material. It can be observed that the DER depends significantly on which model of the NP distribution is selected (shells or solution in water).

The DER increases with increasing concentration of Ta_2O_5 in both NP shell and solution configurations. In the case of the homogeneous solution the DER increases linearly with increasing mass of Ta_2O_5 in water. Instead, in the case of a NP shell distribution, the DER

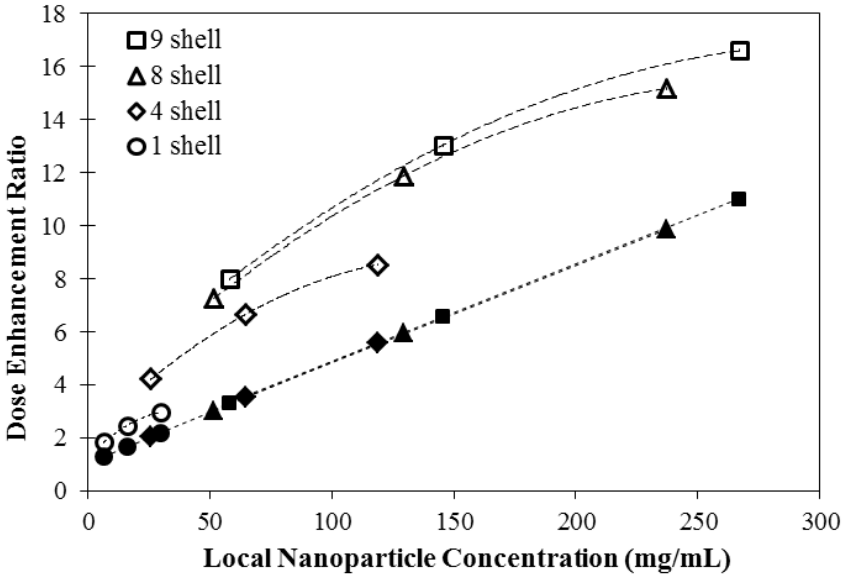

Figure 3.18: Total DER in the μ-phantom per incident photon due to a homogeneous solution of Ta_2O_5 NPs in water (filled symbols) compared to the average dose due to the same ceramic compound arranged as NP shells (unfilled symbols) of various thickness (corresponding to different local concentration) and geometrical distribution.

increases and then saturates with an increase in mass of Ta_2O_5 shell as shown in Figure 3.16. In the case of a homogeneous NP solution, generated secondary electrons do not have to traverse a NP shell in order to deposit dose within the cell and are therefore attenuated only by the homogeneous NP solution which translates to a linear effect on the DER with respect to NP material concentration.

Figure 3.19 reports the kinetic energy spectra of secondary electrons entering in the central cell nucleus in the μ-phantom in the case of NP shells surrounding 9 cells (Figure 3.10a) and in the corresponding NP homogeneous solution in water, with the same concentration.

It is observed that more electrons enter the central cell nucleus with the Ta_2O_5 NPs in shell configuration compared to an equivalent solution of NP. This happens because the NP shell of Ta_2O_5 material surrounding the cell nucleus provides a source of low energy electrons close to the nucleus, in contrast to the a homogeneous NP solution in water producing a

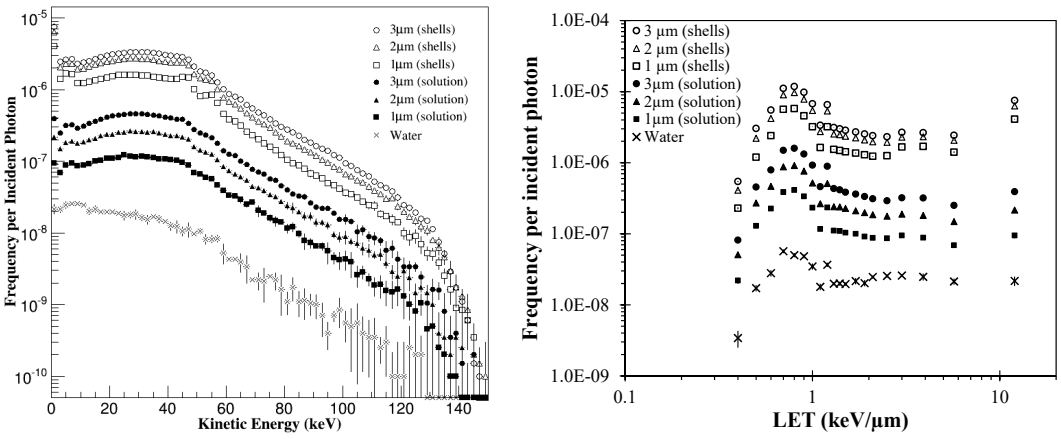

(a) (b)

Figure 3.19: Electron spectra (a) and LET (b) entering central cell nucleus in the µ-phantom with NP distributed in shells (hollow symbols) or in solution (filled symbols) around the cells compared to water.

uniform source of electrons throughout the water medium surrounding the cells. This also explains why the total DER in Figure 3.18 is higher in the NP shell case compared to homogeneous solution.

3.2.3.5 Effect of Atomic Deexcitation

The influence of AD processes on the DER was investigated by performing simulations with and without the AD processes activated. The kinetic energy of AD electrons is constrained by the low energy production threshold of 100 eV. The difference between the DERs calculated with and without the deexcitation is attributed to the effect of the deexcitation electrons. Table 3.6 summarises the results and shows that the AD processes accounted for between about 3% and 7% of the DER at cellular level. The DER due to AD processes is predominantly observed in the cell surrounded by the NP shell and for thinner NP shells. This is explained by the fact that Auger electrons are very low energy and therefore have a short range and can be easily self-absorbed in thicker NP shells. Auger electrons contribute to the DER locally to the NP shell as expected. This means that if in an experimental, *in vitro*,

Table 3.6: Percentage of DER within the central cell attributed to AD processes, for each NP shell configuration and thickness under study.

Shell Distribution	1 μm	2 μm	3 μm
1	(7.23 ± 0.03)%	(5.55 ± 0.03)%	(4.98 ± 0.01)%
8	(4.56 ± 0.04)%	(4.00 ± 0.04)%	(2.73 ± 0.01)%
9	(7.03 ± 0.04)%	(5.38 ± 0.02)%	(4.75 ± 0.01)%

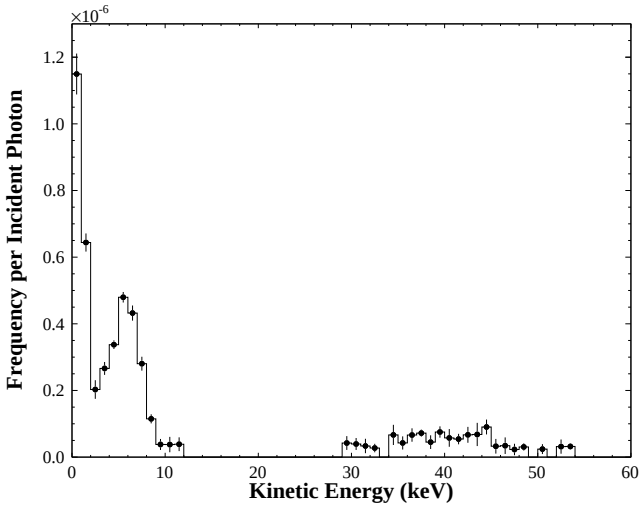

Figure 3.20: Kinetic energy spectrum of secondary electrons produced by AD processes, entering the central cell nucleus with a 3 μm thick Ta_2O_5 NP shell surrounding the cell itself.

situation a particular cell does not have a large uptake of Ta_2O_5 NP forming a shell about the nucleus, it will experience significantly lower DER from low energy AD electrons than neighbouring cells with internalised NP shells.

Figure 3.20 shows the spectra of AD electrons entering the central cell nucleus per incident photon for the 9 shell configuration. This spectrum is calculated by subtracting the spectrum calculated from the simulation without AD processes from that with AD processes. Electrons falling within error of zero are disregarded.

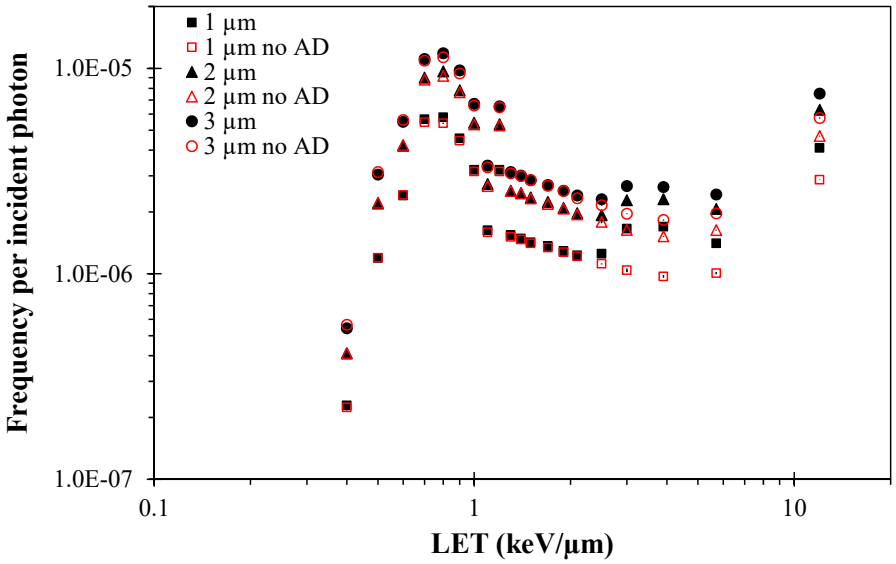

Figure 3.21: Effect of AD on the LET of secondary electrons entering the central cell nucleus in the 9 shell configuration. LET with AD processes activated (filled symbols) is compared to LET with no AD activated (unfilled, red symbols).

It can be seen from Figure 3.20 that AD processes have most effect on the low energy part of the spectra, below 10 keV with peaks in the spectra enhanced around 6 keV and below 1 keV. The mean kinetic energy of secondary electrons is slightly decreased (approximately 1 keV lower) by the inclusion of AD processes in the simulation. This effect is small and indicates Auger electrons with low energy will have the most effect on short ranges from the NP surface.

Figure 3.21 shows the effect of AD processes on the LET of secondary electrons entering the central cell nucleus with respect to increasing shell thickness. The figure shows that the AD has the most effect on the LET of secondary electrons in the case of a 1 µm thick NP shell. The second effect of AD is to increase the number of high LET electrons, as expected.

The number of secondary electrons with LET of 12 keV/µm entering the central cell nucleus increases by 30% with AD processes in the 1 µm case, compared to only 25% and 24% in the 2 µm and 3 µm cases respectively. This is due to the shorter range of low energy, high

LET, AD electrons which have increased probability of absorption in the thicker shells. The proportion of dose enhancement observed to be due to AD in Table 3.6 agrees that the thinner shell provides more AD electrons' dose enhancement in all configurations.

3.2.4 Summary

This work was motivated by the experimental observation that Ta_2O_5 NPs tend to congregate as shells with different thicknesses in colonies of cancer cells. Based on this observation, different scenarios of cells covered with NP shells were investigated in cellular colonies of limited size, in terms of local DER obtained under a 150 kVp irradiation, by means of Monte Carlo simulations.

The local DER becomes saturated with an increasing concentration of NPs and shell thickness for each considered scenario of shell pattern in the μ-phantom. The local DER reaches saturation when the NP shell thickness is larger than 5 μm. The local DER in individual cells in the μ-phantom is significantly increased when the Ta_2O_5 NPs are simulated in realistic shells configurations rather than in the commonly accepted homogeneous solution distribution between all cells with the same concentration of NPs.

Considering a realistic scenario of NP concentration used in experiment in a range of 50 to 500 μg/ml, the conclusion is that only a very small partial volume of the cell culture, which is modelled with the μ-phantom, has a significant local concentration of NPs. This leads to a low DER for most cells in the entire cell population, while obtaining a large local DER, which is not changing essentially the DER averaged over the entire cell population. This conclusion is supported by the simulation results, showing that the enhancement of secondary electrons by Ta_2O_5 NP shells has the most effect on cells in close proximity to the high-Z material and by the DER measured experimentally for cell cultures irradiated with

150 kVp X-ray beam, with NP concentration varying between 50 and 500 μg/ml.

Demonstrated DER in μ-phantom with Ta_2O_5 NPs and the experimental observation that such NPs congregate in shells around cells prompt us that these NPs can be excellent for targeting micrometastasis, based on a single or small number of cells, provided the ability to selectively deliver them to the targeted cancerous cells. In this case even much smaller concentration than 260 mg/ml can potentially provide a DER of about 4-5, based on this study.

3.3 Discussion

It has been shown in this chapter that the shape and distribution of NP material within a micro-volume phantom are important factors to consider when modelling the physical dose enhancement of radiotherapy by NPs. The study of different Bi_2O_3 NP geometries showed the effect of aggregate shape on the DER in the cell population whilst the study of the shell-forming behaviour of Ta_2O_5 NPs was studied and shown to have a large effect on dose enhancement, compared to NPs in solution.

The study of Bi_2O_3 NP aggregated in the cell array showed the increased effectiveness of the Bi_2O_3 platelet morphology [33], with respect to total aggregate mass, compared to more bulky geometrical configurations. The study also showed again the increased effect in the keV photon energy range compared to the MeV photon energy range. Although Bi_2O_3NPs have been shown to have sensitizing effects under both kilovoltage and megavoltage photon irradiation, the simulations showed preferential enhancement in the kV field. This does not mean that the NPs are not expected to be enhancing in the MV, rather that a more complex combination of physical, chemical and biological effects should be considered to be

at play in the cell population. The Geant4 simulation presented in this chapter has modelled the local physical dose enhancement due to increased secondary electron production only. The complex relationship between secondary electron production, and free radical formation [110] is an aspect which could be further investigated by Geant4 simulations using the Geant4-DNA (with recently included chemical modelling of water radiolysis) very low energy extensions of Geant4 to model free radical products in water.

The simulation of Ta_2O_5 NP material distributed in shells around cell nuclei in a cell population demonstrates the high local dose enhancement ratio present in the cell array compared to when NP material is distributed in a homogeneous solution between cells in the simulation. Different NP materials are taken up by cells or distributed within cells in different ways, depending on the NP type, size, morphology and aggregation. These properties and behaviour, when known and understood can potentially be exploited to gain advantage from certain types of NP, in order to optimise the enhancement of radiotherapy. This has been demonstrated in the case of the shell-forming Ta_2O_5 NP in this chapter's Geant4 simulation study as the saturation effect with increasing NP concentration has been investigated.

Although the simulation geometry in ref [85] is vastly different from that presented in this chapter, the reported saturation effect with increasing concentration and shell thickness observed in a cell population study is in agreement with the trend observed in ref [85] for the case of clustered gold NPs in solution.

Results presented in this chapter have shown that it will be important for future simulation work to carefully model the realistic distribution of NPs within cell populations in order to accurately model the effect of high-Z NP induced dose enhancement including the production of secondary electrons and possibility of self-absorption of electrons, depending on the dimensions of the NP material. The uptake by cells of NPs and also the distribution within

cells should be carefully modelled, as the results in this chapter demonstrate the strong dependence of local dose enhancement on NP distribution. A simple model of a homogeneous NP solution in water is not sufficient, on the level of the cell or the cell nucleus, to provide an accurate calculation of the dose enhancement in a cell population.

Chapter 4

Dose Enhancement by Nanoparticles in Proton Therapy

This chapter presents studies at the nanoscale level of the dose enhancement due to different types of NPs in proton therapy by means of Geant4 Monte Carlo simulations. The work presented in this chapter is based largely on articles published in the peer reviewed journals *Physica Medica* and *The European Physical Journal D*, which are also included in this thesis as Appendix C and Appendix D. The contribution made as second author on the paper of Verkhovtsev et al. (2015b) is the Geant4 study described in this chapter.

4.1 Ceramic Oxides in Proton Therapy

4.1.1 Methods

Simulations were performed using Geant4, versions 9.6-patch 2 and 10.1 in order to check the consistency of the results through the Geant4 software's evolving life cycle [67, 68]. Figure 4.1 shows the simulation configuration in the case of a 4 MeV pencil proton beam

incident on the water box. This energy is selected to show the interactions of a low energy proton reaching the NP. The track structure of secondary electrons, shown in red, is more detailed in the liquid water surrounding the NP sphere due to the physics models adopted here, the Geant4-DNA Package (see Chapter 1, Section 1.4.3) modelling particle interactions event-by-event.

The simulation consisted of a monoenergetic proton beam with energy spanning from 5 MeV to 90 MeV, incident normally on a 200 µm liquid water phantom, comparable to a 20 × 20 × 20 cell population adequate to study the dose enhancement locally to the NP. The NP is modelled with a sphere of 100 nm diameter, set in the centre of the water phantom. A smaller diameter NP (20 nm) is simulated as well, for comparison. The material of the NP was defined as gold (Au), tantalum pentoxide (Ta_2O_5), cerium oxide (CeO_2), bismuth oxide (Bi_2O_3) or liquid water for a comparison with no NP present in the phantom. Materials were defined by composition of elements in Geant4, using the densities shown in Table 4.1.

The proton energies were selected to model a proton radiation field typical of the Spread Out

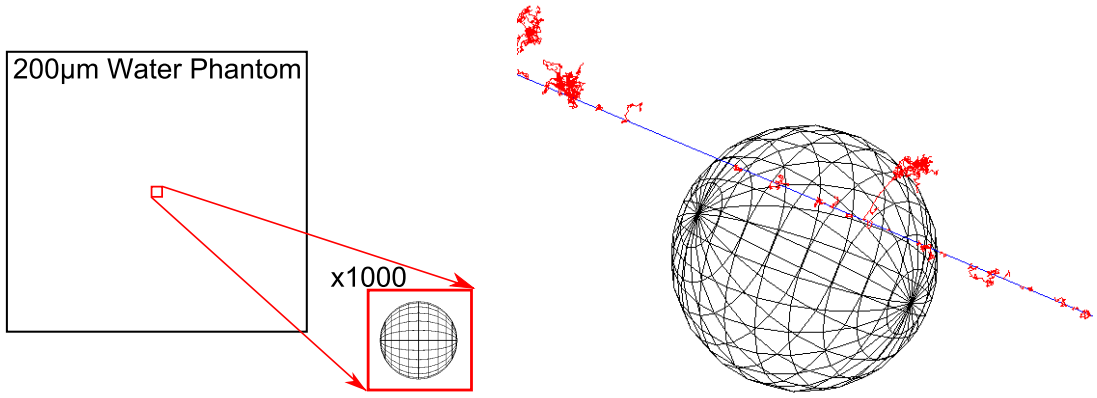

(a) Schematic view of simulated water phantom geometry with zoomed inset showing NP at centre.

(b) Schematic view of simulated nanoparticle with a sample track of a 4 MeV incident proton. The proton trajectory is shown in blue, and secondary electron tracks are red.

Figure 4.1: Schematic views of the simulation set-up.

Table 4.1: NP material data: atomic number (Z), mean excitation energy (I) [106], and density (ρ).

NP Material	Z	I (eV)	ρ (g/cm^2)
Au	79	790	19.32
CeO_2	$Z_{Ce} = 58, Z_O = 8$	407.6	7.215
Ta_2O_5	$Z_{Ta} = 73, Z_O = 8$	523.7	8.20
Bi_2O_3	$Z_{Bi} = 83, Z_O = 8$	706.9	8.90

Bragg Peak region of a hypothetical prostate cancer treatment. For example, the depth-dose profile of a 160 MeV proton beam shows a Bragg Peak at a depth of approximately 180 mm [111, p. 569]. The average proton energy in this peak is less than 20 MeV. The average energy of protons is 90 MeV at a depth about 70 mm shallower than the Bragg Peak. At a depth of 150 mm, or 10 mm from the peak, the average proton energy is 50 MeV.

Figure 4.2 shows the depth-dose profile in a water phantom from a beam of 280 MeV incident protons. The peak is at approximately 45.5 cm depth. The three proton energies investigated in these simulations, 5 MeV, 50 MeV and 90 MeV, would be found at the distal end of the Bragg peak, about 1.8 cm, and 6 cm from the peak respectively. The study of this range of incident beam energies allows the understanding of whether enhancement would be preferentially in the target or more uniform across the beam's path, potentially impacting on healthy tissue.

Protons were originated on one side of the phantom and directed towards the NP as a circular source beam of diameter equal to the NP diameter (here called *broad beam*), or alternatively as a pencil beam with no lateral dimensions (here called *pencil beam*), directed only towards the NP.

The Geant4-DNA Very Low Energy Extensions [89] were adopted to model in detail parti-

cle interactions down to electron volt scale, in the liquid water phantom. The Low Energy electromagnetic physics package, based on Livermore evaluated data libraries or the Penelope approach, was selected to describe particle interactions in the NP. Secondary electron production and transportation within the NP region is limited to those secondaries with kinetic energy greater than 100 eV. Atomic deexcitation (fluorescence, Auger electrons, and PIXE) was modelled as well. The physics processes and models adopted in the NP and in the surrounding water medium are summarised in Table 4.2.

The step in Geant4 is - by default - the distance between two interactions. A particle track is composed of multiple steps through the geometry, as the particle interacts with the medium and crosses boundaries between different materials. Physics models based on condensed history approach used within the NP region result in larger tracking steps as multiple interactions are simulated in a single step. Because of the limited size of the NP, the step was limited to 0.1 nm to calculate the energy deposition with higher spatial accuracy. It is important to note this is only a software solution dictated from the fact that track structure physics models for NP materials are not available in Geant4. In the water phantom,

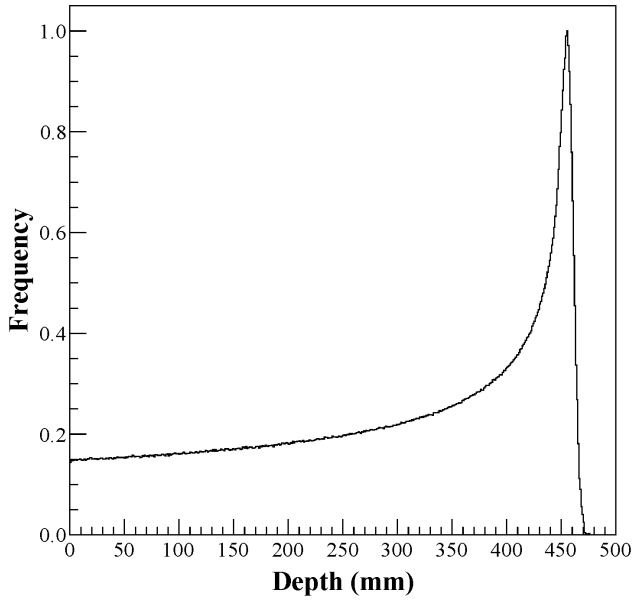

Figure 4.2: Depth dose curve for a 280 MeV proton beam incident on a water phantom.

surrounding the NP, the Geant4-DNA track structure models describe the electromagnetic particle interactions.

Test simulations performed with 5 MeV proton beam incident on a each NP examined the effect of AD processes, including fluorescence, Auger electrons and PIXE, on dose enhancement. Production cuts are implemented in Geant4 in order to control the low energy limits of particle transport. A defined production cut is the low energy threshold, below which particles are not created. If a particle has an interaction which will result in the release of a secondary particle of kinetic energy lower than the production cut, this secondary will not be created and the energy is instead deposited at the point of interaction. Production cuts can be defined in terms of particle range, which will be converted internally in Geant4 to energy cuts, depending on the medium in which the particle travels, or as a low energy threshold regardless of material. The threshold of production of secondary electrons in the NP was set to 100 or 250 eV, corresponding to the recommended low energy limit of the Penelope and Livermore-based physics models respectively.

Since Geant4 version 10.00 the proton ionisation model generates secondary electrons with an inherent energy threshold equivalent to the I of the specific material where in previous versions the threshold corresponded to the cut or the validity of the physics models (e.g. 100 eV in the case of Penelope models). This cut, for example in gold at 790 eV (the mean excitation energy for gold) applies to proton ionisation models and was introduced because the models are not confirmed below this energy level and are therefore assumed to not be accurate[1]. Table 4.1 shows the mean excitation energy data obtained from NIST for the NP materials under study. Any secondary electrons with energy below this threshold are not created and their energy is treated in the simulation as being locally deposited energy at the point of interaction of the proton.

[1]Private communication with Vladimir Ivanchenko, coordinator of the EM Physics Component of Geant4, 8 November 2015

Secondary electrons were created in the NP above an energy threshold set in the Physics List (100 eV in the Penelope physics case, and 250 eV for Livermore), when originated by electron ionisation. In the context of the present study these limitations mean that there may be some underestimation of dose deposited close to the NP surface. Results of the simulations show that the maximum range in water of a 100 eV electron is around 30 nm. This means that for electrons created within the NP with energy less than 100 eV which are not transported in the simulation the range would not be more than this distance from the NP surface. This energy threshold is therefore not expected to have a large impact on the overall dose distribution but should be taken into consideration when examining the results of this simulation.

In the latest versions of Geant4 (version 10 and above), AD electrons originated with energy below 100 eV cut are transported in the high-Z NP regardless of the simulation cuts by using the UI command */process/em/deexcitationIgnoreCut true* to effectively ignore the cut and transport electrons down to 0 eV in the special case of AD processes. Although the recommended low energy limit of physical validity of the Penelope physics models is 100 eV to describe electron, positron and gamma interactions, it is possible to transport Auger electrons with energy below this recommended threshold, with the understanding that the results carry this inherent inaccuracy throughout. However, in order to obtain a first understanding of the effect of very low energy electrons on the energy deposition in the proximity of the NP, the limit of validity is surpassed. This choice was dictated by the current lack in Geant4 of detailed event-by-event physics models addressed to energies below 100 eV in the NP materials under study.

The proton track structure was studied in terms of radial dependence of energy deposition in slices around the proton tracks. Energy deposition was calculated in cylindrical shells (see Figure 4.3, slices 1-4) with 100 nm thickness and 10 nm width, centred with the proton

Table 4.2: Physics processes implemented by region.

Particle Name	NP	Water
Proton	Ionisation (*BraggIonGasModel* and *BetheBlochIonGasModel*), multiple scattering (*Urban*)	Ionisation, excitation, charge decrease
Electron	Multiple scattering (*Urban*), ionisation(*Penelope*), bremsstrahlung (*Penelope*)	Elastic scattering (*Champion*), Excitation, ionisation, vibrational excitation, attachment
H, α, He^+, He	Ionisation (*G4IonIonisation*), multiple scattering (*Urban*)	Excitation, ionisation, charge increase and decrease
Gamma	Rayleigh scattering (*Penelope*), Photoelectric effect (*Penelope*), Compton scattering (*Penelope*), gamma conversion (*Penelope*)	

direction of incidence. The energy deposition was then scaled by the mass of the water of the corresponding cylindrical shell to obtain the dose. Radial dose distributions around the NPs are compared to the dose distribution around a water sphere which models the case of no NP present. The ratio of the NP and water dose distributions is calculated in order to analyse the dose enhancement due to the NP.

The dose deposited in a 1 µm radius cylinder of 400 nm length (in four slices shown in Figure 4.3) is calculated with each NP type under study compared to water. This is used to compare the relative enhancement of local dose deriving from each NP material under study compared to liquid water. The secondary electron spectra produced within each NP and escaping from it are compared, varying the NP material and incident proton energy.

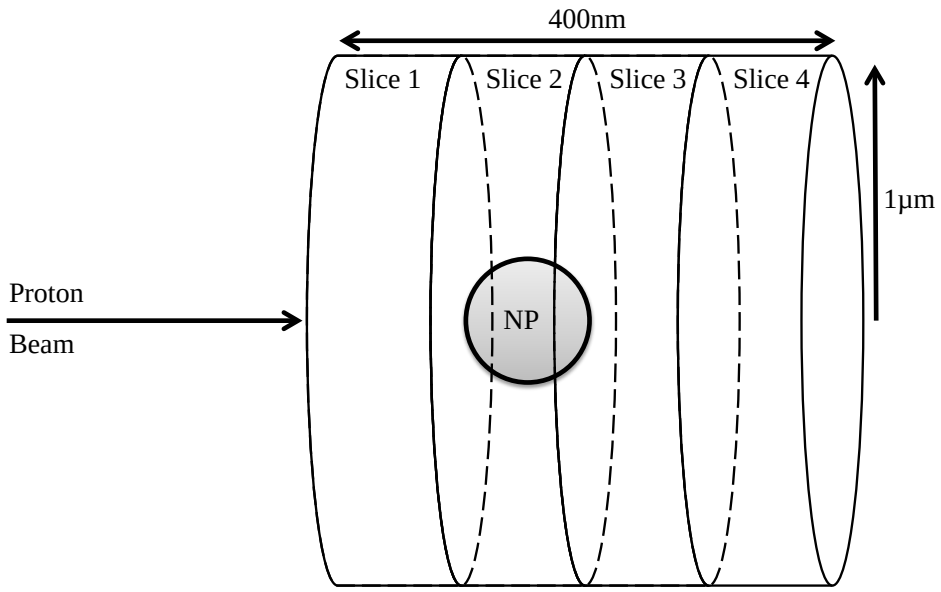

Figure 4.3: The energy deposited is calculated with respect to radial distance around the proton beam direction, in 100 nm thick cylindrical slices out to 1 μm.

4.1.2 Results

4.1.2.1 Dose distribution enhancement by NPs

Figure 4.4 shows the radial dose distribution in 100 nm wide bins. The radial dose distribution was calculated in slices 1, 2, and 3 (shown in Figure 4.3) and scaled to the number of primary protons in the broad beam. The ratio of dose calculated with and without the NP is reported as well.

The relatively short range of secondary electrons produced from the incident proton beam and enhanced by the presence of NPs results in most energy being deposited close to the primary proton tracks, in close proximity to the NP. The majority (more than 99%) of the energy is deposited within the first 300 nm from the beam centre in the water slices (Figure 4.4a and 4.4c). The first bin in slice 2 (Figure 4.4b) contains the NP (50 nm radius), and so has an artificially high dose enhancement ratio compared to the bins in water only. More than 95% of energy is deposited from the NP edge out to 300 nm in slice 2, containing the

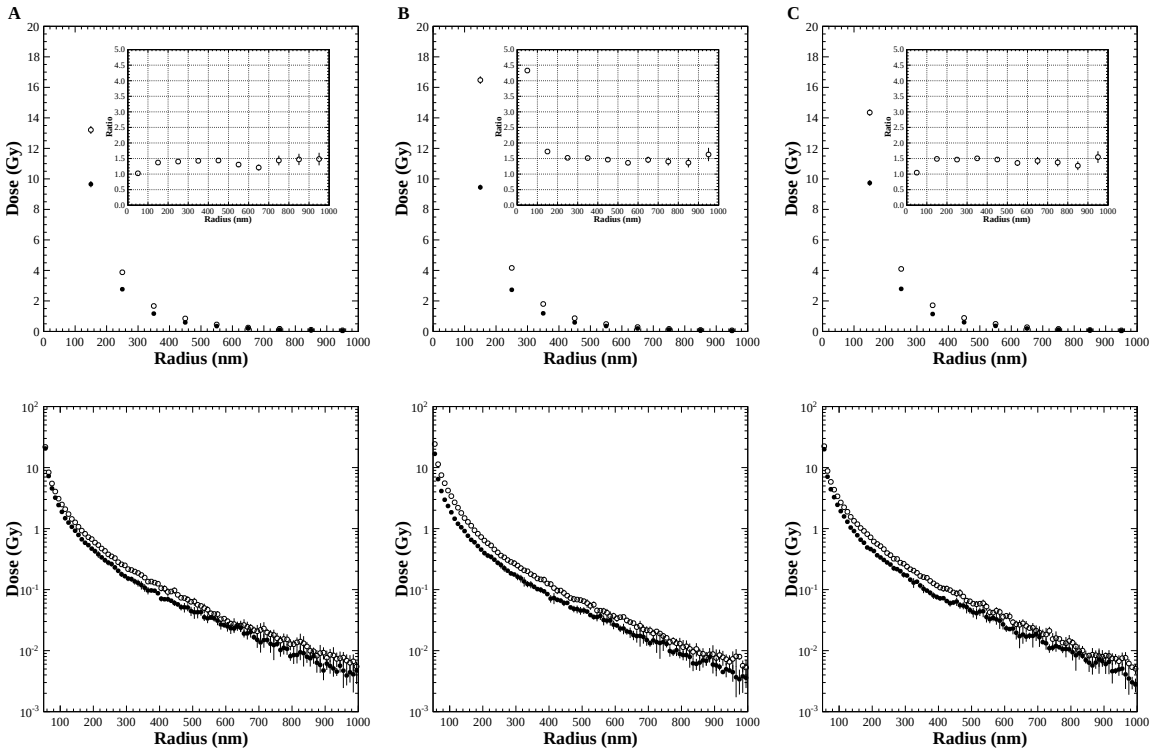

Figure 4.4: Dose deposited in 100 nm bins in slice 1 (A), slice 2 (B), and slice 3 (C) with a 5 MeV proton beam incident on a Au NP (open circles) and in water (solid circles), per incident proton. Linear scale with dose ratio (top row) and logarithmic scale (bottom row) are both shown.

NP. The dose is reduced from (16.5 ± 0.2) Gy in the first bin outside of the Au NP in slice 2 to (1.80 ± 0.05) Gy in the bin above 300 nm, which is a drop of 89%. The logarithmic scale plots show that dose drops off quickly with increasing radial distance from the broad proton beam, however the distribution is still enhanced due to the presence of the NP out to 1 μm. The detailed study of radial dose distribution is examined below 300 nm in the following sections as this is the region of most interest in the study of dose enhancement of primary proton tracks.

Radial dose distributions in 10 nm wide bins in slice 2, containing the NP (see Figure 4.3) for 5 MeV, 50 MeV and 90 MeV incident broad proton beams are shown in Figure 4.5 as well as the calculated dose enhancement ratio. The radial dose distribution local to all four NPs studied was enhanced for all the broad proton beam energies under study. A comparison

of the dose enhancement ratios shown in the inset allows direct comparison of positions along the Bragg peak, although absolute dose deposition varies widely between the studied energies.

Dose enhancement occurs at each beam energy studied, showing there is no significant preference for enhancement in the Bragg peak. All NP materials studied showed some level of dose enhancement with gold showing most enhancement in the plots of radial distribution of deposited dose. The X-ray radioprotector material, CeO_2, shows enhancement of a similar scale to the radiation enhancing Ta_2O_5 in the proton beam. The Bi_2O_3 NP shows relatively high dose enhancement, but was still not as effective as the Au NP.

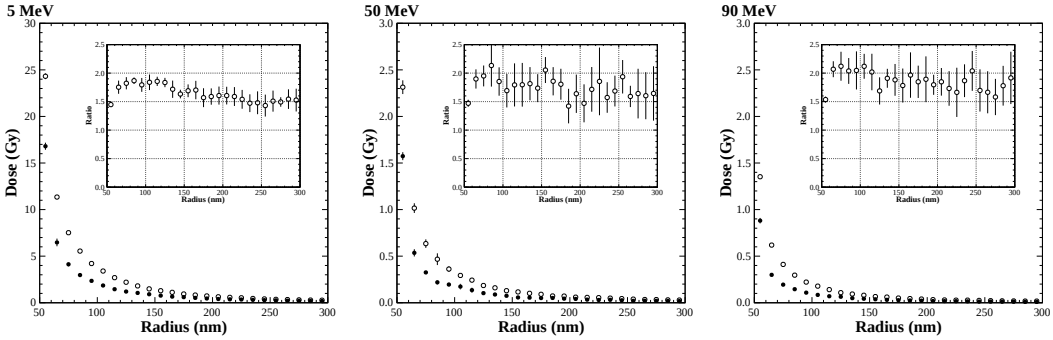

(a) Au NP

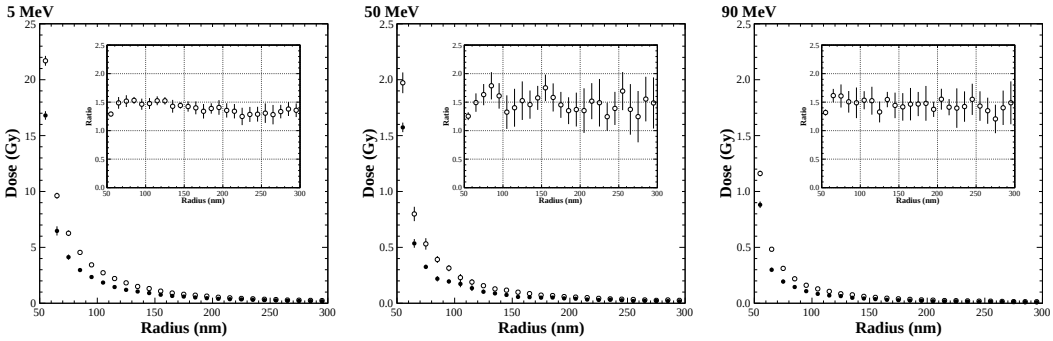

(b) Ta_2O_5 NP

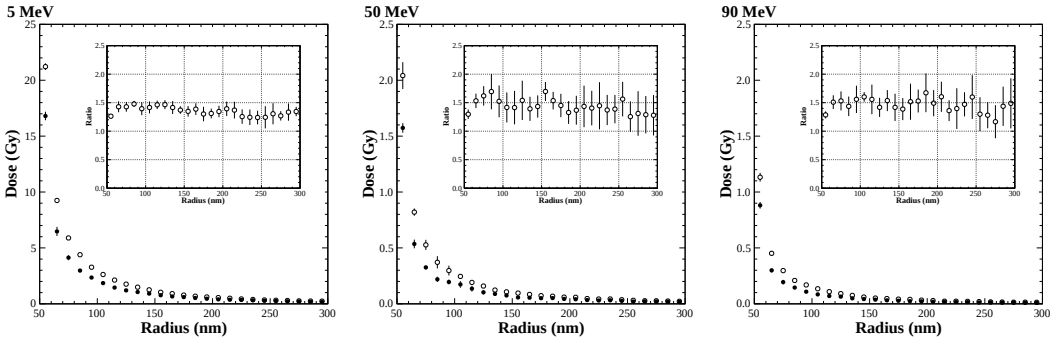

(c) CeO_2 NP

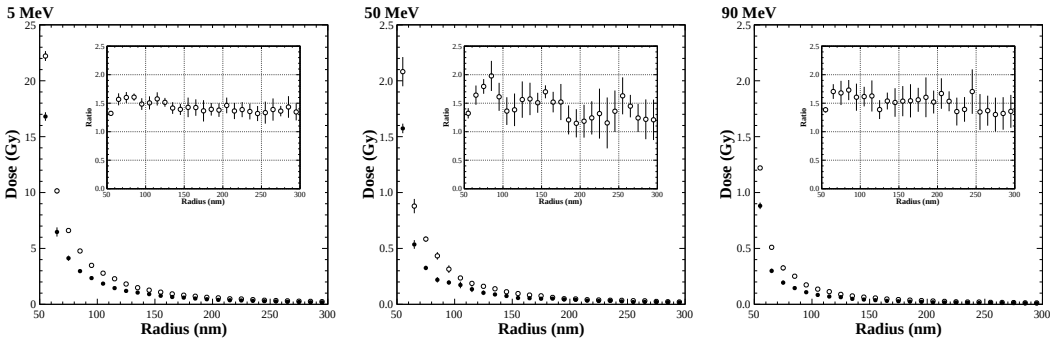

(d) Bi_2O_3 NP

Figure 4.5: Radial distribution of deposited dose in slice 2 with respect to proton beam energy and NP material, compared to dose in water (solid circles), per incident proton.

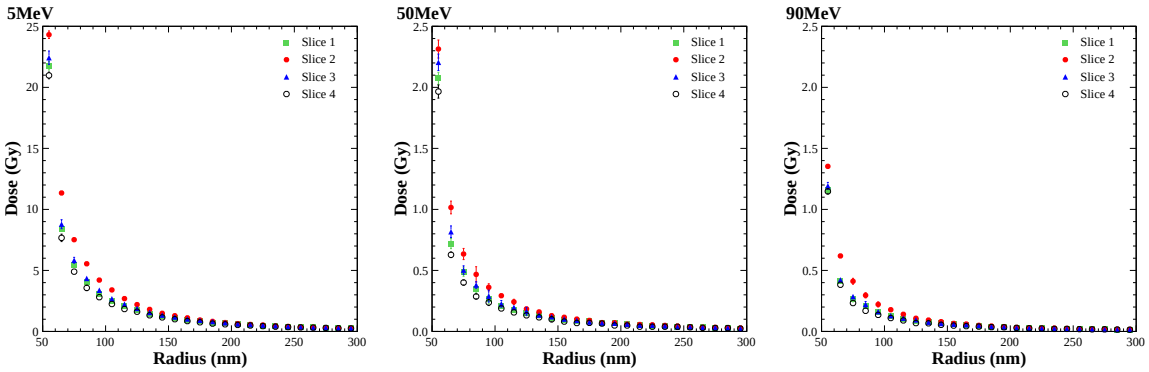

Figure 4.6: Radial dose distribution with respect to slice and for each energy of proton beam incident on a Au NP in water, per incident proton.

The distribution of the energy deposition enhancement with depth is shown in Figure 4.6. All three energies have most dose in slice 2, perpendicular to the NP. The 5 MeV and 50 MeV distributions also show increased dose in slice 3, downstream of the NP, followed by slice 1 upstream. The 90 MeV has a similar distribution upstream as downstream.

The figures show higher deposited dose in the radial distribution in the slice containing the NP compared to the slices upstream or downstream of the NP. This happens because the low energy electrons produced in the NP deposit energy laterally and locally to the NP.

4.1.2.2 Effect of NP Material on Dose Enhancement

A comparison of the radial dose distribution for different NP materials is shown in Figure 4.7. The radial dose is shown in each of the four slices (see Figure 4.3) around the NPs. The dose is enhanced laterally to the NP as well as upstream and downstream of the NP for each of the materials investigated. Enhancement of radial dose distribution is most pronounced in the slice lateral to the NP for Au, CeO_2, Ta_2O_5 and Bi_2O_3 NPs. Significant enhancement is obtained up to 100 nm behind the NP for the Au, CeO_2, Ta_2O_5 and Bi_2O_3 NPs. Dose enhancement upstream of each NP (slice 1) is due to enhanced backscattering of low energy electrons from the high Z NPs. The Au NP offers the greatest dose enhancement

of the materials studied. This is due to the higher density of gold (19.3 g/cm^3) compared to Ta_2O_5 (8.2 g/cm^3), CeO_2 (7.2 g/cm^3), or Bi_2O_3 (8.9 g/cm^3). The proton stopping power equation (see Equation 1.4) is dependent on the density of the medium and inversely dependent on the square of the velocity of the incident particle [28].

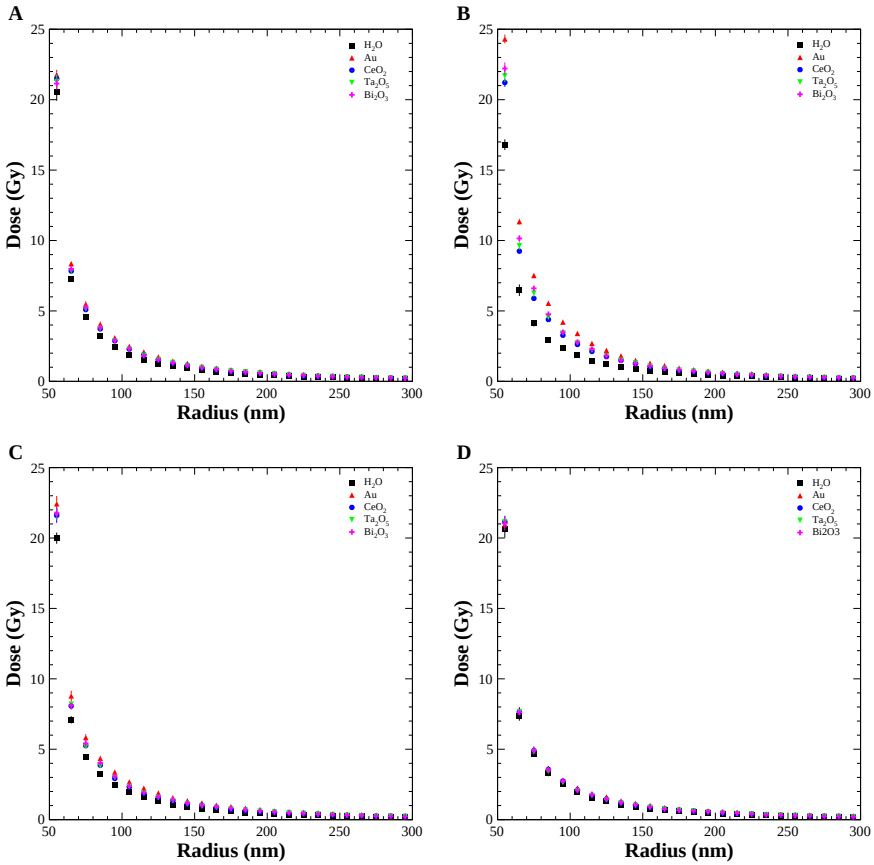

Figure 4.7: Radial dose distribution from a 5 MeV proton beam incident on NPs, and in water in slice 1 (A), slice 2 (B), slice 3 (C), and slice 4 (D), per incident proton.

Table 4.3 shows the overall dose enhancement in water due to presence of the NPs under study, integrating the radial dose over slices 1, 2 and 3 of the water phantom, shown in Figure 4.3, up to a radius of 1 µm, in the simulation set up. The dose is calculated omitting bins within 50 nm radius in slice 2, as these contain the NP, and then compared to dose with water in the NP volume. Similar results were obtained with 50 MeV and 90 MeV proton beams. The average dose enhancement, for all the proton energies considered, is (28 ± 2)%

Table 4.3: Dose enhancement expressed as a % relative difference: $\frac{D_{NP} - D_{water}}{D_{water}}$, where D_{NP} and D_{water} are doses calculated with and without the NP, integrated over the water cylinder represented in Figure 4.3. The statistical uncertainty is below 1%.

NP Material	% relative difference		
	5 MeV	50 MeV	90 MeV
Au	26	27	31
Ta_2O_5	16	16	17
CeO_2	14	15	17
Bi_2O_3	17	17	20

for Au NP, (17.9 ± 0.2)% for Bi_2O_3, (16.6 ± 0.6)% for Ta_2O_5 NP, and (15 ± 1)% CeO_2 NP. Atomic deexcitation accounted for less than 1% of the dose enhancement from gold in this volume and particular size of NPs, as low energy electrons deposit energy very close to the NP surface and so create enhancement on a smaller scale. The treatment of AD processes in Geant4 is discussed in more detail in Section 4.1.2.4.

4.1.2.3 Spectra of secondary electrons from different NP materials

The number of secondary electrons produced within the NP and escaping from it was calculated. Figure 4.8 shows the secondary electron spectra created with the different NPs, compared to water. These are the total secondary electron spectra from all interactions, and do not take into account whether or not the electrons will escape the NP or not. Figure 4.9 then shows the secondary electron spectra emitted from the four different NPs, compared to water.

The number of secondary electrons increases with the placement of a Au, Bi_2O_3, Ta_2O_5 and CeO_2 NP, compared to water, as expected. The Au NP is characterised by the highest number of secondary electrons emitted, compared to Bi_2O_3, Ta_2O_5 and CeO_2, however the

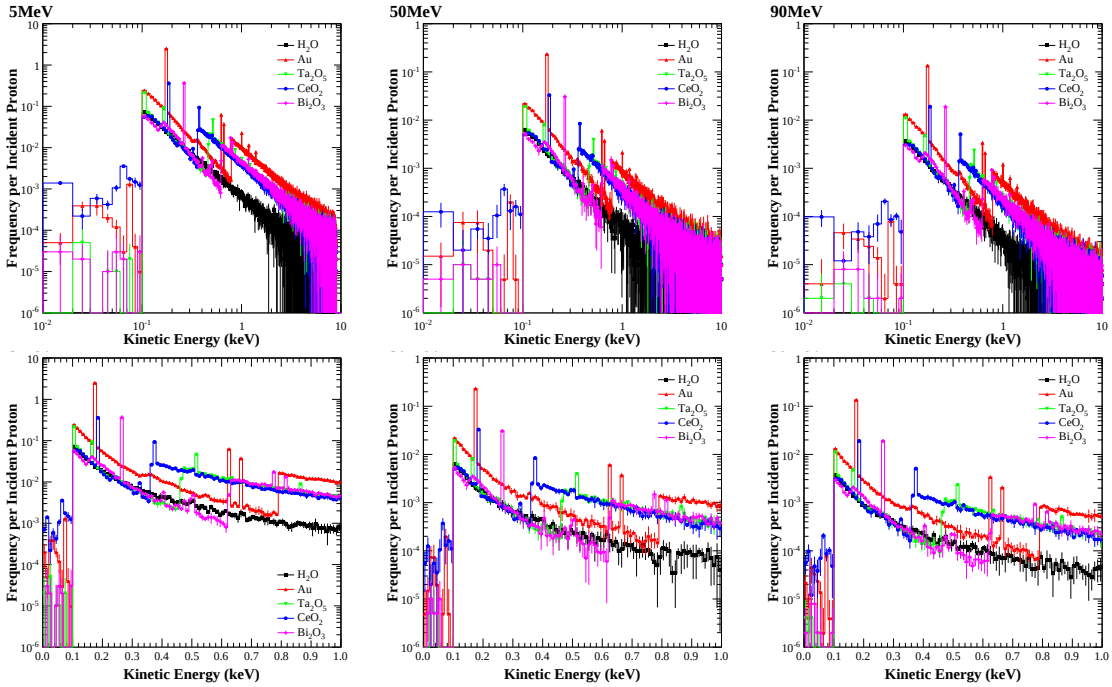

Figure 4.8: Spectra of secondary electrons created within each NP, for 5 MeV, 50 MeV and 90 MeV incident protons, per incident proton.

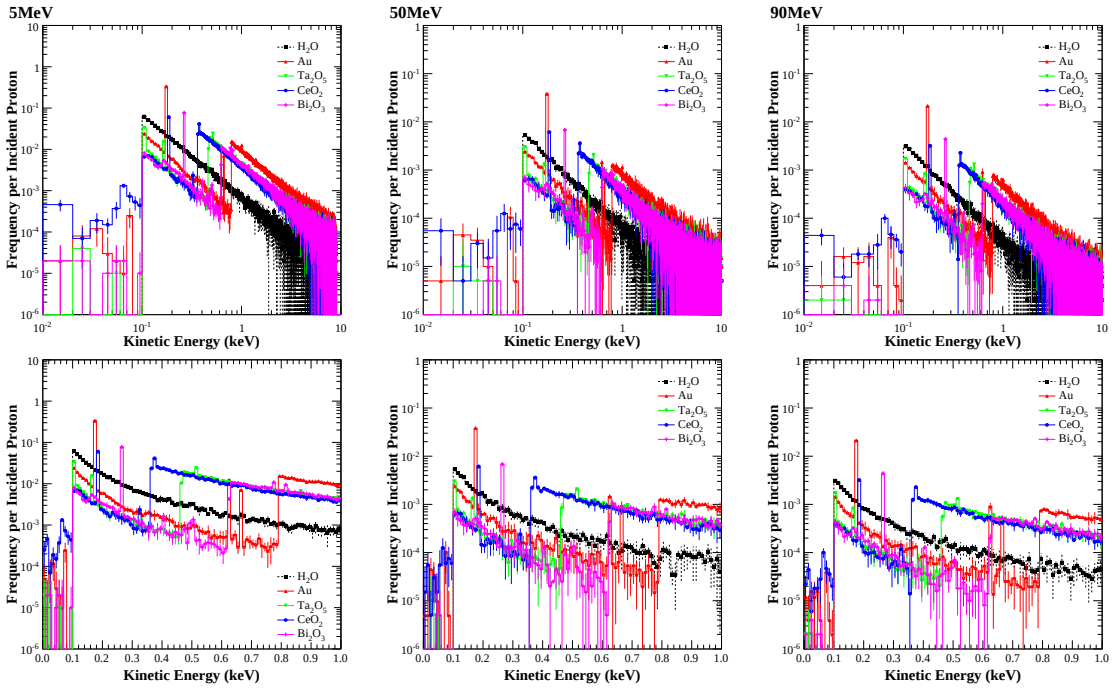

Figure 4.9: Spectra of secondary electrons created within and then escaping each NP, for 5 MeV, 50 MeV and 90 MeV incident protons, per incident proton.

lower densities of Bi_2O_3, Ta_2O_5 and CeO_2 with respect to Au allows a greater proportion of secondary electrons created within the NPs to escape.

Figures 4.8 and 4.9 both show that the low energy electrons dominate the spectrum. Approximately 50%, 60% and 70% of the escaping secondary electrons having kinetic energy of less than 1 keV with a proton beam incident on a Au, Ta_2O_5 and CeO_2 NP, respectively. These values are averaged over the proton energies studied and compare to approximately 90% of secondary electrons with kinetic energy of less than 1 keV escaping from the NP filled with water. The difference in the low energy spectra with and without NP occurs due to the internal cut in the proton ionisation models implemented in Geant4, combined with the high-Z NPs absorbing some of the secondary electrons produced.

Due to the majority of electrons having kinetic energy below 1 keV, secondary electrons escaping the NP predominantly deposit energy locally. The range of a 10 keV electron (approximate maximum energy of secondary electrons generated by a 5 MeV incident proton) in water is 2.5 μm whereas in gold it is only around 410 nm [106]. Most secondary electrons have much lower energy than this and would therefore have even shorter range in gold, leading to an increased number of these electrons being absorbed by the NP when the beam is incident on the centre of the particle.

A test simulation was performed to calculate the maximum range of electrons in the Geant4-DNA water. An isotropic electron source was placed at the centre of a water phantom and the radius at which energy was deposited was simulated in spherical shells. Figure 4.10 shows the results for 100 eV and 1 keV isotropic sources.

The results showed all energy deposition by the 1 keV electrons is deposited within a (150 ± 10) nm radius sphere around the source. The 100 eV electrons, on the other hand,

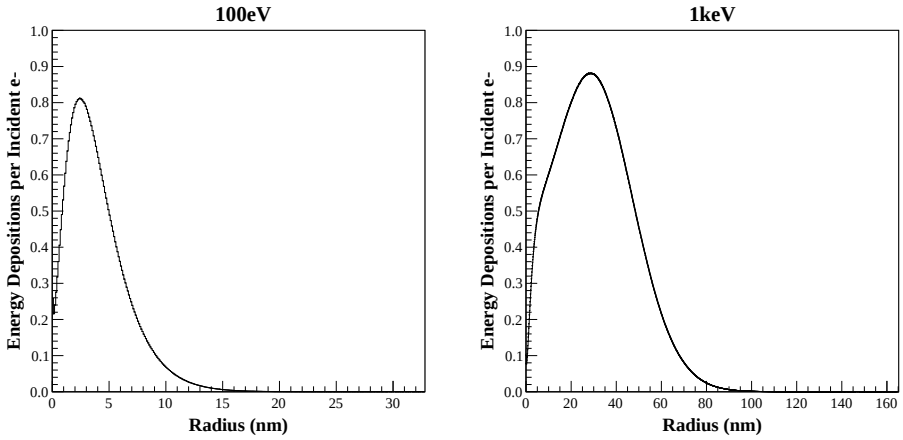

Figure 4.10: Location of energy deposition from an isotropic electron source in water, in spherical radial bins.

have a maximum range of just (31 ± 1) nm. This means that most energy from secondaries emitted from the NP is deposited within a short range of the NP surface.

It is observed that (31 ± 1)% of electrons created within the gold NP escape the NP compared to (58.0 ± 0.6)% and (57.9 ± 0.3)% escaping Ta_2O_5 and CeO_2 NPs, respectively. This proportion becomes (92.1 ± 0.2)% when the NP is substituted with a water sphere of the same dimensions, due to the longer range of low energy electrons in water compared to the material of the NP.

The average number of electrons produced and subsequently leaving the NP as a ratio to the number of electrons leaving a water sphere, across all proton energies under investigation, was (2.7 ± 0.4), (1.3 ± 0.1), (1.5 ± 0.1), and (1.8 ± 0.1) with a Au, Bi_2O_3, Ta_2O_5 and CeO_2 NP, respectively. This shows the combined effect of the increased number of interactions counteracted by the lower range of secondary electrons with increasing density of the NP. The highest-Z NP, the Au NP provides the highest enhancement ratio however when comparing the ceramic oxide NPs, the CeO_2 NP shows the advantage of the number of escaping electrons due to a low density combined with a relatively high-Z and lower mean excitation

Table 4.4: Number of electrons, per incident proton, produced with broad 5 MeV proton beam.

	Total	Escape	AD electrons	% of AD spectra < 200 eV
Au	5.58 ± 0.05	1.63 ± 0.02	0.00746	35.5
Bi_2O_3	1.65 ± 0.02	0.82 ± 0.01	0.00805	23.6
Ta_2O_5	1.71 ± 0.01	0.98 ± 0.01	0.02504	70.3
CeO_2	1.99 ± 0.02	1.14 ± 0.01	0.05597	74.7
H_2O	0.728 ± 0.004	0.671 ± 0.003	-	-

energy (see Table 4.1).

4.1.2.4 Effect of Atomic Deexcitation on Dose Enhancement

The inclusion of AD processes in the physics processes has only a minor effect on dose enhancement in this study. Atomic deexcitation electrons are originated with discrete energy spectrum up to approximately 8 keV, however more than 70% fall below 1 keV. The previously described simulation of the range in water of 100 eV electrons from an isotropic source showed that all energy is deposited within 30 nm radius sphere. This means that most energy from low energy AD electrons is deposited close to the NP surface, within 30 nm. In this simulation study the dose enhancement in the first 30 nm beyond the Au NP surface is approximately 5% when AD is modelled.

Table 4.4 shows the number of secondary electrons and AD electrons produced for each NP type under study as well as the proportion of the AD spectra which falls below 200 eV.

Figure 4.11 shows the kinetic energy spectra of electrons produced from AD processes in the simulation of 5 MeV protons incident on NP. The spectra of atomic deexcitation (AD) electrons was determined by running the simulations for each NP type studied with and without

atomic deexcitation processes activated in the physics models. The spectra of secondary electrons was taken at the point of creation within each NP. In order to isolate the spectra of atomic deexcitation electrons from the total spectra, the spectra without AD activated was subtracted from the spectra obtained with AD active. The spectra were corrected to omit counts within error of zero or values within error of the original spectra.

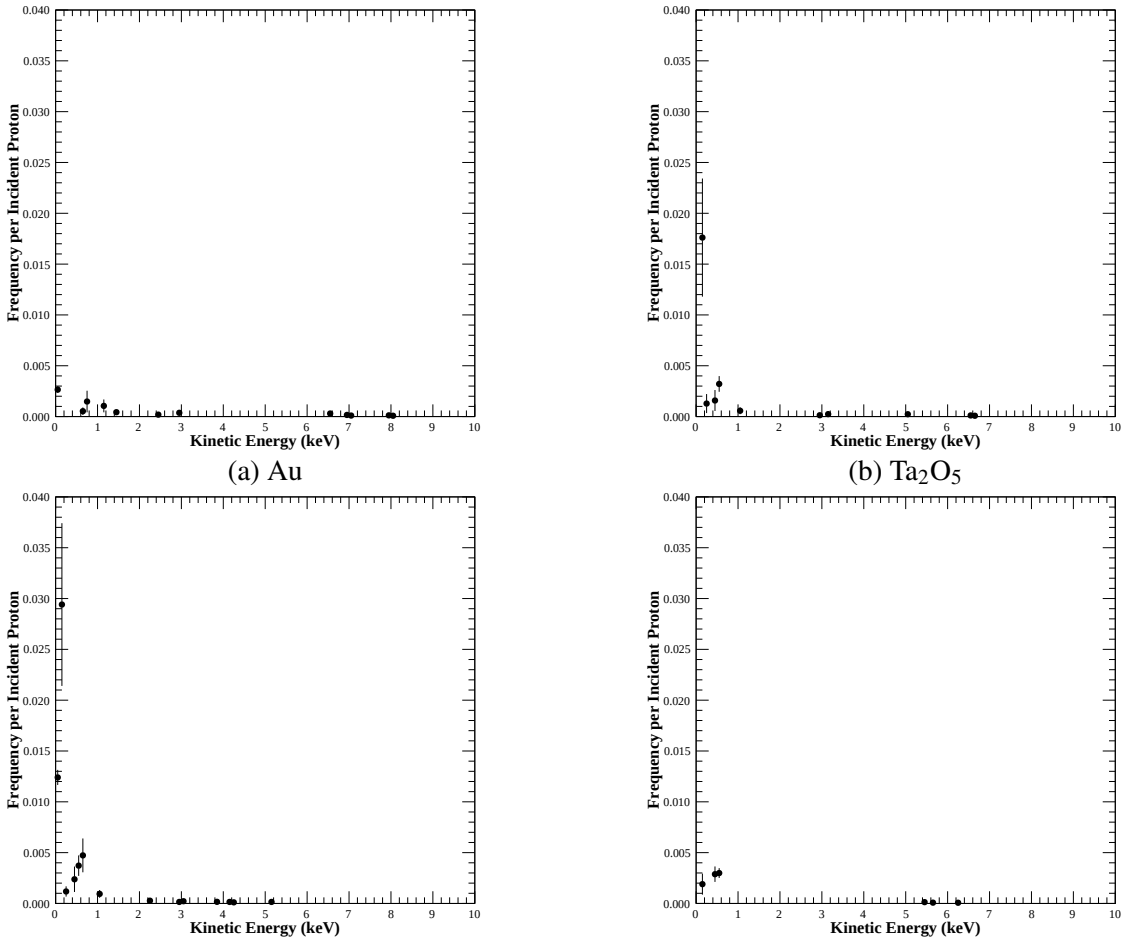

(a) Au (b) Ta_2O_5

(c) CeO_2 (d) Bi_2O_3

Figure 4.11: Auger electrons from 5 MeV protons incident on NP

The mean kinetic energy of the total spectra created within each NP are shown in Table 4.5. It is clear from the table that the mean energy is not changed significantly by the inclusion of AD processes, with most values falling within error of each other, or very close.

The Auger electrons form a small part of the total number of electrons emitted from the

Table 4.5: Mean kinetic energy of electrons (in eV) from 5 MeV proton beam

	Au	CeO_2	Ta_2O_5	Bi_2O_3
with AD	570 ± 6	701 ± 6	814 ± 7	849 ± 7
w/o AD	569 ± 3	715 ± 5	829 ± 7	864 ± 7

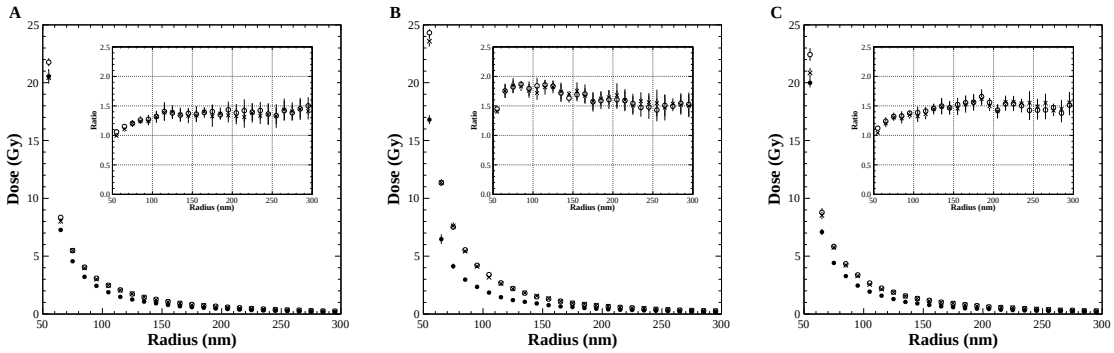

Figure 4.12: Radial dose distribution in slice 1 (A), slice 2 (B), and slice 3 (C) with (circles) and without atomic deexcitation (crosses, no AD) for 5 MeV protons incident on Au NP, compared to water (black circles).

NPs, thus not contributing significantly to the energy deposited in the water around the NP and have only contributed to the dose on the nanoscale. The total dose enhancement within the previously described 1 μm radius, 300 nm long water cylinder (slices 1-3 in Figure 4.3) increases from (25.3 ± 0.3)% to (26.0 ± 0.3)% in the case of a Au NP with 5 MeV incident protons when including AD. Figure 4.12 shows the radial dose distribution calculated with and with AD processes. The effect is small because of the low number of Auger electrons produced compared to ionisation electrons, and the short range of their effect.

4.1.2.5 Effect of beam size on NP dose enhancement

Figure 4.13 shows the radial distribution of the ratio of dose calculated with and without the NP with the broad beam proton source (100 nm diameter beam) compared to a pencil beam (no lateral dimensions).

It can be observed that the broad beam configuration is characterised by a higher dose enhancement in slice 2. This happens because secondary electrons are produced along the proton tracks. In the broad beam case, a larger number of electrons are produced close to the NP surface and, therefore, they have higher probability to escape from the NP. In the pencil beam case protons instead pass through the centre of the NP and thus produce electrons which must traverse a longer path in the NP before escaping and depositing dose in the surrounding water medium.

The ratio of the number of secondary electrons produced within a Au NP, compared to water, for various beam configurations indicates the effect of the distance of interaction from the surface of a NP. In the case of a pencil beam incident directly on the centre of the NP, the number of secondary electrons escaping the NP is increased (compared to water) by the ratio (2.26 ± 0.01). In the case of the broad beam which covers the entire NP cross-sectional area, this ratio is higher (2.43 ± 0.02). When a larger, 500 nm radius, source is used, the ratio remains essentially the same at (2.4 ± 0.4), however due to the lower number of protons directly incident on the NP, the statistical uncertainty is higher.

A simulation test was done with a beam of protons passing close to, but not directly impacting the NP. The resulting increase in secondary electrons emitted from the NP is due

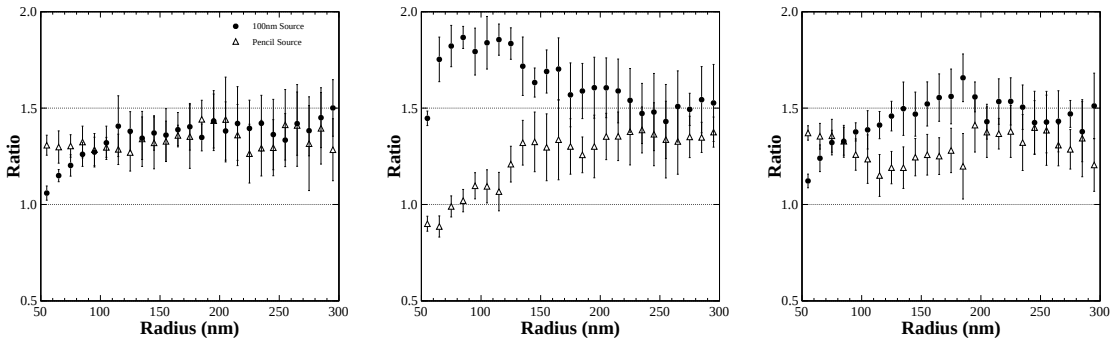

(a) Slice 1 (b) Slice 2 (c) Slice 3

Figure 4.13: Radial DER expressed as a ratio of dose calculated with and without the Au NP, with respect to beam geometry. Slices defined as shown in Figure 4.3.

therefore to the secondary interactions of electrons with the NP. The ratio of secondary electrons escaping the Au NP, compared to water, in this case is increased to (4.7 ± 0.4). This is due to the fact that as the particle source is always external to the NP and so the secondary electrons are more likely to be produced close to the surface where the originating secondary electron enters the NP.

The position (in terms of radial distance from the centre of the NP) of the creation point of secondary electrons which are not absorbed within, and therefore escape, the NP varies depending on NP material, and proton beam configuration. Figure 4.14 shows the radial distance from the centre of the NP at which secondary electrons, which then go on to leave the NP, are created.

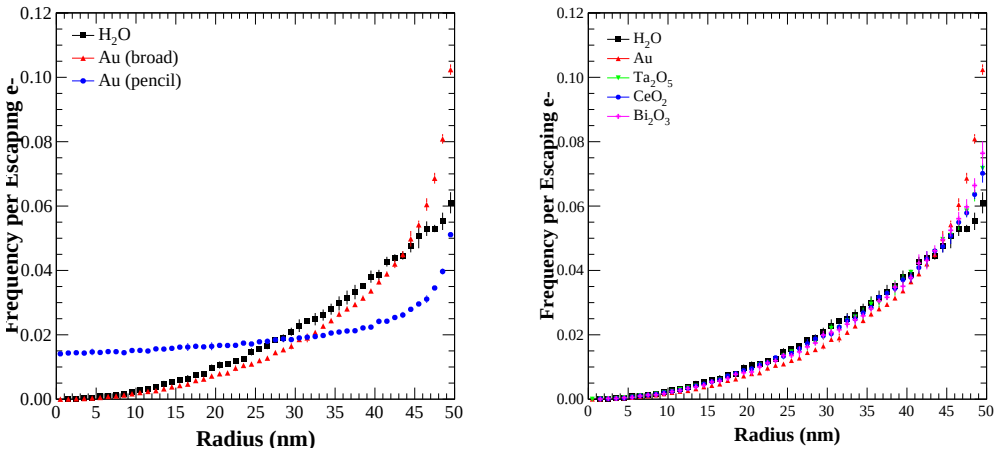

(a) Beam geometry (b) NP type

Figure 4.14: Radial position within NPs from which escaping electrons are generated with respect to beam geometry (broad or pencil) and NP types. The beam configuration is a broad beam incident on the water volume in (a) and all NPs presented in (b). Incident protons are 5 MeV in all cases.

Compared to the case of the water-filled NP, there is a higher proportion of electrons escaping closer to the surface of the Au NP in the case of the broad proton source incident on the NP. The average radial depth within the NP at which escaping electrons are created is (12.5 ± 0.1) nm, (10.6 ± 0.1) nm, and (20.9 ± 0.1) nm for the water, Au with broad and Au

with pencil beam, respectively. The depths in the other NP materials are (12.0 ± 0.1) nm, (11.9 ± 0.1) nm, (11.7 ± 0.1) nm from CeO_2, Ta_2O_5 and Bi_2O_3 respectively. The dependence on NP material is due to the different elemental composition of each NP material and therefore the range of electrons within each NP. The high-Z gold results in more self-absorption of electrons created close to the NP centre and therefore a higher proportion of electrons escaping from closer to the NP surface. The highest density NP, gold has preferential escaping of electrons produced within 10 nm of the NP surface.

Similar results are obtained with the broader proton source, extending beyond the NP, as expected, as there remains a uniform distribution of protons incident on the NP surface, but with lower statistical probability of direct hit. The case of the pencil beam incident directly on the centre of the NP shows a higher proportion of the escaping secondary electrons are generated within a 25 nm radius from the NP centre. This is evidence of the bias introduced with a directly incident proton source as the likelihood of interaction at the centre of the NP is increased, and therefore the likelihood of an escaping electron having been created deep within the NP is greater.

The results of this simulation study indicate the importance of beam geometry in the design of any simulations of NP induced dose enhancement in proton therapy and the interpretation of results of simulation studies. These results demonstrate the enhancement when there are direct proton hits on the NP, and subsequent secondary electron interactions.

4.1.2.6 Effect of NP size on dose enhancement

A simulation of a smaller, 20 nm diameter, NP was performed with a Au NP and a 5 MeV incident proton beam of the same diameter. The percentage dose enhancement in the three slices (1, 2, and 3) around the Au NP (omitting bins from 0 - 10 nm, containing the NP in

slice 2) is (11.2 ± 0.1)% compared to (26.0 ± 0.3)% with the 100 nm diameter particle, shown in previous results (see Table 4.3).

Figure 4.15 shows the radial distribution of deposited dose and dose enhancement ratio in three slices around the 20 nm Au NP. The radial distributions of deposited dose surrounding a 20 nm NP can be compared to Figure 4.5a on page 115 presenting the dose enhancement due to a 100 nm diameter Au NP. The lower dose enhancement observed locally to the Au NP is due to the fact that there are in total fewer proton interactions in the smaller diameter NP, resulting in reduced probability of an increased production of secondary electrons.

Figure 4.16 shows the secondary electron spectra generated with respect to NP size, comparing 20 nm and 100 nm diameter NPs with corresponding water volumes. Examination of the generated secondary electron spectra show a lower number of secondaries generated in the smaller diameter NP. The number of secondary electrons produced within the Au NP, per primary proton, was calculated to be (5.58 ± 0.05) and (0.60 ± 0.01) in the 100 nm and 20 nm diameter NPs respectively.

When a pencil beam is incident on a NP of each size studied, the number of secondary

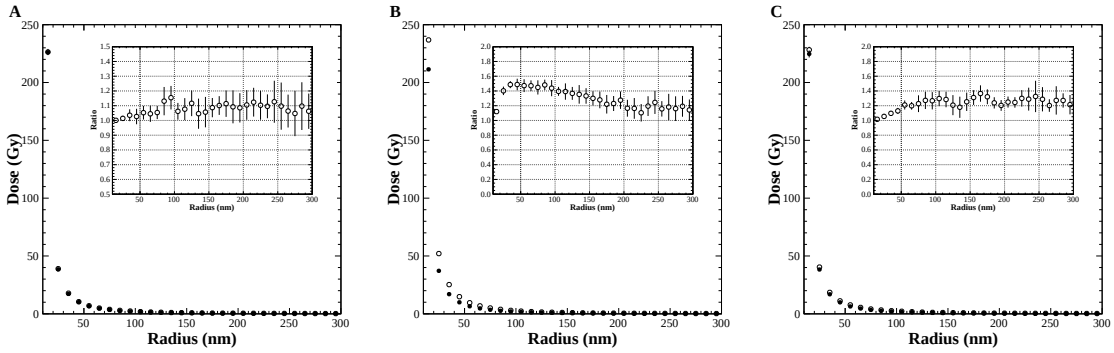

Figure 4.15: Radial dose distribution about a 20 nm Au NP (hollow circles) compared to water (black circles) with 5 MeV incident protons. Dose per incident proton is presented in slice 1 (A), slice 2 (B) and slice 3(C). The ratio of the dose with NP to dose with water is shown in the inset figures.

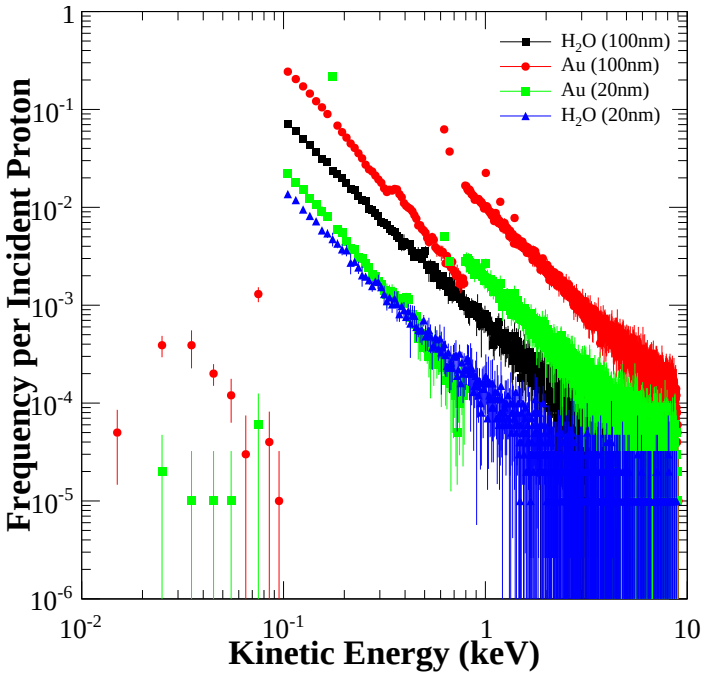

Figure 4.16: Kinetic energy spectra of secondary electrons generated within a 20 nm Au NP with 5 MeV incident protons. Frequency per incident proton is presented with logarithmic scales.

electrons produced, per incident proton is increased from (1.01 ± 0.01) to (9.29 ± 0.05) from the 20 nm to 100 nm diameter NPs (an increase similar to that found in the broad beam case). This again comes down to the fact that, for the smaller NP, the incident protons have a maximum of 20 nm of NP material in which to interact and create secondary electrons, whereas the larger NP has 100 nm of NP material (or five times) for the protons to interact in, although this is not a linear increase.

Another factor which plays a role is the proportion of secondary electrons produced within a NP which are able to escape the NP. With increasing NP size, the probability of electrons produced close to the centre of the NP is reduced due to the limited range of electrons in the high-Z NP materials. This translates to a lower number of electrons, per incident proton in the broad beam, escaping the NP, corresponding to (1.63 ± 0.02) and (0.36 ± 0.01) from the 100 nm and 20 nm diameter NPs respectively. The frequency of escaping electrons, per primary proton in the pencil beam, was (2.27 ± 0.01) and (0.545 ± 0.004) from the 100 nm

and 20 nm diameter NPs respectively (a similar level of increase compared to that found in the broad beam case).

The proportion of secondary electrons created within a 100 nm diameter gold NP which go on to leave the NP volume is around 30%. This value increased to approximately 60% for a smaller, 20 nm diameter NP. This effect occurs due to the increased proportion of secondary electrons able to be generated close to the NP surface, rather than deep in the NP volume, described by the increased surface area to volume ratio (SA:V). With an increase in NP radius from 10 nm to 50 nm (5-fold increase) the SA:V decreases in the same proportion. In water spheres of the same dimensions the escaping proportion of secondary electrons is increased from 92% to 97% with decreasing diameter.

4.1.2.7 Geant4 regression test for NP studies

As Geant4 and Geant4-DNA are constantly evolving software it is important to perform regression testing to evaluate how the results of a specific study change with the version of Geant4. This section present a regression test in one specific case. A 5 MeV proton beam was incident on a 100 nm diameter Au NP in the test case. The subsequent radial dose distribution was calculated as well as the total DER in a 300 nm long, 1 μm radius cylinder around the NP. Figure 4.17 shows the radial distribution of deposited dose from a 5 MeV proton beam incident on Au NP with respect to program version.

The radial distributions in Figure 4.17 show that with the later version of Geant4 the difference in dose distribution between water and Au NP is reduced. This can also be seen in the reduced total DER calculated between versions. Version 10.1 gives a DER in the cylinder of (1.26 ± 0.01) compared to (1.32 ± 0.01) in the previous version.

The secondary electron spectra of all electrons created within the NP region is analysed

in terms of the type of interaction originating the secondary electrons and those electrons escaping the NP region.

The secondary electron spectra in version 10.1 are different from the previous due to the internal cuts in the proton ionisation model discussed in Chapter 1. The spectra of secondary electrons change between versions of Geant4 due to changes in the physics cross-sections. Simulations were performed with the later version 10.1, and dose enhancement was compared for the updated models in this version. The proton ionisation cross-section implemented in version 10.1 are different from previous versions in that a low energy threshold is implemented intrinsically in the cross-sections and do not allow electron ionisation below the mean excitation energy of a material. The restriction of proton ionisation models to the creation of secondaries only above the mean excitation energy of materials was not introduced before version 10, therefore more low energy electrons are created in simulations run on early versions of Geant4.

Figure 4.18 shows a comparison of the secondary electron spectra between versions of Geant4. It is clear from the plot that the cross-sections result in the same secondary electron spectra above the internal 790 eV cut, however there are differences below this cut, and

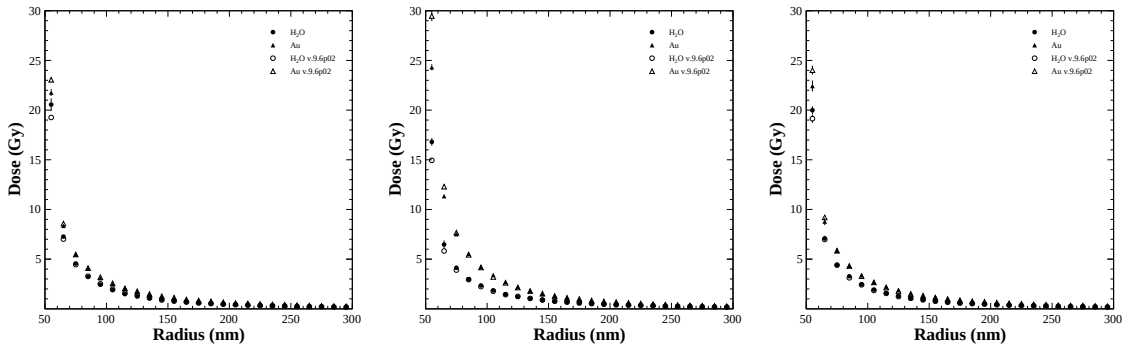

(a) (b) (c)

Figure 4.17: Radial dose distribution in slice 1 (a), slice 2 (b), and slice 3 (c) with respect to program version for 5 MeV protons incident on Au NP, compared to water (circles).

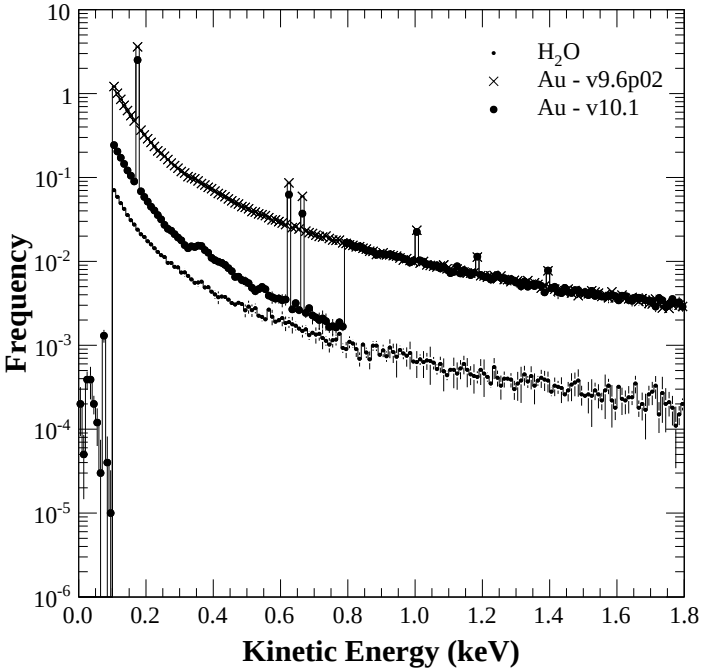

Figure 4.18: Spectra of secondary electrons created within the Au NP with 5 MeV incident protons, comparing Geant4 v9.6p02 and v10.1, per incident proton.

below 100 eV. In the latest version of Geant4, atomic deexcitation electrons are seen to be produced below the 100 eV low energy limit of Penelope models, set in the Physics List.

As expected, the proportion of secondary electrons produced with kinetic energy below 1 keV is higher in simulations with the previous version of Geant4. Approximately 90% of the escaping secondary electrons having kinetic energy of less than 1 keV regardless of NP type. This would have an effect on dose enhancement close to the NP surface (within 150 nm).

The low range of low energy electrons (seen in Figure 4.10 on page 121) means that the secondary electrons omitted from the spectra when using the updated physics models of version 10 would only contribute dose to those bins within 150 nm of the NP surface. This effect can be observed in the results analysing the effect of beam geometry on the dose

Table 4.6: Dose enhancement in a water cylinder surrounding an Au, Ta_2O_5 or CeO_2 NP compared to water. The results using Geant4 version 9.6p02 (left top) are compared to version 10.1 (right top). The statistical uncertainty is <1%. The percentage difference from the v.10.1 results is shown in the lower section of the table.

NP		9.6.p02			10.1	
Material	5 MeV	50 MeV	90 MeV	5 MeV	50 MeV	90 MeV
Au	32	31	32	26	27	31
Ta_2O_5	16	17	18	16	16	17
CeO_2	14	15	15	14	15	17

% Difference between above DERs calculated with updated program version

	5 MeV	50 MeV	90 MeV
Au	- 19%	- 13%	- 3%
Ta_2O_5	0%	- 6%	- 6%
CeO_2	0%	0%	+ 13%

enhancement ratio.

The effect on overall dose enhancement is observed in the total dose enhancement within slices 1-3, compared for each program version in Table 4.6. This data shows that the highest dose enhancement comes from the Au NP, with Ta_2O_5 and CeO_2 showing similar enhancement, for both Geant4 versions.

Dose enhancement is generally lower in the version 10.1 results due to the different secondary electron spectra produced in the NPs. Fewer highly enhancing low energy electrons are emitted from the NP due to the cut in the proton ionisation models (see Figure 4.18). This means that compared to water, the calculation shows NPs to be less enhancing in the later version, however enhancement by higher energy secondary electrons from proton ionisation and electrons released by means of electron ionisations still occurs. Due to the short range of low energy secondary electrons the impact of the modelling difference between program versions is shown to be limited to the region close to the NP surface where there is a reduction in the dose deposited. For the most extreme example, in the 5 MeV beam in the

first bin outside the NP in slice 2 the dose deposited is ≈20% higher when calculated using the previous version of Geant4, compared to version 10.1. However, this difference does not translate to a significance difference in dose at radial distances of more than 10 nm from the NP surface.

4.1.3 Discussion

The number of interactions an incident proton or secondary electron encounters is increased compared to water for all NP materials considered in this study when directly impacted by protons. The dose enhancement in the region around a high-Z NP is due to an increased number of secondary electrons transporting energy to the surrounding water volume. This increase in secondary electrons is due to the increased number of ionizations in the NP.

In the case of an incident proton beam, the majority of Auger electrons have a kinetic energy below 1 keV, in agreement with Wälzlein et al. (2014), and contribute a small fraction to the total number of secondary electrons, as the major part is originated by proton and electron ionisation. Increase in energy deposition by Auger electrons within 30 nm of the NP surface was found to be approximately 5%. The greatest effect from atomic deexcitation is shown to be in the first few tens of nm of the radial dose distribution and this agrees with the results of Wälzlein et al. (2014), reporting high dose enhancement within the first 5 nm from the surface of the NP.

This work shows that dose enhancement occurs in the presence of Au, Bi_2O_3, Ta_2O_5 or CeO_2 NPs with incident proton broad beams. The secondary electron emission from each of the studied NPs, increases by factors of (2.7 ± 0.4), (1.3 ± 0.1), (1.5 ± 0.1), and (1.8 ± 0.1) for Au, Bi_2O_3, Ta_2O_5, or CeO_2 NPs respectively, indicating potential increased biological effectiveness enhancement due to secondary electrons. As the secondary electron spectra

show, proton interactions produce a large number of high-LET electrons with energy lower than 1 keV.

The benefit of proton therapy is due to the proton's densely ionizing track, especially at low energy, in the Bragg peak region. The large number of low energy electrons creates complex damage in DNA. An increase in the production of low energy secondary electrons due to the placement of a NP close to DNA may enhance the biological effectiveness of proton therapy. Local dose enhancement within a cylinder (300 nm long, 1 μm radius) was observed to be (28 ± 2)% for Au NP, (18 ± 1)% for Bi_2O_3 NP, (16.6 ± 0.6)% for Ta_2O_5 NP, and (15 ± 1)% CeO_2 NP. The local dose enhancement around the CeO_2 NP indicates this material has dose enhancement effects that are in counteraction to the free radical scavenging properties discussed in the literature.

The dose enhancement ratio demonstrated in the present study shows a maximum value of approximately 2 for 5 MeV protons lateral to the Au NP (slice 2 of Figure 4.3). This result is comparable with the results of the study by Wälzlein et al. (2014) although there are differences in the geometrical set-up of the simulations.

The importance of beam geometry in the simulation design is clear as dose enhancement is vastly increased when protons impact directly on NPs. This is an important consideration when relating simulation results to realistic experimental situations. In reality, the concentration of NPs in a cell population of tumour tissue and distribution within these are widely variable and so there will not necessarily be a high probability of a proton interacting with a NP directly.

4.2 Dose Enhancement by Carbon NPs

In addition to dose enhancement by metallic or ceramic oxide NPs in radiotherapy the enhancement by means of carbon NPs is a recent area of research interest [58, 59]. The enhanced production of secondary electrons from metallic, ceramic oxide or carbon NPs is expected to result in increased damage to cells and DNA. The understanding of the basic physical interactions of protons with carbon NPs and production of low energy secondary electrons will allow a basis for continuing research in this direction. This chapter examines the secondary electron production from a C_{60} NP with incident proton beam comparing different simulation and analytical modelling techniques.

Plasmons are collective excitations of electrons in metals. Plasmon excitation and electrons produced in their decay are an important mechanism of dose enhancement by metallic NP in ion therapy [112]. Plasmon excitation cross-section data for the C_{60} molecule in this project was developed and calculated by Alexey Verkhovtsev from MBN Research Center, Frankfurt am Main, Germany by means of the plasmon resonance approximation (PRA).

A Geant4 Monte Carlo simulation study to calculate secondary electron creation in, and emission from, carbon NPs was developed as part of this PhD project. The results obtained were compared with analytical methods of calculating low energy secondary electron yield from a carbon NP. Results obtained by means of this Geant4 Monte Carlo simulation were compared to results obtained by the analytical calculation (see Appendix C).

The calculation based on the dielectric formalism was performed by Pablo de Vera from Departament de Física Aplicada, Universitat d'Alacant, Alicante, Spain and Department of Physical Sciences, The Open University, Milton Keynes, UK.

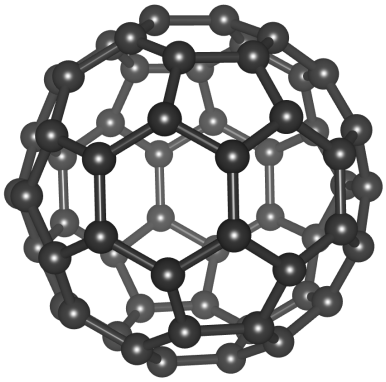

(a) Structure of C_{60} molecule - image created using VESTA software.

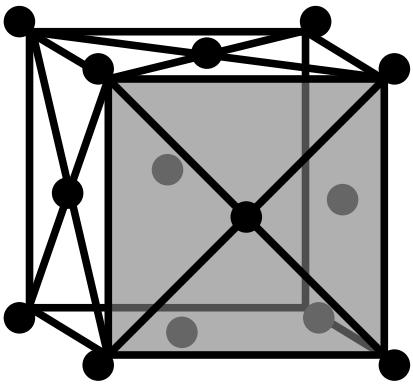

(b) Illustration of the molecule positions in a face-centred cubic structure of C_{60} molecules.

Figure 4.19: Diagrams of C_{60} molecule geometry and arrangement of molecular positions in a face-centred cubic structure.

Figure 4.19 shows the geometry and elementary lattice structure of particles simulated and modelled in this chapter based on a form of carbon (C_{60}). Each C_{60} molecule (Figure 4.19a) occupies a position in a face-centred cubic structure (Figure 4.19b). In the Monte Carlo simulation an approximation of this structure is necessary, as described further in the Methods below.

In the published work [101], the interaction of protons with metallic NPs or carbon NPs (C_{60}) is studied in detail by means of Monte Carlo simulations using Geant4 and compared to calculations performed by collaborators modelling the decay of plasmon excitations and calculations based on dielectric formalism. The Monte Carlo simulation consisted of placement of an approximated carbon or water NP in a water phantom. The secondary electron yield per incident proton was calculated and this part of the collaborative work is detailed in this section of this thesis.

4.2.1 Methods

The low energy electron production in a carbon NP calculated using the PRA was compared to results from the Geant4 simulation developed in this PhD project. The PRA calculation is based on an isolated C_{60} molecule so is extended to the case of a large solid carbon NP with C_{60} molecules in a fullerite structure [101]. The Monte Carlo simulation described in Section 4.1 in this chapter was modified to model the carbon NP for this project.

In order for Geant4 to calculate secondary electron production in a material it is necessary to include the density and composition of the material in the simulation set up. The density of the fullerite was calculated from the mass of a single carbon atom (m_C = 12 u) and the lattice parameter of the molecules packed in a fcc crystalline lattice (a = 1.417 nm) using Equation 4.1.

$$\begin{aligned} \rho \text{ (fullerite)} &= \frac{4 \times 60 m_C}{a^3} \\ &= 1.68 \text{ g/cm}^3 \end{aligned} \tag{4.1}$$

Geant4 does not model the individual molecules or the lattice geometry explicitly, however, the 50 nm diameter NP modelled would consist of approximately 92,000 of the C_{60} molecules shown in Figure 4.19a.

As described in the first part of this chapter, the secondary electrons created in the NP with a 1 MeV incident proton were analysed with respect to their kinetic energy.

4.2.2 Results

Secondary electron yield within the 50 nm C_{60} particle and an equivalent volume of liquid water are compared in Figure 4.20. The number of electrons per unit energy produced from an incident 1 MeV proton is shown in these graphs. Some electrons produced within the C_{60} or H_2O volumes will naturally be absorbed within the volume. Figure 4.20 does not take into account the effect of this self-absorption, however, the proportion self-absorbed in each volume is generally small.

Further details of the plasmon resonance approximation and calculations based on the dielectric formalism are available in the published paper and other literature [101, 113, 114].

The proportion of these secondary electrons created within each material and then escaping the NP volume are shown in Table 4.7. A comparison of the effect of the selection of physics models (Geant4-DNA vs. Livermore) is included for the case of the liquid water sphere.

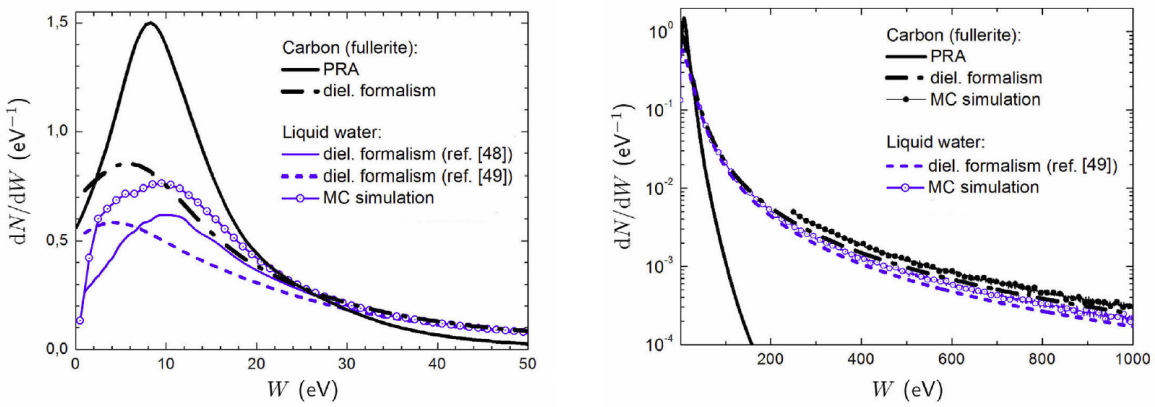

Figure 4.20: Number of electrons per unit energy produced by irradiation of a 50 nm carbon NP by a single 1 MeV proton (black), and in the equivalent volume of liquid water (blue). Open circles illustrate the data obtained in this PhD project by means of Monte Carlo simulations using the Geant4-DNA simulation tool. The black curves represent the data obtained by the PRA approach. Solid and dashed blue curves represent the results obtained with the dielectric formalism by Scifoni et al. (labelled ref. [48], see ref. [113]) and de Vera et al. (labelled ref. [49], see ref. [114]), respectively. Figure reproduced from ref [101].

Table 4.7: Calculated proportion of secondary electrons escaping 50 nm diameter sphere.

NP Material	Proportion Escaped (%)
H_2O (*Geant4-DNA*)	(38.9)%
H_2O	(98.5)%
Au	(95.7)%
C_{60}	(98.5)%

The proportion of secondary electrons created within the liquid water sphere (with Geant4-DNA models implemented) and escaping is significantly lower than the other cases. This is due to the higher number of electrons created with kinetic energy less than the 250 eV cut implemented in the other cases being more like to be self-absorbed within the water sphere.

4.2.3 Discussion

The collaborative work presented in this chapter is an important comparison of methods to calculate secondary electron yield from carbon NPs. The work performed as part of this thesis contributed the Geant4 Monte Carlo simulation results in the case of carbon NPs, and water NPs. These simulations were compared in the paper (see ref. [101]) with analytical models.

The results show enhancement of secondary electron emission from a carbon NP, compared to water. This is an important result as it shows the potential for use of carbon NPs in the enhancement of proton therapy. A thorough understanding of the mechanisms of enhancement in NP enhanced radiotherapy, including proton therapy is an important aspect of study in the push towards implementation of NP enhancement in a clinical setting.

The results of this work show the potential importance of low energy electron contributions from NPs which are not currently modelled in Geant4, due to limitations of cross-sections available. Geant4 Monte Carlo simulations are currently limited in their ability to model secondary electron production at very low energies (below ~100 eV) in NP materials. A potentially useful area of future study is the implementation of plasmon excitations within low energy models in Geant4.

4.3 Conclusion

The work in this chapter shows that the fundamental concept of dose enhancement by NPs in proton therapy is evident on a nanoscale and therefore biological effectiveness of proton therapy may be increased due to this localized increased secondary electron density.

The results in Section 4.1 showed that more than 95% of dose deposition occurs within 300 nm of the proton beam and NP centre. Most dose enhancement was observed in the slice containing the NP, with some enhancement also observed upstream and downstream of the NP in the proton beam.

All proton energies studied showed similar levels of dose enhancement, indicating no specific advantage is achieved in or close to the Bragg peak region of the dose distribution. The lower energy protons (5 MeV and 50 MeV) showed enhancement upstream and downstream of the NP however this was less significant in the higher energy proton case.

The highest dose enhancement was observed for the Au NP followed by Bi_2O_3. The Ta_2O_5 and CeO_2 NPs showed a similar level of dose enhancement. This result is due to the dependence of the proton stopping power equation (Equation 1.4) on the density and the inverse square of the velocity of the incident particle. The average dose enhancement due to the

Au NP is (28 ± 2)%. This compares to (17.9 ± 0.2)%, (16.6 ± 0.6)%, and (15 ± 1)% from the Bi_2O_3, Ta_2O_5, and CeO_2 NPs, respectively.

The proportion of the secondary electron spectra with kinetic energy less than 1 keV increased with decreasing NP density from 50% in the Au NP to 90% in the H_2O NP. This demonstrates the effect of the self-absorption of secondary electrons within higher density NPs. The overall secondary electron yield from NPs compared to water is highest from Au-NP: (2.7 ± 0.4) times that of water. The ceramic oxides result in an increase in the total yield of secondary electrons of (1.3 ± 0.1), (1.5 ± 0.1), and (1.8 ± 0.1) times the yield from a water NP for the Bi_2O_3, Ta_2O_5, and CeO_2, respectively.

The results showed that the increase in energy deposited observed within 30 nm of the ceramic oxide NPs was approximately 5 % due to the action of Auger electrons. This observed result is in agreement with studies by other researchers (see ref [82]). Less than 1% of the total dose enhancement effect is attributed to atomic deexcitation to the short range of these secondary electrons.

The simulation studies showed that secondary electrons are mostly emitted from close to the NP surface, due to the high probability of self-absorption of low energy electrons created deeper within the NP. The smaller NP modelled (20 nm diameter) showed a lower overall dose enhancement effect than the 100 nm diameter particle, (11.2 ± 0.1)% v.s. (26 ± 0.3)%. However, the secondary electron yield increases from (2.43 ± 0.02) to (2.6 ± 0.1) times the yield from water when the NP diameter is decreased from 100 nm to 20 nm. This is due to the increased proportion of electrons produced within the smaller volume being able to escape the nanosphere without being self-absorbed in the particle.

The production and transportation of free radicals in water was not modelled in this study.

This is a limitation of this work as the action of free radicals may contribute a non-trivial part of the damage from proton therapy resulting in cell death. However, it can be noted that the increase in low energy secondary electrons, whilst contributing to increased direct damage in clustered hits to DNA, would also likely result in an increase in water radiolysis. This increase in free radicals would further enhance the efficacy of a proton beam in proximity to a NP, in the absence of radical scavenging, such as the action of CeO_2.

The short range of the low energy electrons emitted from the NP would necessitate the NP being relatively close (within a μm scale) to critical structures within the cell to induce direct DNA damage. For this reason, coupled with sub-μm dimensions of fabricated NPs, nanodosimetric track structure simulations are an important investigation tool to understand the physical effects of NP dose enhancement in radiotherapy, however event by event particle tracking is currently not implemented in Geant4 in solid state materials, excluding silicon. Given the limitations of the physics models adopted when describing particle interactions in the NPs, the results of this project are intended to provide a basic physics understanding beyond the mechanism of dose enhancement produced by NPs and a first comparison of ceramic oxide NP materials with respect to gold. The results shown in this study should be refined in the future with inclusion of more sophisticated physics models for a more detailed description of particle tracks in NP materials.

In the final part of this chapter the secondary enhancement yield due to a carbon NP was calculated using the same Monte Carlo simulation set up. This calculation was compared to analytical techniques performed by collaborators on the paper in Appendix C. The plasmon resonance approximation approach demonstrated the enhanced production of very low-energy secondary electrons in the carbon-NP compared to water. This highlights the possibility of carbon based nano-structures to be developed with the proposed aim to produce a radiation sensitizing effect similar to metallic NPs [101].

The evaluation of the physics models of Geant4 has shown an impact on the calculation of dose, DER, and secondary electron spectra therefore it is something to be taken into consideration in future simulation studies. Further work in this project, and ongoing research in this field, will need to include the modelling of the production and transport of free radicals, which has been recently released in Geant4 [115, 116]. This will provide an insight into the broad observed effect of NP enhancing cell killing in proton therapy. Hadronic interactions should also be modelled in the next stage of the study to evaluate the effect of these interactions in the NP dose enhancement. The plasmon excitation decays should also be modelled in a full simulation [112] to study their possible effect on the nanoscale dose enhancement. The low energy part of the spectra would play an important role in dose escalation to structures within close proximity to NPs in cells.

Chapter 5

Conclusion

5.1 Summary

This thesis has described a body of work examining the fundamental techniques for assessing the physical dose enhancement due to ceramic oxide NPs in several radiation therapy fields. Four NP materials were the focus; Ta_2O_5, CeO_2, Bi_2O_3, and gold for comparison. The fundamental concept of the escalation of radiation dose delivered to cells and/or DNA in conventional therapy as well as proton therapy by means of ceramic oxide NPs has been studied by means of Monte Carlo simulation on the micron- and nano-scale. Carbon (C_{60}, fullerite) was also investigated for it's potential to increase low-energy secondary electron yield in proton therapy.

This thesis has presented the results of several Monte Carlo simulations developed during this PhD project which investigate the dose enhancement of radiation therapy by NPs on the cellular level, and on the scale of the DNA. Chapter 2 introduced the Monte Carlo simulation code and presented results comparing dose enhancement in kilovoltage and megavoltage photon beams for the various ceramic oxide NPs. In Chapter 3 this formalism was extended to examine the effect of ceramic oxide NP aggregate geometry. Dose enhancement in proton

therapy was studied on the nanoscale in Chapter 4.

5.2 Dose Enhancement in X-ray Radiotherapy

Chapters 2 and 3 in this thesis presented investigations of the use of novel ceramic oxide NPs to improve the clinical outcome of conventional kilovoltage and megavoltage photon radiation therapy. The fundamental dose enhancement due to ceramic oxide NPs in terms of the dose to cells in an experimentally relevant configuration has been investigated in this project. The different physical interactions of several radiation therapy types with NPs has been modelled using Geant4 Monte Carlo simulations.

The results in Chapter 2 showed that gold NPs have a greater enhancement effect in the kV and MV photon fields, compared to the ceramic oxides studied. However, DERs due to the ceramic oxide NPs were shown to be significant compared to the well known radiation enhancing material, gold, on the micron scale in a cell model with incident photon fields. Of particular interest from this chapter are the results showing that the radio-protector CeO_2 NP also has significant dose enhancement properties. The gold NP showed a total DER in the 125 kVp photon field of (2.34 $\pm$ 0.01) followed by the Bi_2O_3 NPs with a calculated DER of (2.18 $\pm$ 0.01). This compares to total DER of (1.90 $\pm$ 0.01) and (1.74 $\pm$ 0.01) in the presence of Ta_2O_5 and CeO_2 NPs, respectively.

Results presented show the enhancing effect of ceramic oxide (and gold) NPs is greatest in the kilovoltage photon fields, compared to the megavoltage radiation field. Simulation results showed that beam energy has a large influence on the magnitude of dose enhancement, due to the increased photoelectron absorption probability at lower photon energies, present in kilovoltage radiation fields. The DER drops from around 2 in the kV photon fields to

close to 1 (i.e. no enhancement) with all NPs studied under MV photon irradiation. This is due to the difference in the photon attenuation cross-section at higher photon energies.

The first part of this study compares only the dose enhancement effect due to the effective Z of each NP and so does not take into account the vastly different distributions within cell populations that each NP will have in realistic experiments.

The different NPs studied have different uptake properties, different aggregate shape and behaviour. The detailed Monte Carlo studies presented in Chapter 3 show the importance of taking factors such as these into account when designing a simulation to model dose enhancement by NPs in radiation therapy. As discussed in Section 3.1, the shape of the NP aggregate was shown to be important when calculating dose enhancement. Results show that the platelet morphology of Bi_2O_3 NPs approximated in the cell array is the most efficient (per unit NP mass) radiation enhancer in the 125 kVp and 10 MV photon radiation fields. When DER was scaled to the mass of the NP, the simulations showed that the plate geometry (with a higher surface area to volume ratio) has increased efficiency of enhancement per unit of NP mass. The total DER_w in the 125 kVp field was calculated to be $(5.34 \pm 0.02) \times 10^8$ /g compared to around 2.5×10^8 /g in the case of the cube or sphere shape. This effect is due to the variable surface area to volume ratio from different NP morphologies. An increased surface area to volume ratio increases the likelihood of electrons created within the bulk of the NP to be able to escape to the surface of the particle.

Section 3.2 in Chapter 3 presented results demonstrating the importance of careful modelling of NP distribution on the cellular level by comparison of dose enhancement in cell nuclei with NP distributed in shells compared to the more traditional method of modelling NP in a homogeneous solution. It is observed that the dose enhancement increased sharply with increasing shell thickness before reaching a plateau at 5 μm aggregate shell thickness.

This is due to the increasing influence of secondary electrons being reabsorbed within the NP shell and not contributing to dose deposition in the cell nucleus.

A high level of dose enhancement is observed in cell nuclei in close proximity to NP shells, compared to dose enhancement with an equivalent local homogeneous solution of NP in water. For example, the total DER in the cell array due to a 3 μm shell on the central cell nucleus was calculated to be (2.96 ± 0.01) compared to (2.18 ± 0.01) in the case of an equivalent homogeneous solution in the volume. This effect is local and shows a saturation in dose enhancement to cell nuclei with increasing shell thickness, resulting from increasing local concentration of NPs applied.

The studies reported in Chapter 3 show there is a large difference in the local effect when NP material is distributed in shells compared to solution and this work has been published in a peer-reviewed journal article (refer Appendix B). This detailed modelling can help to explain non-linear sensitisation enhancement observed in cell studies by showing a saturation of the physical dose enhancement for shells greater than a described thickness.

5.3 Proton Radiation Therapy

The dose enhancement in proton therapy due to NPs was investigated with nanoscale simulations of the track structure around high-Z NPs. The radial dose distributions with respect to NP type, NP size, and proton beam energy were calculated and compared on the nanometre scale using event-by-event Monte Carlo tracking code Geant4-DNA in Chapter 4.

Results showed that the dose is deposited predominantly very close to the primary proton track and enhancement effects are therefore highest here in the region close to the NP. More than 95% of dose was observed to be deposited within the first 300 nm of the NP surface.

The radial distribution of deposited dose drops off sharply beyond the NP surface. The dose is enhanced compared to water in the first 10 nm bin outside the NP by 45% for the Au, 32% for the Bi_2O_3, 29% for the Ta_2O_5 and 26% for the CeO_2 NPs. The results presented showed that for dose enhancement to be most effective in the goal of increasing the damage to the DNA, NPs must be located within the cell, in close proximity to cell nucleus, or within the cell nucleus.

By comparing the dose enhancement in three proton beam energies the simulation study did not demonstrate any dose enhancement advantage of placing NPs in the Bragg Peak region, compared to the higher proton energy. Therefore targeting tumour cells with radio-enhancing NPs is an important factor to increase impact on tumour control without causing additional damage to health tissues.

The gold NP demonstrates the highest dose enhancement due to the effect of proton stopping power in the NP material. The simulations showed a total dose enhancement of (28 $\pm$ 2)% from the Au NP, (17.9 $\pm$ 0.2)% from the Bi_2O_3 NP, (16.6 $\pm$ 0.6)% from the Ta_2O_5 NP, and (15 $\pm$ 1)% from the CeO_2 NP. Atomic deexcitation was shown in Chapter 4 to account for less than 1% of the dose enhancement in the calculation volume. This is increased to 5% within the first 30 nm of the NP surface due to the short range of the low energy atomic deexcitation electrons.

Results demonstrated the importance of the beam configuration and NP geometry in the design of a nanoscale simulation. The study presented in this thesis focused on the development of the Monte Carlo simulation to model directly incident protons on ceramic oxide and gold NPs. In reality the direct hit of a NP with a primary proton is unlikely to occur and so the modelling of secondary electrons incident on the NP to contribute to radiosensitisation would be an interesting area to investigate further.

The effect of the decay of plasmon excitations on the secondary electron yield originating from a carbon NP, due to an incident proton beam typical of the Bragg peak position in proton therapy was compared to Geant4 Monte Carlo simulation in Chapter 4. This work was performed in collaboration the MBN Research Center in Frankfurt, Germany and the Monte Carlo simulation study was developed as part of this PhD project. The results demonstrated an increase in the calculated secondary electron yield from a carbon NP, compared to liquid water however significant very low energy electron production in a carbon-NP is not currently modelled in Geant4. The results of this collaborative work showed the potential for proton therapy to be enhanced by carbon NPs as well as the potential importance of low energy electron contributions from NPs which are not currently modelled in the Geant4 Monte Carlo code.

5.4 Future Work

Several Monte Carlo simulation studies in this PhD project have demonstrated the physical dose enhancement mechanism of ceramic oxide NPs in different radiation therapy modalities.

The ongoing adaptation of the Monte Carlo simulations developed during this PhD project has allowed the investigation of dose enhancement by NPs in a wider range of specialised radiation therapy techniques, for example the case of Microbeam Radiation Therapy [42]. The careful modelling of NP distributions within cell populations and within tumour tissue has been shown to be significant and important for the calculation of physical dose enhancement on the level of the cell and DNA. This work is ongoing.

Future work in this project will require the extension of the Monte Carlo simulations to also

describe chemical products and their diffusion on the nanoscale [92, 115]. The diffusion of radiolytic products will be important when NPs are internalised by cells and/or cell nucleus. These processes have been shown experimentally [66] to play a significant role in the enhancement of DNA damage and cell killing in radiation therapy. The latest releases of Geant4 include the low energy extension - Geant4-DNA, which now also has the capability to model the physico-chemistry of nanoscale processes and the incorporation of these models into the simulation developed in this thesis is an important next step to further develop this work.

In addition to the modelling of these chemical products of radiation interactions, the radiobiological behaviour of cancer cells with the application of ceramic oxide NPs, and the connection between dose delivered, dose enhancement, and cell survival curves will be an important avenue of further research.

Hadronic interactions should also be included in the simulation physics models to evaluate the effect of these interactions and improve the modelling of enhancement of dose by NPs.

The continual evolution of the Geant4 simulation toolkit will mean there will be increasingly detailed and accurate physics models becoming available for applications in nanoparticle enhanced radiation therapy. As improvements and extensions are released the work presented in this thesis can be further refined in some cases to include superior modelling of the low energy interactions in high-Z materials such as gold, and ceramic oxides, as well as the extension to include chemical products of water radiolysis processes.

References

[1] M. A. Śmiałek, P. Limão Vieira, N. J. Mason, and A. V. Solov'yov, "Radiation damage of biomolecular systems: Nano-scale insights into ion-beam cancer therapy. 2nd Nano-IBCT conference," *The European Physical Journal D*, vol. 68, no. 10, pp. 1–2, 2014.

[2] B. W. Stewart and C. Wild, *World Cancer Report 2014*. Lyon, France : International Agency for Research on Cancer, 2014., 2014.

[3] G. Delaney, S. Jacob, C. Featherstone, and M. Barton, "The role of radiotherapy in cancer treatment: estimating optimal utilization from a review of evidence-based clinical guidelines," *Cancer*, vol. 104, no. 6, pp. 1129–1137, 2005.

[4] H. L. Byrne, W. Domanova, A. L. McNamara, S. Incerti, and Z. Kuncic, "The cytoplasm as a radiation target: an in silico study of microbeam cell irradiation," *Physics in Medicine and Biology*, vol. 60, no. 6, p. 2325, 2015.

[5] G.-Y. Liou and P. Storz, "Reactive oxygen species in cancer," *Free radical research*, vol. 44, no. 5, pp. 479–479, 2010.

[6] B. Halliwell and J. M. C. Gutteridge, *Free radicals in biology and medicine*. Oxford: Oxford University Press, 2007.

[7] H. Nikjoo, P. O'Neill, M. Terrissol, and D. T. Goodhead, "Quantitative modelling of

DNA damage using Monte Carlo track structure method," *Radiation and Environmental Biophysics*, vol. 38, no. 1, pp. 31–38, 1999.

[8] R. Baskar, K. A. Lee, R. Yeo, and K.-W. Yeoh, "Cancer and radiation therapy: Current advances and future directions," *International Journal of Medical Sciences*, vol. 9, no. 3, pp. 193–199, 2012.

[9] R. Hanai, M. Yazu, and K. Hieda, "On the experimental distinction between ssbs and dsbs in circular DNA," *International Journal of Radiation Biology*, vol. 73, no. 5, pp. 475–479, 1998.

[10] R. Kanaar, J. H. J. Hoeijmakers, and D. C. van Gent, "Molecular mechanisms of DNA double-strand break repair," *Trends in Cell Biology*, vol. 8, no. 12, pp. 483–489, 1998.

[11] D. Séhédic, A. Cikankowitz, F. Hindré, F. Davodeau, and E. Garcion, "Feature review: Nanomedicine to overcome radioresistance in glioblastoma stem-like cells and surviving clones," *Trends in Pharmacological Sciences*, vol. 36, pp. 236–252, 2015.

[12] C. Adamson, O. O. Kanu, A. I. Mehta, C. Di, N. Lin, A. K. Mattox, and D. D. Bigner, "Glioblastoma multiforme: a review of where we have been and where we are going," *Expert Opinion on Investigational Drugs*, vol. 18, no. 8, pp. 1061–1083, 2009.

[13] SAHMRI, "Australian Bragg Centre for Proton Therapy and Research: first patients to be treated by 2020," 3 November 2017. https://www.medianet.com.au/releases/147152/

[14] SAHMRI, "Proton therapy and research," 2017. www.australianbraggcentre.com/#clinical_care

[15] P. Metcalfe, T. Kron, and P. Hoban, *The physics of radiotherapy x-rays from linear accelerators*. Madison, Wis. : Medical Physics Pub., c1997., 1997.

[16] W. P. Levin, H. Kooy, J. S. Loeffler, and T. F. DeLaney, "Proton beam therapy," *Br J Cancer*, vol. 93, no. 8, pp. 849–854, 2005.

[17] D. S. Gridley, R. S. Grover, L. N. Loredo, A. J. Wroe, and J. D. Slater, "Proton-beam therapy for tumors of the CNS," *Expert Review of Neurotherapeutics*, vol. 10, no. 2, pp. 319–330, 2010.

[18] H. Paganetti, "Nuclear interactions in proton therapy: dose and relative biological effect distributions originating from primary and secondary particles," *Physics in Medicine and Biology*, vol. 47, no. 5, pp. 747–764, 2002.

[19] F. H. Attix, *Introduction to Radiological Physics and Radiation Dosimetry*. Wiley-VCH Verlag GmbH, 2004.

[20] A. Briggs, S. Corde, S. Oktaria, R. Brown, A. Rosenfeld, M. Lerch, K. Konstantinov, and M. Tehei, "Cerium oxide nanoparticles: influence of the high-Z component revealed on radioresistant 9L cell survival under X-ray irradiation," *Nanomedicine-Nanotechnology Biology and Medicine*, vol. 9, no. 7, pp. 1098–1105, 2013.

[21] S. Jain, J. A. Coulter, A. R. Hounsell, K. T. Butterworth, S. J. McMahon *et al.*, "Cell-specific radiosensitization by gold nanoparticles at megavoltage radiation energies," *International Journal of Radiation Oncology*Biology*Physics*, vol. 79, no. 2, pp. 531–539, 2011.

[22] R. Brown, M. Tehei, S. Oktaria, A. Briggs, C. Stewart, K. Konstantinov, A. Rosenfeld, S. Corde, and M. Lerch, "High-Z nanostructured ceramics in radiotherapy: First evidence of Ta_2O_5-induced dose enhancement on radioresistant cancer cells in an MV photon field," *Particle and Particle Systems Characterization*, 2013.

[23] M. Alqathami, A. Blencowe, U. J. Yeo, R. Franich, S. Doran, G. Qiao, and M. Geso, "Enhancement of radiation effects by bismuth oxide nanoparticles for kilovoltage x-

ray beams: A dosimetric study using a novel multi-compartment 3D radiochromic dosimeter," *Journal of Physics: Conference Series*, vol. 444, no. 1, p. 012025, 2013.

[24] M. Douglass, E. Bezak, and S. Penfold, "Monte Carlo investigation of the increased radiation deposition due to gold nanoparticles using kilovoltage and megavoltage photons in a 3D randomized cell model," *Medical Physics*, vol. 40, no. 7, pp. –, 2013.

[25] P. Zygmanski, P. Tsiamas, W. Hoegele, F. Cifter, W. Ngwa, R. Berbeco, M. Makrigiorgos, and E. Sajo, "A stochastic model of cell survival for high-Z nanoparticle radiotherapy," *Medical Physics*, vol. 40, no. 2, 2013.

[26] M. Berger, J. Hubbell, S. Seltzer, J. Chang, J. Coursey, R. Sukumar, D. Zucker, and K. Olsen, "XCOM: Photon cross section database (version 1.5). [online]," 2010. http://physics.nist.gov/xcom

[27] D. Poole, "X-ray absorption edges, characteristic x-ray lines and fluorescence yields," 2017. http://www.kayelaby.npl.co.uk/atomic_and_nuclear_physics/4_2/4_2_1.html

[28] D. E. Groom and S. R. Klein, "Passage of particles through matter," *European Physical Journal C - Particles and Fields*, vol. 15, no. 1-4, pp. 163–173, 2000.

[29] E. B. Podgorsak, "Radiation physics for medical physicists," 2010.

[30] C.-J. Liu, C.-H. Wang, S.-T. Chen, H.-H. Chen, W.-H. Leng *et al.*, "Enhancement of cell radiation sensitivity by pegylated gold nanoparticles," *Physics in Medicine and Biology*, vol. 55, no. 4, p. 931, 2010.

[31] J. C. Polf, L. F. Bronk, W. H. P. Driessen, W. Arap, R. Pasqualini, and M. Gillin, "Enhanced relative biological effectiveness of proton radiotherapy in tumor cells with internalized gold nanoparticles," *Applied Physics Letters*, vol. 98, no. 19, 2011.

[32] R. Brown, S. Corde, S. Oktaria, K. Konstantinov, A. Rosenfeld, M. Lerch, and M. Tehei, "Nanostructures, concentrations and energies: an ideal equation to extend therapeutic efficiency on radioresistant 9L tumor cells using ceramic nanostructured particles," *Biomedical Physics & Engineering Express*, vol. 3, no. 1, p. 1, 2017.

[33] C. Stewart, S. Corde, A. Rosenfeld, M. Tehei, K. Konstantinov *et al.*, "Engineering of bismuth oxide nanoparticles to induce differential biochemical activity in malignant and nonmalignant cells," *Particle & Particle Systems Characterization*, vol. 31, no. 9, pp. 960–964, 2014.

[34] C. Stewart, K. Konstantinov, S. McKinnon, S. Guatelli, M. Lerch, A. Rosenfeld, M. Tehei, and S. Corde, "First proof of bismuth oxide nanoparticles as efficient radiosensitisers on highly radioresistant cancer cells," *Physica Medica*, vol. 32, no. 11, pp. 1444–1452, 2016.

[35] K. Bogusz, M. Tehei, C. Stewart, M. McDonald, D. Cardillo, M. Lerch, S. Corde, A. Rosenfeld, H. K. Liu, and K. Konstantinov, "Synthesis of potential theranostic system consisting of methotrexate-immobilized (3-aminopropyl)trimethoxysilane coated α-Bi_2O_3 nanoparticles for cancer treatment," *RSC Advances*, vol. 4, no. 46, pp. 24 412–24 419, 2014.

[36] J. Colon, L. Herrera, J. Smith, S. Patil, C. Komanski, P. Kupelian, S. Seal, D. W. Jenkins, and C. H. Baker, "Protection from radiation-induced pneumonitis using cerium oxide nanoparticles," *Nanomedicine: Nanotechnology, Biology, and Medicine*, vol. 5, no. 2, pp. 225–231, 2009.

[37] R. W. Tarnuzzer, J. Colon, S. Patil, and S. Seal, "Vacancy engineered ceria nanostructures for protection from radiation-induced cellular damage," *NANO LETTERS*, vol. 5, no. 12, pp. 2573–2577, 2005.

[38] D. J. Grdina, J. S. Murley, and Y. Kataoka, "Radioprotectants: Current status and new directions," *Oncology*, vol. 63, no. 2, pp. 2–10, 2002.

[39] D. B. Chithrani, S. Jelveh, F. Jalali, M. Van Prooijen, C. Allen, R. G. Bristow, R. P. Hill, and D. A. Jaffray, "Gold nanoparticles as radiation sensitizers in cancer therapy," *Radiation Research*, vol. 173, no. 6, pp. 719–728, 2010.

[40] S. J. McMahon, W. B. Hyland, M. F. Muir, J. A. Coulter, S. Jain *et al.*, "Biological consequences of nanoscale energy deposition near irradiated heavy atom nanoparticles," *Scientific Reports*, vol. 1, 2011.

[41] S. J. McMahon, W. B. Hyland, M. F. Muir, J. A. Coulter, S. Jain *et al.*, "Nanodosimetric effects of gold nanoparticles in megavoltage radiation therapy," *Radiotherapy and Oncology*, vol. 100, no. 3, pp. 412–416, 2011.

[42] E. Engels, S. Corde, S. McKinnon, S. Incerti, K. Konstantinov, A. Rosenfeld, M. Tehei, M. Lerch, and S. Guatelli, "Optimizing dose enhancement with Ta_2O_5 nanoparticles for synchrotron microbeam activated radiation therapy," *Physica Medica*, vol. 32, no. 12, pp. 1852–1861, 2016.

[43] L. Smith, Z. Kuncic, K. K. Ostrikov, and S. Kumar, "Nanoparticles in cancer imaging and therapy," *Journal of Nanomaterials*, vol. 2012, p. 7, 2012.

[44] J. F. Hainfeld, D. N. Slatkin, and H. M. Smilowitz, "The use of gold nanoparticles to enhance radiotherapy in mice," *Physics in Medicine and Biology*, vol. 49, no. 18, pp. N309–N315, 2004.

[45] Y. Zheng and L. Sanche, "Gold nanoparticles enhance DNA damage induced by anticancer drugs and radiation," *Radiation Research*, vol. 172, no. 1, pp. 114–119, 2009.

[46] W. N. Rahman, N. Bishara, T. Ackerly, C. F. He, P. Jackson, C. Wong, R. Davidson, and M. Geso, "Enhancement of radiation effects by gold nanoparticles for superficial

radiation therapy," *Nanomedicine: Nanotechnology, Biology, and Medicine*, vol. 5, no. 2, pp. 136–142, 2009.

[47] K. T. Butterworth, J. A. Coulter, S. Jain, J. Forker, S. J. McMahon, G. Schettino, K. M. Prise, F. J. Currell, and D. G. Hirst, "Evaluation of cytotoxicity and radiation enhancement using 1.9 nm gold particles: potential application for cancer therapy," *Nanotechnology*, vol. 21, no. 29, p. 295101, 2010.

[48] J. Turkevich, P. C. Stevenson, and J. Hillier, "A study of the nucleation and growth processes in the synthesis of colloidal gold," *Discussions of the Faraday Society*, vol. 11, no. 0, pp. 55–75, 1951.

[49] E. Brun, L. Sanche, and C. Sicard-Roselli, "Parameters governing gold nanoparticle X-ray radiosensitization of DNA in solution," *Colloids and Surfaces B-Biointerfaces*, vol. 72, no. 1, pp. 128–134, 2009.

[50] S. K. Libutti, G. F. Paciotti, A. A. Byrnes, J. Alexander, H. R., W. E. Gannon, M. Walker, G. D. Seidel, N. Yuldasheva, and L. Tamarkin, "Phase I and pharmacokinetic studies of CYT-6091, a novel PEGylated colloidal gold-rhTNF nanomedicine," *Clin Cancer Res*, vol. 16, no. 24, pp. 6139–49, 2010.

[51] E. Porcel, K. Kobayashi, N. Usami, H. Remita, C. Le Sech, and S. Lacombe, "Photosensitization of plasmid-dna loaded with platinum nano-particles and irradiated by low energy x-rays," *Journal of Physics Conference Series: Cost Chemistry CM0603-Melusyn Joint Meeting:*, vol. 261, no. 012004, 2011.

[52] S. Khoei, S. R. Mahdavi, H. Fakhimikabir, A. Shakeri-Zadeh, and A. Hashemian, "The role of iron oxide nanoparticles in the radiosensitization of human prostate carcinoma cell line DU145 at megavoltage radiation energies," *International Journal Of Radiation Biology*, vol. 90, no. 5, pp. 351–356, 2014.

[53] E. Porcel, S. Lacombe, O. Tillement, F. Lux, P. Mowat, N. Usami, K. Kobayashi, Y. Furusawa, C. Le Sech, and S. Li, "Gadolinium-based nanoparticles to improve the hadrontherapy performances," *Nanomedicine: Nanotechnology, Biology and Medicine*, vol. 10, no. 8, pp. 1601–1608, 2014.

[54] L. Sancey, C. Rodriguez-Lafrasse, M. Janier, M. Dutreix, M. Barberi-Heyob *et al.*, "The use of theranostic gadolinium-based nanoprobes to improve radiotherapy efficacy," *The British Journal of Radiology*, vol. 87, no. 20140134, 2014.

[55] S.-J. Seo, S.-M. Han, J.-H. Cho, K. Hyodo, A. Zaboronok, H. You, K. Peach, M. Hill, and J.-K. Kim, "Enhanced production of reactive oxygen species by gadolinium oxide nanoparticles under core–inner-shell excitation by proton or monochromatic x-ray irradiation: implication of the contribution from the interatomic de-excitation-mediated nanoradiator effect to dose enhancement," *Radiation and Environmental Biophysics*, pp. 1–9, 2015.

[56] G. Le Duc, F. Lux, T. Epicier, P. Perriat, S. Roux *et al.*, "Toward an image-guided microbeam radiation therapy using gadolinium-based nanoparticles," *ACS nano*, vol. 5, no. 12, pp. 9566–9574, 2011.

[57] Y. Jiang, N. Lin, S. Huang, C. Lin, N. Jin, Z. Zhang, J. Ke, Y. Yu, J. Zhu, and Y. Wang, "Tracking nonpalpable breast cancer for breast-conserving surgery with carbon nanoparticles: Implication in tumor location and lymph node dissection," *Medicine*, vol. 94, no. 10, p. e605, 2015.

[58] K. Andrius, R. Sandra, S. Sushant, S. Ya-Ping, and J. Petras, "Carbon-core silver-shell nanodots as sensitizers for phototherapy and radiotherapy," *Nanotechnology*, vol. 24, no. 32, p. 325103, 2013.

[59] J. I. Shin, I. Cho, S. Cho, E. H. Kim, Y. Song *et al.*, "Simulation study of dose

enhancement in a cell due to nearby carbon and oxygen in particle radiotherapy," *Journal of the Korean Physical Society*, vol. 67, no. 1, pp. 209–217, 2015.

[60] W. Jiang, B. Y. S. Kim, J. T. Rutka, and W. C. W. Chan, "Nanoparticle-mediated cellular response is size-dependent," *Nature Nanotechnology*, vol. 3, no. 3, pp. 145–150, 2008.

[61] J. K. Kim, S. J. Seo, H. T. Kim, K. H. Kim, M. H. Chung, K. R. Kim, and S. J. Ye, "Enhanced proton treatment in mouse tumors through proton irradiated nanoradiator effects on metallic nanoparticles," *Physics in Medicine and Biology*, vol. 57, no. 24, pp. 8309–8323, 2012.

[62] G. R. Souza, D. R. Christianson, F. I. Staquicini, M. G. Ozawa, E. Y. Snyder, R. L. Sidman, J. H. Miller, W. Arap, and R. Pasqualini, "Networks of gold nanoparticles and bacteriophage as biological sensors and cell-targeting agents," *Proceedings of the National Academy of Sciences*, vol. 103, no. 5, pp. 1215–1220, 2006.

[63] J. K. Kim, S. J. Seo, K. H. Kim, T. J. Kim, M. H. Chung, K. R. Kim, and T. K. Yang, "Therapeutic application of metallic nanoparticles combined with particle-induced x-ray emission effect," *Nanotechnology*, vol. 21, no. 42, 2010.

[64] G. Dollinger, "Comment on 'Therapeutic application of metallic nanoparticles combined with particle-induced x-ray emission effect'," *Nanotechnology*, vol. 22, no. 24, 2011.

[65] C. Le Sech, K. Kobayashi, N. Usami, Y. Furusawa, E. Porcel, and S. Lacombe, "Comment on 'Therapeutic application of metallic nanoparticles combined with particle-induced x-ray emission effect'," *Nanotechnology*, vol. 23, no. 7, 2012.

[66] E. Porcel, S. Li, N. Usami, H. Remita, Y. Furusawa, K. Kobayashi, C. Le Sech, and

S. Lacombe, "Nano-sensitization under gamma rays and fast ion radiation," *Journal of Physics Conference Series*, vol. 373, no. 1, 2012.

[67] J. Allison, K. Amako, J. Apostolakis, H. Araujo, P. A. Dubois *et al.*, "Geant4 developments and applications," *Nuclear Science, IEEE Transactions on*, vol. 53, no. 1, pp. 270–278, 2006.

[68] S. Agostinelli, J. Allison, K. Amako, J. Apostolakis, H. Araujo *et al.*, "Geant4-a simulation toolkit," *Nuclear Instruments and Methods in Physics Research Section A: Accelerators, Spectrometers, Detectors and Associated Equipment*, vol. 506, no. 3, pp. 250–303, 2003.

[69] J. Allison, K. Amako, J. Apostolakis, P. Arce, M. Asai *et al.*, "Recent developments in Geant4," *Nuclear Inst. and Methods in Physics Research, A*, 2016.

[70] "Physics Reference Manual," 2012. http://geant4.web.cern.ch/geant4/UserDocumentation/UsersGuides/PhysicsReferenceManual/BackupVersions/V9.6/fo/PhysicsReferenceManual.pdf

[71] E. W. Larsen, "A theoretical derivation of the Condensed History Algorithm," *Annals of Nuclear Energy*, vol. 19, no. 10-12, pp. 701–714, 1992.

[72] M. J. Berger, "Monte Carlo calculation of the penetration and diffusion of fast charged particles," *Methods in Computational Physics*, vol. 1, pp. 135–215, 1963.

[73] S. Chauvie, Z. Francis, S. Guatelli, S. Incerti, B. Mascialino, P. Moretto, P. Nieminen, and M. G. Pia, "Geant4 physics processes for microdosimetry simulation: Design foundation and implementation of the first set of models," *IEEE Transactions on Nuclear Science*, vol. 54, no. 6, pp. 2619–2628, 2007.

[74] H. Paganetti and M. Goitein, "Biophysical modelling of proton radiation effects based

on amorphous track models," *International Journal of Radiation Biology*, vol. 77, no. 9, pp. 911–928, 2001.

[75] M. Scholz and G. Kraft, "Track structure and the calculation of biological effects of heavy charged particles," *Advances in Space Research*, vol. 18, no. 1-2, pp. 5–14, 1996.

[76] F. A. Cucinotta, H. Nikjoo, and D. T. Goodhead, "Applications of amorphous track models in radiation biology," *Radiat Environ Biophys*, vol. 38, no. 2, pp. 81–92, 1999.

[77] B. L. Jones, S. Krishnan, and S. H. Cho, "Estimation of microscopic dose enhancement factor around gold nanoparticles by Monte Carlo calculations," *Medical Physics*, vol. 37, no. 7, pp. 3809–3816, 2010.

[78] E. Lechtman, N. Chattopadhyay, Z. Cai, S. Mashouf, R. Reilly, and J. P. Pignol, "Implications on clinical scenario of gold nanoparticle radiosensitization in regards to photon energy, nanoparticle size, concentration and location," *Physics in Medicine and Biology*, vol. 56, no. 15, pp. 4631–4647, 2011.

[79] I. Martínez-Rovira and Y. Prezado, "Monte Carlo dose enhancement studies in microbeam radiation therapy," *Medical Physics*, vol. 38, no. 7, pp. 4430–4439, 2011.

[80] J. C. L. Chow, M. K. K. Leung, S. Fahey, D. B. Chithrani, and D. A. Jaffray, "Monte Carlo simulation on low-energy electrons from gold nanoparticle in radiotherapy," *Journal of Physics: Conference Series*, vol. 341, no. 1, 2012.

[81] S. Jain, D. G. Hirst, and J. M. O'Sullivan, "Gold nanoparticles as novel agents for cancer therapy," *British Journal of Radiology*, vol. 85, no. 1010, pp. 101–113, 2012.

[82] C. Wälzlein, E. Scifoni, M. Krämer, and M. Durante, "Simulations of dose enhancement for heavy atom nanoparticles irradiated by protons," *Physics in Medicine and Biology*, vol. 59, no. 6, pp. 1441–1458, 2014.

[83] Y. Lin, S. J. McMahon, M. Scarpelli, H. Paganetti, and J. Schuemann, "Comparing gold nano-particle enhanced radiotherapy with protons, megavoltage photons and kilovoltage photons: a Monte Carlo simulation," *Physics in Medicine and Biology*, vol. 59, no. 24, p. 7675, 2014.

[84] A. Yahya Abadi, M. Ghorbani, A. A. Mowlavi, and C. Knaup, "A Monte Carlo evaluation of dose enhancement by cisplatin and titanocene dichloride chemotherapy drugs in brachytherapy with photon emitting sources," *Australasian Physical and Engineering Sciences in Medicine*, vol. 37, no. 2, pp. 327–336, 2014.

[85] P. Zygmanski, B. Liu, P. Tsiamas, F. Cifter, M. Petersheim, J. Hesser, and E. Sajo, "Dependence of Monte Carlo microdosimetric computations on the simulation geometry of gold nanoparticles," *Physics in Medicine and Biology*, vol. 58, no. 22, pp. 7961–7977, 2013.

[86] V. A. Semenenko, J. E. Turner, and T. B. Borak, "NOREC, a Monte Carlo code for simulating electron tracks in liquid water," *Radiat Environ Biophys*, vol. 42, no. 3, pp. 213–7, 2003.

[87] M. Scholz and T. Elsässer, "Biophysical models in ion beam radiotherapy," *Advances in Space Research*, vol. 40, no. 9, pp. 1381–1391, 2007.

[88] E. Delage, Q. T. Pham, M. Karamitros, H. Payno, V. Stepan, S. Incerti, L. Maigne, and Y. Perrot, "PDB4DNA: Implementation of DNA geometry from the Protein Data Bank (PDB) description for Geant4-DNA Monte-Carlo simulations," *Computer Physics Communications*, vol. 192, pp. 282–288, 2015.

[89] S. Incerti, G. Baldacchino, M. Bernal, R. Capra, C. Champion *et al.*, "The Geant4-DNA Project," *International Journal of Modeling, Simulation, and Scientific Computing*, vol. 1, no. 2, pp. 157–178, 2010.

[90] R. D. Stewart, W. E. Wilson, J. C. McDonald, and D. J. Strom, "Microdosimetric properties of ionizing electrons in water: a test of the PENELOPE code system," *Physics in Medicine and Biology*, vol. 47, no. 1, p. 79, 2002.

[91] J. Sempau, J. M. Fernández-Varea, E. Acosta, and F. Salvat, "Experimental benchmarks of the Monte Carlo code PENELOPE," *Nuclear Inst. and Methods in Physics Research, B*, vol. 207, no. 2, pp. 107–123, 2003.

[92] M. A. Bernal, M. C. Bordage, J. M. C. Brown, M. Davídková, E. Delage *et al.*, "Track structure modeling in liquid water: A review of the Geant4-DNA very low energy extension of the Geant4 Monte Carlo simulation toolkit," *Physica Medica*, vol. 31, no. 8, pp. 861–874, 2015.

[93] S. Incerti, A. Ivanchenko, M. Karamitros, A. Mantero, P. Moretto *et al.*, "Comparison of GEANT4 very low energy cross section models with experimental data in water," *Medical Physics*, vol. 37, no. 9, pp. 4692–4708, 2010.

[94] "The Geant4-DNA Project." http://geant4-dna.org

[95] S. Incerti, B. Suerfu, J. Xu, V. Ivantchenko, A. Mantero, J. M. C. Brown, M. A. Bernal, Z. Francis, M. Karamitros, and H. N. Tran, "Simulation of Auger electron emission from nanometer-size gold targets using the Geant4 Monte Carlo simulation toolkit," *Nuclear Instruments and Methods in Physics Research Section B: Beam Interactions with Materials and Atoms*, vol. 372, pp. 91–101, 2016.

[96] S. Incerti, M. Psaltaki, P. Gillet, P. Barberet, M. Bardiees *et al.*, "Simulating radial dose of ion tracks in liquid water simulated with Geant4-DNA: A comparative study," *Nuclear Instruments & Methods in Physics Research Section B-Beam Interactions with Materials and Atoms*, vol. 333, pp. 92–98, 2014.

[97] H. L. Byrne, A. L. McNamara, W. Domanova, S. Guatelli, and Z. Kuncic, "Radiation damage on sub-cellular scales: beyond DNA," *PHYSICS IN MEDICINE AND BIOLOGY*, vol. 58, no. 5, pp. 1251–1267, 2013.

[98] A. L. McNamara, S. Guatelli, D. A. Prokopovich, M. I. Reinhard, and A. B. Rosenfeld, "A comparison of X-ray and proton beam low energy secondary electron track structures using the low energy models of Geant4," *International journal of radiation biology*, vol. 88, no. 1-2, pp. 164–170, 2012.

[99] P. Lazarakis, M. U. Bug, E. Gargioni, S. Guatelli, S. Incerti, H. Rabus, and A. B. Rosenfeld, "Effect of a static magnetic field on nanodosimetric quantities in a DNA volume," *International journal of radiation biology*, vol. 88, no. 1-2, pp. 183–188, 2012.

[100] P. Lazarakis, M. U. Bug, E. Gargioni, S. Guatelli, H. Rabus, and A. B. Rosenfeld, "Comparison of nanodosimetric parameters of track structure calculated by the Monte Carlo codes Geant4-DNA and PTra," *Physics in Medicine and Biology*, vol. 57, no. 5, pp. 1231–1250, 2012.

[101] A. Verkhovtsev, S. McKinnon, P. de Vera, E. Surdutovich, S. Guatelli, A. V. Korol, A. Rosenfeld, and A. V. Solov'yov, "Comparative analysis of the secondary electron yield from carbon nanoparticles and pure water medium," *The European Physical Journal D*, vol. 69, no. 4, pp. 1–9, 2015.

[102] P. Lazarakis, S. Corde, A. B. Rosenfeld, M. Lerch, M. Tehei, S. Guatelli, S. Incerti, V. Ivanchenko, I. Kyriakou, and D. Emfietzoglou, "Investigation of track structure and condensed history physics models for applications in radiation dosimetry on a micro and nano scale in geant4," *Biomedical Physics and Engineering Express*, vol. 4, no. 2, 2018.

[103] S. Chauvie, S. Guatelli, V. Ivanchenko, F. Longo, A. Mantero *et al.*, "Geant4 low energy electromagnetic physics," in *Nuclear Science Symposium Conference Record, 2004 IEEE*, vol. 3, 2004, Conference Proceedings, pp. 1881–1885 Vol. 3.

[104] J. E. Lye, D. J. Butler, G. Ramanathan, and R. D. Franich, "Spectral differences in 6 MV beams with matched PDDs and the effect on chamber response," *Physics in Medicine and Biology*, vol. 57, no. 22, pp. 7599–7614, 2012.

[105] G. Poludniowski, G. Landry, F. DeBlois, P. M. Evans, and F. Verhaegen, "SpekCalc: a program to calculate photon spectra from tungsten anode x-ray tubes," *Physics in Medicine and Biology*, vol. 54, no. 19, pp. N433–N438, 2009.

[106] M. J. Berger, J. S. Coursey, M. A. Zucker, and J. Chang, "ESTAR, PSTAR, and ASTAR: Computer programs for calculating stopping-power and range tables for electrons, protons, and helium ions (version 1.2.3)," 2005. http://physics.nist.gov/Star

[107] "Centre for Medical Radiation Physics (CMRP)," 2018. https://eis.uow.edu.au/cmrp/index.html

[108] "IHMRI: Our research," 2018. www.ihmri.org.au/our-research/

[109] S. McKinnon, E. Engels, M. Tehei, K. Konstantinov, S. Corde, S. Oktaria, S. Incerti, M. Lerch, A. Rosenfeld, and S. Guatelli, "Study of the effect of ceramic Ta_2O_5 nanoparticle distribution on cellular dose enhancement in a kilovoltage photon field," *Physica Medica*, vol. 32, no. 10, pp. 1216–1224, 2016.

[110] M. Tubiana, J. Dutreix, and A. Wambersie, *Introduction to Radiobiology*. London, New York, Philadelphia: Taylor & Francis, 1990.

[111] H. Paganetti, *Proton Therapy Physics*, ser. Series in Medical Physics and Biomedical Engineering. Boca Raton: CRC, 2012.

[112] A. V. Verkhovtsev, A. V. Korol, and A. V. Solov'yov, "Revealing the mechanism of the low-energy electron yield enhancement from sensitizing nanoparticles," *Physical Review Letters*, vol. 114, no. 6, p. 063401, 2015.

[113] E. Scifoni, E. Surdutovich, and A. V. Solov'yov, "Spectra of secondary electrons generated in water by energetic ions," *Physical Review E*, vol. 81, no. 2, 2010.

[114] P. De Vera, R. Garcia-Molina, I. Abril, and A. V. Solov'Yov, "Semiempirical model for the ion impact ionization of complex biological media," *Physical Review Letters*, vol. 110, no. 14, 2013.

[115] M. Karamitros, S. Luan, M. A. Bernal, J. Allison, G. Baldacchino *et al.*, "Diffusion-controlled reactions modeling in Geant4-DNA," *Journal of Computational Physics*, vol. 274, no. 0, pp. 841–882, 2014.

[116] H. N. Tran, M. Karamitros, V. N. Ivanchenko, S. Guatelli, S. McKinnon *et al.*, "Geant4 Monte Carlo simulation of absorbed dose and radiolysis yields enhancement from a gold nanoparticle under MeV proton irradiation," *Nuclear Instruments and Methods in Physics Research Section B: Beam Interactions with Materials and Atoms*, vol. 373, pp. 126–139, 2016.

[117] S. McKinnon, S. Guatelli, S. Incerti, V. Ivanchenko, M. Tehei, M. Lerch, S. Corde, K. Konstantinov, and A. Rosenfeld, "Local dose enhancement of proton therapy by ceramic oxide nanoparticles investigated with geant4 simulations," *Physica Medica*, vol. 32, no. 12, pp. 1584–1593, 2016.

Appendices

Appendix A

The following published article [34] includes work done in collaboration with UoW research student Callum Stewart. My role in this project was the design and development of the Monte Carlo simulation study which complemented the experimental findings of the co-authors. All Monte Carlo simulations in this paper were performed by me, under the supervision of my principle supervisor, Dr Susanna Guatelli. The paper is derived from work presented in Chapter 3, Section 3.1 of this thesis.

Callum Stewart, Konstantin Konstantinov, Sally McKinnon, Susanna Guatelli, Michael Lerch, Anatoly Rosenfeld, Moeava Tehei, and Stéphanie Corde (2016) "First proof of bismuth oxide nanoparticles as efficient radiosensitisers on highly radioresistant cancer cells" *Physica Medica* 32(11): 1444-52.

Physica Medica 32 (2016) 1444–1452

Contents lists available at ScienceDirect

Physica Medica

journal homepage: http://www.physicamedica.com

Original paper

First proof of bismuth oxide nanoparticles as efficient radiosensitisers on highly radioresistant cancer cells

Callum Stewart [a,b,c], Konstantin Konstantinov [b,c], Sally McKinnon [d], Susanna Guatelli [c,d], Michael Lerch [c,d], Anatoly Rosenfeld [c,d], Moeava Tehei [c,d,*], Stéphanie Corde [c,d,e]

[a] School of Chemistry, University of Wollongong, Northfields Ave, NSW 2522, Australia
[b] Institute of Superconducting and Electronic Materials (ISEM), University of Wollongong, Squires Way, North Wollongong, NSW 2500, Australia
[c] Illawarra Health and Medical Research Institute (IHMRI), University of Wollongong, Northfields Ave, NSW 2522, Australia
[d] Centre of Medical and Radiation Physics (CMRP), University of Wollongong, Northfields Avenue, Wollongong, NSW 2522, Australia
[e] Radiation Oncology Department, Prince of Wales Hospital, Randwick, High Street, NSW 2031, Australia

ARTICLE INFO

Article history:
Received 29 May 2016
Received in Revised form 14 September 2016
Accepted 18 October 2016
Available online 27 October 2016

Keywords:
Bismuth oxide nanoparticles
Radiosensitisers
Dose enhancement
Monte Carlo simulation

ABSTRACT

This study provides the first proof of the novel application of bismuth oxide as a radiosensitiser. It was shown that on the highly radioresistant 9L gliosarcoma cell line, bismuth oxide nanoparticles sensitise to both kilovoltage (kVp) or megavoltage (MV) X-rays radiation. 9L cells were exposed to a concentration of 50 $\mu g.mL^{-1}$ of nanoparticle before irradiation at 125 kVp and 10 MV. Sensitisation enhancement ratios of 1.48 and 1.25 for 125 kVp and 10 MV were obtained *in vitro*, respectively. The radiation enhancement of the nanoparticles is postulated to be a combination of the high Z nature of the bismuth ($Z = 83$), and the surface chemistry. Monte Carlo simulations were performed to elucidate the physical interactions between the incident radiation and the nanoparticle. The results of this work show that Bi_2O_3 nanoparticles increase the radiosensitivity of 9L gliosarcoma tumour cells for both kVp and MV energies. Monte Carlo simulations demonstrate the advantage of a platelet morphology.

1. Introduction

External X-ray Radiation Therapy is a common treatment for many cancers, which has been used extensively for many years. Despite the improvement of this cancer modality [1,2], there are still unwanted side effects which need to be addressed [3].

One possible solution to improve the efficacy of X-ray radiotherapy exists in the use of metal nanoparticles (NPs) as individual radiosensitising agents. Investigations into gold NPs [4–7] and Platinum [8,9] NPs were performed to quantify the biocompatibility of the proposed nanomaterials. The metallic NPs were shown to be radioenhancing under kilovolt (kVp) and megavolt (MV) radiation fields, however, they presented two problems. First, there was no guarantee that these nanomaterials would be biocompatible on the nanoscale. Studies into pure metal NPs showed that the size and morphology of the nanoparticle often resulted in varying degrees of toxicity [10,11]. Metal NPs with diameters below 5 nm can freely diffuse into the nucleus and interact directly to DNA, resulting in necrosis [9,10]. Second, the metals used for radiosensitisation require a high atomic number (high Z), and are also heavy metals. It was shown that these NPs induced toxicity as the treatment concentrations increased.

To solve these two issues, high Z nanoceramics, such as the promising tantalum pentoxide Ta_2O_5 [12], have started to be investigated. The Ta_2O_5 nanoparticle aggregates demonstrated the required radiosensitisation provided by the heavy Ta metal, and also the necessary biocompatibility thanks to the oxide form.

Bismuth is a better candidate for high Z radiosensitiser research since it is one of the heaviest naturally occurring elements of the periodic table [13]. Bismuth oxide and other bismuth-based compounds are also known to be biocompatible [14]. They have been extensively used in many medical and cosmetic applications for many years [15]. In addition, Stewart et al. [16] showed that bismuth oxide nanoparticles could be tailored with different oxygen contents, inducing cell proliferation or toxicity. Another paper by Bogusz et al. [17] highlighted that a theranostic system based on bismuth oxide nanoparticles would be highly effective in the treatment of cancer.

This research is aimed to investigate the novel application of high Z bismuth oxide nanoparticles as radiosensitisers for cancer therapy. The bismuth oxide nanoparticles were synthesised and irradiated with clinical 125 kVp and 10 MV X-ray beams. The cell

* Corresponding author at: Centre of Medical Radiation Physics (CMRP), University of Wollongong, Northfields Avenue, Wollongong, NSW 2522, Australia.
E-mail address: moeava@uow.edu.au (M. Tehei).

http://dx.doi.org/10.1016/j.ejmp.2016.10.015
1120-1797/

clonogenic and internalisation assays were then performed. Monte Carlo simulations performed complemented the experimental work providing insight into the physical mechanisms behind dose enhancement and the effect of the particle morphology on these physical mechanisms.

2. Methods and materials

2.1. Experimental

2.1.1. Synthesis

The bismuth based compounds were fabricated at the Institute of Superconducting and Electronic Materials (ISEM). The biocompatible Bi_2O_3 nanoparticles were synthesised via the precipitation route [16,18]. Bismuth Nitrate (99.9%, Sigma-Aldrich, Australia) was dissolved in 70% Nitric acid (50–70% Merck, Australia), and then 30% Ammonium Hydroxide (Sigma Aldrich, Australia) was added in small increments until a white precipitate appeared. This was extracted using a centrifuge and washed with deionised (DI) water. The precipitate was transferred to a beaker of DI water and stirred continuously for 5.5 h at 100 °C. The precursor was extracted and washed as before then annealed under argon for 4 h in a tube furnace at 530 °C.

2.1.2. X-ray diffraction (XRD)

The Bi_2O_3 was examined using an Enhanced Mini-Materials Analyser (EMMA) X-ray Diffractometer at 40 kV and 25 mA. The X-ray diffractometer scanned between 20° and 80° at a step rate of 2.00°min^{-1} and step size of 0.02°. The mean crystalline size was determined using the Scherrer equation, while the material phase was extracted from the ICDD database using the Traces software [19,20].

2.1.3. Surface area

The surface area of the nanoparticles was examined using the methylene blue test due to negative effects induced by the drying process of Brunauer Emmet Teller (BET) gas adsorption surface area method. Bismuth oxide (100 mg) was dispersed in 50 mL deionised (DI) water and 12 mg of Methylene Blue (MB) added. After stirring and leaving overnight, a sample was taken from the stock and diluted accordingly for UV–vis analysis. The absorption at 665 nm of the MB solution was measured using a Shimatzu 3600 NIR UV–vis Spectrophotometer (Shimadzu, Kyoto, Japan). After examination, 4 mg of MB was added to the stock with 5 mL of DI. This was repeated for three days until the ideal concentration was determined. The concentrations were converted to weight ratios of the adsorbed MB: Bi_2O_3 and the added MB: Bi_2O_3. The ratio values were plotted against each other to produce the Langmuir curve and the ion replacement concentration point was used to determine the specific surface area (SSA) according to the following equation [21]:

$$SSA = \frac{m_{MB}}{319.87} . A_V \cdot A_{MB} \cdot \frac{1}{m_s} \quad (1)$$

where m_{MB} is the weight of MB added, 319.87 g.mol^{-1} is the MB molecular weight, A_V is Avogadro's number (6.023*10^{23} mol^{-1}), A_{MB} is the accepted surface area of a single adsorbed MB molecule (130 $Å^2$) [21] and m_s is the weight of the Bismuth oxide.

2.1.4. Cell internalisation

Cell internalisation was performed at the Illawarra Health and Medical Research Institute (IHMRI). A LSRII (BD, Franklin Lakes, NJ, USA) Fluorescence Activated Cell Sorting (FACS) flow cytometer was used in order to determine the degree of internalisation of the nanomaterials into the cultured 9L cells. This was done as part of an oxidative stress assay [16]. The cells were brought to 90% confluence in T12.5 cm^2 flasks (Falcon®, Corning). Twenty-four hours before the procedure, 2×10^4 cells were transferred to 5 mL flow cytometer tubes and freshly prepared NP solution was added to the designated NP sample tubes, filling to 0.5 mL total volume at 50 μg.mL^{-1}. After 24 h the tubes were agitated to dislodge the cells and were analysed with a flow rate of 60 mL.min^{-1} until 10 000 events were recorded. The degree of internalisation of the nanomaterials was determined with FACSDiva software, assessing both forward and side scatter intensities [17,22].

2.1.5. Media preparation

The 9L gliosarcoma cells were maintained in a T75cm^2 flask with completed Dulbecco's Modified Eagle Medium (c-DMEM) (DMEM from GIBCO, supplemented with 10% Fetal Bovine Serum (FBS) and 1% Penicillin and Streptomycin) and incubated at 37 °C with 5% (v/v) CO_2 [12].

2.1.6. Determination of Bi_2O_3 k-edge and optimum kVp radiation

To optimise the dose enhancement effects of the bismuth oxide the correct filter and beam energy needed to be calculated. This optimal energy was the closest to the maximum photon mass absorption energy for the bismuth oxide compared to water, maximising the secondary photoelectric particle production. Using the Xmudatv1.0.1 program the photo attenuation coefficients for water and bismuth oxide were generated based on total mass energy absorption. The ratio between the two curves was graphed as a function of energy [12].

2.1.7. Irradiation with kVp and MV beams

All irradiation experiments were carried out at the radiation oncology department of the Prince of Wales Hospital (Randwick, NSW, Australia). Beam energies of 125 kVp and 10 MV were generated by a Nucletron Oldelft Therapax DXT 300 Series 3 Orthovoltage unit (Nucletron B.V., Veenendaal, The Netherlands) and an Elekta Axesse™ LINAC (Elekta AB, Kungstensgatan, Stockholm, Sweden), respectively.

Cell culturing and clonogenic assays were performed at IHMRI. The 9L cell culture was brought to 90% confluence a day prior to irradiation. 50 μg.mL^{-1} of Bismuth oxide NPs was prepared via sonication with a double step Branson 250 Digital sonifier at 70% amplitude for 3 × 10 min runs. The suspension was added to the cell culture medium of the treated samples for 24 h while the untreated controls were not. For kVp experiments, 9L cells were irradiated in T12.5 cm^2 flasks (BD Falcon™) with 6 mm of medium. For MV experiments, T12.5 cm^2 flasks were completely filled with Hank's Balanced Salt Solution (HBSS). No air bubbles were present inside the flask to ensure that electronic equilibrium was obtained at cell monolayer depth. All doses (1, 2, 3, 5, & 8 Gy) were delivered in single fractions at room temperature. Tissue culture flasks were laid horizontally and surrounded sides and back by a 30x30x10 cm^3 solid water phantom to ensure backscattering effects were taken into account. The flasks were then irradiated with the source perpendicular (z-axis) to the flasks. Irradiated flasks of the same dosage were irradiated together to reduce individual dose variation. Non-irradiated control samples, with and without bismuth oxide NPs, were handled under the same conditions as the irradiated samples [12]. The experiments were performed in triplicate with multiple repetitions.

2.1.8. Clonogenic cell survival assay

Clonogenic assay was used as the radiobiological endpoint to assess the effects of 50 μg.mL^{-1} concentration of bismuth oxide NPs on cell survival, compared to control (no NPs). After irradiation, cells were sub-cultured at low density into 100 mm diameter Petri dishes (Sigma) with 10 mL c-DMEM and incubated for 15

doubling times. Following this, each dish was washed with 5 mL PBS (with calcium and magnesium ions) and fixed and stained with 5 mL of a (25% crystal violet, 75% ethanol) solution. Colonies consisting of no less than 50 cells were counted (n) and compared with initial seeding values (I) to obtain the plating efficiency (PE) [12,16], expressed as:

$$PE = n/I \quad (2)$$

For each group, the surviving fraction (SF) is determined as the ratio of the PE of the irradiated sample (PE_x) by PE of the non-irradiated control (PE_c):

$$SF = PE_x/PE_c \quad (3)$$

2.1.9. Cell survival analysis

Survival curves were fit according to the linear quadratic model (LQM) using the associated error bars of each point as weighting factors. The LQM describes cell surviving fraction (SF) mathematically as a function of absorbed dose (D). The fit parameters, α (Gy^{-1}) and β (Gy^{-2}), are indicative of cell radiosensitivity and repair effectiveness, respectively [7]. They are derived from the LQM Eq. (4):

$$SF\ (D) = \exp(-\alpha D - \beta D^2) \quad (4)$$

We quantified the degree of dose enhancement introduced by the NPs by means of the Sensitisation Enhancement Ratio (SER), defined as the ratio of doses giving 10% cell surviving fraction. SER represents a radioenhancement based on the radiobiological endpoint from the LQM curves, and is dependent upon the delivered dose [5].

2.2. Monte Carlo simulation

Simulations were performed using Geant4 (version 9.6 patch 2), a Monte Carlo code modelling particle transport through matter [23], at the Centre for Medical and Radiation Physics (CMRP). The simulation set-up was modelled to retain the essential characteristics of the experimental configuration necessary to investigate the physical mechanisms behind the results of the cell experiments and to investigate the effect of the shape of the NP aggregate on the energy deposition enhancement.

The geometry consisted of a cell population modelled as an array of spherical water cell volumes with 10 μm diameter (shown in Fig. 1), placed in a water phantom at a depth of 6 mm and 25 mm for kVp and MV beams, respectively, to obtain electronic equilibrium. The dimensions of the phantom reflect the sizes of the real phantom used in the experiments. Geant4 Low Energy electromagnetic physics was used with Penelope models to describe the interactions of particles down to 100 eV in the cell population. Atomic deexcitation processes (including both fluorescence and Auger electron emission) were activated in the simulation.

The NP aggregate was modelled as a sphere of 10 μm diameter, a cube with 10 μm sides or a plate with dimensions 10 μm × 10 μm × 1 μm, placed at the centre of the cell populations, as shown in Fig. 1.

The energy spectra of 125 kVp and 10 MV X-ray beams were simulated using SpekCalc v 1.1 [24] and provided by ARPANSA [25], respectively. A 100 μm × 100 μm beam of photons was incident normally on the phantom edge, along the Z axis (see Fig. 2). A total of 6×10^6 and 3.5×10^6 primary photons were incident on the phantom in order to achieve sufficient statistical results in the kVp and MV beam simulations, respectively.

The energy deposited in each cell was calculated with and without the NP. In this study, the dose enhancement factor (DEF) was defined as a ratio D_{NP}/D_C^*, where D_{NP} and D_C^* are the doses calculated with and without the Bi_2O_3 NP aggregate placed in the cell array, as shown in Fig. 1. Water substituted Bi_2O_3 in the simulation configuration without the NP. The DEF represents the physical dose enhancement due to the interactions of incident photon beam and the NP, and is independent of delivered dose.

The DEF was calculated for the different shapes of the NP nanomaterial under study. This factor depends on the mass and shape of the NP aggregate. In order to isolate the effect of the increasing mass of the NP aggregates, the DEF was scaled with respect to the NP aggregate mass. The scaled DEF, referred to as DEF_S, was calculated as DEF/m_{NP} where m_{NP} is the mass of the NP aggregate placed in the cell population. In order to evaluate the effect of the NP aggregate shape (in terms of increasing surface area to volume ratio), the DEF and DEF_S were compared.

The spectra and the Linear Energy Transfer (LET) of secondary electrons produced by the incident X-ray beam were calculated.

3. Results

3.1. Experimentation

3.1.1. X-ray diffraction

The bismuth oxide nanoparticles were characterised as alpha phase [26] by the XRD spectrum. The Scherrer equation was applied to the three peaks (1 2 0), (2 0 0), and (−2 2 1) which showed the Bi_2O_3 nanoparticles had a size range of range of 50–70 nm. This can be observed in Fig. 3, denoted by the transparency of the platelets.

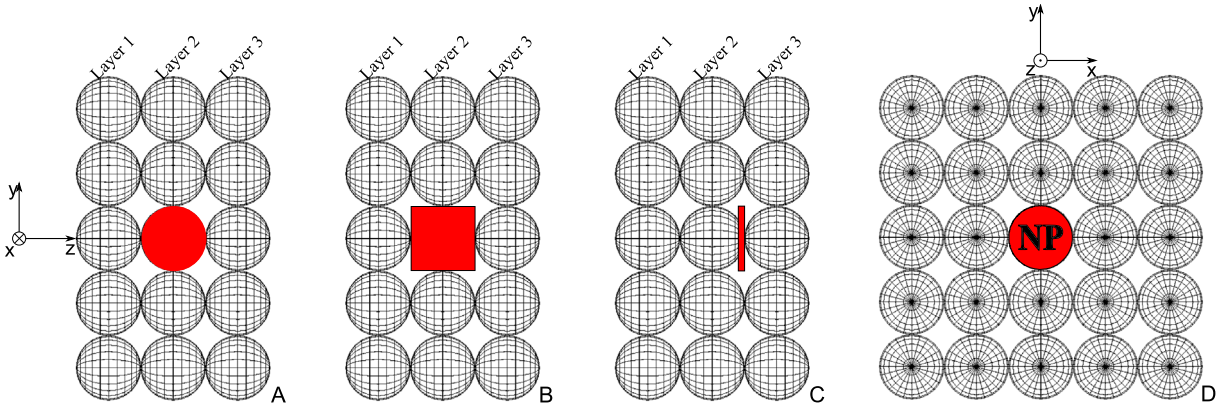

Figure 1. Cross-section in y–z plane of cell population with the NP modelled as a sphere (A), cube (B) or a plate (C) with the photon beam incident on the cell layer from the left along the Z axis. D: Cross-section in x–y plane through layer 2 of cells arrayed around 10 μm diameter sphere of Bi_2O_3.

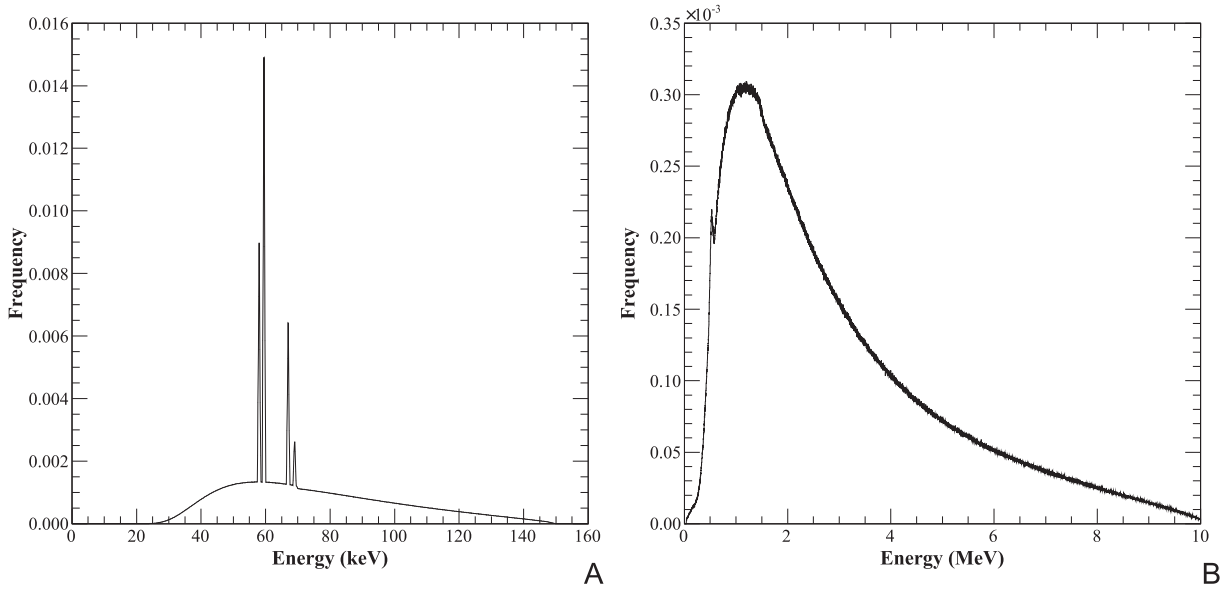

Figure 2. 150 kVp (A) and 10 MV (B) photon energy spectra, provided in terms of relative frequency per incident photon [26].

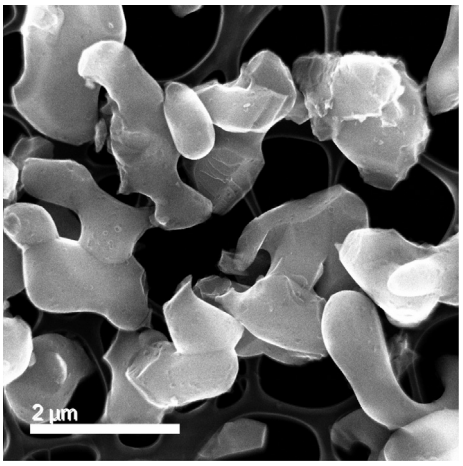

Figure 3. High resolution – transmission electron microscopy (HR-TEM) image of Bi_2O_3 nanoparticles platelets.

3.1.2. Surface area

The optimal MB concentration for the 100 mg of bismuth oxide nanoparticles was determined to be 0.26 ± 0.02 mg.mL^{-1}. Using the cation replacement point, the surface area of the NPs was determined to be 48.7 ± 4.5 cm^2.g^{-1}. There is currently no literature value for comparison. Correct sonication played a crucial role in this process due to the tendency of the nanoparticles to aggregate.

3.1.3. Cell internalisation

The comparison of side scatter (SSC) v.s. forward scatter (FSC) light values at 24 h showed a dramatic increase in the side scatter of the NPs samples over the control. The SSC is proportional to the cell granularity and can be used to examine the cellular uptake of the nanoparticles [27]. The relative increase in scatter is 7 times higher than the controls indicating that a large quantity of nanoparticles had been taken into the cells, as denoted by the dramatic change in scatter distribution (Fig. 4).

3.1.4. kVp energy determination

The maximum differential absorption energy is around 40 keV with the K-edge being located at 91 keV (Fig. 5). These values were then examined against the available spectra for the kVp orthovoltage unit at Prince of Wales Hospital and it was determined that filter 4 would be the most suitable. Filter 4 is an additional filtration of 0.1 mm Cu and 0.25 mm Al; in combination with an X-ray tube potential of 125 kVp orthovoltage beam, it produces photons with an effective energy of 46.7 keV (Fig. 2).

3.1.5. Intrinsic toxicity, survival curves, and radiosensitivity parameters

The Bi_2O_3 NP used in this experiment underwent argon annealing and were found to have no cytotoxicity on 9L cells as previously described [16]. The first radiation energy examined was 125 kVp, which corresponds to the calculated optimum energy of Bi_2O_3 (see Fig. 5), and is used for treatment of superficial cancers. The extracted α and β parameters from the linear quadratic curves were 0.075 ± 0.040 Gy^{-1} and 0.017 ± 0.006 Gy^{-2} for the control sample and 0.355 ± 0.003 Gy^{-1} and 0 Gy^{-2} for the cells with Bi_2O_3. This lead to an SER of 1.48 for the Bi_2O_3 NP at 125 kVp, demonstrating that the material is a highly effective radiosensitiser (Fig. 6).

The effect of bismuth oxide nanoparticles was also examined with 10 MV radiation to investigate how effective it would be for treating deeper seeded cancers, like brain cancer (Fig. 7). The extracted α and β parameters from the linear quadratic curves were 0.150 ± 0.030 Gy^{-1} and 0.013 ± 0.005 Gy^{-2} for the control sample and 0.256 ± 0.054 Gy^{-1} and 0.009 ± 0.007 Gy^{-2} for the cells with Bi_2O_3. The analysis of the curves produced an SER of 1.25 for the Bi_2O_3 nanoparticles.

3.2. Results of the simulation study

3.2.1. Effect of NP aggregate geometry in dose enhancement

The physical dose enhancement produced by the Bi_2O_3 sphere, cube, and plate placed in the cell population was calculated in terms of DEF and DEF$_S$ as explained in the Methodology section. Fig. 8 shows the DEF and DEF$_S$ in cells with respect to radial distance from NP centre in cell layer 3, downstream of the NP, and cell layer 2, containing the NP, in the 125 kVp X-ray field.

Table 1 shows the total DEF and DEF$_S$ obtained when considering the three alternative Bi_2O_3 NP aggregate geometries. It can be observed that the DEF obtained in the case of a cube is larger than

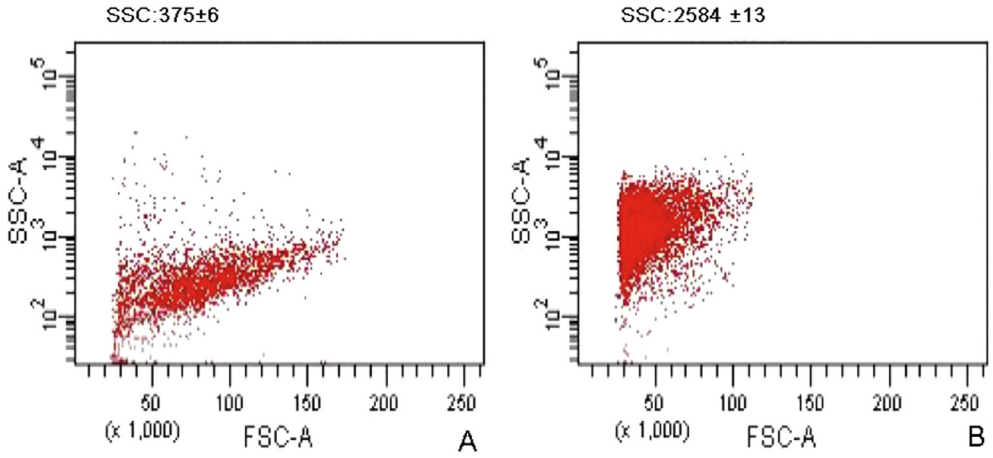

Figure 4. Nanoceramic internalisation, Side scatter (SSC) of 9L cells without (A) and with (B) nanoceramic.

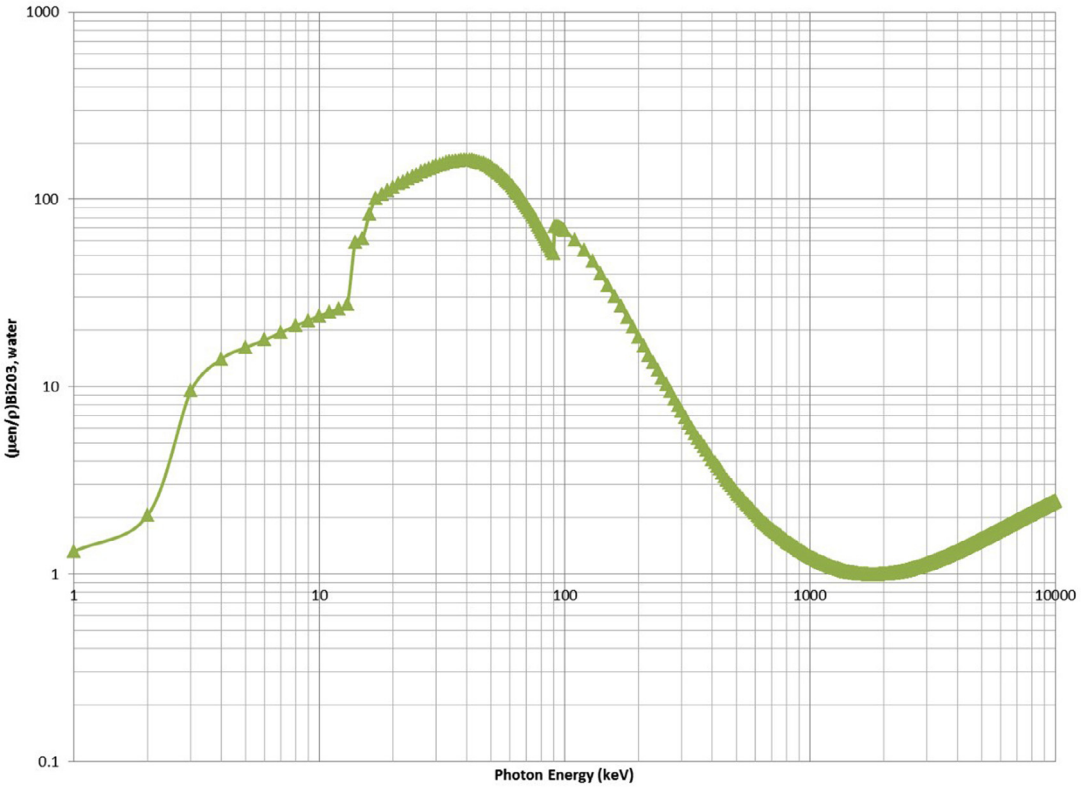

Figure 5. Ratio of mass energy absorption coefficient of Bi_2O_3 relative to water.

that of the sphere and plate configurations, however, when the DEF_S is considered, the plate geometry is superior in terms of dose enhancement. This is due to the higher surface area to volume ratio in the case of the plate (2.4×10^6), compared to the surface area to volume ratios of the cube and sphere (both equal to 0.6×10^6). Since the *in vitro* conditions assume a monolayer of cells at the time of irradiation, the cells in the bottom layer (layer 3 in Fig. 1) below the NP aggregate are also shown in Table 1.

3.2.2. Secondary electron spectra

The kinetic energy and LET spectra of secondary electrons entering all the cells in the population were analysed to assess the change in the quality of the secondary electrons due to the presence of each NP aggregate shape. The results are shown for the kVp and MV beam in Fig. 9 where the spectra are shown per incident photon on the water phantom. It can be observed that the secondary electron spectra and LET are not significantly enhanced by the Bi_2O_3 NP in the 10 MV photon field. This is in contrast to the kilovoltage case where there is a clear enhancement of the secondary electron production. In particular, the greatest increase in number of secondary electrons is observed in the case of the cube geometry, followed by the sphere and plate.

These secondary electron spectra results agree with the DEF reported in Table 1 for the 125 kVp and 10 MV photon fields, respectively. The enhancement of secondary electron production is dependent on the geometry with the cube geometry providing the highest number of secondary electrons due to the absolute increase in the mass of Bi_2O_3 NP material placed in the cell population.

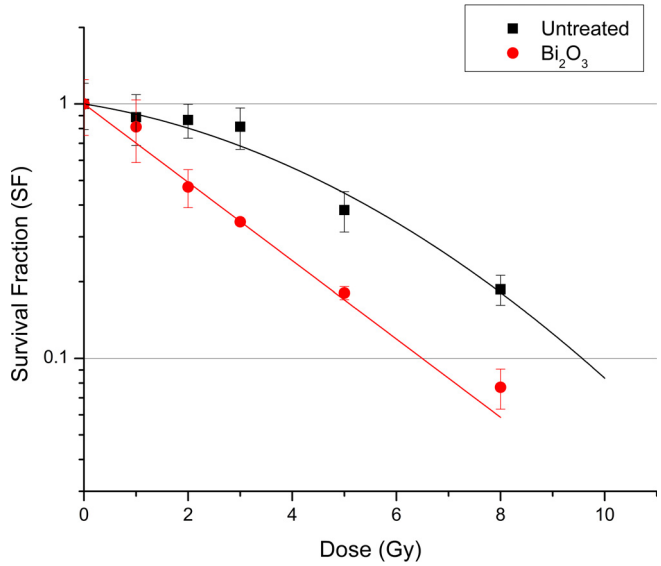

Figure 6. Survival curves of 9L untreated and treated with 50 μg/ml of Bi_2O_3 nanoparticles and exposed to 125 kVp X-ray radiation doses. Surviving fractions were normalised against the non-irradiated controls, averages taken from a sample size of 3 and errors given ±1 standard deviation from the mean.

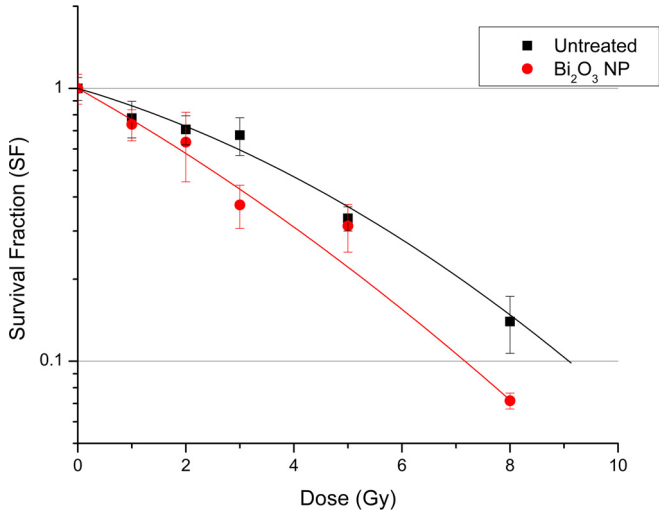

Figure 7. Survival curves of 9L cells untreated and treated with 50 μg/ml of Bi_2O_3 nanoparticles and exposed to 10 MV X-ray radiation doses. Surviving fractions were normalised against the non-irradiated controls, averages taken from a sample size of 3 and errors given ±1 standard deviation from the mean.

When the DEF_s is calculated, it is observed that the plate geometry is the most efficient enhancer. This is due to the increased chance of secondary electrons to be absorbed within the NP aggregate itself with increasing geometrical size and lower surface area to volume ratio. The plate geometry allows more electrons to escape the surface, as the thickness of the plate is only 1 μm, and the range of which is less than the range in Bi_2O_3 of a 12 keV electron [28], meaning most of the electrons will be able to escape the NP geometry. By contrast, the range of a 50 keV electron in Bi_2O_3 is 10.6 μm which means that electrons originate in the cube with energy lower than this value will have a reduced probability of escaping.

4. Discussion

The MB surface area method provided two advantages over the BET. The first was that the suspension was a closer match for the liquid cell environment, closer simulating the actual particle size found during testing. The second was that in suspension, the full surface area could be measured as the nanoplatelets aggregate when dried and lose access to the majority of their surface area.

Cell internalisation measurement showed that the nanoparticles were highly internalised after 24 h (Fig. 4). However, due to the physical parameters of the nanoparticles, the Bi_2O_3 NPs should not penetrate the nucleus and interfere with the DNA resulting in NP induced apoptosis, as is the case of nanoparticles with diameters smaller than 5 nm [10].

Both Geant4 simulations and *in vitro* experiments were essential for this study. The simulations provided insight into the physical processes behind physical dose enhancement in the cells, whereas *in vitro* measurements allowed the study of the synergy among physical, chemical, and biological mechanisms when enhancing radiotherapy treatment by means of nanoparticles.

The Geant4 simulations demonstrated that in the kVp X-ray field, Bi_2O_3 had considerable physical dose enhancement properties, with a dependence on the NP aggregate geometrical shape, related to Surface Area to Volume ratio (SA/V). The dose enhancement was shown to be significant (DEF around 2–3 in the cell population studied, depending on the geometry of the nanoparticle aggregate) in the 125 kVp photon field compared to no significant dose enhancement calculated in the 10 MV field. This is due to the strong increase in photoelectric effect cross-section in the kVp energy range for high Z materials, whereas, electron pair production dominates at 10 MV with contributions from Compton scattering. This effect is caused by the strong Z-dependence (approximately power 3–4) of the photoelectric effect compared to pair production (above 1.022 MeV), which has mass attenuation coefficient approximately proportional to Z, and Compton scattering, which is not strongly Z-dependent [29]. This means that the higher energy photons in the 10 MV spectra are unlikely to strongly contribute to radiation dose enhancement. The megavoltage simulation study found no significant enhancement for any NP morphologies studied. The simulation results for Bi_2O_3 under a kilovoltage beam are in agreement with the experimental data published by Alqathami et al. [30].

The cell survival curves (Figs. 6 and 7) showed that the bismuth oxide has an SER of 1.48 and 1.25 in kVp and MV beam, respectively. The highest SER values for Au NPs is an enhancement of 1.41 obtained at 150 kVp on a less radioresistant cell line. The SER reduced when the Au NPs were examined in more resistant cells [5]. Tantalum oxide has shown an SER of 1.33 on 9L cells at 10 MV [12]. The DEF observed in the simulated cell population was 1.87 ± 0.01 in the layer of cells below the Bi_2O_3 NP plate in the 125 kVp X-ray field. This is a DEF calculated in a small number of cells close to the NP aggregate in this simulation and cannot be compared directly to the experimental SERs observed. However, the High-Z dose enhancement properties of Bi_2O_3 NPs are an important factor influencing increased SER and the calculated DEF from the Monte Carlo simulation reflects this.

The effectiveness of any nanoparticle system in radiation fields is due to a number of factors including cell line, radiation energy, particle morphology, subcellular localisation, and concentration. The 9L gliosarcoma cells used in this study are known to be more radio-resistant and more hypoxic than most of other cancerous cells. Oxygen levels in cells have been shown to alter the effectiveness of radiation therapy, as oxygen is responsible for indirect damage through radiation induced radicals [31]. Therefore, observations on 9L cells should be amplified on less radio-resistant and hypoxic cells.

The surface chemistry of the nanoparticles also has an important effect on the effectiveness of the radiosensitiser as indirect damage is the major mechanism behind cancer apoptosis in radiation therapy [32]. It has been shown that nanoparticles can

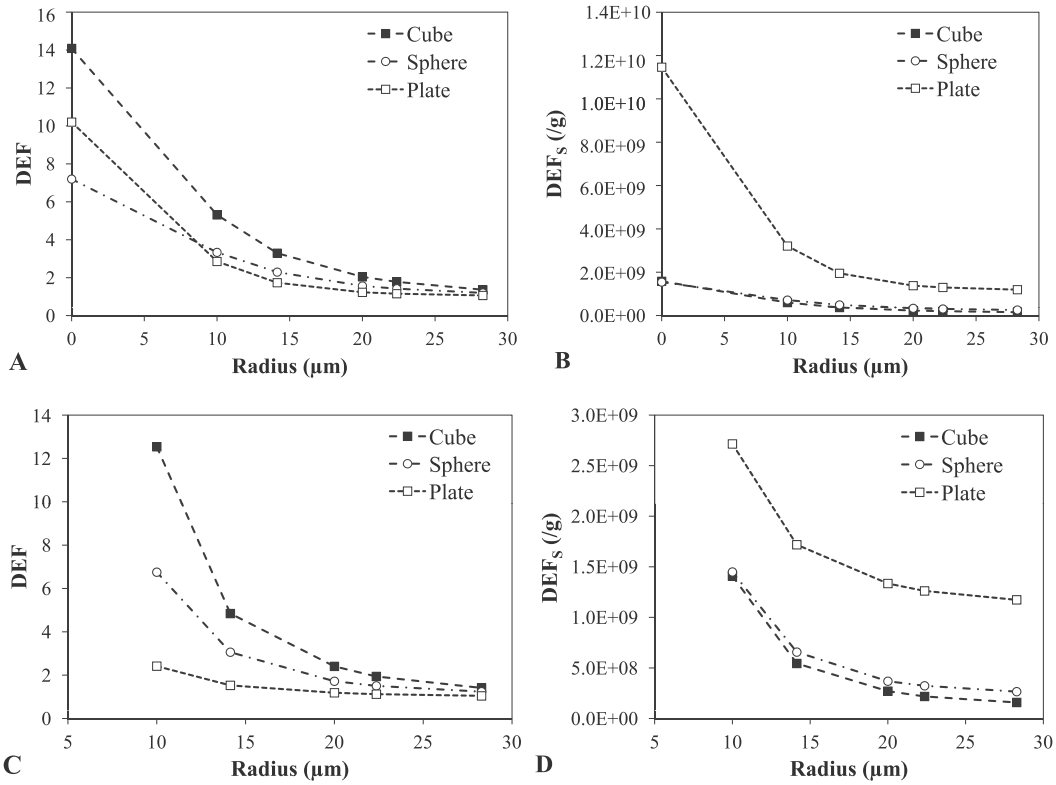

Figure 8. Radial DER (A & C) and DER$_S$ (B & D) in layer 3 (A & B) and layer 2 (C & D) in 125 kVp photon radiation field with Bi_2O_3 NP material in different geometrical configurations (Sphere, Cube, Platelet).

Table 1
DER and DER$_S$ due to each NP aggregate configuration with 125 kVp and 10 MV incident photon fields. DER is calculated for the entire cell population and for the cells in layer 3 of the cell population (below the NP aggregate) to represent the monolayer of cells seen in cell survival experiments.

		Sphere	Cube	Plate
125 kVp				
Total cell population	DER	2.18 ± 0.01	3.27 ± 0.02	1.48 ± 0.01
	DER$_S$ (g_{NP}^{-1})	(4.67 ± 0.02) × 10^8	(3.68 ± 0.02) × 10^8	(16.58 ± 0.07) × 10^8
Cells in layer 3	DER	2.09 ± 0.02	3.06 ± 0.02	1.87 ± 0.01
	DER$_S$ (g_{NP}^{-1})	(4.48 ± 0.03) × 10^8	(3.44 ± 0.03) × 10^8	(21.1 ± 0.2) × 10^8
10 MV				
Total cell population	DER	1.005 ± 0.004	1.020 ± 0.007	1.002 ± 0.005
	DER$_S$ (g_{NP}^{-1})	(2.16 ± 0.01) × 10^8	(1.15 ± 0.01) x10^8	(11.26 ± 0.05) × 10^8
Cells in layer 3	DER	1.007 ± 0.004	1.021 ± 0.004	1.00 ± 0.01
	DER$_S$ (g_{NP}^{-1})	(2.16 ± 0.01) × 10^8	(1.147 ± 0.005) × 10^8	(11.29 ± 0.06) × 10^8

demonstrate catalytic behavior under radiation fields becoming radiocatalysts. In the case of our NPs, it is hypothesized that the energy of the photons excite the NPs, causing them to act as radiocatalysts and split water molecules into HO· and H· radicals [33]. This produces additional ROS which increases the effectiveness of the radiosensitiser and would not be predicted in simulations.

The morphology (SA/V) of the radiosensitising NPs also plays an important role in their effectiveness. The Monte Carlo simulations were designed to model the experimental set up, as stated in Section 2.2, with the incident X-ray beam along the Z-axis. Each 10 μm diameter cell within the array was measured and the average DEF taken for the entire population. Comparatively, the internalisation assay demonstrated high levels of NP internalisation 24 h after NP exposure within the biological cell monolayer (Section 3.1.3.), with the incident X-ray beam passing along the z-axis, perpendicular to the cell monolayer (Section 2.1.7). The Monte Carlo simulations demonstrated that the platelet morphology of Bi_2O_3 NP aggregates leads to more effective radiation damage, especially in kVp photon field, due to a larger SA/V ratio compared to the other morphologies as demonstrated by our Monte Carlo simulations in Section 3.2. Therefore, according to the local effect model the platelet morphology leads to a more preferential dose spike distribution in the individual cellular environments for the same weighted concentration of NPs.

The apparent disparity between the Monte Carlo simulations and the *in vitro* survival curves can be explained through a comparison of the analysis techniques [34]. DEF calculations are the physical ratio of energy deposited with a NP aggregate compared to a pure water phantom. This produces DEF values which are independent of therapeutic dose for a given X-ray energy, i.e. 125 kVp or 10 MV. Alternatively, the SER is a radiobiological endpoint based on a quadratic exponential equation (Eq. (4)), with the radioenhancement being dependent upon the dose for a given X-ray energy, as seen in Figs. 6 and 7, and does not scale linearly.

The Local Effect Model (LEM) for radiation enhancement assists in describing the NP-radiation interactions in the biological

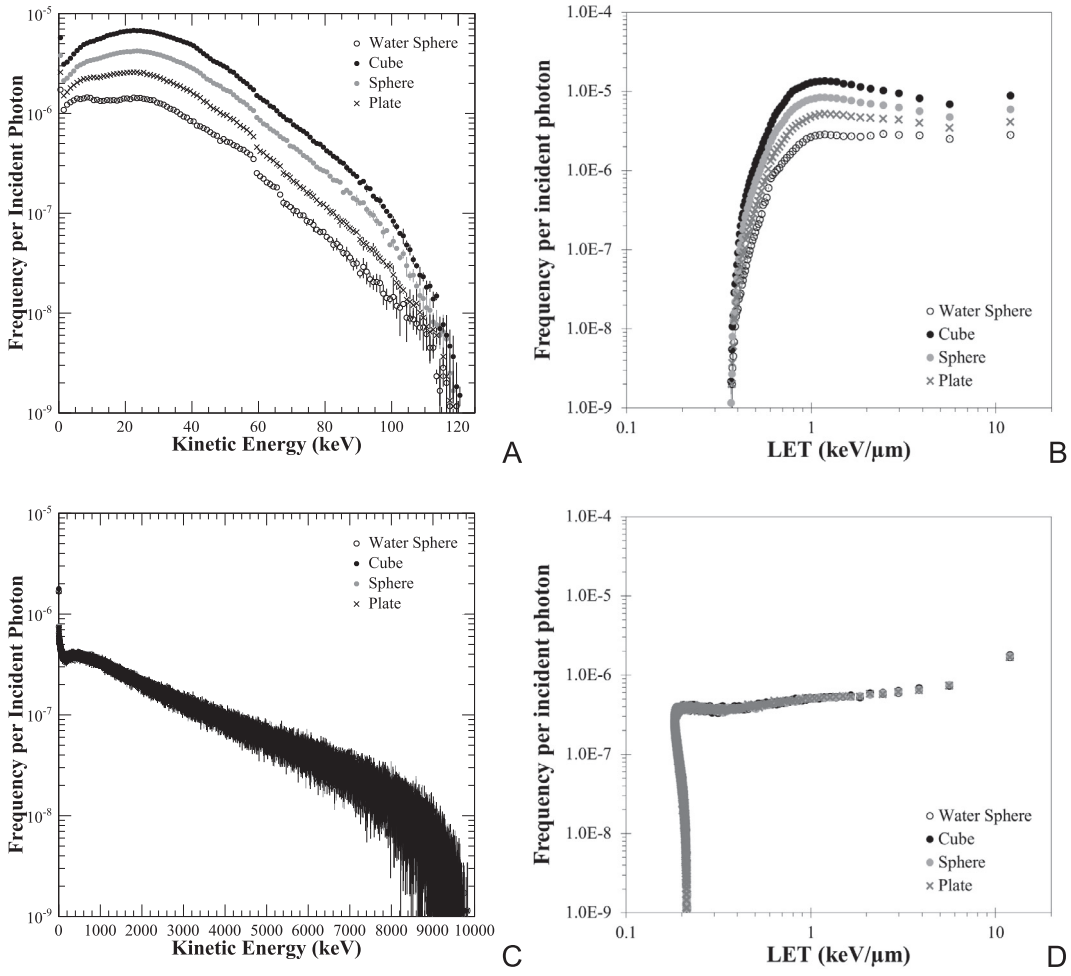

Figure 9. Kinetic energy and LET spectra of secondary electrons entering cells in the array with 125 kVp photon field, (A) and (B), and 10 MV photon field, (C) and (D). Bi_2O_3 sphere (grey circles) compared to cube (black circles), plate (crosses) and water (hollow circle).

context. It states that the dose enhancement of a single particle is effective only to a small subvolume of the total, i.e. the cytoplasm of a cell with an internalised NP. As shown in the Monte Carlo simulations, 50 keV electron has a range of up to 10.6 μm, meaning the subvolume affected by the NP under radiation is confined to the inside of a cell, given the average diameter of a eukaryotic cell is approximately 20–50 μm. Each subvolume produces a slight variation in the dose determined by the NP's interaction with the incident radiation field (dose spike distribution) [32]. While the amplitude and shape of the local dose spikes is different in the kVp and MV photon fields due to the LET of the radiation fields [35], both lead to a large SER. The physical dose enhancement is the cumulative effect of these NP-radiation field interactions, and produce the observed SER in combination with the previously mentioned radiocatalytic and SA/V factors.

5. Conclusion

This work provided the first *in vitro* study of the radiosensitising capacity of bismuth oxide nanoparticles on the highly radioresistant 9L gliosarcoma cells. The XRD and MB analysis showed that the nanoparticles have a platelet morphology with a thickness of 50–70 nm and a surface area of 48.7 ± 4.5 $cm^2.g^{-1}$. The Bi_2O_3 NP were irradiated with 125 kVp and 10 MV X-ray beams, producing SERs of 1.48 and 1.25 respectively. These values are resultant from a combination of the high Z of the bismuth, radiocatalytic activity, and the favourable dose distribution resulting from the advantageous geometrical shape of the nanoparticles on the highly radioresistance 9L cells.

Monte Carlo simulations are a valuable tool to examine the physical dose enhancement of NP enhanced radiotherapy and the importance of careful simulation design to accurately model NP geometry has been demonstrated. Simulations showed that the platelet morphology per unit of Bi_2O_3 mass, is the most effective for enhancing the dose, compared to the cubic and spherical morphologies. The DEF reported by the simulation study are lower than the biological SER found by means of the cell survival experiments in both the kVp and MV radiation fields due to the non-linear dose enhancement nature of biological systems. The means that the physical dose enhancement induced by the High-Z of Bi_2O_3 is only one of multiple factors influencing the sensitisation and this is the only factor accounted for in the simulated DEF in the cell population compared to the experimental SER measurements.

Acknowledgement

Funding: This work was supported by the National Health and Medical Research Council (NHMRC) Grant [APP1084994].

References

[1] Connell P, Hellman S. Advances in radiotherapy and implications for the next century: a historical perspective. Cancer Res 2009;69(2):383–92.

[2] Baskar R, Lee K, Yeo R, Yeoh K. Cancer and radiation therapy: current advances and future directions. Int J Med Sci 2012;9(3):193–9.
[3] Bentzen S. Preventing or reducing late side effects of radiation therapy: radiobiology meets molecular pathology. Nat Rev Cancer 2006;6(9):702–13.
[4] Cifter G, Chin J, Cifter F, Altundal Y, Sinha N, Sajo E, et al. Targeted radiotherapy enhancement during electronic brachytherapy of accelerated partial breast irradiation (APBI) using controlled release of gold nanoparticles. Phys Med 2015;31(8):1070–4.
[5] Jain S, Coulter J, Hounsell A, Butterworth K, McMahon S, Hyland W, et al. Cell-specific radiosensitisation by gold nanoparticles at megavoltage radiation energies. Int J Radiat Oncol 2011;79(2):531–9.
[6] Rahman W, Geso M, Corde S, Yagi N, Aziz S, Annabell N. Optimal energy for cell radiosensitivity enhancement by gold nanoparticles using synchrotron-based monoenergetic photon beams. Int J Nanomed 2014;9:2459–67.
[7] Butterworth KT, Coulter J, Jain S, Forker J, Mcmahon S, Schettino G, et al. Evaluation of cytotoxicity and radiation enhancement using 1.9 nm gold particles: potential application for cancer therapy. Nanotechnology 2010;21(29):1–9. 295101.
[8] Asharani P, Xinyi N, Hande M, Valiyaveettil S. DNA damage and p53-mediated growth arrest in human cells treated with platinum nanoparticles. Nanomedicine 2010;5(1):51–64.
[9] Porcel E, Liehn S, Remita H, Usami N, Kobayashi K, Furusawa Y. Platinum nanoparticles: a promising material for future cancer therapy? Nanotechnology 2010;21(8):1–7. 085103.
[10] Pan Y, Neuss S, Leifert A, Fischler M, Wen F, Simon U, et al. Size-dependent cytotoxicity of gold nanoparticles. Small 2007;3(11):1941–9.
[11] Sun YN, Wang CD, Zhang XM, Ren L, Tian XH. Shape dependence of gold nanoparticles on in vivo acute toxicological effects and biodistribution. J Nanosci Nanotechnol 2011;11(2):1210–6.
[12] Brown R, Tehei M, Oktaria S, Briggs A, Stewart C, Konstantinov K, et al. High-Z nanostructured ceramics in radiotherapy: first evidence of Ta_2O_5-induced dose enhancement on radioresistant cancer cells in an MV photon field. Part Part Syst Charact 2013;31(4):500–5.
[13] Hossain M, Su M. Nanoparticle location and material-dependent dose enhancement in X-ray radiation therapy. J Phys Chem C 2012;116(43):23047–52.
[14] Levason W, Reid G. In: Meyer TJ, editor. Comprehensive coordination chemistry II. p. 465–544 [Pergamon, Oxford].
[15] Kim E, Lee B, Chang H, Lee W, Hong C. Evaluation of the radiopacity and cytotoxicity of Portland cements containing bismuth oxide. Oral Surg Oral Med Oral Pathol Oral Radiol Endod 2008;105(1):54–7.
[16] Stewart C, Konstantinov K, McDonald M, Bogusz K, Cardillo D, Oktaria S, et al. Engineering of bismuth oxide nanoparticles to induce differential biochemical activity in malignant and nonmalignant cells. Part Part Syst Charact 2014;31(9):960–4.
[17] Bogusz K, Tehei M, Stewart C, McDonald M, Cardillo D, Lerch M, et al. Synthesis of potential theranostic system consisting of methotrexate-immobilized (3-aminopropyl) trimethoxysilane coated α-Bi_2O_3 nanoparticles for cancer treatment. RSC Adv 2014;4(46):24412–9.
[18] Patil M, Deshpande V, Dhage S, Ravi V. Synthesis of bismuth oxide nanoparticles at 100 °C. Mater Lett 2005;59(19–20):2523–5.
[19] Cardillo D, Tehei M, Lerch M, Corde S, Rosenfeld A, et al. Highly porous hematite nanorods prepared via direct spray precipitation method. Mater Lett 2014;117:279–82.
[20] Warren B. X-ray diffraction. In: Metallurgy and materials. Addison-Wesley; 1969. p. 382.
[21] Santamarina JC, Klein KA, Wang YH, Prencke E. Specific surface: determination and relevance. Can Geotech J 2002;39(1):233–41.
[22] Böhme S, Stärk H-J, Meißner T, Springer A, Reemtsma T, Kühnel D, et al. Quantification of Al_2O_3 nanoparticles in human cell lines applying inductively coupled plasma mass spectrometry (neb-ICP-MS, LA-ICP-MS) and flow cytometry-based methods. J Nanopart Res 2014;16(9):1–15.
[23] Allison J, Amakoc K, Apostolakis J, Arce P, Asai M, Aso T, et al. Recent developments in Geant4. Nucl Instr Meth Phys Res A 2016. http://dx.doi.org/10.1016/j.nima.2016.06.125.
[24] Poludniowski G, Landry G, DeBlois F, Evans P, Verhaegen F. SpekCalc: a program to calculate photon spectra from tungsten anode X-ray tubes. Phys Med Biol 2009;54(19):N433–8.
[25] Lye JE, Butler DJ, Ramanathan G, Franich RD. Spectral differences in 6MV beams with matched PDDs and the effect on chamber response. Phys Med Biol 2012;57(22):7599–614.
[26] La J, Huang Y, Luo G, Lai J, Liu C, Chu G. Synthesis of bismuth oxide nanoparticles by solution combustion method. Particul Sci Technol 2013;31(3):287–90.
[27] Suzuki H, Toyooka T, Ibuki Y. Simple and easy methods to evaluate uptake potential of nanoparticles in mammalian cells using a flow cytometric light scatter analysis. Environ Sci Technol 2007;41(8):3018–24.
[28] Berger MJ, Coursey JS, Zucker MA, Chang J. ESTAR, PSTAR, and ASTAR: computer programs for calculating stopping-power and range tables for electrons, protons, and helium ions (version 1.2.3), 2005. Retrieved 04/04/2014 from: <http://physics.nist.gov/Star>.
[29] Attix F. Introduction to radiological physics and radiation dosimetry. New York: Wiley; 1986.
[30] Alqathami M, Blencowe A, Yeo U, Franich R, Doran S, Qiao G, et al. Enhancement of radiation effects by bismuth oxide nanoparticles for kilovoltage x-ray beams: a dosimetric study using a novel multi-compartment 3D radiochromic dosimeter. J Phys Conf Ser 2013;444:012025. http://dx.doi.org/10.1088/1742-6596/444/1/012025.
[31] Brown J, Wilson W. Exploiting tumour hypoxia in cancer treatment. Nat Rev Cancer 2004;4(6):437–47.
[32] Kelada, O. Advantages and disadvantages of charged particle therapy – Particle Therapy Cancer Research Institute. [online] Ptcri.ox.ac.uk. 2014. Available at: <http://www.ptcri.ox.ac.uk/about/literaturereview.shtml>.
[33] Geng F, Song K, Xing J, Yuan C, Yan S, Yang, et al. Thio-glucose bound gold nanoparticles enhance radio-cytotoxic targeting of ovarian cancer. Nanotechnology 2011;22(28):285101.
[34] Ballarini F. From DNA radiation damage to cell death: theoretical approaches. J Nucleic Acids 2010:1–8.
[35] Friedrich T, Grün R, Scholz U, Elsässer T, Durante M, Scholz M. Sensitivity analysis of the relative biological effectiveness predicted by the local effect model. Phys Med Biol 2013;58(19):6827–49.

Appendix B

The following published article [109] is derived from work presented in Chapter 3, Section 3.2 of this thesis. My role in this project was the design and development of the Monte Carlo simulation study which forms the basis of this paper. All Monte Carlo simulations in this paper were performed by me, under the supervision of my principle supervisor, Dr Susanna Guatelli.

Sally McKinnon, Elette Engels, Moeava Tehei, Konstantin Konstantinov, Stéphanie Corde, Sianne Oktaria, Sebastien Incerti, Michael Lerch, Anatoly Rosenfeld, Susanna Guatelli (2016) "Study of the effect of ceramic Ta_2O_5 nanoparticle distribution on cellular dose enhancement in a kilovoltage photon field" *Physica Medica* 32(10): 1216-24.

Physica Medica 32 (2016) 1216–1224

Contents lists available at ScienceDirect

Physica Medica

journal homepage: http://www.physicamedica.com

Original paper

Study of the effect of ceramic Ta_2O_5 nanoparticle distribution on cellular dose enhancement in a kilovoltage photon field

Sally McKinnon [a], Elette Engels [a], Moeava Tehei [a,b,c], Konstantin Konstantinov [b,d], Stéphanie Corde [a,e], Sianne Oktaria [a,b,c], Sebastien Incerti [f,g], Michael Lerch [a,b], Anatoly Rosenfeld [a,b], Susanna Guatelli [a,b,*]

[a] Centre for Medical Radiation Physics (CMRP), University of Wollongong, NSW, Australia
[b] Illawarra Health and Medical Research Institute (IHMRI), University of Wollongong, NSW, Australia
[c] Centre for Medical and Molecular Bioscience, University of Wollongong, NSW, Australia
[d] Institute for Superconducting and Electronic Materials, University of Wollongong, NSW, Australia
[e] Radiation Oncology Department, Prince of Wales Hospital, Randwick, NSW, Australia
[f] CNRS/IN2P3, Centre d'Etudes Nucléaires de Bordeaux-Gradignan, UMR-5797, chemin du solarium, 33175 Gradignan, France
[g] Université Bordeaux, Centre d'Etudes Nucléaires de Bordeaux-Gradignan, UMR-5797, chemin du solarium, 33175 Gradignan, France

ARTICLE INFO

Article history:
Received 2 March 2016
Received in Revised form 5 September 2016
Accepted 7 September 2016
Available online 22 September 2016

Keywords:
Ceramic nanoparticles
Dose enhancement
X-ray radiotherapy
Monte Carlo method
Geant4

ABSTRACT

The application of nanoparticles (NPs) in radiotherapy is an increasingly attractive technique to improve clinical outcomes. The internalisation of NPs within the tumour cells enables an increased radiation dose to critical cellular structures. The purpose of this study is to investigate, by means of Geant4 simulations, the dose enhancement within a cell population irradiated with a 150 kVp photon field in the presence of a varying concentration of tantalum pentoxide (Ta_2O_5) NP aggregates, experimentally observed to form shells within tumour cells. This scenario is compared to the more traditionally simulated homogeneous solution of NP material in water with the same weight fraction of Ta_2O_5, as well as to a cell population without NPs present. The production of secondary electrons is enhanced by increased photoelectric effect interactions within the high-Z material and this is examined in terms of their kinetic energy spectra and linear energy transfer (LET) with various NP distributions compared to water. Our results indicate that the shell formation scenario limits the dose enhancement at 150 kVp. The underlying mechanism for this limit is discussed.

1. Introduction

Nanoparticle (NP) enhanced radiation therapy is an increasingly popular area of research with studies showing potential increase in the effectiveness of radiotherapy with the application of NPs to cancerous tumour cells [1–6]. By increasing the effectiveness of dose delivery to the tumour, the probability of tumour control can be increased whilst minimising the dose delivered to normal tissue if NPs are preferentially taken up by tumour rather than normal cells. The physical dose enhancement is due to the high-Z component of the NP leading to an increased photoelectric effect cross-section for incident photon irradiation. Increased secondary electron production, including enhanced Auger electron emission, in the NP translates to more energy deposition within the cell population.

Various properties of NPs, such as size, fabrication material and coating [7], have been shown to have an influence on dose enhancement and increased cell death. The energy of the incident photon beam affects the dose enhancement, as well as the photon interaction cross-sections depending strongly on photon energy and Z of the target material.

Gold NPs (GNPs) are widely studied due to their relative biological compatibility combined with high atomic number ($Z_{Au} = 79$). Passive uptake of gold NPs by tumours is also an advantage [8]. The leaky vasculature of tumours results in GNPs being preferentially accumulated within cancer tissue rather than in normal tissue [1]. Hainfeld et al. (2010) found 1.9 nm GNPs intravenously administered to mice with head and neck squamous cell carcinoma model (SCCVII) leg tumours were more effective radiosensitizers at a lower beam energy (68 keV compared to 157 keV) with the same dose [1]. They found increased therapeutic enhancement for higher doses at both energies when mice had received intravenous injections of GNPs.

McMahon et al. (2011) found enhanced radiosensitation of plasmid DNA across a range of kV X-ray beams with the use of 11.9 and

* Corresponding author at: Centre For Medical Radiation Physics (CMRP), University of Wollongong, Wollongong, NSW, Australia.
E-mail address: susanna@uow.edu.au (S. Guatelli).

http://dx.doi.org/10.1016/j.ejmp.2016.09.006
1120-1797/

37.5 nm diameter GNPs [9]. Dose enhancement is also reported in the case of MV photon beams where Compton scattering and pair production are dominant [10]. The effectiveness of 6 MV and 15 MV photon irradiations of MDA-MB-231 breast cancer cells was shown by Jain et al. (2011) to be increased by sensitizer enhancement ratios (SER) of 1.29 and 1.16, respectively [10].

The concept to use ceramic compounds containing high-Z elements in NP enhanced radiotherapy as radiosensitizers in megavoltage irradiation has first been reported in [2]. Results with kilovoltage irradiation are currently under review for publication [11]. The ceramic based compounds have different aggregation properties compared to NPs based on noble metals. They tend to aggregate much easier, which may limit their migration so as to localize them better in the desired target region. Due to this, the expected radioenhancement may differ compared to GNPs. Ceramic NPs also have the ability to be non-toxic, radioprotectors and/or inducers of differential biochemical activity in malignant and non malignant cells [2,12,13]. Brown et al. (2014) showed that radioresistant 9L rat-brain gliosarcoma cancer cells are more successfully treated with 10 MV photon irradiation when internalising Ta_2O_5 NPs [2]. Ta_2O_5 has a high effective atomic number, due to the high-Z of tantalum (Z_{Ta} = 73) and a resulting sensitization enhancement ratio (SER) of 1.33 was measured for a concentration of 50 μg/mL. Toxicity results are also reported elsewhere (see Ref [2]). The presence of a high-Z material results in an increased production of secondary electrons and subsequently increased direct and indirect damage to the cell. A Monte Carlo based study into any further sensitisation enhancement with higher Ta_2O_5 concentration was therefore considered with respect to NP distribution between and within cells, compared to the more traditionally simulated homogeneous solution of NP material in water [14].

2. Experimental motivation of the study

Cytotoxicity experiments conducted by Brown et al. (2014) showed that exposure of the 9L cells to a higher concentration (up to 500 μg/mL) of Ta_2O_5 NPs does not significantly increase the toxicity [2]. In particular, photon irradiations using 150 kVp X-rays [11] have shown that irradiated 9L cells, exposed to a 10-fold increase in Ta_2O_5 NP concentration, do not correspondingly indicate a significant decrease in cell survival, as may be expected.

Confocal images of the cell population with a Ta_2O_5 solution indicate that some NPs are internalised and begin to form a "shell" around the cell nucleus. Fig. 1 shows representative confocal microscopic images of 9L cells with Ta_2O_5 NPs. The Ta_2O_5 NPs are observed to form "shells" in the confocal image of the 500 μg/mL concentration (Fig. 1c), compared to the 50 μg/mL concentration (Fig. 1b).

Confocal images show that increasing the Ta_2O_5 concentration triggers the formation of shells of NP material around cell nuclei with an increasing shell thickness, whilst leaving, on average, a higher number of cells bare or with a limited number of NPs. This phenomenon also translates to a lower number of cell nuclei surrounded by NPs, separated, on average, by greater distances. This means that some colonies within the cell population have a small concentration of NPs, whereas other colonies have several neighbouring cells with Ta_2O_5 shells, with high local concentration of NP material, as shown in Fig. 1.

Our hypothesis is that in the cell colonies experiencing a high local Ta_2O_5 concentration, the NP shell contributes to physically protect the cell nucleus from the otherwise expected impact on cell survival. Increasing the thickness of the Ta_2O_5 NPs shell will increase the probability of photon interaction and subsequent secondary electron production. However, an increased Ta_2O_5 shell thickness also increases the energy loss of any secondary electrons traversing the shell and produces more self-absorption of low energy Auger electrons generated within the shell. This could translate to a saturation effect where adding more NP material does not produce higher dose enhancement.

This work intends to investigate our hypothesis behind the results of the cell experiments, by studying the physical effect on the dose enhancement of varying the NP shell thickness and distribution within a cell colony (called μ-phantom in the following sections), characterised by a high local NP concentration. The simulation model is based on the local NP distribution observed in the cell population, in the confocal images shown in Fig. 1.

3. Materials and methods

3.1. Monte Carlo simulation set-up

An ad-hoc Monte Carlo simulation study was performed to characterise the dose enhancement by means of Ta_2O_5 NPs in the presence of a 150 kVp photon field. The dose enhancement was studied varying the NP shell thickness and distribution in the cell colony. Geant4, version 9.6 patch 2 [15,16], was the Monte Carlo code adopted.

The simulation set-up resembled the configuration of cellular irradiation experiments carried out to determine the clonogenic survival curves. A $70 \times 70 \times 70\ \mu m^3$ cell population (called here μ-phantom) was modelled corresponding to experimental observations of different NP shell distributions in cellular colonies (see Fig. 1), which are limited portions of the entire irradiated cellular population. Cells/cell nuclei were modelled as simple water spheres with 8 μm diameter, and were placed in 3 layers of 5×5 such spheres giving a total of 75 cells in the μ-phantom. The distance between the cell centres was 14 μm to allow for surrounding

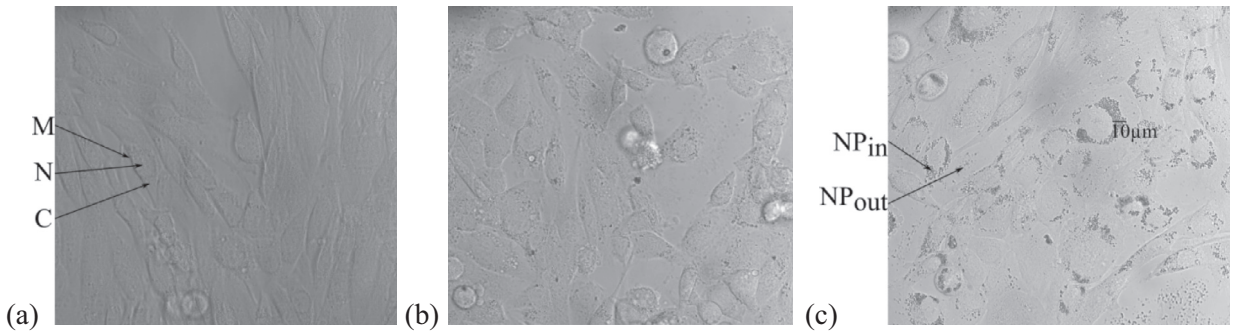

Fig. 1. Confocal microscopic image of elliptical 9L gliosarcoma cells with Ta_2O_5 NPs; control (a), after exposure of concentration 50 μg/mL (b), and 500 μg/mL (c). In the control image M = cell membrane, N = cell nucleus, C = cytoplasm. In 500 μg/mL image (c) NP_{in} = Ta_2O_5 NPs inside cell, NP_{out} = Ta_2O_5 NPs outside cells.

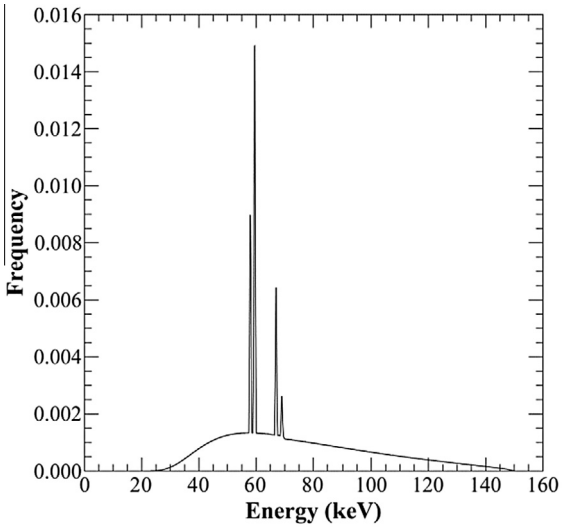

Fig. 2. 150 kVp photon energy spectrum modelled in the simulation study, in terms of relative frequency per primary photon [20].

the spheres with 3 μm thick NP shells without encountering geometry overlaps. This cell spacing has been set as an approximation arbitrarily as currently the average distance between shells is not quantified experimentally. The μ-phantom was set in a larger water phantom, at a depth of 6 mm along the direction of the incident photon beam, corresponding to the depth of the cells in the cellular irradiation experiments. The water phantom has lateral side length of 30 cm and total length in the direction of incidence of the beam equal to 10.6 cm. The position of the μ-phantom and the phantom sizes correspond to the real configuration used in the cell experiments conducted by the Targeted Nano-Therapies research group at the University of Wollongong [2,11,12].

A 100 μm × 100 μm beam of X-rays was incident normally on the phantom, irradiating the entire cell population of the μ-phantom. The chosen size of the beam, which is significantly smaller with respect to the 10 × 10 cm^2 field adopted in the experiments, allows to obtain a relative comparison of the dose effect of the different NP distributions under the same irradiation conditions, whilst at the same time reducing the required simulation execution times to approximately 800–900 h on a single 3 GHz CPU for each shell configuration. The use of small incident beam sizes is common in Monte Carlo simulation studies to investigate nanoparticle enhanced radiotherapy [17–19]. Leung et al. (2011) and Li et al. (2014) employ a photon source of nanometre dimensions set at a distance of 1 mm from a GNP in Monte Carlo simulation studies [17,19]. Furthermore, the study by Chow et al. (2012) uses a 100 nm diameter photon source incident on a GNP in a water phantom of variable size [18].

The 150 kVp spectrum (Fig. 2) was simulated using SpekCalc v 1.1 and corresponds to the beam generated by a Nucletron Oldelft Therapax DXT 300 Series 3 Orthovoltage unit (Nucletron B.V., Veenendaal, The Netherlands) peak energy of 150 kV, Tungsten anode, inherent filtration of 3 mm Beryllium, additional filtration of 1.5 mm Aluminium and 0.35 mm Copper; 1st half value layer of 0.67 mm Cu [20]. Multiple NP configurations were studied with the simulation of 2 × 10^{10} primary photon histories in each case, to achieve an adequate statistical uncertainty.

The Geant4 Low Energy electromagnetic physics package [21] with Penelope physics models was selected to describe particle interactions. This choice was dictated by the capability of Penelope models to track secondary electrons down to 100 eV, which is the low energy limit recommended in Sempau et al. (2003) [22], coupled with shorter simulation execution times with respect to the

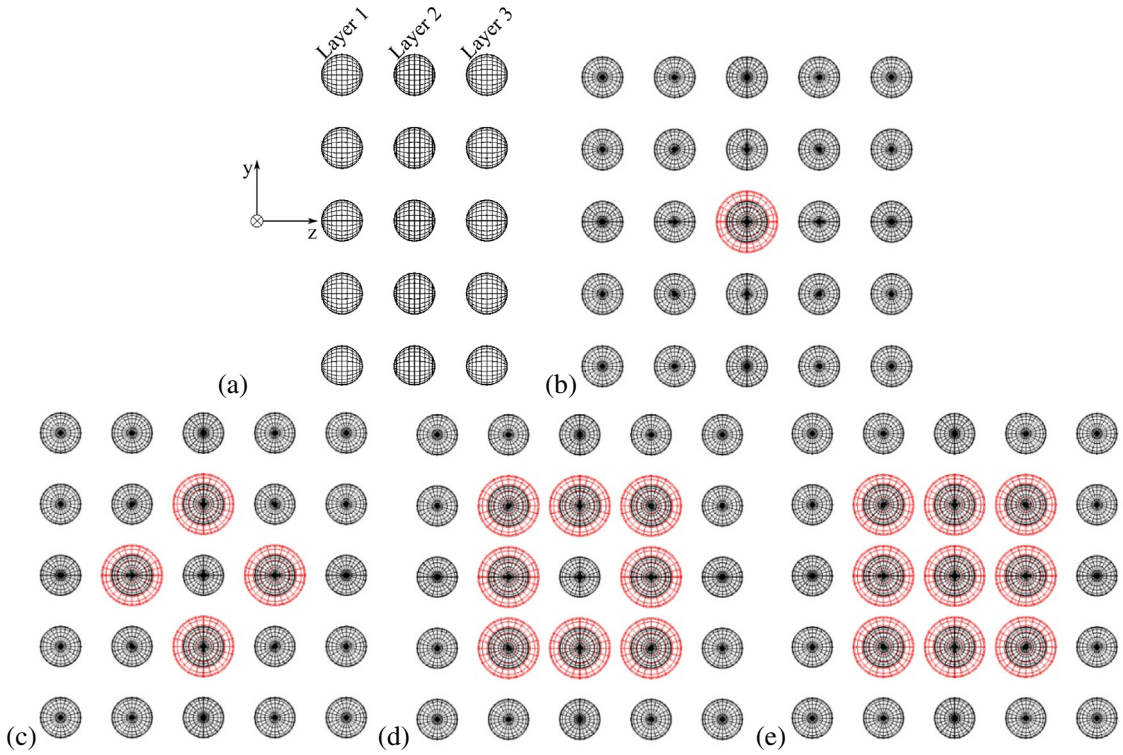

Fig. 3. Simulation geometry: cross section of the μ-phantom where three layers of 5 × 5 cell array with photon beam incident along z-axis from the left (a); view of cells of layer 2 with 2 μm thick NP shells (red) coating 1 (b), 4 (c), 8 (d) and 9 (e) cells. (For interpretation of the references to colour in this figure legend, the reader is referred to the web version of this article.)

Table 1
Calculated concentration of Ta_2O_5 NP in the μ-phantom with respect to shell thickness and configuration.

Shell distribution	1 μm thick (*mg/mL*)	2 μm thick (*mg/mL*)	3 μm thick (*mg/mL*)
1	6.5	16.2	29.7
4	26.0	64.7	118.7
8	51.9	129.4	237.4
9	58.4	145.5	267.1

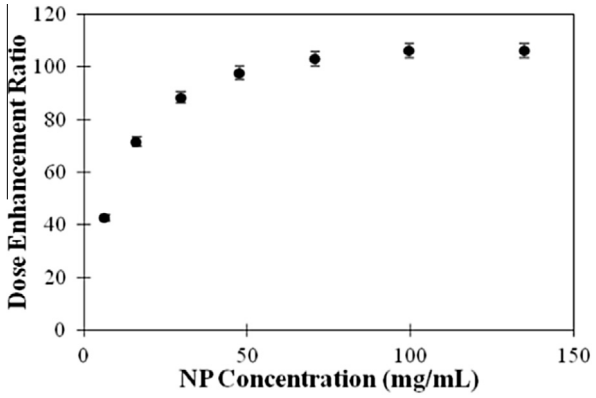

Fig. 4. DER in central cell of μ-phantom with increasing shell thickness of 1–7 μm (expressed as local NP concentration) of Ta_2O_5 NP shell around the central cell itself, per incident photon.

Geant4 Very Low Energy Extensions (Geant4-DNA) [23]. Although event-by-event Monte Carlo codes, such as Geant4-DNA, are the state of the art to study the effect of radiation at cellular and sub-cellular level, Stewart et al. (2002) showed that Penelope physics models can be used to estimate physical quantities of interest at cellular level with an agreement between 1 and 25% with event-by-event Monte Carlo codes when calculating the mean specific energy [24]. Atomic deexcitation, including Auger electron emission and fluorescence, were modelled in the simulation.

The total dose deposited in each of the cells of the μ-phantom was calculated with different NP shell configurations as described in Section 3.2. By calculating the dose in micron scale cell volumes the simulation by design avoids a potential for inaccuracies in dose distribution introduced by sub-micron voxelized scoring volumes on the nanoscale, which were described in [25].

The kinetic energy spectra and LET of the secondary electrons, produced by the kVp beam in the μ-phantom and in the NP shells, entering the cells have been calculated to evaluate the change in radiation quality responsible for the cell damage. The LET was calculated on the basis of the electron energy, using data from reference [26]. The effect of atomic deexcitation was examined as well.

The dose enhancement ratio (DER) was evaluated as D_{NP}/D_{Water}, where D_{NP} and D_{Water} are the doses calculated in the cells, with and without Ta_2O_5 NPs distributed in the μ-phantom, respectively. The dose enhancement was examined with respect to increasing the NP concentration in the μ-phantom, compared to the dose without the NP present.

3.2. Nanoparticle distributions under study

The NP material, Ta_2O_5, was defined in the Geant4 simulation with a density of 8.2 g/cm^3. Two different types of NP distribution geometry were modelled: (1) shells of NP material placed around the water spheres, modelling cell/cell nuclei (*shell distribution*) and (2) a homogeneous distribution (*homogeneous distribution*) of NP material in water around the spheres. Configurations (1) and (2) have the same total concentration of NP material.

The geometry with the shell distribution is shown in Fig. 3 presenting the side view (Fig. 3a) and beams-eye-view (Fig. 3b–e) of the μ-phantom. Several configurations of shells were investigated in this study, from one single shell (Fig. 3b) to a maximum of 9 shells placed around the 9 central spheres of layer 2 (Fig. 3e). 4 and 8 shells were considered as well (Fig. 3c and d, respectively). In Fig. 3 all of the shells have a thickness of 2 μm. These shell distributions were selected to model the behaviour observed in cellular irradiation experiments, where some cells were observed to have no NP uptake, some section had only few isolated cells with shells, whereas other sections had many cells with shells close together in the colony.

The DER in the central sphere of layer 2 in the μ-phantom was investigated for different shell distribution in order to study the effect of a NP shell touching the cell, the effect of nearby shells and the combination of these effects.

3.3. Simulation studies

A first study was conducted to investigate the influence of the NP shell thickness on the dose enhancement. Simulation configuration depicted in Fig. 3b was adopted. The NP shell around the water sphere was increased between 1 and 7 μm. The DER was calculated in the central cell and compared for increasing shell thickness. This study was performed to determine the thickness of the NP shell where a "saturation effect" can start to be observed. The average range of secondary electrons originated by a 150 kVp beam in

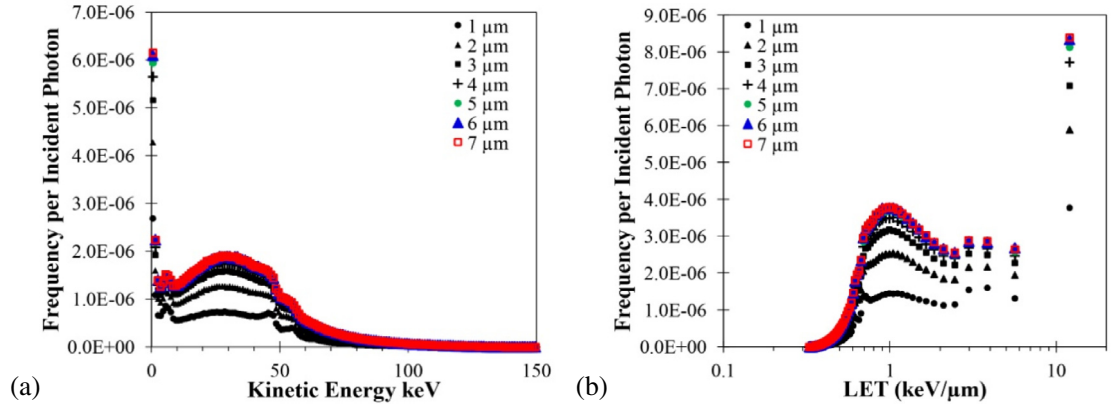

Fig. 5. Secondary electron kinetic energy spectra (a) and LET (b) entering central cell with increasing shell thickness of Ta_2O_5 NP shell around central cell per incident photon.

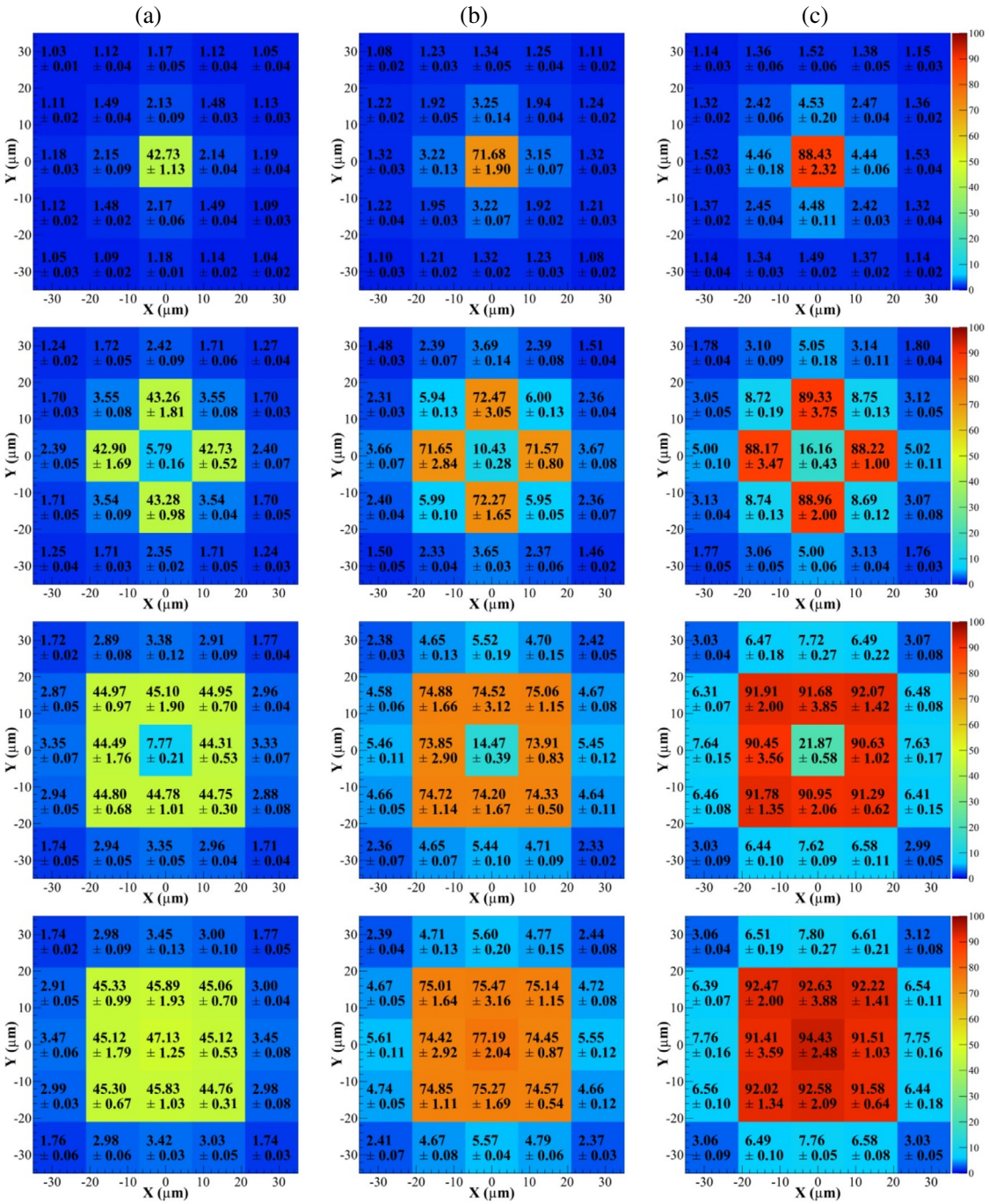

Fig. 6. Dose enhancement ratio in each cell volume in layer 2 (see Fig. 3(b–e)) with Ta_2O_5 shell of 1 μm (a), 2 μm (b), and 3 μm (c) thickness of a single shell (top row), 4 (second row), 8 (third) or 9 shells (bottom).

Ta_2O_5 is less than 5 μm [26], therefore electrons which deposit energy in the cell are those produced in a spherical layer of the NP with thickness equal to or less than their range in Ta_2O_5. This means that the dose enhancement capability of thicker NP shells is impeded by internal absorption of electrons, which translated to a saturation effect on the DER when increasing the NP shell thickness.

A second study was performed to compare the DER calculated with a distribution of NP shells in the μ-phantom (shown in Fig. 3), as observed experimentally (shown in Fig. 1), and, alternatively, with a homogeneous distribution of NP material in water, with the same simulated concentration. This study allows the comparison of the DER due to NP distribution on the micron scale and the tendency of the NPs in the cell culture to congregate in shells around the cells, compared to being uniformly distributed among cells. The shell thickness was set equal to 1 μm, 2 μm or 3 μm in each cell configuration investigated, to obtain higher concentrations of NPs in the cell population. Such shell thicknesses were selected on the basis of the microscope observations as the one depicted in Fig. 1.

Table 1 reports the calculated equivalent local concentration of Ta_2O_5 in water for each simulated number of shells and shell thick-

nesses. The local NP concentrations calculated within the μ-phantom are high due to the localisation of material in a small volume of water.

4. Results and discussion

4.1. Effect of shell thickness on dose enhancement in a single cell

Dose enhancement due to a Ta_2O_5 NP shell placed on the central cell in the μ-phantom, as shown in Fig. 3b, is represented against the NP shell thickness in Fig. 4.

From the simulation results, the calculated DER increases quickly and then the increase slows down for larger shell thickness. The initial increase in the DER is due to the increasing quantity of high-Z Ta_2O_5 NP material in close proximity to the cell. However, the rate of increase of DER is reducing with thicker NP shells because of self-absorption of secondary electrons originated in the NP ceramic at a distance from cell surface larger than their range.

At the same time the thickness of the NP shell does not affect the global photon fluence reaching the "active shell" close to the cells, from which the originated electrons will reach the cell nucleus. Further increasing the shell thickness will eventually lead to decreasing DER due to photon attenuation.

The kinetic energy spectra and corresponding LET of electrons entering the central cell are shown in Fig. 5. The number of secondary electrons per incident photon increases with the shell thickness (t) up to a t of approximately 5 μm. For shell thicknesses greater than 5 μm the number of secondary electrons does not increase significantly.

The DER increases by 3 per mg/mL increase in NP concentration when varying the NP shell thickness from 1 μm to 2 μm. This increase is only 0.1 per mg/mL increase in NP concentration when the NP shell thickness varies from 5 μm to 6 μm, which is an insignificant enhancement when the error margins are taken into account. This means that the effectiveness of the NP to enhance dose in cells is reduced with increasing concentration of NP, eventually resulting in no further enhancement at all, and finally decreasing DER.

Fig. 5 shows the energy spectra of secondary electrons for an NP shell thickness varying between 1 μm and 7 μm. The mean kinetic energy of the secondary electrons is (31 ± 1) keV. Therefore, the average electron would have a range of less than 19 μm in water and about 4.5 μm in Ta_2O_5 [26]. This means that for shell thicknesses greater than this range in Ta_2O_5 the enhancement is expected to be reduced due to electron absorption by the NP shell.

4.2. Effect of spatial distribution of shells on the dose enhancement

Fig. 6 shows the DER in the four alternative spatial distributions of NP shells represented in Fig. 3(b–e). It can be observed that – for the NP shell thicknesses under study – the DER increases with increasing thickness of Ta_2O_5 NPs and with the number of shells. Most dose enhancement occurs within the cells about which shells are placed, significant enhancement is still seen in neighbouring cells, with the greatest dose effect in those closest to the NP shells (e.g. DER in the central cell in the case of NP shells surrounding 8 cells). This means that NP shells have significant dose effect within approximately 20 μm. However, a DER above 1 is observed at larger distances because of electrons with kinetic energy greater than average. For example, in the case of the NP shell surrounding the central cell only, the average DER in the furthest cells (at a distance of 39.6 μm from the central cell) is (1.14 ± 0.02) for 3 μm shell thickness. This compares to an average DER of (3.47 ± 0.02) in the eight cells surrounding the central cell.

4.3. Secondary electron kinetic energy spectra and LET

Fig. 7a shows the kinetic energy spectra and LET of secondary electrons entering into the central cell of layer 2 in the μ-phantom, varying the Ta_2O_5 shell thickness in the case of the 9 shell NP distribution (Fig. 3e), with respect to the case of no NP material in the μ-phantom. The 9, 8, and 1 NP shell distributions are compared in Fig. 7b in order to see the effect of a local shell, the effect of nearby shells and the combination of these.

The mean kinetic energy of secondary electrons created within the Ta_2O_5 NP shells is around 1.5 keV. Electrons with kinetic energy less than 10 keV have a range of less than 1 μm in Ta_2O_5, as shown in Table 2, reporting the range of electrons with varying kinetic energy in water, solid Ta_2O_5 NP, and homogeneous Ta_2O_5 solution [26]. This results in a large proportion of the low energy electrons being absorbed by the Ta_2O_5 shell and not contributing to the DER in the nearby cells. The mean kinetic energy of secondary electrons escaping the NP shell was found to be around 33 keV, increasing slightly with larger shell thickness. This happens because only higher energy electrons can escape the NP shell with increasing shell thickness, whilst the only low energy electrons originating from the NP and contributing to the dose in the cell are produced in proximity to the inner surface of the shell.

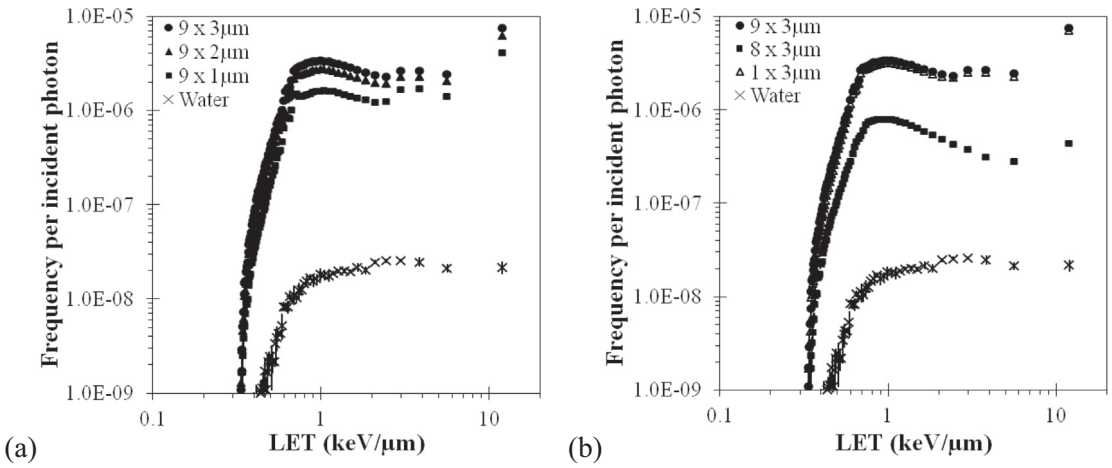

Fig. 7. LET of electrons entering the central cell in the μ-phantom with Ta_2O_5 NPs distributed in 9 shells, compared to configuration without NPs (Water) (a). The 9, 8 and 1 NP shell configurations are compared for the 3 μm thick shell case (b).

Table 2
Range of electrons in water, Ta_2O_5, and a solution of Ta_2O_5 in water [26].

Energy (keV)	Range in water (μm)	Range in Ta_2O_5 (μm)	Range in 267.1 mg/mL Ta_2O_5 solution (μm)
10	2.51	0.74	2.33
20	8.57	2.25	7.84
30	17.56	4.40	16.0
40	29.19	7.09	26.5
50	43.20	10.29	39.1
150	281.7	62.0	252.6

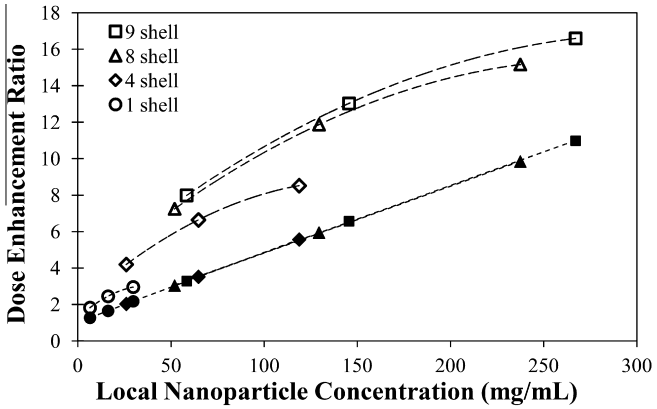

Fig. 8. Total DER in the μ-phantom per incident photon due to a homogeneous solution of Ta_2O_5 in water (filled symbols) compared to the average dose due to the same ceramic compound arranged as NP shells (unfilled symbols) of various thickness (corresponding to different local concentration) and geometrical distribution.

4.4. Comparison of NP distributed in shells to homogeneous solution

Fig. 8 reports the DER calculated in the different NP shell configurations under study, for different local concentrations (corresponding to different NP shell thicknesses), and with a corresponding homogeneous distribution of NP material in water, integrated over the cells in the entire μ-phantom. The NP shell configuration and the homogeneous solution have the same total concentration of NP material. It can be observed that the DER depends significantly on the geometrical model of the NP distribution in water and indicates a saturation effect which has been described in Section 4.1.

The DER increases with increasing concentration of Ta_2O_5 in both NP shell and solution configurations. In the case of the homogeneous solution the DER increases linearly with increasing mass of Ta_2O_5 in water. Instead, in the case of a NP shell distribution, the DER increases and then saturates with an increase in mass of Ta_2O_5 shell as explained in Section 4.1. In the case of a homogeneous NP solution, generated secondary electrons do not have to traverse a NP shell in order to deposit dose within the cell and are therefore attenuated only by the homogeneous NP solution which translates to a linear effect on the DER with respect to NP material concentration.

Fig. 9 reports the energy spectra of secondary electrons entering in the central cell of the μ-phantom in the case of NP shells surrounding 9 cells (Fig. 3e) and in the corresponding NP homogeneous solution in water, with the same concentration.

It is observed that more electrons enter the central cell with the Ta_2O_5 NPs in shell configuration compared to an equivalent solution of NP. This happens because the NP shell of Ta_2O_5 material surrounding the cell provides a source of low energy electrons close to the cell, in contrast to a homogeneous NP solution in water producing a uniform source of electrons throughout the water medium surrounding the cells. This also explains why the total DER in Fig. 8 is higher in the NP shell case compared to homogeneous solution.

4.5. Effect of atomic deexcitation

The influence of atomic deexcitation on the DER was investigated by performing simulations with and without atomic deexcitation activated. The kinetic energy of atomic deexcitation electrons is constrained by the low energy production threshold of 100 eV recommended in these simulations [22]. The difference between the DER calculated with and without the deexcitation is summarised in Table 3 and shows that the atomic deexcitation processes accounted for between approximately 3% and 7% of the DER at the cellular level. The DER due to atomic deexcitation is pre-

Table 3
Percentage of DER within the central cell attributed to atomic deexcitation, for each NP shell configuration and thickness under study.

Shell distribution	1 μm thickness	2 μm thickness	3 μm thickness
1	(7.23 ± 0.03)%	(5.55 ± 0.03)%	(4.98 ± 0.01)%
8	(4.56 ± 0.04)%	(4.00 ± 0.04)%	(2.73 ± 0.01)%
9	(7.03 ± 0.04)%	(5.38 ± 0.02)%	(4.75 ± 0.01)%

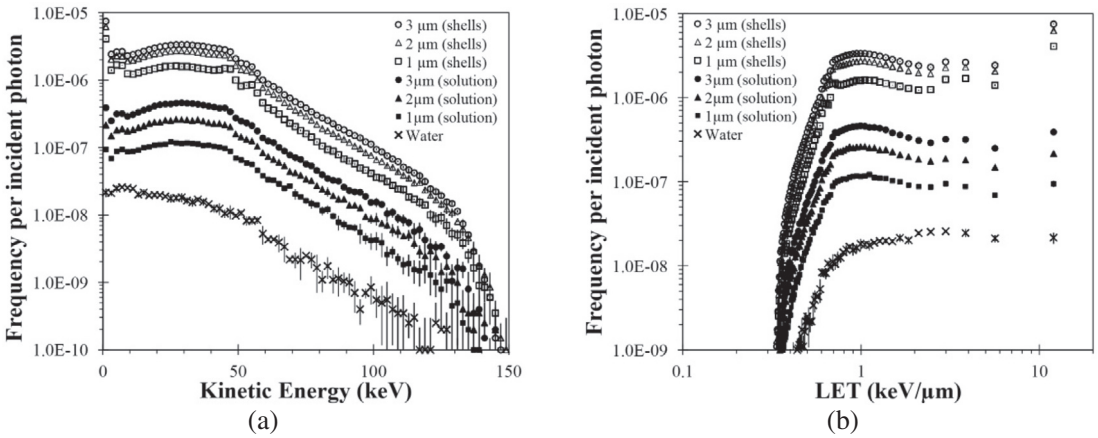

Fig. 9. Energy spectra (a) and LET (b) of electrons entering the central cell in the μ-phantom with NPs distributed in shells (hollow symbols) or in solution (filled symbols) around the cells compared to water.

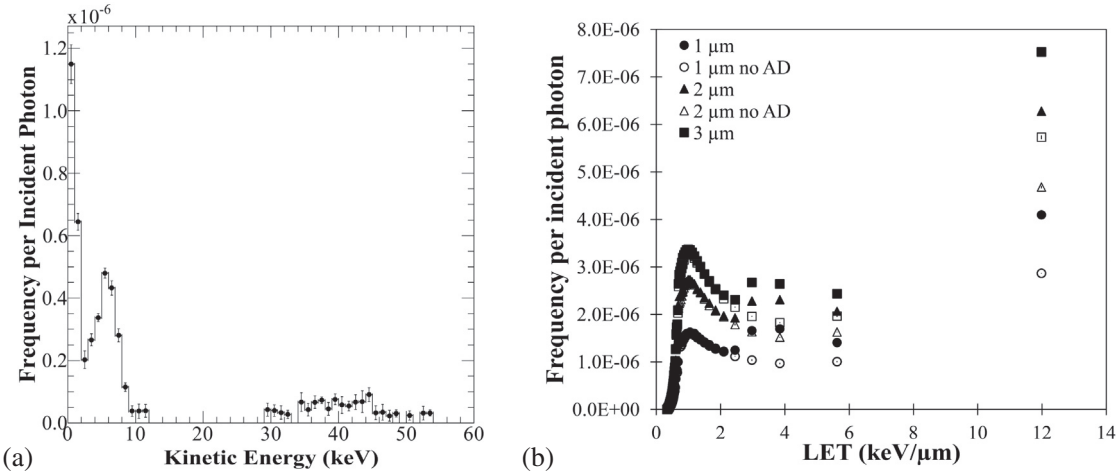

Fig. 10. Kinetic energy spectrum of secondary electrons produced by atomic deexcitation, entering the central cell with a 3 μm thick NP shell surrounding the cell itself (a) and the LET of secondary electrons entering the central cell in the 9 shell configuration (b). LET with AD processes activated (filled symbols) is compared to LET with no AD activated (unfilled symbols).

dominantly observed in the cell surrounded by the NP shell and for thinner NP shells. This is explained by the fact that Auger electrons are very low energy and therefore have a short range and can be easily self-absorbed in thicker NP shells. Auger electrons contribute to the DER in the cell surrounded by the NP shell as expected. This means that if in an experimental situation a particular cell does not have a NP shell, it will receive a significantly lower DER from low energy atomic deexcitation electrons than neighbouring cells with internalised NP shells.

The spectra of atomic deexcitation electrons per incident photon entering the central cell is shown in Fig. 10a for the 9 shell configuration. This spectrum is calculated by subtracting the spectra calculated from the simulation without atomic deexcitation from that with atomic deexcitation. Electrons falling within error of zero are disregarded. The effect of atomic deexcitation on the LET of secondary electrons entering the central cell is shown in Fig. 10b.

It can be seen from Fig. 10a that atomic deexcitation has the most effect on the energy spectra below 10 keV, with peaks around 6 keV and below 1 keV. The mean kinetic energy of secondary electrons is slightly decreased (approximately 1 keV lower) by the inclusion of atomic deexcitation in the simulation. Fig. 10b shows that atomic deexcitation increases the number of high LET electrons as expected, and has the most effect on the LET of secondary electrons in the case of a 1 μm thick NP shell.

5. Conclusions

This work was motivated by the experimental observation that Ta_2O_5 NPs tend to congregate as shells with different thicknesses in colonies of cancer cells. Based on this observation, different scenarios of cells/cell nuclei coated with NP shells were investigated in cellular colonies of limited size, in terms of local DER obtained under a 150 kVp irradiation, by means of Monte Carlo simulations.

The local DER becomes saturated with an increasing concentration of NPs and shell thickness for each considered scenario of shell pattern in the μ-phantom. The local DER reaches saturation when the NP shell thickness is larger than 5 μm. The local DER in individual cells in the μ-phantom is significantly increased when the Ta_2O_5 NPs are simulated in realistic shells configurations rather than in a homogeneous solution distribution between all cells with the same concentration of NPs.

Zygmanski et al. (2013) showed by means of Monte Carlo simulations that increasing gold NP clustering in X-ray radiotherapy translates to a nonlinear dose enhancement [27]. Our work differentiates from Ref [27] in the type of nanoparticle aggregate considered and in the shape of the aggregate, dictated by our experimental observations as shown in Section 2. Although the simulation geometry in Ref [27] is vastly different from that presented in the present work, the saturation result with increasing concentration and shell thickness observed in our cell population study is in agreement with the trend observed for the case of clustered gold NPs in solution. Our study further examines and compares the effect of a completely homogeneous distribution of NP materials as well as the magnitude of the effect of atomic deexcitation on the DER.

Recent advances included in the evolving physics models of Geant4 allow for the simulation of complete Auger cascades in version 10.2Beta, on top of the Auger electron emissions currently simulated in the version used in the present study [28]. As a possible future extension of this study it would be interesting to investigate the effect of full Auger electron cascades in proximity of the NP by using the most recent beta version of Geant4.

Upon considering the experimentally observed scenario of NP internalisation for concentrations in the range of 50–500 μg/mL, we concluded that only a very small partial volume of the total cell culture had a high local concentration of NPs. We modelled the experimentally observed scenario via a μ-phantom with effectively a non-uniform uptake distribution in our radiation transport simulations. The results of the simulations show that a non-uniform NP uptake leads to a huge local DER, but does not significantly change the DER averaged over the entire cell population. The non-uniform uptake model of NPs could therefore possibly explain the lack of increase in the DER with increasing concentration observed in cell study currently under review for publication [11]. In this case we could conclude that the enhancement of secondary electrons by Ta_2O_5 NP shells has the most effect on cells in close proximity to the shells with a saturation effect shown for high concentrations. The small changes in survival vs dose are obviously due to the entire cell culture and are therefore related to the average DER as well as the local saturation effect.

Acknowledgement

We would like to thank the University of Wollongong Information Technology Services (ITS) for computing time on the UOW High Performance Computing Cluster.

The authors acknowledge the financial support from the National Health and Medical Research Council (APP1084994).

References

[1] Hainfeld JF, Dilmanian FA, Zhong Z, Slatkin DN, Kalef-Ezra JA, Smilowitz HM. Gold nanoparticles enhance the radiation therapy of a murine squamous cell carcinoma. Phys Med Biol 2010;55:3045–59.

[2] Brown R, Tehei M, Oktaria S, Briggs A, Stewart C, Konstantinov K, et al. High-Z nanostructured ceramics in radiotherapy: first evidence of Ta_2O_5-induced dose enhancement on radioresistant cancer cells in an MV photon field. Part Part Syst Charact 2014;31(4):500–5.

[3] Jain S, Hirst DG, O'Sullivan JM. Gold nanoparticles as novel agents for cancer therapy. Br J Radiol 2012;85:101–13.

[4] McMahon SJ, Hyland WB, Muir MF, Coulter JA, Jain S, Butterworth KT, et al. Biological consequences of nanoscale energy deposition near irradiated heavy atom nanoparticles. Sci Rep 2011;10.

[5] Rahman WN, Bishara N, Ackerly T, He CF, Jackson P, Wong C, et al. Enhancement of radiation effects by gold nanoparticles for superficial radiation therapy. Nanomedicine 2009;5:136–42.

[6] Cifter G, Chin J, Cifter F, Altundal Y, Sinha N, Sajo E, Ngwa W. Targeted radiotherapy enhancement during electronic brachytherapy of accelerated partial breast irradiation (APBI) using controlled release of gold nanoparticles. Physica Med 2015;31(8):1070–4.

[7] Liu C-J, Wang C-H, Chen S-T, Chen H-H, Leng W-H, Chien C-C, et al. Enhancement of cell radiation sensitivity by pegylated gold nanoparticles. Phys Med Biol 2010;55:931.

[8] Treuel L, Jiang X, Nienhaus GU. New views on cellular uptake and trafficking of manufactured nanoparticles. J R Soc Interface 2013;10:20120939.

[9] McMahon SJ, Hyland WB, Brun E, Butterworth KT, Coulter JA, Douki T, et al. Energy dependence of gold nanoparticle radiosensitization in plasmid DNA. J Phys Chem C 2011;115:20160–7.

[10] Jain S, Coulter JA, Hounsell AR, Butterworth KT, McMahon SJ, Hyland WB, et al. Cell-specific radiosensitization by gold nanoparticles at megavoltage radiation energies. Int J Radiat Oncol Biol Phys 2011;79:531–9.

[11] Brown R, Corde S, Oktaria S, Konstantinov K, Rosenfeld A, Lerch M, et al. Nanostructures, concentrations and energies: An ideal equation to extend therapeutic efficiency on radioresistant 9L tumour cells using Ta2O5 ceramic nanostructured particles. Biomed Phys Eng Express 2016 [under review].

[12] Briggs A, Corde S, Oktaria S, Brown R, Rosenfeld A, Lerch M, et al. Cerium oxide nanoparticles: influence of the high-Z component revealed on radioresistant 9L cell survival under X-ray irradiation. Nanomedicine 2013;9:1098–105.

[13] Stewart C, Corde S, Rosenfeld A, Tehei M, Konstantinov K, McDonald M, et al. Engineering of bismuth oxide nanoparticles to induce differential biochemical activity in malignant and nonmalignant cells. Part Part Syst Charact 2014;31:960–4.

[14] Jones BL, Krishnan S, Cho SH. Estimation of microscopic dose enhancement factor around gold nanoparticles by Monte Carlo calculations. Med Phys 2010;37:3809–16.

[15] Agostinelli S, Allison J, Amako K, Apostolakis J, Araujo H, Arce P, et al. Geant4-a simulation toolkit. Nucl Instrum Methods Phys Res A 2003;506:250–303.

[16] Allison J, Amako K, Apostolakis J, Araujo H, Dubois PA, Asai M, et al. Geant4 developments and applications. IEEE Trans Nucl Sci 2006;53:270–8.

[17] Leung MKK, Chow JCL, Chithrani BD, Lee MJG, Oms B, Jaffray D. Irradiation of gold nanoparticles by X-rays: Monte Carlo simulation of dose enhancements and the spatial properties of the secondary electrons production. Med Phys 2011;38:624–31.

[18] Chow JCL, Leung MKK, Fahey S, Chithrani DB, Jaffray DA. Monte Carlo simulation on low-energy electrons from gold nanoparticle in radiotherapy. J Phys Conf Ser 2012;341.

[19] Li WB, Müllner M, Greiter MB, Bissardon C, Xie WZ, Schlatll H, Oeh U, Li JL, Hoeschen C. Monte Carlo simulations of dose enhancement around gold nanoparticles used as X-ray imaging contrast agents and radiosensitizers. Proc. SPIE Med Imaging 2014 Phys Med Imaging 2014. 9033.

[20] Poludniowski G, Landry G, DeBlois F, Evans PM, Verhaegen F. SpekCalc: a program to calculate photon spectra from tungsten anode X-ray tubes. Phys Med Biol 2009;54:N433.

[21] Chauvie S, Guatelli S, Ivanchenko V, Longo F, Mantero A, Mascialino B, et al. Geant4 low energy electromagnetic physics. IEEE Nucl Sci Conf R 2004;3:1881–5.

[22] Sempau J, Fernández-Varea JM, Acosta E, Salvat F. Experimental benchmarks of the Monte Carlo code PENELOPE. Nucl Instrum Methods Phys Res B 2003;207:107–23.

[23] Bernal MA, Bordage MC, Brown JMC, Davídková M, Delage E, El Bitar Z. Track structure modeling in liquid water: A review of the Geant4-DNA very low energy extension of the Geant4 Monte Carlo simulation toolkit. Physica Medica 2015;31(8):861–74.

[24] Stewart RD, Wilson WE, McDonald JC, Strom DJ. Microdosimetric properties of ionizing electrons in water: a test of the PENELOPE code system. Phys Med Biol 2002;47:79.

[25] Spirou SV, Makris D, Loudos G. Does the setup of Monte Carlo simulations influence the calculated properties and effect of gold nanoparticles in radiation therapy? Phys Med 2015;31(7):817–21.

[26] Berger MJ, Coursey JS, Zucker MA, Chang J. ESTAR, PSTAR, and ASTAR: Computer programs for calculating stopping-power and range tables for electrons, protons, and helium ions (version 1.2.3); 2005 04/04/2014; Available from: http://physics.nist.gov/Star.

[27] Zygmanski P, Liu B, Tsiamas P, Cifter F, Petersheim M, Hesser J, et al. Dependence of Monte Carlo microdosimetric computations on the simulation geometry of gold nanoparticles. Phys Med Biol 2013;58:7961–77.

[28] Incerti S, Suerfu B, Xu J, Ivantchenko V, Mantero A, Brown JMC, et al. Simulation of Auger electron emission from nanometer-size gold targets using the Geant4 Monte Carlo simulation toolkit. Nucl Instrum Methods Phys Res B 2016;372:91–101.

Appendix C

The following article [117] is derived from work presented in Chapter 4 of this thesis. My role in this project was the design and development of the Monte Carlo simulation study which forms the basis of this paper. All Monte Carlo simulations in this paper were performed by me, under the supervision of my principle supervisor, Dr Susanna Guatelli.

Sally McKinnon, Susanna Guatelli, Sebastien Incerti, Vladimir Ivanchenko, Moeava Tehei, Michael Lerch, Stéphanie Corde, Konstantin Konstantinov, Anatoly Rosenfeld (2016) "Local dose enhancement of proton therapy by ceramic oxide nanoparticles investigated with Geant4 simulations" *Physica Medica* 32(12): 1584-93.

Physica Medica 32 (2016) 1584–1593

Contents lists available at ScienceDirect

Physica Medica

journal homepage: http://www.physicamedica.com

Original paper

Local dose enhancement of proton therapy by ceramic oxide nanoparticles investigated with Geant4 simulations

Sally McKinnon [a], Susanna Guatelli [a,b,*], Sebastien Incerti [c,d], Vladimir Ivanchenko [e,f], Konstantin Konstantinov [b,g], Stéphanie Corde [a,h], Michael Lerch [a,b], Moeava Tehei [a,b,i], Anatoly Rosenfeld [a,b]

[a] Centre for Medical Radiation Physics, University of Wollongong, NSW, Australia
[b] Illawarra Health and Medical Research Institute, University of Wollongong, NSW, Australia
[c] CNRS/IN2P3, Centre d'Etudes Nucléaires de Bordeaux-Gradignan, UMR-5797, chemin du solarium, 33175 Gradignan, France
[d] Université Bordeaux, Centre d'Etudes Nucléaires de Bordeaux-Gradignan, UMR-5797, chemin du solarium, 33175 Gradignan, France
[e] Geant4 Associates International Ltd, United Kingdom
[f] Ecoanalytica, 119899 Moscow, Russian Federation
[g] Institute for Superconducting and Electronic Materials, University of Wollongong, NSW, Australia
[h] Radiation Oncology Department, Prince of Wales Hospital, Randwick, NSW, Australia
[i] Centre for Medical and Molecular Bioscience, University of Wollongong, NSW, Australia

ARTICLE INFO

Article history:
Received 7 January 2016
Received in Revised form 5 August 2016
Accepted 20 November 2016
Available online 1 December 2016

Keywords:
Nanoparticles
Proton therapy
Monte Carlo
Geant4

ABSTRACT

Nanoparticles (NPs) have been shown to enhance X-ray radiotherapy and proton therapy of cancer. The effectiveness of radiation damage is enhanced in the presence of high atomic number (high-Z) NPs due to increased production of low energy, higher linear energy transfer (LET) secondary electrons when NPs are selectively internalized by tumour cells. This work quantifies the local dose enhancement produced by the high-Z ceramic oxide NPs Ta_2O_5 and CeO_2, in the target tumour, for the first time in proton therapy, by means of Geant4 simulations. The dose enhancement produced by the ceramic oxides is compared against gold NPs. The energy deposition on a nanoscale around a single nanoparticle of 100 nm diameter is investigated using the Geant4-DNA extension to model particle interactions in the water medium. Enhancement of energy deposition in nano-sized shells of water, local to the NP boundary, ranging between 14% and 27% was observed for proton energies of 5 MeV and 50 MeV, depending on the NP material. Enhancement of electron production and energy deposition can be correlated to the direct DNA damage mechanism if the NP is in close proximity to the nucleus.

1. Introduction

Proton therapy is a highly conformal radiation therapy technique, widely used for the treatment of eye, prostate, lung and brain tumours. With respect to conventional photon or electron beam therapy, proton therapy has the advantage of higher treatment conformity due to the proton Bragg peak as well as higher radiobiological effectiveness (on average 1.1 as accepted currently in clinical practice) [1,2].

Damage to tumour cells from therapeutic irradiation occurs through direct and indirect mechanisms [3]. Direct damage occurs when secondary electrons hit DNA within the cell nucleus whereas indirect damage includes damage to DNA and other cell structures deriving from free radical production, including change of chemical properties within the cell. In proton therapy an increase in the number of already high-LET particles in the Spread Out Bragg Peak region will theoretically improve tumour control outcomes.

Nikjoo et al. [3] showed computationally the factors which contribute to the biological effectiveness of electrons, protons and alpha particles. This study shows that for a 4 MeV proton, 61% of DSBs are caused by direct damage, i.e. due to low energy δ-electrons, while 39% are due to indirect damage deriving from free radicals.

Nanoparticles (NPs) are materials or structures produced with sizes ranging from 1 nm to 100 nm [4]. NPs are currently studied as contrast agents, radiation protectors or sensitizers, and for drug delivery. Nanomaterials under investigation include gold, platinum, gadolinium and ceramic nanostructured particles [4–8]. The widespread investigation of gold (Au) NPs in radiation therapy enhancement is due to the relative biocompatibility at low concentrations and the high atomic number ($Z_{Au} = 79$). Extensive studies have presented the dose enhancement in X-ray radiation therapy

* Corresponding author at: Centre for Medical Radiation Physics, University of Wollongong, NSW, Australia.
E-mail address: susanna@uow.edu.au (S. Guatelli).

http://dx.doi.org/10.1016/j.ejmp.2016.11.112
1120-1797/

by the application of high-Z NPs, including investigations of the influence of particle size, methods to encourage uptake by cells, cell specific response, energy of incident radiation and dose [9–14].

Kilovoltage photon interaction with high-Z gold NPs results in enhanced photoelectron emission [15]. Increased emission of low energy secondary electrons causes a localized dose enhancement (within a short distance of the NP surface, due to the relative short range of the low energy enhancement electrons) and increased water radiolysis. If NPs are selectively accumulated within a tumour through internalization within tumour cells, the localized secondary electrons can target damage to the tumour cells. High-Z NPs are expected to have the highest dose enhancement under kilovoltage X-ray irradiation compared to higher energies, due to the higher mass energy absorption coefficient relative to water in this range. However, dose enhancement has also been observed in megavoltage studies [7,16].

In proton therapy an increase in low energy electron production is the result of physical proton or secondary electron interaction with a high density NP, and these enhancement electrons will induce further direct and indirect damage to cells. Experimental studies show enhancement of proton and heavy ion therapy by the means of NPs. Polf et al. [17] studied the enhancement of the relative biological effectiveness (RBE) in prostate tumour cells exposed to a 160 MeV proton beam (cells placed within the Spread Out Bragg Peak region) with and without internalized gold NPs of (44 ± 8) nm diameter compared to ^{60}Co irradiated control cells. These researchers found a potential 15–20% increase of the RBE of proton therapy due to the presence of gold NPs during treatment.

Porcel et al. [18] have shown enhanced damage to DNA in the presence of platinum NPs irradiated by fast helium ions, carbon ions or gamma rays. The number of SSB or DSB in plasmid DNA with and without platinum NPs was compared for different Linear Energy Transfer (LET) incident particles. They found that SSBs decreased with increasing LET of incident radiation, while DSBs increased, indicating more complex damage to DNA from higher LET particles with more dense secondary electron track structure. The action of water radicals was investigated by Porcel et al. [18] by including a radical scavenger to effectively eliminate DNA damage resulting from indirect action of radicals in the water. The study showed that more than 90% of damage enhancement after both gamma (^{60}Co, LET = 0.2 keV/μm) and C^{6+} (LET = 13 keV/μm) beam irradiations could be attributed to the action of free radicals. Liu et al. [19] reported the effect of increasing concentration of Au NP on the enhancement effect of hydroxyl radical production under X-ray or carbon ion irradiation. Porcel et al. [20] have also demonstrated the ability of gadolinium-based NPs to enhance the cell killing in helium and carbon heavy-ion therapy.

Kim et al. [21,22] investigated the enhancement of a 40 MeV therapeutic proton beam treating CT26 tumours in mice with the application of gold and iron NPs with diameter of (14 ± 1.2) nm and (10.6 ± 0.8) nm, respectively. NPs were administered intravenously and an increase in complete tumour regression ranging between 37% and 62% was observed when the Bragg Peak was located in the tumour. The production of free radicals within tumour cells was found to be enhanced with the application of gold or iron NPs.

In the context of dose enhancement, gold NPs have been reported to be effective, however these NPs have also shown significant toxicity at concentration as low as 100 μg/mL [23]. High-Z ceramic oxides now offer a prospective alternative to gold as dose enhancers [7]. These high-Z nanoceramics used for dose enhancement are known to be biocompatible materials and could be selectively tailored to protect normal cells while being toxic for tumour cells [24]. Furthermore, the oxide of these ceramics provides a linkage for the NPs to be functionalized and made to target tumour cells [25]. Ceramics have been also used in radiation imaging applications [26,27], emphasizing the research opportunities they present as theranostic materials.

Tantalum pentoxide (Ta_2O_5) is a ceramic compound which, when engineered as a nanostructured particle, has been shown to be an effective radiosensitizer for radiation resistant rat brain 9L cancer cells exposed to 10 MV photon irradiation [7]. The high-Z of tantalum ($Z_{Ta} = 73$) causes Ta_2O_5 to behave as a high-Z NP while it is also biocompatible. Brown et al. [7] found a sensitisation enhancement ratio (SER) of 1.33 with 50–70 nm Ta_2O_5 NPs in case of 10 MV X-ray irradiation.

Cerium oxide (CeO_2) NPs have been investigated for use as a radioprotector in cells under photon irradiation [28,29]. The application of a radioprotector allows for sufficient damage to tumour cells to be achieved while normal cells are less susceptible to the damage due to protective particles working to the advantage of normal cells. At the same time CeO_2 NPs are effectively high-Z NPs ($Z_{Ce} = 58$) and therefore will enhance secondary electron production in proportion to Z^n where n is 4–5 depending on photon energy [6]. The protective nature of these particles is deduced from their applicability as antioxidants, which outweighs the negative effect of increased production of secondary electrons due to their high Z.

Monte Carlo simulations are a useful tool to understand the physics mechanism of dose enhancement produced by NPs in radiotherapy and to characterise important associated physics quantities such as the energy deposition and the energy spectrum of the electrons emitted by the NP, to provide an insight both in the direct and indirect damage of radiation [11–13,25,26].

The dose enhancement produced by NPs in proton therapy has recently been studied by means of simulation studies [30–32]. Wälzlein et al. [30] studied the dose enhancement by various metallic NPs by means of a customised Monte Carlo simulation. Lin et al. [31] used a Geant4 based software tool, TOPAS, to simulate and compare the dose enhancement from a gold NP with incident proton or photon beams. Lin et al. [32] showed sensitizer enhancement ratios (SERs) are lower in proton therapy with gold NPs compared to kV and MV photon irradiation due to the lower probability of interaction with the NPs. This study also showed the effect of NP size on SER, with smaller NPs having a larger effect when the same weight of NPs is used.

Martínez-Rovira and Prezado [33] recently published a study examining nanoscale dose enhancement of gold and gadolinium NPs in proton therapy. This study reported a small dose enhancement local to NPs studied with a dependence on simulation geometry.

The goal of this work is to quantify for the first time the dose enhancement produced by novel ceramic oxide NPs such as Ta_2O_5 and CeO_2 in proton therapy. The dose enhancement produced by ceramic NPs is compared to gold NPs which have previously been shown by several studies to be dose enhancing in proton therapy [17,21–22,25–28].

2. Method

Simulations were performed using Geant4, version 10.1 [34,35]. Geant4 was adopted because it is the only open source and freely available general purpose code which allows to perform studies from dosimetry to micro- and nano-dosimetry. The simulation consisted of monoenergetic proton beams with energy of 5 and 50 MeV, alternatively. The proton energy range was selected to model a proton radiation field typical of the Spread Out Bragg Peak (SOBP) region of a prostate cancer treatment. As protons lose energy continuously with greater depth in water, the lower energy (5 MeV) protons in this study are representative of the protons

typically occurring in the distal part of the SOBP while the 50 MeV protons demonstrate the effect of NP closer to the surface of the patient, but still within the tumour target. Protons were originated on one side of a 200 μm sized water phantom and directed towards the centre of the NP as a pencil beam (null lateral size) or as a broad beam of 100 nm diameter.

The NP is modelled with a sphere of 100 nm diameter, set in the centre of the water phantom. The material of the NP was alternatively gold (Au), tantalum oxide (Ta_2O_5), cerium oxide (CeO_2) and liquid water.

Table 1 summarises the physics models and processes selected for each particle, in the NP and in the surrounding water medium.

The Geant4-DNA very low energy extensions [36,37], which are available for liquid water only, were adopted to model in detail event-by-event particle interactions down to approximately 10 eV for electrons and 100 eV for protons/hydrogen, in the water phantom.

The Low Energy Electromagnetic Physics Package, based on the Penelope model and adopting a condensed-history random-walk scheme approach, was selected to describe photon and electron interactions in the NP. The Geant4 Urban model was selected to describe the multiple scattering of protons, electrons and ions in the NP. The threshold of production of secondary electrons in the NP was set to 100 eV, corresponding to the recommended low energy limit of the Penelope-based physics models [38]. Photons have the same physics models throughout the experimental set-up (in the NP and in the surrounding liquid water medium). Atomic de-excitation (fluorescence and Auger electrons) was modelled in the whole experimental set-up, allowing atomic de-excitation electron production below the 100 eV threshold.

Fig. 1a shows the track (represented in blue) of a 50 MeV proton in the NP and in the surrounding liquid water medium. The track structure of secondary electrons, shown in red, is more detailed in the liquid water due to the physics models adopted in this medium, the Geant4-DNA extension, describing particle interactions event by event. Physics models based on condensed history approach used within the NP region result in tracking steps as multiple interactions are simulated in a single step.

The proton track structure was studied in terms of radial energy deposition in slices around the proton tracks, calculated in cylindrical shells (see Fig. 1b, slices 1–4). The slices are 100 nm wide along the direction of the incident proton beam and the NP is located in slice 2, shown in Fig. 1b. The energy deposition was then scaled by the mass of the water of the corresponding cylindrical shell to obtain the dose. In all the presented results, the dose enhancement is expressed as the ratio of dose calculated with and without NP.

Table 1
Physics processes describing the interactions of the particles in the NP and in the surrounding liquid water medium in the Geant4 simulation. The models are indicated when required in parenthesis.

Particle	NP (*Condensed-history random-walk scheme*)	Water (*Geant4-DNA very low energy extension*)
Proton	Ionisation, multiple scattering	Ionisation, excitation, charge decrease
Electron	Multiple scattering, ionisation (*Penelope*), bremsstrahlung (*Penelope*)	Elastic scattering (*partial wave model*), excitation, ionisation, vibrational excitation, attachment
H, α, He^+, He	Ionisation, multiple scattering	Excitation, ionisation, charge increase and decrease
Photon	Rayleigh scattering (*Penelope*), Photoelectric effect (*Penelope*), Compton scattering (*Penelope*), gamma conversion (*Penelope*)	

The spectra of secondary electrons produced inside the NP and escaping from it were also examined for assessment of the LET of the secondary electrons.

Between 1×10^5 and 5×10^5 events were simulated for each NP material, depending on the incident proton energy. The uncertainties are smaller in the case of lower energy protons due to the increased number of interactions in NP occurring with higher LET protons, thus producing higher statistics.

The calculated uncertainties of the results deriving from this work are statistical only and the uncertainties of the underlying physics models should also be taken into account for a complete discussion of the results. At this stage it is not possible to quantify the uncertainties affecting the physics cross sections adopted in this work given the lack of nanodosimetric experimental measurements in liquid water, however, Incerti et al. [36] compared the cross sections of the Geant4 extension against existing experimental data in water vapour providing an appreciation of the plausibility of the implemented physics models. The simulation is modelling an ideal case of protons directly incident on the NP, where in reality direct interaction of protons with NP imbedded in a tumour will have a lower probability.

3. Results

3.1. Effect of gold NPs on the radial dose distribution

The radial dose distribution was calculated in slices 1, 2 and 3 shown in Fig. 1b and scaled to the number of incident protons in the broad beam. The radial dose distribution in 100 nm wide bins within these slices is shown in Fig. 2 in case of Au NPs. The ratio of dose calculated with and without the Au NP is reported as well (shown in red in Fig. 2).

The relatively short range of secondary electrons produced from the incident 5 MeV proton beam and enhanced by the presence of NPs results in most energy being deposited in proximity to the NP. The majority (more than 99%) of the energy is deposited within the first 300 nm from the beam centre in the water slices (Fig. 2a and c). More than 95% of energy is deposited from the NP edge out to 300 nm in slice 2, containing the NP. The dose drops approximately 97%, from (9.35 ± 0.07) Gy to (0.31 ± 0.01) Gy, between the edge of the Au NP and 300 nm distance, in slice 2. Although the dose drops off sharply in the first few hundred nanometres, the relative difference between the dose distribution with the Au NP compared to water (shown in red by the ratio of the dose plots) remains significant even at distances up to 1 μm from the central axis, although as can be seen from the increase in the error bars the number of events depositing energy at this distance is low. Therefore the radial dose distribution produced by the NP is examined up to 300 nm distance in the following sections as this is the region of most interest in the study of dose enhancement of primary proton tracks.

3.1.1. Effect of proton energy

Radial dose distribution in 10 nm wide bins in slice 2, containing the NP as shown in Fig. 1b, for 5 MeV and 50 MeV incident broad proton beams, are shown in Fig. 3 as well as the calculated dose enhancement ratio. Radial dose local to a gold NP was enhanced for each proton beam energy under study, as shown in Fig. 3 insets. The absolute value of the dose deposited is much higher in the case of the lower energy proton beam due to the higher LET of these protons. The distribution of delta-electrons produced will be inversely dependent on the energy of the incident particle [39]. The approximately 10-fold increase in energy deposited when the proton energy is decreased by a factor of 10

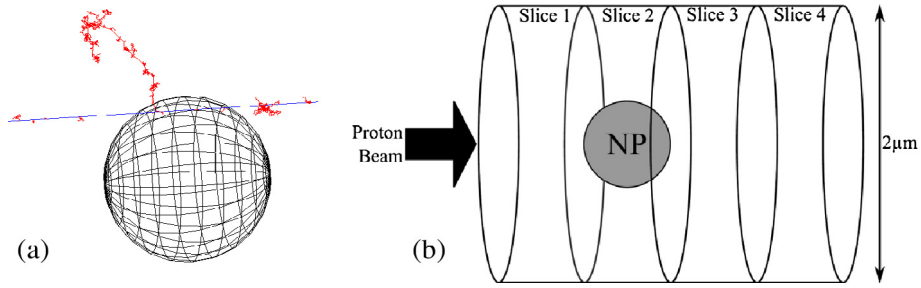

Fig. 1. Simulation geometrical set-up. An example 50 MeV proton (blue) and secondary electron tracks (red) through a 100 nm diameter gold NP and surrounding water medium (a). The radial energy deposited is calculated around the proton beam direction, in 100 nm thick cylindrical slices (b). (For interpretation of the references to colour in this figure legend, the reader is referred to the web version of this article.)

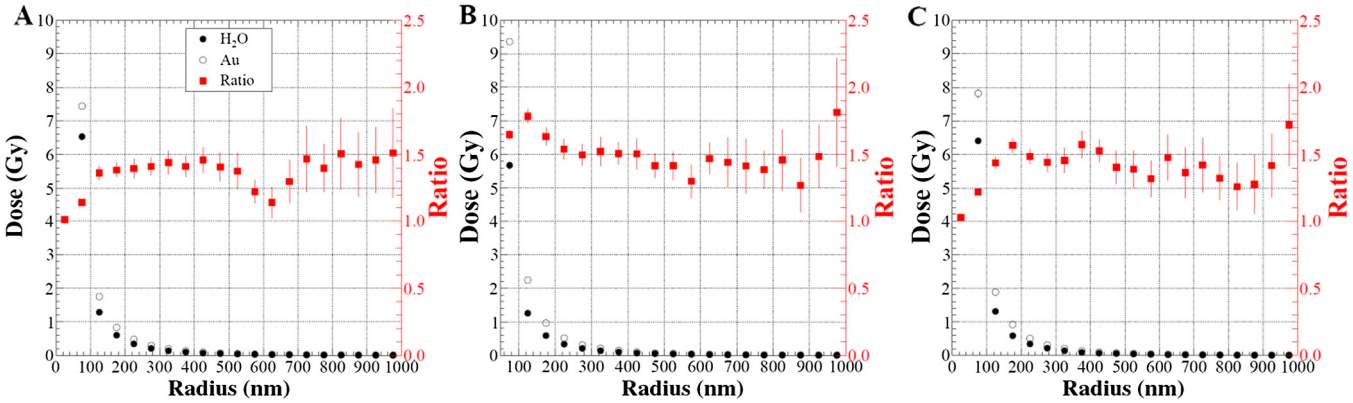

Fig. 2. Dose enhancement in 100 nm bins in slice 1 (A), slice 2 (B), and slice 3 (C) with a 5 MeV proton beam incident on a Au NP (open circles) and in water (solid circles), per incident proton. The ratio of the dose calculated with and without the Au NP is shown on the Y axis in red on the right of the plots. (For interpretation of the references to colour in this figure legend, the reader is referred to the web version of this article.)

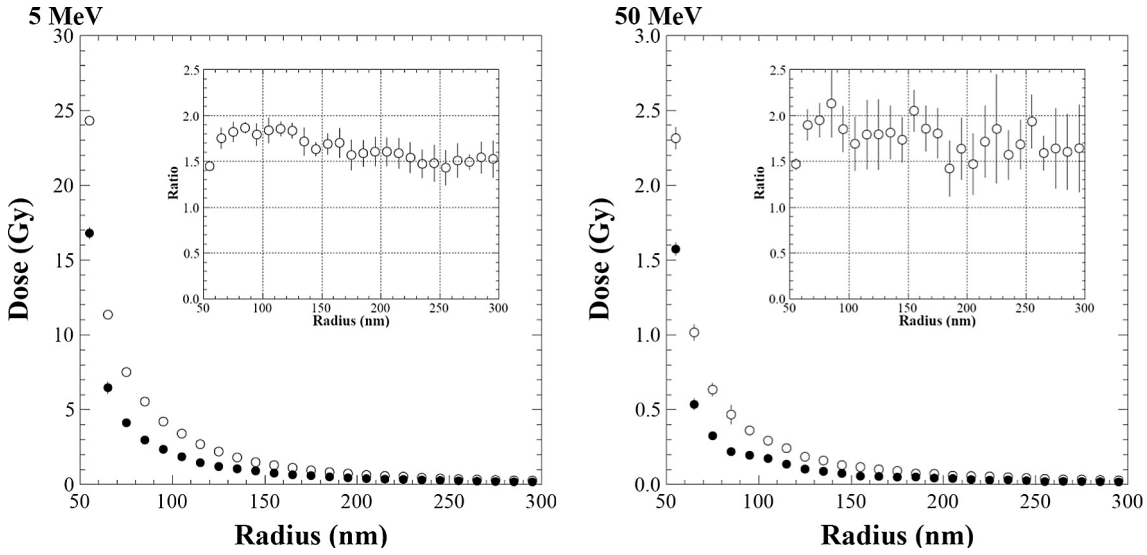

Fig. 3. Dose enhancement in slice 2 (see Fig. 1b) with a 5 MeV and 50 MeV proton broad beam incident on a Au NP (open circles) and a water sphere (solid circles), per incident proton.

(from 50 MeV to 5 MeV) is evidence in the simulation of this expected behaviour.

In the case of the 5 MeV proton beam, Fig. 3 shows the dose enhancement ratio increases from the NP edge to a maximum value of (1.87 ± 0.06) at 30 nm from the NP edge (in slice 2) and remains above 1.5 for several hundred nanometres. The 50 MeV proton beam shows a similar behaviour, reaching a maximum ratio of (2.1 ± 0.4) at 30 nm from the NP edge.

The radial dose distribution with respect to depth of slice is shown in Fig. 4. The figures compare energy deposition between slices 1–4 with a gold NP in slice 2. The figure shows higher radial energy deposition in the slice containing the NP (slice 2) compared to the slices upstream or downstream of the NP. This happens because the low energy electrons produced in the NP deposit energy locally to the NP. A similar behaviour is observed in both the 5 MeV and 50 MeV proton beams, demonstrating highest

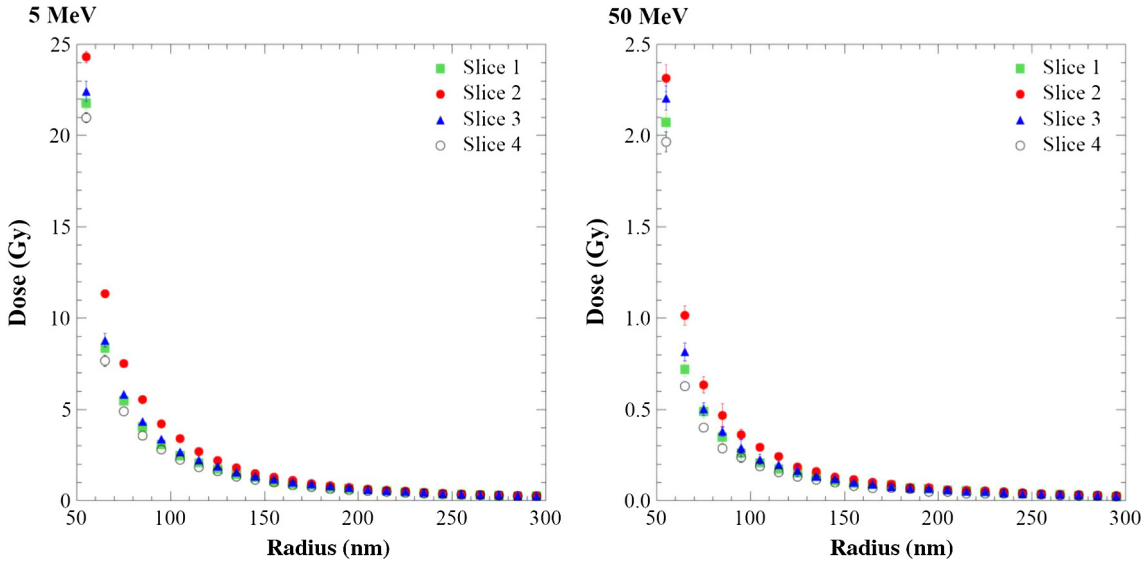

Fig. 4. Comparison of radial dose distribution in water in slice 1 (green squares), slice 2 (red solid circles), slice 3 (blue triangles) and slice 4 (open circles) (as shown in Fig. 1b) per incident proton with a broad 5 MeV and 50 MeV proton beam incident on a gold NP. (For interpretation of the references to colour in this figure legend, the reader is referred to the web version of this article.)

energy deposition in slice 2, followed by slice 3 (downstream of the NP) and then slice 1 (upstream of the NP).

3.1.2. Effect of beam geometry

The effect of changing the beam geometry from broad beam, incident uniformly on the NP, to a pencil beam directed towards the centre of the NP is shown in Fig. 5. It can be observed that the broad beam configuration is characterised by a higher dose enhancement in slice 2. This happens due to the short range of most of the secondary electrons produced by protons in the NP. Low energy secondary electrons escape the NP if generated by proton tracks close to the surface of the NP. In the case of the pencil beam only higher energy secondary electrons are likely to escape the NP and their partial contribution to the radial dose is much less.

3.1.3. Study of different NP materials

A comparison of the radial dose distribution for different NP materials is shown in Fig. 6. The radial dose is shown in each of the four slices (see Fig. 1b) around the NPs. The ratio of dose calculated with and without the NP is represented as well.

The radial dose is enhanced laterally to the NP as well as upstream and downstream of the NP for each of the materials investigated. Radial dose enhancement is most pronounced in the slice containing the NP for Au, CeO_2 and Ta_2O_5 NPs. Significant enhancement is obtained up to 100 nm behind the NP for the Au, Ta_2O_5 and CeO_2 NPs. Dose enhancement upstream of each NP (slice 1) is due to enhanced backscattering of low energy electrons from high Z NPs.

The Au NP offers the greatest dose enhancement of the materials studied. This is due to the higher density of gold (19.3 g/cm^3) compared to Ta_2O_5 (8.2 g/cm^3) or CeO_2 (7.2 g/cm^3). The cross section of production of secondary electrons is dependent on the density of the medium and inversely dependent on the square of the velocity of the incident particle [39].

Table 2 shows the dose enhancement in water due to presence of the NPs under study, integrating the radial dose over slices 1, 2 and 3 of the water phantom, shown in Fig. 1b, up to a radius of 1 μm, in the simulation geometry (equating to a sensitive volume of 0.3 μm^3). The dose enhancement is calculated omitting bins within 50 nm radius in slice 2, as they contain the NP (reducing

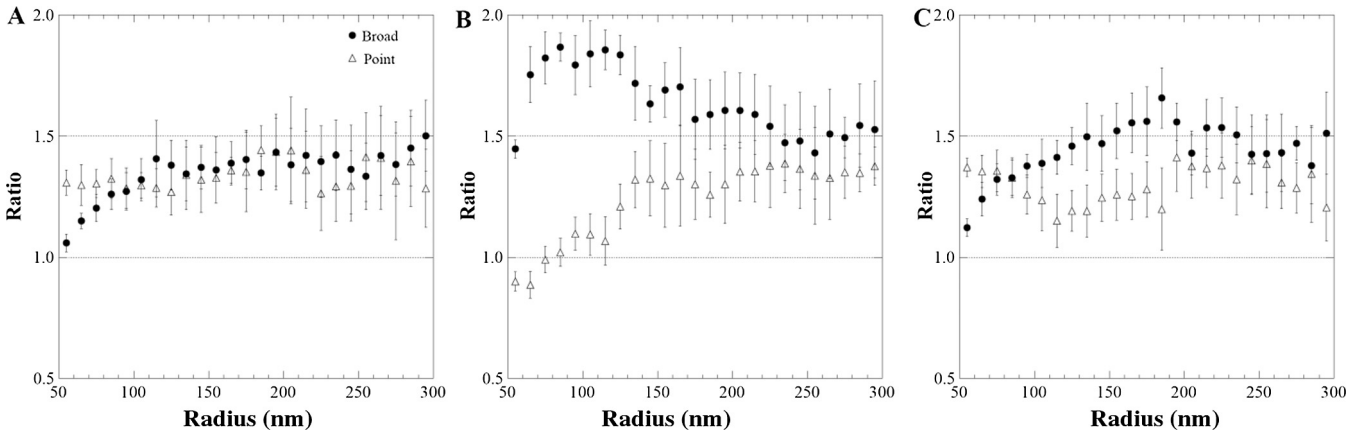

Fig. 5. Ratio of radial dose in water per incident proton with and without the gold NP, for a 5 MeV proton beam incident as a pencil beam (triangles) or a broad beam (black circles). (A): slice 1; (B): slice 2; (C): slice 3 (see Fig. 1b).

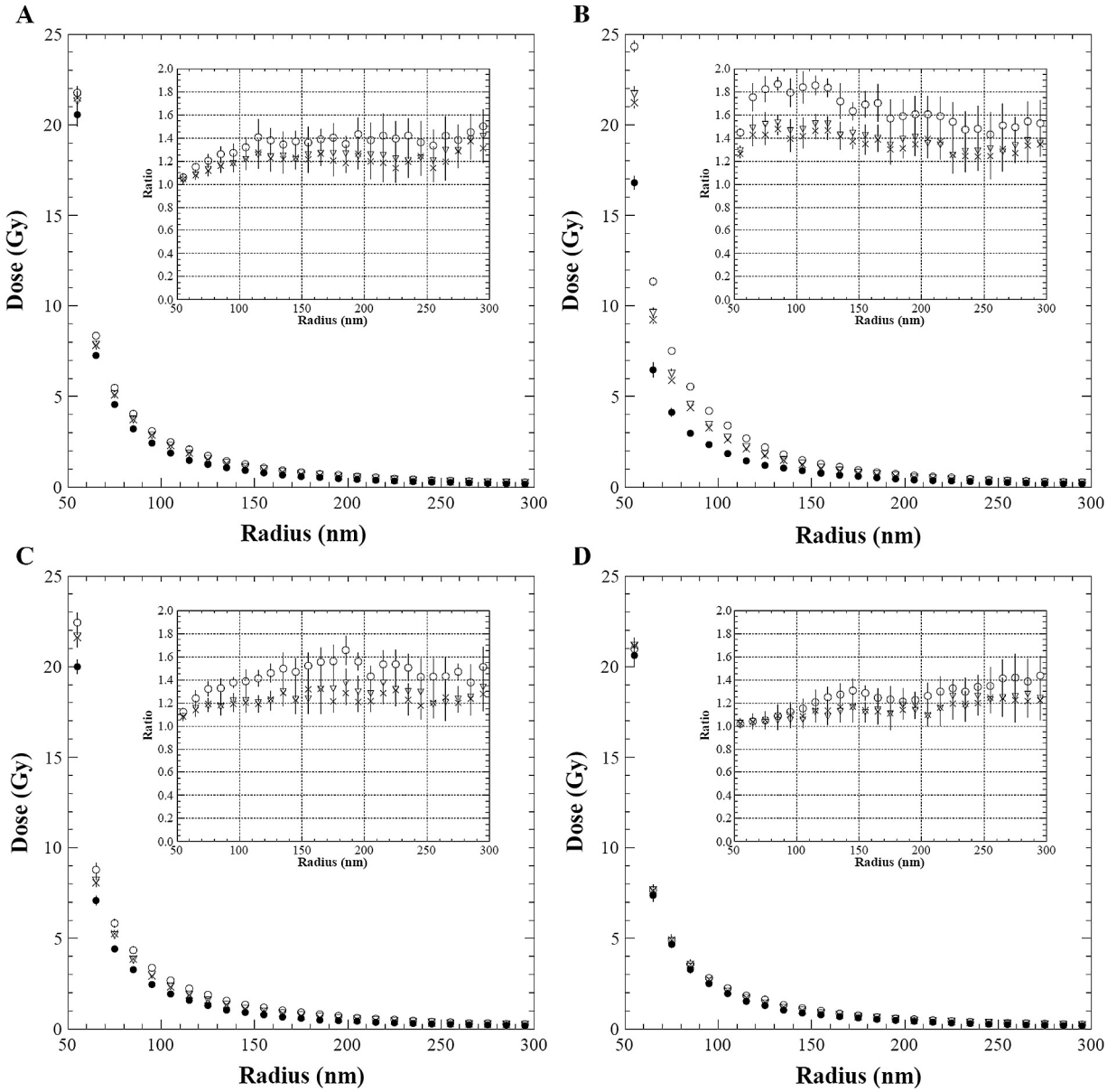

Fig. 6. Radial dose distribution deriving from a 5 MeV proton broad beam incident without NP (solid circles), Au NP (open circles), CeO_2 NP (crosses) and Ta_2O_5 NP (triangles) per incident proton. Comparison of radial dose in slice 1 (A), slice 2 (B), slice 3 (C) and slice 4 (D) (see Fig. 1b). The insert shows radial dependence of the ratio of dose in water calculated with and without NP.

Table 2
Dose enhancement expressed as a percentage of $\frac{D_{with\ NP} - D_{water}}{D_{water}}$, where $D_{with\ NP}$ and D_{water} are doses calculated with and without the NP, integrated over the water cylinder represented in Fig. 1b. The statistical uncertainty is below 1%.

NP material	5 MeV (%)	50 MeV (%)
Au	26	27
Ta_2O_5	16	16
CeO_2	14	15

the sensitive volume by a small amount). Similar results were obtained with a 50 MeV proton beam.

The average dose enhancement, for both of the proton energies considered, is (26.4 ± 0.4)% for Au NP, (16.15 ± 0.04)% for Ta_2O_5 NP, and (14.5 ± 0.2)% CeO_2 NP. Atomic deexcitation accounted for less than 1% of the dose enhancement from gold in this volume and particular size of NPs, as low energy electrons deposit energy very close to the NP surface and therefore the resulting enhancement is not significant when all energy deposited is averaged over the volume of the cylindrical slice.

3.2. Study of secondary electron spectra

Secondary electrons were created in the NP above an energy threshold of 100 eV, when originated by electron ionisation. When originated by proton ionisation, the threshold of production of secondary electrons is fixed by default in Geant4 v10.1 to the mean excitation energy of the materials (for example 790 eV for gold). Any secondary electrons with energy below this threshold are not created and their energy is treated in the simulation as being locally deposited energy at the point of interaction of the proton.

Atomic deexcitation electrons originated with energy below 100 eV cut are transported in the high-Z NP regardless of the simulation cuts by using the UI command */process/em/deexcitationIgnoreCut true* to effectively ignore the cut and transport

electrons down to 0 eV in the special case of atomic deexcitation processes. Although the recommended low energy limit of physical validity of the Penelope physics models is 100 eV to describe electron, positron and photon interactions, our adopted strategy was to transport Auger electrons with energy below this recommended threshold to obtain a first indication of their effect on the energy deposition in the proximity of the NP. This choice was dictated by the current lack in Geant4 of detailed event by event physics models addressed to energies below 100 eV in the NP materials under study.

The number of secondary electrons produced within the NP and escaping from it was calculated. Fig. 7 shows the secondary electron spectra emitted from the three different NPs, compared to water.

The number of secondary electrons increases with the placement of a Au, Ta_2O_5 or CeO_2 NP, compared to water, as expected. Fig. 7 shows that low energy electrons dominate the spectrum; approximately 50%, 60% and 70% of the escaping secondary electrons having kinetic energy of less than 1 keV with a proton beam incident on a Au, Ta_2O_5 and CeO_2 NP, respectively. These values are averaged over the proton energies studied and compare to approximately 90% of secondary electrons with kinetic energy of less than 1 keV escaping from the equivalent volume of water. It should be noted that the accuracy of these results is limited by the fact that a part of the difference in the low energy spectra with and without NP occurs due to the internal cut in the proton ionisation model implemented in Geant4, as is evident in the spectra below 1 keV (at the mean excitation energy of each NP material) in Fig. 7. The results may be refined in the future provided there will be a more accurate proton ionisation model at low energies.

Due to the majority of electrons having kinetic energy below 1 keV, secondary electrons escaping the NP predominantly deposit energy locally. The Au NP is characterised by the highest number of secondary electrons emitted, compared to Ta_2O_5 and CeO_2, however the lower densities of Ta_2O_5 and CeO_2 with respect to Au allows a greater proportion of secondary electrons created within the NPs to escape. The range of a 10 keV electron (approximate maximum energy of secondary electrons generated by a 5 MeV incident proton) in water is 2.5 μm whereas in gold it is only around 410 nm [40]. Most secondary electrons have much lower energy than this and would therefore have even shorter range in gold, leading to an increased number of these electrons being absorbed by the NP when the beam is incident on the centre of the particle. A simulation of the range in water with Geant4-DNA cross-sections of 1 keV electrons from an isotropic source shows that all energy is deposited within a (150 ± 12) nm radius sphere around the source. This means that most energy from secondaries emitted from the NP is deposited within a short range of the NP surface.

(31 ± 2)% of electrons created within the gold NP escape the NP compared to (58 ± 1)% and (57.8 ± 0.5)% escaping Ta_2O_5 and CeO_2 NPs, respectively. This proportion becomes (92.2 ± 0.1)% when the NP is substituted with a water sphere of the same dimensions, due to the longer range of low energy electrons in water compared to in the NPs under study. The average number of electrons produced and subsequently leaving the NP as a ratio of the number of electrons leaving a water sphere, across both of the proton energies under investigation, was (2.6 ± 0.5), (1.5 ± 0.1), and (1.8 ± 0.1) with a Au, Ta_2O_5, or CeO_2 NP, respectively.

3.3. Effect of atomic deexcitation

The inclusion of atomic deexcitation in the physics processes has only a minor effect on dose enhancement in this study. Fig. 8 shows the effect on secondary electron spectra and subsequent radial dose distribution in slices surrounding a Au NP, with a 5 MeV incident proton beam. Atomic deexcitation electrons are originated with discrete energy spectrum up to approximately 8 keV, however more than 70% fall below 1 keV and approximately 50% have kinetic energy below 200 eV.

The Auger electrons form a small part of the total number of electrons emitted from the NPs, thus not contributing significantly to the energy deposited in the water around the NP. The total dose enhancement within the previously described 1 μm radius, 300 nm long water cylinder (slices 1–3 in Fig. 1b) increases from (25.3 ± 0.3)% to (26.0 ± 0.3)% in the case of a Au NP with 5 MeV incident protons. The effect is small because of the low number of Auger electrons produced compared to ionisation electrons, and the short range of their effect.

A simulation of the range in water with Geant4-DNA cross-sections of 100 eV electrons from an isotropic source shows that all energy is deposited within 30 nm radius sphere. This

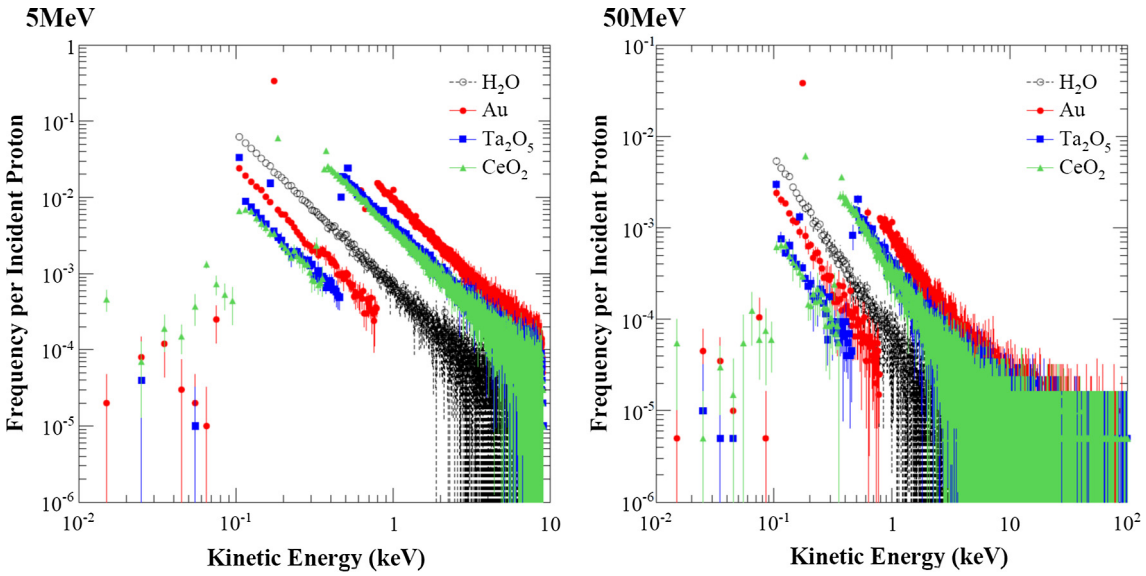

Fig. 7. Spectra of the secondary electrons leaving the NP with a 5 and 50 MeV incident proton broad beam (left and right panels, respectively), in comparison with electron spectra generated by the same initial kinetic energy protons in water (open circles). The NPs are Au, Ta_2O_5 and CeO_2.

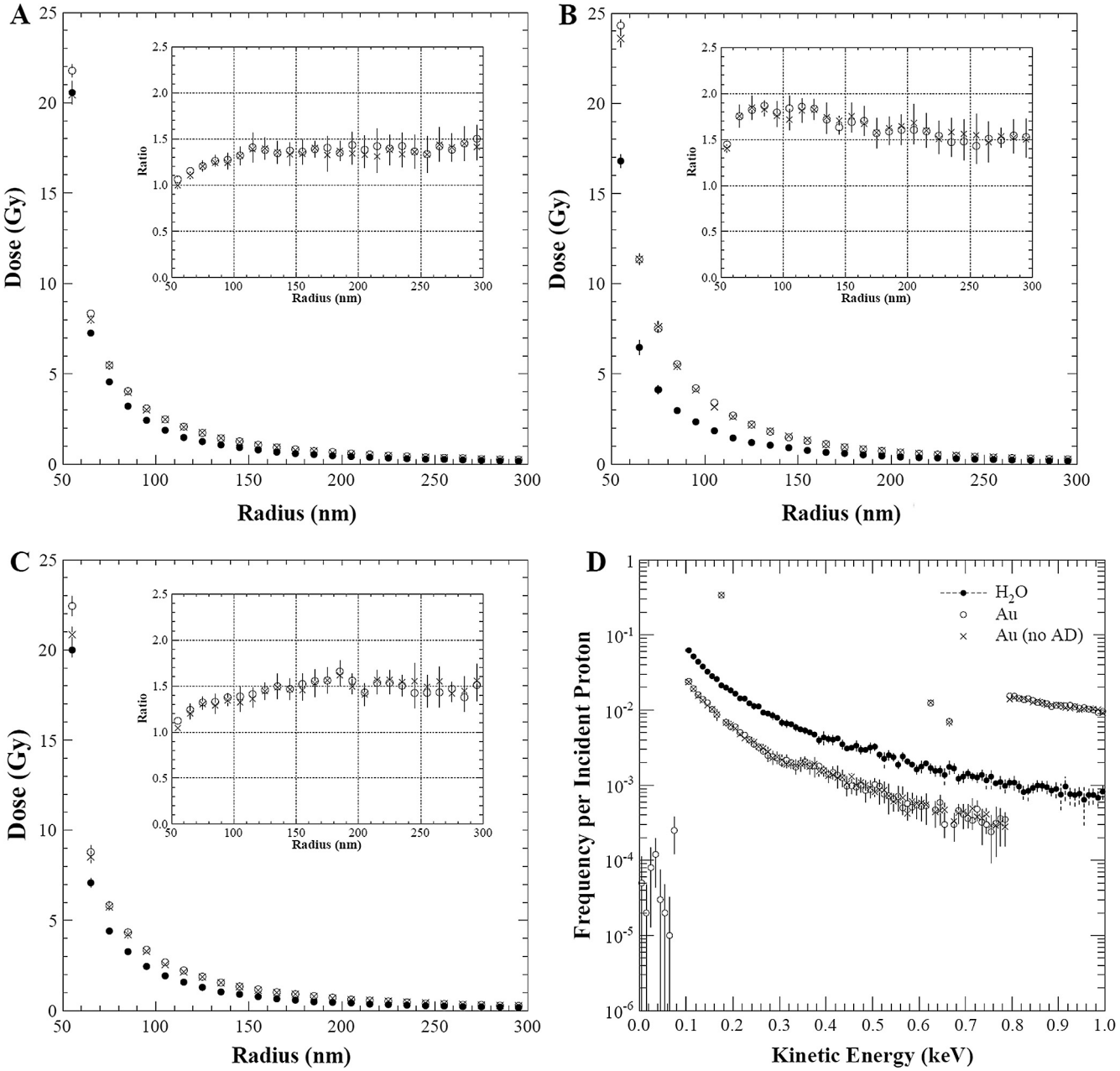

Fig. 8. Radial dose distribution in slice 1 (A), slice 2 (B), and slice 3 (C) and secondary electron spectra leaving the NP (D) with (circles) and without atomic deexcitation (crosses, no AD) for 5 MeV protons incident on Au NP, compared to water (black circles).

means that most energy from low energy atomic deexcitation electrons is deposited close to the NP surface, within 30 nm. In this simulation study the dose enhancement in the first 30 nm beyond the Au NP surface is approximately 5% when atomic deexcitation is modelled.

4. Discussion

This study shows that the number of interactions an incident proton or secondary electron encounters is increased compared to water for all NP materials. The dose enhancement in the region around a high-Z NP is due to an increased number of secondary electrons transporting energy to the surrounding water volume. This increase in secondary electrons is due to the increased number of ionizations in the NP. In the case of an incident proton beam, the majority of Auger electrons have a kinetic energy below 1 keV, in agreement with Wälzlein et al. [30], and contribute a small fraction to the total number of secondary electrons, as the major part is originated by proton and electron ionisation. Increase in energy deposition by Auger electrons within 30 nm of the NP surface was found to be approximately 5%. The greatest effect from atomic deexcitation is shown to be in the first few tens of nm of the radial dose distribution and this agrees with the results of Wälzlein et al. [30], reporting high dose enhancement within the first 5 nm from the surface of the NP however the small total effect on dose enhancement observed in this study is in agreement with the results reported by Martínez-Rovira and Prezado [41].

The secondary electron production due to the presence of the NPs, increases by factors of (2.6 ± 0.5), (1.5 ± 0.1), and (1.8 ± 0.1) for Au, Ta_2O_5, or CeO_2 NPs respectively. As the secondary electron spectra show, proton interactions produce a large number of higher LET electrons with energy lower than 1 keV.

The benefit of proton therapy is due to the proton's densely ionising track, especially at low energy, in the Bragg peak region. The large number of low energy electrons can result in complex damage to DNA. An increase in the production of low energy secondary electrons due to the placement of a NP close to the nucleus, and thus to radiosensitive DNA, or close to other sensitive cell structures enhances the already high radiobiological effectiveness of low energy protons at the distal part of the Spread Out Bragg Peak. The average local dose enhancement within a cylinder (300 nm long, 1 μm radius) was observed to be (26.4 ± 0.4)% for Au NP, (16.15 ± 0.04)% for Ta_2O_5 NP, and (14.5 ± 0.2)% CeO_2 NP. The local dose enhancement around the CeO_2 NP indicates this material has dose enhancement effects that are in counteraction to the free radical scavenging properties discussed in the literature.

The short range of the low energy electrons emitted from the NP would necessitate the NP being relatively close (within μm scale) to critical structures within the cell to induce direct DNA damage. For this reason, coupled with sub μm dimensions of fabricated NPs, nanodosimetric track structure simulations are an important investigation tool to understand the physical effects of NP dose enhancement in radiotherapy, however event by event particle tracking is currently not implemented in Geant4 in solid state materials, excluding silicon. Given the limitations of the physics models adopted when describing particle interactions in the NPs (based on a condensed-history, random-walk scheme approach), the results of this project are intended to provide a basic physics mechanism understanding of the dose enhancement produced by NPs and a first comparison of ceramic NP materials with respect to gold. The results shown in this study should be refined in the future with inclusion of more sophisticated physics models for a more detailed description of particle tracks in NP materials as well as a more detailed study of variable NP shape and size as well as simulation geometry and beam configuration. The plasmon interactions [42] in the NPs should also be modelled in the simulation to study their possible effect on the dose enhancement.

A limitation of this work is that the Geant4 proton ionisation does not produce secondary electrons with kinetic energy below the mean ionisation and excitation energy I of the NP material. The addition of new proton models simulating secondary electrons with energy below I may affect the dose enhancement observed in the vicinity of NP.

The dose enhancement ratio demonstrated in the present study shows a maximum value of approximately 2 for 5 MeV protons lateral to the Au NP (slice 2 of Fig. 1b). This result is comparable with the results of the study by Wälzlein et al. [30] although there are differences in the geometrical set-up and in the physics modelling of the simulations. The study reported by Martínez-Rovira and Prezado [33] showed a smaller dose enhancement than in previous studies and the study presented in this paper. This is attributable to the differences in simulation geometry and beam configuration.

5. Conclusion

This work shows that the fundamental concept of NP enhancement in proton therapy is evident on a nanoscale in the ideal case of protons incident directly on the NP. Therefore biological effectiveness of proton therapy may be increased due to this localized increase in secondary electron density, provided an adequate concentration of NPs in the tumour. The present study has shown the applicability of novel ceramic oxide NPs to the local dose enhancement in proton therapy, by the comparison with the known gold local dose enhancer. The dose enhancement occurs in the presence of Au, Ta_2O_5 or CeO_2 NPs with incident proton broad beams.

Further work in this project includes the modelling of the production and transport of free radicals [43]. Hadronic interactions should also be modelled in the next stage of the study to evaluate the effect of these interactions in the NP dose enhancement.

Recent advances in the latest release of Geant4 (version 10.2Beta) allows for the simulation of complete Auger cascades, on top of the Auger electron emissions currently simulated in the version used in the present study [44] and the inclusion of these cascades would be an interesting addition to the simulation in the future.

Acknowledgement

We would like to thank the University of Wollongong Information Technology Services (ITS) for computing time on the UOW High Performance Computing Cluster.

References

[1] Paganetti H. Proton therapy physics. In: Webster JG, Tabakov S, Ng K-H, editors. Series in medical physics and biomedical engineering. Boca Raton: CRC; 2012.
[2] Paganetti H et al. Relative biological effectiveness (RBE) values for proton beam therapy. Int J Radiat Oncol Biol Phys 2002;53(2):407–21.
[3] Nikjoo H et al. Quantitative modelling of DNA damage using Monte Carlo track structure method. Radiat Environ Biophys 1999;38(1):31–8.
[4] Jain S, Hirst DG, O'Sullivan JM. Gold nanoparticles as novel agents for cancer therapy. Br J Radiol 2010;85(1010):101–13.
[5] Porcel E et al. Platinum nanoparticles: a promising material for future cancer therapy? Nanotechnology 2010;21(8).
[6] Briggs A et al. Cerium oxide nanoparticles: influence of the high-Z component revealed on radioresistant 9L cell survival under X-ray irradiation. Nanomed Nanotechnol Biol Med 2013;9(7):1098–105.
[7] Brown R et al. High-Z nanostructured ceramics in radiotherapy: first evidence of Ta_2O_5-induced dose enhancement on radioresistant cancer cells in an MV photon field. Part Part Syst Charact 2014;31(4):500–5.
[8] Sancey L et al. The use of theranostic gadolinium-based nanoprobes to improve radiotherapy efficacy. Br J Radiol 2014;87(20140134).
[9] Kong T et al. Enhancement of radiation cytotoxicity in breast-cancer cells by localized attachment of gold nanoparticles. Small 2008;4(9):1537–43.
[10] Hainfeld JF et al. Gold nanoparticles enhance the radiation therapy of a murine squamous cell carcinoma. Phys Med Biol 2010;55(11):3045–59.
[11] Jones BL, Krishnan S, Cho SH. Estimation of microscopic dose enhancement factor around gold nanoparticles by Monte Carlo calculations. Med Phys 2010;37(7):3809–16.
[12] McMahon SJ et al. Biological consequences of nanoscale energy deposition near irradiated heavy atom nanoparticles. Sci Rep 2011;1.
[13] Chow JCL et al. Monte Carlo simulation on low-energy electrons from gold nanoparticle in radiotherapy. J Phys: Conf Ser 2012;341(1).
[14] Cifter G et al. Targeted radiotherapy enhancement during electronic brachytherapy of accelerated partial breast irradiation (APBI) using controlled release of gold nanoparticles. Physica Med 2015;31(8):1070–4.
[15] Butterworth KT et al. Physical basis and biological mechanisms of gold nanoparticle radiosensitization. Nanoscale 2012;4(16):4830–8.
[16] Jain S et al. Cell-Specific Radiosensitization by Gold Nanoparticles at Megavoltage Radiation Energies. Int J Radiat Oncol Biol Phys 2011;79(2):531–9.
[17] Polf JC et al. Enhanced relative biological effectiveness of proton radiotherapy in tumor cells with internalized gold nanoparticles. Appl Phys Lett 2011;98(19).
[18] Porcel E et al. Nano-sensitization under gamma rays and fast ion radiation. J Phys: Conf Ser 2012;373(1).
[19] Liu Y et al. The dependence of radiation enhancement effect on the concentration of gold nanoparticles exposed to low- and high-LET radiations. Physica Med 2015;31(3):210–8.
[20] Porcel E et al. Gadolinium-based nanoparticles to improve the hadrontherapy performances. Nanomed Nanotechnol Biol Med 2014;10(8):1601–8.
[21] Kim JK et al. Therapeutic application of metallic nanoparticles combined with particle-induced X-ray emission effect. Nanotechnology 2010;21(42).
[22] Kim JK et al. Enhanced proton treatment in mouse tumors through proton irradiated nanoradiator effects on metallic nanoparticles. Phys Med Biol 2012;57(24):8309–23.
[23] Butterworth K et al. Evaluation of cytotoxicity and radiation enhancement using 1.9 nm gold particles: potential application for cancer therapy. Nanotechnology 2010;21(29).
[24] Stewart C et al. Engineering of bismuth oxide nanoparticles to induce differential biochemical activity in malignant and nonmalignant cells. Part Part Syst Charact 2014;31(9):960–4.
[25] Bogusz K et al. Synthesis of potential theranostic system consisting of methotrexate-immobilized (3-aminopropyl)trimethoxysilane coated α-Bi_2O_3 nanoparticles for cancer treatment. RSC Adv. 2014;4:24412–9.
[26] Chan D et al. Radiopacity of tantalum oxide nanoparticle filled resins. Dent Mater 1999;15(3):219–22.

Appendix D

The following article [101] is derived from work presented in Chapter 4, Section 4.2 of this thesis. My role in this project was the design and development of the Monte Carlo simulation study which forms the basis of this paper. All Monte Carlo simulations in this paper were performed by me, under the supervision of my principle supervisor, Dr Susanna Guatelli and the research team at the MBN Research Center, Frankfurt am Main, Germany.

Alexey Verkhovtsev, Sally McKinnon, Pablo de Vera, Eugene Surdutovich, Susanna Guatelli, Andrei V. Korol, Anatoly Rosenfeld, Andrey V. Solov'yov (2015) "Comparative analysis of the secondary electron yield from carbon nanoparticles and pure water medium." *The European Physical Journal D* 69(4): 1-9.

Eur. Phys. J. D (2015) 69: 116
DOI: 10.1140/epjd/e2015-50908-y

THE EUROPEAN PHYSICAL JOURNAL D

Regular Article

Comparative analysis of the secondary electron yield from carbon nanoparticles and pure water medium*

Alexey Verkhovtsev[1,2,a], Sally McKinnon[3], Pablo de Vera[4,5], Eugene Surdutovich[6], Susanna Guatelli[3,7], Andrei V. Korol[1,8], Anatoly Rosenfeld[3,7], and Andrey V. Solov'yov[1,2]

[1] MBN Research Center, Altenhöferallee 3, 60438 Frankfurt am Main, Germany
[2] A.F. Ioffe Physical-Technical Institute, Politekhnicheskaya ul. 26, 194021 St. Petersburg, Russia
[3] Centre for Medical Radiation Physics (CMRP), University of Wollongong, NSW, Australia
[4] Departament de Física Aplicada, Universitat d'Alacant, Alicante, Spain
[5] Department of Physical Sciences, The Open University, Milton Keynes, UK
[6] Department of Physics, Oakland University, Rochester, Michigan 48309, USA
[7] Illawarra Health and Medical Research Institute (IHMRI), University of Wollongong, NSW, Australia
[8] Department of Physics, St. Petersburg State Maritime Technical University, Leninskii pr. 101, 198262 St. Petersburg, Russia

Received 23 December 2014 / Received in final form 24 February 2015
Published online 23 April 2015 – © EDP Sciences, Società Italiana di Fisica, Springer-Verlag 2015

Abstract. The production of secondary electrons generated by carbon nanoparticles and pure water medium irradiated by fast protons is studied by means of model approaches and Monte Carlo simulations. It is demonstrated that due to a prominent collective response to an external field, the nanoparticles embedded in the medium enhance the yield of low-energy electrons. The maximal enhancement is observed for electrons in the energy range where plasmons, which are excited in the nanoparticles, play the dominant role. Electron yield from a solid carbon nanoparticle composed of fullerite, a crystalline form of C_{60} fullerene, is demonstrated to be several times higher than that from liquid water. Decay of plasmon excitations in carbon-based nanosystems thus represents a mechanism of increase of the low-energy electron yield, similar to the case of sensitizing metal nanoparticles. This observation gives a hint for investigation of novel types of sensitizers to be composed of metallic and organic parts.